Ellipsometric Investigations of Plasmonic Nanostructures and Thin Films

Von der Fakultät Mathematik und Physik der Universität
Stuttgart zur Erlangung der Würde eines Doktors der
Naturwissenschaften (Dr. rer. nat.) genehmigte Abhandlung

vorgelegt von

Ievgen Voloshenko
aus Kiew

Hauptberichter: Prof. Dr. Martin Dressel

Mitberichter: Apl.-Prof. Dr. Jürgen Weis

Tag der mündliche Prüfung: 11.10.2019
Prüfungsvorsitzende: Prof. Dr. Erik Lutz

1. Physikalisches Institut der Universität Stuttgart

November 2019

Природа с красоты своей
Покрова снять не позволяет,
И ты машинами не вынудишь у ней,
Чего твой дух не угадает.

Владимир Сергеевич Соловьёв

Declaration

I hereby declare that except where specific reference is made to the work of others, the contents of this dissertation are original and have not been submitted in whole or in part for consideration for any other degree or qualification in this, or any other university. This dissertation is my own work and contains nothing which is the outcome of work done in collaboration with others, except as specified in the text and Acknowledgements.

Ievgen Voloshenko
November 2019

Abstract

Die Wechselwirkung von Licht und Materie im Nanobereich spielt eine wichtige Rolle bei der Definition der optischen Eigenschaften und des visuellen Erscheinungsbilds von Materie. Die Natur hat eine Vielzahl von faszinierenden Beispielen, wenn mikroskopische Strukturen zu einem außergewöhnlichen makroskopischen Erscheinungsbild führen. Zum Beispiel die blaue Farbe, die sich in Schmetterlingsflügeln und Pfaufedern befindet, ist eher eine Folge der strukturellen Anordnung als einer Pigmentierung, wie in Fig. 5(a,b) [1] gezeigt. Die goldenen oder grünen Schalen der Skarabäuskäferflügel lassen sich auch durch die strukturellen Anordnung erklären, welche auch in ungewöhnlichen Polarisationseigenschaften auftritt, Fig. 5(c) [2]. Die Fähigkeit, Materie in solchen kleinen Maßstäben zu erforschen und zu manipulieren, erlauben uns nicht nur diese optischen Effekte zu reproduzieren, sondern auch Effekte zu realisieren, die keine Gegenstücke in der Natur haben.[3].

Metalle spielen in der Nanophotonik eine ganz besondere Rolle. Seit der Zeit des antiken Griechenlands, wurden die optischen Eigenschaften von Metallen von Künstler genutzt, um farbenfrohe Farbstoffe und Glasarbeiten herzustellen, obwohl zu dieser Zeit der physikalische Hintergrund des Effekts nicht verstanden wurde. Es ist heute bekannt, dass die phänomenalen optischen Eigenschaften von Metallen durch das Vorhandensein von freien Ladungsträgern bestimmt werden und, was noch wichtiger ist, deren kollektiven Schwingungen, die als Plasmonen bezeichnet werden. Kleine Metallparti-

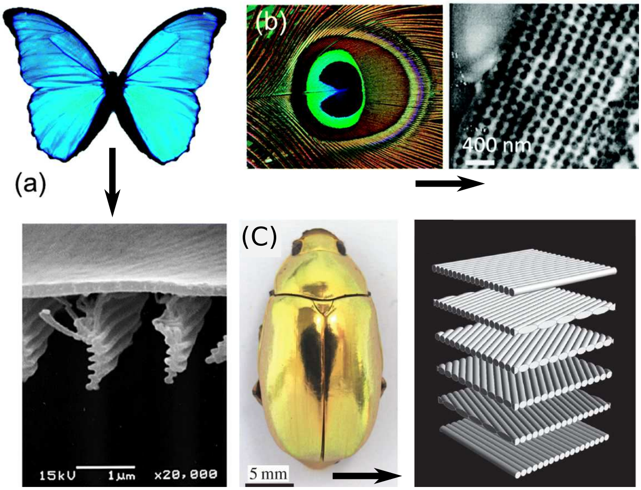

Abbildung 1 (a) Das blau schillernde und SEM-Bild der 1D-Struktur des Morpho-Schmetterlings [1]. (b) Mehrfarbige Pfauenfeder und TEM-Aufnahme eines Querschnitts der 2D-Struktur des blauen Bereichs eines Flügels [1]. (c) Rückansicht von Chrysina resplendens, aufgenommen unter unpolarisierter Beleuchtung, zusammen mit einer Explosionsansicht eines helikoidalen Satzes von Filamentebenen [2].

keln bilden geometrische Hohlräume für Plasmaoszillationen, die resonanten Absorptionseffekten ergeben und zu einer gesättigten, farbigen optischen Reaktion führen.

Metallische Nanopartikel haben jedoch nützlichere physikalische Eigenschaften, weshalb sie zu einem Kern einiger neuer mikroskopischer und spektroskopischer optischer Techniken geworden sind. Durch den Plasmonresonanzeffekt wird das elektromagnetische Feld, das das Teilchen erregt, auf ein kleineres Volumen um das Teilchen beschränkt, was zu einer Erhöhung der Felddichte führt. Dadurch wird zum einen, eine höhere räumliche Auflösung unterhalb der Beugungsgrenze erreicht und zum anderen, ist eine bessere Einkopplung der elektromagnetischen Welle aufgrund höherer Felddichten möglich, was für die Molekülspektroskopie von Vorteil ist. Auf diese Weise können Entitäten, die so klein wie ein einzelnes Molekül sind, entdeckt werden.

In dieser Arbeit werden diese Effekte benutzt, um sowohl technische als auch gründsätzliche Fragen zu den Eigenschaften der Verbundwerkstoffe zu beantworten. Als hauptsächliche spektroskopische Methode wird die Müller-Matrix spektroskopiesche Ellipsometrie verwendet. Die Technik ermöglicht es, eine vollständige polarimetrische Reaktion des Mediums zu erhalten, die auf 16 Müller-Matrix-Elemente reduziert ist. Das, zusammen mit dem Zugriff auf eine Vielzahl von Einfallswinkeln, bietet eine Vielzahl von Parametern für die exakte Wiederherstellung der optischen Eigenschaften des Mediums. Die Untersuchungen wurden an zwei Probentypen durchgeführt, künstlichen plasmonischen Kristallen, die mit lithografischen Methoden hergestellt wurden und an VO_2 dünnen Schichten, die den Isolator-Metall-Übergang bei erhöhten Temperaturen unterstützen, mit lokalisierten plasmonischen Zuständen im Zwischenregime. Die erhaltenen Ergebnisse können wie folgt zusammengefasst werden:

Metrologie von plasmonischen lithographischen Nanostrukturen

Manuskript veröffentlich: I. Voloshenko, B.Gompf, A. Berrier, M. Dressel, G. Schnoering, M. Rommel und J. Weis, Müller matrix metrology: depolarization reveals size distribution, *Appl. Phys. Lett*, **115**, 063106 (2019)

In diesem Teil werden sechs Proben aus Goldnanoscheiben, die durch Elektronenstrahllithographie hergestellt wurden, untersucht. Die Nanoscheiben haben eine Höhe von 30 nm und einen Durchmesser von 190 nm. Die Anordnung der Nanoscheiben ist für jede Probe unterschiedlich. Für drei Proben sind die Scheiben in quadratischen Anordnungen mit unterschiedlichen Teilchenabständen von 439, 312 und 262 nm angeordnet, was der Teilchendichte von 5, 10 und 15 Scheiben/μm^2 entspricht. Das zweite Set von drei Proben enthält die zufällige Anordnung der Nanoscheiben mit der

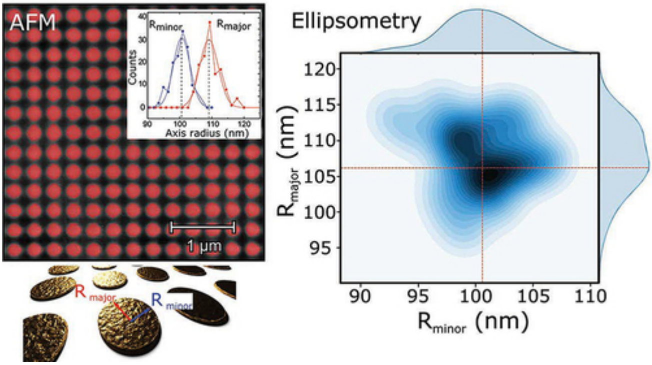

Abbildung 2 Rasterkraftmikroskopische Aufnahme einer Probe mit Segmentierungsmaske (rot) zur Partikelgrößenschätzung, die als Einschaltbild demonstriert wird. Unten ist die künstlerische Ansicht der goldenen Nanoscheiben. Auf der rechten Seite ist die bivariate Verteilung des kleinen und großen Radius der Nanoscheiben dargestellt, die durch Regression der ellipsometrischen Daten der Müller-Matrix extrahiert wurde.

gleichen Teilchendichte. Müller-Matrix Spektren, die sowohl in Transmission als auch in Reflexion aufgenommen wurden, zeigten eine gut definierte Anisotropie der optischen Eigenschaften, ausgedrückt in linearem Dichroismus und Doppelbrechung. Um die Herkunft der Anisotropie zu verstehen, wurden verschiedene numerische Techniken verwendet. Zunächst wurde mit Hilfe eines einfachen Fresnel-Modells die beobachtete Anisotropie mit der Asymmetrie der Partikel in Beziehung gesetzt, die ein nicht beabsichtigtes Artefakt der Produktionsmethode ist. Die Teilchen haben eine elliptische Basis anstatt einer kreisförmigen, obwohl sie häufig eine Exzentrizität von nur 0,14 (kleinster beobachteter Wert) aufweisen. Anschließend wurden mit Hilfe der gekoppelten Dipolannäherung die Abmessungen von kleinen und großen Teilchenradius ermittelt. Es wurde gefunden, dass die erhaltenen Ergebnisse in guter Übereinstimmung mit denen der Rasterkraftmikroskopie sind, die als komplementäre Technik verwendet wird.

Weiter wurden die gemessenen Depolarisationsspektren mit der Größenverteilung von Nanopartikeln über die Probenfläche in Verbindung gebracht. Um die Verteilungsparameter zu bewerten, wurde eine diskrete Dipolannäherung verwendet, um ein Set von Müller-Matrizen zu erzeugen, die der Reaktion von Partikeln mit unterschiedlichen Größen entsprechen. Diese Matrizen werden für die auf der Summenzerlegung basierende Regressionsanalyse verwendet. Eine einfache lineare Regression ermöglicht es, die vollständige bivariate Verteilung der kleinen und großen Partikelradien wiederherzustellen. Der Hauptvorteil dieses Vorgehens besteht darin, dass ein potenziell unbegrenzter Fläche in einer Aufnahme charakterisiert werden kann, was mit anderen mikroskopischen und optischen Techniken nicht möglich ist.

Modellierung des Isolator-Metall-Übergangs in VO_2 Dünnschichten mit anisotroper Brugemann-Annäherung des effektiven Mediums

Manuskript veröffentlich: I. Voloshenko, F. Kuhl, B.Gompf, A. Polity, G. Schnoering, A. Berrier and M. Dressel, Microscopic nature of the asymmetric hysteresis in the insulator-metal transition of VO_2 revealed by spectroscopic ellipsometry, *Appl. Phys. Lett*, **113**, 201906 (2018)

Diese Studie befasst sich mit einer alten Frage der Modellierung der physikalischen Eigenschaften von VO_2 Material über den Isolator-Metall-Übergang. Als Untersuchungssystem wird der 100 nm dicke VO_2 Schicht untersucht. Der Übergang ist ein Perkolationsübergang, bei dem sich die Cluster der metallischen Phasen in der Isolator-Matrix entwickeln. Somit ist der Zwischenzustand ein Verbundwerkstoff und seine Eigenschaften können durch die effektive Medium Annäherung beschrieben werden. In unserer Arbeit haben wir zunächst bestätigt, dass das statische BEMA-Modell, wo die Form der sich entwickelnden Metallcluster befestigt ist, die optischen Eigenschaften in der Nähe der Perkolation nicht reproduziert. Wir haben das Modell auf den anisotropen Fall erweitert, bei dem der Depolarisationsfaktor, der die Partikelform beschreibt, als zusätzlicher Anpassungsparameter verwendet wird. Ein solches Modell schien sehr erfolgreich zu sein, um die optischen Daten über den gesamten thermodynamischen Zyklus zu reproduzieren. Zudem zeigte das Modell, dass sich die Form der Metallcluster im Verlauf des Übergangs ändert und interessanterweise während des Erhitzens und Abkühlens nicht dieselbe ist, was die Asymmetrie der Hysterese erklärt.

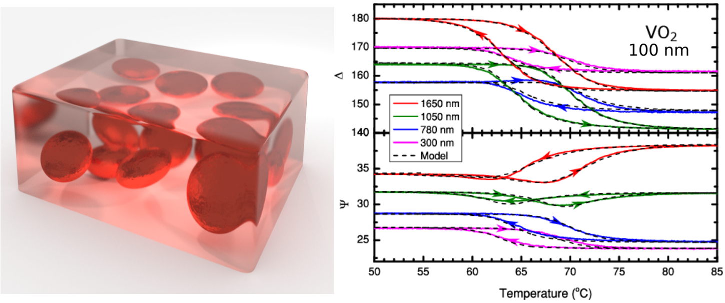

Abbildung 3 Künstlerische Darstellung des Verbundmediums, bei der metallische Cluster (rote Flecken) in der Isolator Matrix sichtbar gemacht werden. Unten sehen Sie das Ergebnis der temperaturabhängigen Anpassung der ellipsometrischen Parameter Ψ und Δ bei unterschiedlichen Wellenlängen für 100 nm dicke VO_2 Schichte unter Verwendung des anisotropen BEMA-Modells.

Infolge ermöglicht das Modell nicht nur den Zugriff auf die optischen Parameter des Systems über den gesamten Zyklus, sondern gibt auch Auskunft über die mikroskopische Natur des Übergangs und wirft neue Fragen zu den am Übergang beteiligten physikalischen Prozessen auf.

Dickenabhängige Messungen des Metall-Isolator-Übergangs in VO_2 Dünnschichten

Manuskript veröffentlich: I. Voloshenko, B.Gompf, A. Berrier, G. Schnoering A. Polity, F. Kuhl and M. Dressel, Interplay between electronic and structural transitions in VO_2 revealed by ellipsometry, *Jour. Vac. Sci. Tech. B*, **37**, 061202 (2019)

In diesem Teil wenden wir das vorgeschlagene Modell an, um Schichten unterschiedlicher Dicke zu untersuchen. Ziel der Studie ist es, den Isolator-Metall-Übergang in VO_2 dünnen Schichten besser zu verstehen und die Fragen nach dem Ursprung der Variation der Clusterform während des Übergangs, der Asymmetrie der Hysterese und der im Übergangsbereich beobachteten erhöhten Absorption zu beantworten . Insgesamt wurden Schichten mit fünf Dicken von 100, 200, 400, 600 und 800 nm untersucht. Die aus den Messungen des Gleichstromwiderstands abgeleitete Übergangstemperatur senkt mit zunehmender Schichtdicke, was ein Zeichen für die Abnahme der inneren Spannung in den Schichten ist. Infolgedessen bieten fünf Proben einen Zugang zu einem bestimmten Bereich des Temperatur-Dehnungs-Phasendiagramms in der Nähe der Volumenübergangstemperatur.

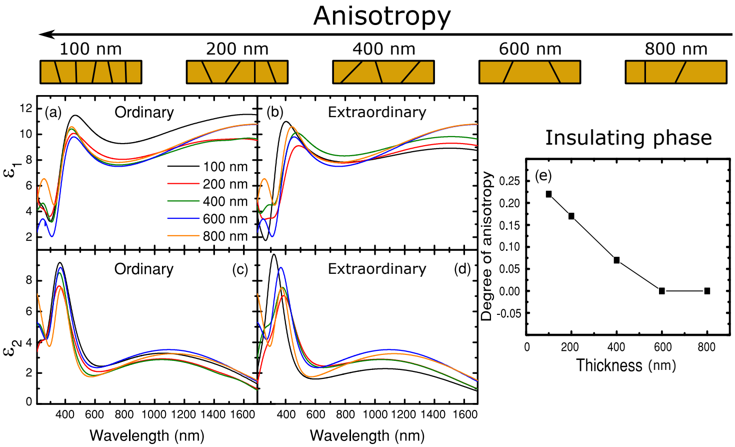

Abbildung 4 Dickenabhängigkeit der Dielektrizitätskonstante von VO_2 dünnen Schichten in der Isolierphase entlang der gewöhnlichen (a, c) und der außerordentlichen (b, d) optischen Achse. Das obige Schema stellt die Dichte der Korngrenzen dar, die mit dem Grad der Anisotropie korreliert, der durch ellipsometrische Modellierung erhalten wird.

Dies korreliert mit der Zunahme der optischen Anisotropie des Schichten mit abnehmender Dicke, die sich aus der Modellierung der ellipsometrischen Parameter ergibt, wie in Abb. 8. Eine detaillierte Analyse der erhaltenen temperaturabhängigen spektroskopischen Daten und der Rauheit zeigt, dass die Variationen der Clusterform durch die Strukturumwandlung in Verbindung mit dem Spannungsrelaxationsprozess bestimmt werden. Dadurch wird der Zusammenhang zwischen kritischer Temperatur und mittlerer Korngröße festgestellt.

Weiterhin wird die Temperaturabhängigkeit der optischen Parameter der Schichten mit Hilfe des BEMA-Modells extrahiert. Das Temperaturverhalten des Imaginärteils der Dielektrizitätskonstante zeigt eine Zunahme der Absorption im Perkolationsregime. Dieser Effekt wird auf die lokalisierte Plasmonresonanzabsorption zurückgeführt, die durch die Bildung getrennter Metallcluster bedingt ist. Die spektralen Eigenschaften der Resonanz werden dann verwendet, um eine grobe Abschätzung einer durchschnittlichen Größe von getrennten Clustern bei der kritischen Temperatur durchzuführen. Schließlich werden die Depolarisationsspektren über den Heizzyklus untersucht, um Informationen über die räumliche Homogenität des Übergangs zu erhalten.

Abstract

Light-matter interaction on the nanoscale plays an important role in defining the optical properties and the visual appearance of matter. Nature has a variety of fascinating examples where microscopic structure results in extraordinary macroscopic appearance. For instance, the blue color observed in butterfly wings and peacock feather is a result of the structural arrangement, rather than pigmentation, as demonstrated in Fig. 5(a,b) [1]. The golden or green shells of the scarab beetle wings are also explained by the microscopic structural arrangements, which also result in uncommon polarization properties, Fig. 5(c) [2]. The ability to probe and manipulate matter on such small scales allows us not only to reproduce these optical effects but to realize effects having no counterparts in nature [3].

Metals play a very special role in the field of nanophotonics. Since the time of ancient Greece, the optical properties of metals have been used by artists to produce colorful dyes and glassworks although, at that time the physical background of the effect was not understood. Today, it is well known that the phenomenal optical properties of metals are governed by the presence of free charge carriers and more importantly their collective oscillations called plasmons. Small metallic particles form geometrical cavities for plasma oscillations resulting in a resonant absorption effects and leading to saturated, colorful optical response.

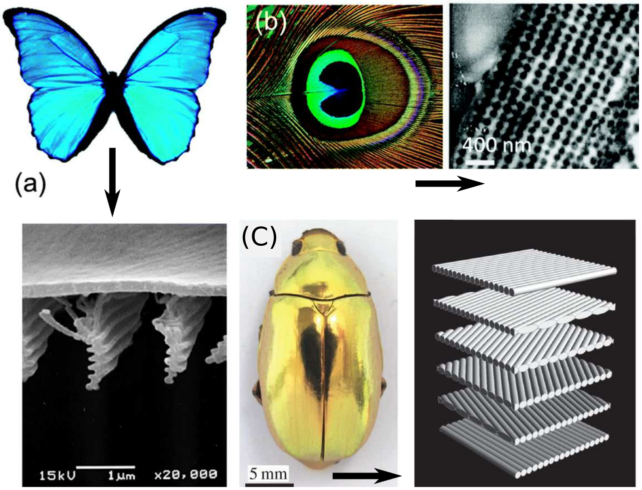

Figure 5 (a) The blue iridescence and SEM image of the 1D structure of the Morpho butterfly [1]. (b) Multi-coloured peacock feather and TEM image of transverse cross section of the 2D structure of the blue area of a wing [1]. (c) Dorsal view of Chrysina resplendens photographed under unpolarized illumination together with an exploded view of a helicoidal set of filament planes [2].

Metallic nanoparticles however, have more useful physical properties, because of which they have become a core component of some new microscopic and spectroscopic optical techniques. Governed by the plasmon resonance effect, the electromagnetic field, exciting the particle, is confined into a smaller volume around the particle, leading to the field density enhancement. Thus, on the one hand higher spatial resolution, below the diffraction limit, is achieved. On the other, a better coupling of the electromagnetic wave due to higher field densities is possible, beneficial for molecular spectroscopy. In such a way, entities as small as single molecule can be detected.

In this work these effects are utilized to answer both technical and fundamental questions regarding the properties of the composite materials. As a main spectroscopic method, Mueller matrix spectroscopic ellipsometry is used. The technique allows one to obtain a complete polarimetric response of the medium, reduced to 16 Mueller matrix elements. This, together with an access to a wide range of incident angles, offers a rich set of parameters for an exact recovery of the optical properties of the medium. The studies have been conducted on two types of samples, artificial plasmonic crystals, produced by lithographic methods and on VO_2 thin films supporting insulator-metal transition at elevated temperatures, with localized plasmonic states in the intermediate regime. The obtained results can be summarized as follows:

Metrology of lithographic plasmonic nanostructures

Manuscript published: I. Voloshenko, B.Gompf, A. Berrier, M. Dressel, G. Schnoering, M. Rommel and J. Weis, Mueller matrix metrology: depolarization reveals size distribution, *Appl. Phys. Lett*, **115**, 063106 (2019)

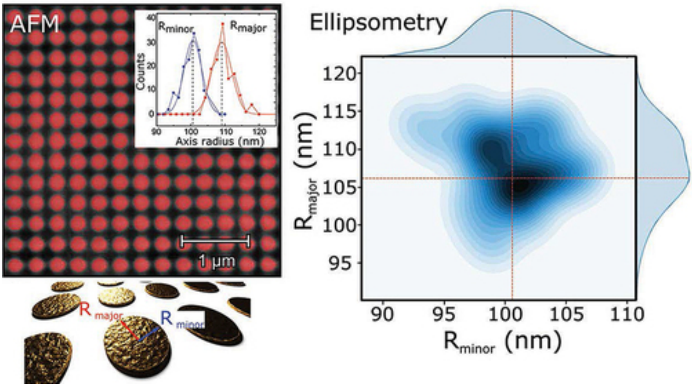

Figure 6 Atomic force microscopy image of one of the sample, with segmentation mask(red) for particle size estimation, which is demonstrated as an inset. Below, the artistic view of the golden nanodiscs. On the right is the bivariate distribution of the nanodisc minor and major radius extracted by regression of the Mueller matrix ellipsometric data.

In this part, six samples consisting of gold nanodiscs, produced by electron beam lithography are investigated. The nanodiscs have a height of 30 nm and 190 nm diameter. The arrangement of the nanodiscs is different for each sample. For three samples, the discs are arranged in square arrays with different interparticle distances of 439, 312, and 262 nm, which corresponds to the particle density of 5, 10 and 15 discs/μm^2 respectively. The second set of three samples contains the random arrangement of the nanodiscs with the same particle density. Mueller matrix spectra collected both in transmission and reflection, has shown a well defined anisotropy of the optical response, expressed in linear dichroism and birefringence. To understand the origin of the anisotropy several numerical techniques were utilized. First, with the help of simple Fresnel model, the observed anisotropy was related to the asymmetry of the particles, which is a non-intended artifact of the production method. The particles have elliptical base, instead of circular, although often with eccentricity as small as 0.14 (smallest observed value). Next, with the help of coupled dipole approximation the dimensions of the particle minor and major radii were recovered. The obtained results were found to be in a good correspondence with the one obtained from atomic force microscopy, used as a complementary technique.

Further, the measured depolarization spectra was associated with the size distribution of nanoparticles over the sample area. To evaluate the distribution parameters, discrete dipole approximation was used to generate a set of Mueller matrices corresponding to the response of particle with different sizes. These matrices are used for regression analysis based on sum-decomposition. A simple linear regression allows us to recover the complete bivariate distribution of particle minor and major radii. The main advantage of this approach is that a potentially unlimited area can be characterized in one shot, which is not possible with other microscopic and optical techniques.

Modeling of the insulator-metal transition in VO_2 thin films with anisotropic Bruggeman effective medium approximation

Manuscript published: I. Voloshenko, F. Kuhl, B.Gompf, A. Polity, G. Schnoering, A. Berrier and M. Dressel, Microscopic nature of the asymmetric hysteresis in the insulator-metal transition of VO_2 revealed by spectroscopic ellipsometry, *Appl. Phys. Lett*, **113**, 201906 (2018)

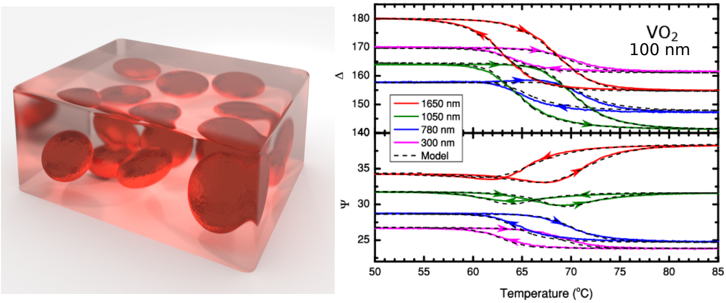

Figure 7 Artistic representation of the composite medium, where metallic clusters (red blobs) are visualized in the insulating matrix. Below is the result of the temperature-dependent fit of ellipsometric parameters Ψ and Δ at different wavelengths for 100 nm thick VO_2 film, using the anisotropic BEMA model.

This study addresses an old question of modeling the physical properties of VO_2 material over the insulator-metal transition. As a system for investigation, the 100 nm thick VO_2 film is used. The transition is a percolation transition, where the clusters of metallic phase develop within the insulating matrix. Thus, the intermediate state is a composite and its properties can be described by the effective medium approximation. In our work we have first confirmed that the static BEMA model, where the shape of the developing metallic clusters is fixed, fails to reproduce the optical properties in the vicinity of the percolation. We further extended the model to the anisotropic case, where the depolarization factor, which describes the particle shape, is used as an additional fitting parameter. Such a model appeared to be very successful reproducing the optical data over the complete thermodynamic cycle. Moreover the model revealed that the shape of the metallic clusters changes over the transition, and interestingly is not the same during heating and cooling, which explains the asymmetry of the hysteresis. As a result, the model not only gives an access to the optical parameters of the system over the complete cycle but also provides an information about the microscopic nature of the transition and opens new questions about the physical processes involved in the transition.

Thickness-dependent measurements of insulator-metal transition in VO_2 thin films.

Manuscript published: I. Voloshenko, B.Gompf, A. Berrier, G. Schnoering A. Polity, F. Kuhl and M. Dressel, Interplay between electronic and structural transitions in VO_2 revealed by ellipsometry, *Jour. Vac. Sci. Tech. B*, **37**, 061202 (2019)

In this part we apply the proposed model to study the films of different thickness. The objective of the study is to obtain a broader understanding of the insulator-metal transition in VO_2 thin films and to answer the questions about the origin of cluster shape variation during the transition, the asymmetry of the hysteresis and the increased absorption observed in the transition region. In total, films of five thicknesses of 100 , 200, 400, 600 and 800 nm were studied. The transition temperature, deduced from the dc-resistivity measurements, decreases with increasing films thickness, being a sign of the decrease of the internal strain in the films. As a result, five samples provide an access to a certain region of the temperature-strain phase diagram, in the vicinity of the bulk transition temperature. This correlates with the increase of film optical anisotropy towards thinner films, obtained from modeling the ellipsometric parameters, as demonstrated in Fig. 8. A detailed analysis of the obtained temperature-dependent spectroscopic and roughness data reveals that

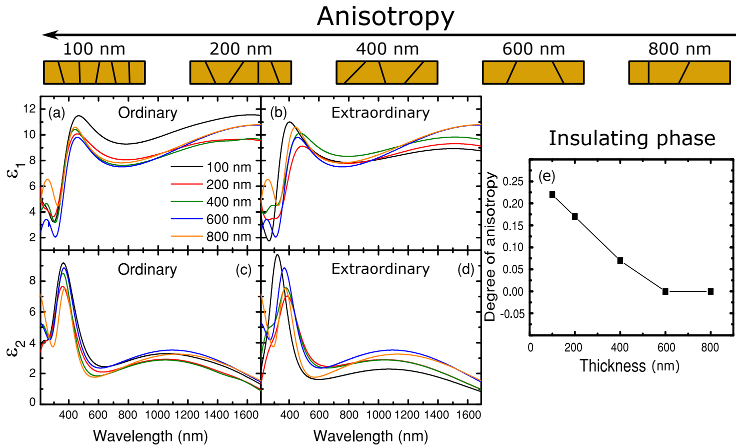

Figure 8 Thickness dependence of the dielectric constant of VO_2 thin films in the insulating phase along ordinary (a,c) and extraordinary (b,d) optical axes. The schematics above represents the grain boundary density, which correlates with the degree of anisotropy obtained from ellipsometric modeling.

the variations in the cluster shape are governed by the structural transformation accompanied by the stress relaxation process. As a result, the connection between critical temperature and the average grain size is established.

Further, the temperature-dependence of the optical parameters of the films are extracted with the help of BEMA model. The temperature behavior of the imaginary part of dielectric constant ε_2 displays an increase in absorbance in the percolation regime. This effect is attributed to the localized plasmon resonance absorption governed by the formation of disconnected metallic clusters. The spectral properties of the resonance is then used to perform a rough estimation of an average size of disconnected clusters at the critical temperature. Finally, the depolarization spectra, during heating, is investigated to obtain information about the spatial homogeneity of the transition.

Contents

List of Figures **xxvii**

List of Tables **xlvii**

1 Theory **1**

1.1 Basic concepts of electromagnetism 1
1.2 Polarization of electromagnetic waves 4
1.3 Dielectric properties of matter 8
  1.3.1 Models of dielectric function 10
  1.3.2 Anisotropic materials 13
  1.3.3 Optical evaluation of dielectric properties 15
  1.3.4 Fresnel equations 17
1.4 Inhomogeneous medium 22
  1.4.1 Mie theory 24
  1.4.2 Electrostatic approximation 27
  1.4.3 Discrete dipole approximation 29
  1.4.4 Coupled dipole approximation 31
  1.4.5 Effective medium approximation 33
  1.4.6 Percolation theory 38
1.5 Plasmonic effects 40
  1.5.1 Surface plasmon-polaritons 41

1.5.2 Localized plasmon-polariton 43
1.6 Mueller matrix formalism 47
1.6.1 Sum decomposition 50
1.6.2 Regression sum decomposition 51
1.6.3 Differential decomposition 52

2 Experimental techniques and instrumentation 55
2.1 Ellipsometry 55
2.1.1 Rotating analyser ellipsometer 56
2.1.2 Rotating compensator ellipsometer 60
2.2 Atomic force microscope 64
2.3 Resistivity measurements 65

3 Results on plasmonic nanostructures 69
3.1 Investigated samples 72
3.2 Square and random arrays 76
3.2.1 Critical dimension analysis with Mueller matrix ellipsometry 76
3.2.1.1 Measured Mueller matrices 80
3.2.1.2 Simulation of optical properties 85
3.2.1.3 Regression analysis 94
3.2.2 Polarization conversion properties 101
3.3 Honeycomb structures 114
3.3.1 Particle symmetry 114
3.3.2 Polarization conversion properties 117
3.4 Conclusion 121

4 Results on metal-insulator transition in VO_2 125
4.1 VO_2 properties 125
4.2 Preliminary characterization of the samples 131
4.3 Properties of the insulating and the metallic phases 140

4.4 Temperature dependence of the VO_2 thin films 148
4.5 Discussion 159
4.6 Conclusion 173

Bibliography 177

Appendix A More information on the Mueller matrices of nanodisc samples 195
A.1 Linecut plots of the measured Mueller matrices on nanodisc samples 195
A.2 Evaluation of the Mueller matrix from the dipole polarization 196
A.3 Validation of the regression analysis 198

Appendix B More information on VO_2 measurements 205
B.1 Depolarization in the samples 205
B.2 Isotropic BEMA model 206
B.3 FTIR measurements 207
B.4 Films topography 208

List of Figures

1 (a) Das blau schillernde und SEM-Bild der 1D-Struktur des Morpho-Schmetterlings [1]. (b) Mehrfarbige Pfauenfeder und TEM-Aufnahme eines Querschnitts der 2D-Struktur des blauen Bereichs eines Flügels [1]. (c) Rückansicht von Chrysina resplendens, aufgenommen unter unpolarisierter Beleuchtung, zusammen mit einer Explosionsansicht eines helikoidalen Satzes von Filamentebenen [2]. viii

2 Rasterkraftmikroskopische Aufnahme einer Probe mit Segmentierungsmaske (rot) zur Partikelgrößenschätzung, die als Einschaltbild demonstriert wird. Unten ist die künstlerische Ansicht der goldenen Nanoscheiben. Auf der rechten Seite ist die bivariate Verteilung des kleinen und großen Radius der Nanoscheiben dargestellt, die durch Regression der ellipsometrischen Daten der Müller-Matrix extrahiert wurde. x

3 Künstlerische Darstellung des Verbundmediums, bei der metallische Cluster (rote Flecken) in der Isolator Matrix sichtbar gemacht werden. Unten sehen Sie das Ergebnis der temperaturabhängigen Anpassung der ellipsometrischen Parameter Ψ und Δ bei unterschiedlichen Wellenlängen für 100 nm dicke VO_2 Schichte unter Verwendung des anisotropen BEMA-Modells. xii

4 Dickenabhängigkeit der Dielektrizitätskonstante von VO_2 dünnen Schichten in der Isolierphase entlang der gewöhnlichen (a, c) und der außerordentlichen (b, d) optischen Achse. Das obige Schema stellt die Dichte der Korngrenzen dar, die mit dem Grad der Anisotropie korreliert, der durch ellipsometrische Modellierung erhalten wird. xiii
5 (a) The blue iridescence and SEM image of the 1D structure of the Morpho butterfly [1]. (b) Multi-coloured peacock feather and TEM image of transverse cross section of the 2D structure of the blue area of a wing [1]. (c) Dorsal view of Chrysina resplendens photographed under unpolarized illumination together with an exploded view of a helicoidal set of filament planes [2]. xvi
6 Atomic force microscopy image of one of the sample, with segmentation mask(red) for particle size estimation, which is demonstrated as an inset. Below, the artistic view of the golden nanodiscs. On the right is the bivariate distribution of the nanodisc minor and major radius extracted by regression of the Mueller matrix ellipsometric data. xvii
7 Artistic representation of the composite medium, where metallic clusters (red blobs) are visualized in the insulating matrix. Below is the result of the temperature-dependent fit of ellipsometric parameters Ψ and Δ at different wavelengths for 100 nm thick VO_2 film, using the anisotropic BEMA model. . . xix
8 Thickness dependence of the dielectric constant of VO_2 thin films in the insulating phase along ordinary (a,c) and extraordinary (b,d) optical axes. The schematics above represents the grain boundary density, which correlates with the degree of anisotropy obtained from ellipsometric modeling. xxi

1.1 (a) Linearly polarized electromagnetic wave, when $\delta_x - \delta_y$=0. (b) Circularly polarized electromagnetic wave, when $\delta_x - \delta_y$=$\pi/2$ and $E_x = E_y$. (c) Elliptically polarized electromagnetic wave, with $\delta_x - \delta_y$=$\pi/4$ and $E_x = E_y$. 5
1.2 Poincare sphere representing polarization states of electromagnetic wave in terms of Stokes S_1, S_2, S_3 unit vectors. LH stands for linear-horizontal polarization, LV represents linear-vertical, L±45° is linear polarization at ±45°, RCP and LCP are right and left circular polarization respectively. 7
1.3 Schematic representation of the transformation between two Cartesian coordinate frames, using the Euler angles α, β and γ. The green axis N, represents the intersection of planes xy and XY. 14
1.4 Sketch of the electromagnetic wave normal to the interface of two media. 15
1.5 Sketch of the oblique incidence of electromagnetic wave on an interface. The angle of incidence is equal to angle of reflection $\theta_i = \theta_r$. θ_t is the refraction angle. n_i and n_t are the complex refractive indices of incident and refracted material. 19
1.6 Angle of incidence-dependent behavior of (a) amplitude coefficients, (b) absolute value of amplitude coefficients, (c) phase for p and s polarizations of reflected and transmitted waves on the interface of two media with refractive indices of $n_i = 1.3$ and $n_t = 2.0$. 20
1.7 Schematic representation of the electromagnetic wave falling on the spherical scatterer. E_{is} and E_{ip} indicate the incident s- and p-polarized electromagnetic waves respectively. r stands for the radius of the sphere. ϕ and θ represent the azimuthal and polar angles respectively. 25

1.8 Mie scattering coefficients a_n at wavelength λ=900 nm as a function of the Au particle radius r, for dipolar (blue) and quadrupolar (red) modes. 27

1.9 Sphere with $r_a = r_b = r_c$, prolate spheroid with $r_a = r_b << r_c$, and oblate spheroid with $r_a = r_b >> r_c$ in respect to the electric field along c-axis. 28

1.10 (a) A desired shape for a simulation, with two materials. (b) A typical representation of the shapes in Discrete Dipole Approximation algorithm, where each sphere represents a dipole. The color in the visualization encodes the dielectric constant of the material. 30

1.11 (a) Calculated extinction cross section C_{ext} for a hexagonal 10x10 lattice of Au nanodiscs with in-plane radius of 70 nm and height of 46 nm, arranged with the lattice spacing a of 220 nm in the ambient medium with refractive index $n = 1.25$ (b) Absolute value of the electric field around the lattice center, excited with the vertical polarization, measured at the distance of 100 nm above the surface. The white line indicate the hexagon containing triangular unit cells. 33

1.12 Schematic representation of the Maxwell-Garnett and the Bruggeman models. The images on the bottom represent the simplified sketch of the boundaries between two constituent media. 35

1.13 Effective dielectric constant as a function of volume fraction of two materials with dielectric constants $\varepsilon_a = 2 + 0.01i, \varepsilon_b = 6 + 0.01i$ for different value of depolarization factor $L_\perp$=0, 0.333, 1. 37

1.14 Dependence of the critical volume fraction on the aspect ratio a/b,where a is axis of symmetry of ellipsoid, obtained with the Monte-Carlo simulations [4] 39

1.15 (a) Dispersion diagram of bulk plasmon-polariton (green) and surface plasmon-polariton (red). The horizontal dashed lines show asymptotic values of ω_p and ω_s. The dashed straight lines represent the light lines in air (orange) and in the prism with permittivity ε_p (blue). (b) Schematic diagram of the SPP excited on the metal-dielectric interface. (c) Schematic diagram of the LSPP on the spherical nanoparticles. 41

1.16 (a) LSPR for spherical nanoparticles with radius 35 nm, composed of different materials; Ag, Al, Au, Cr, Cu, Ni. (b) Spectral response of the gold particles, with radius ranging from 5 to 95 nanometers. (c) Spectral response of the gold nanoparticles with radius of 60 nm emerged in the medium with refractive index n, ranging from 1 to 5. (d) Spectral position of the LSPR as a function of the aspect ratio r_z/r_x for a Au oblate particle. (e) Spectral position of the LSPR as a function of the aspect ratio r_x/r_z for a Au prolate particle. 44

1.17 (a) Extinction cross-section attributed to the collective plasmon resonance for Au spherical nanoparticles arranged in a hexagonal, random and square arrays in comparison to the single particle LSPR. (b) Coupling of the LSPR to the RWA for square arrangements of cylindrical Ag particles with lattice constant of 375 nm, simulated at 0° (green) and 10° (blue) AOI, compared to the single particle LSPR. (c) Schematic diagram of the reciprocal space of the square lattice. (d) Degenerate diffraction orders along Γ-X direction of the reciprocal square lattice as a function of the AOI. The black lines represent grazing diffraction orders emerging from air, and green lines from medium with refractive index n=1.5, calculated according to the equation 1.89 46

1.18 (a) A scheme representing the concept of the differential decomposition. The method allows us to separate optical contributions from infinitesimal slices with differential thickness *z*, along the propagation of the electromagnetic wave. (b) A scheme representing the concept of the Sum decomposition. The method allows us to separate the optical contributions from different regions in-plane, perpendicular to the propagation direction. 53

2.1 Schematic diagram of several ellipsometric configurations. (a) General consideration of Stokes vector transformation. (b) Rotating analyser ellipsometer (RAE). (c) Rotating compensator ellipsometer (RCE). (d) Dual rotating compensator ellipsometer (RC2). The subscript *r* of the elements denote that the element is rotating. 56
2.2 An image of the VASE ellipsometer from the J. A. Woollam company. 59
2.3 An image of the RC2-UI ellipsometer from the J. A. Woollam company. The schematics bellow display the optical beam path with focusing probes of numerical aperture NA=0.1 installed. In the schematics, the Hydrogen lamp is omitted, QWP stands for quarter-wave plate. 63
2.4 (a) Interaction potential as a function of distance to the surface, described be Lenard-Jones equation. The inset demonstrates the scheme of the AFM measurement. (b) Bruker Dimension Icon atomic force microscope, used for measurements in this thesis. 65
2.5 Scheme of the van der Pauw dc-measurement configuration. 66

3.1 SEM images of the samples with the particle densities of 5, 10 and 15 per μm^2. The upper row corresponds to the square lattice arrangements with periodicity of 439 nm for OD05, 312 nm for OD10 and 262 nm for OD15. The bottom row shows the arrangements of the random samples RD05, RD10 and RD15. 74
3.2 5x5 μm AFM image of the honeycomb arrangement of Au nanoparticles with radius $r = 80$ nm, height $h = 30$ nm, arranged with a lattice constant a= 190 nm, measured with 4.5 nm/px resolution. 76
3.3 Ratio of the measured extinction of ordered and random samples with the same particle density. 77
3.4 (a) Measured transmission intensity of the OD05 sample measured at azimuthal angle ϕ=0°, for AOI= 0°-20°. The dispersion of the LSPR is observed due to the RWA with the substrate refractive index $n_{sub} = 1.49$. (b) Azimuthal rotation polar plot of the transmission intensity measured at 16° AOI for wavelength from 400 nm (center) to 1100 nm (outer ring). The dashed line indicates the (1,0) RWA. 78
3.5 Measured ellipsometric parameters (a-b) Ψ and (c-d) Δ, for ordered (left column) and random (right column) samples, with the disc densities of 5 disc/μm^2 (red curve), 10 disc/μm^2 (olive curve) and 15 disc/μm^2 (blue curve). The vertical dashed lines denote the wavelength where Ψ changes sign (crossover) for each of the samples. Horizontal black dashed lines are the guideline for the expected values for an isotropic sample. 79

3.6 Measured normalized Mueller matrix for OD10 sample. The first element M_{11} represents the unpolarized transmission intensity. Radially, the data spans from 400 nm (center) to 1000 nm (outer ring) wavelength, and the azimuthal angle increases in counter-clockwise direction. The factor, above each element, represents the amplitude multiplication factor, for clarity reasons. 81
3.7 Differential (a) mean L_m and (b) uncertainty L_u matrices of OD10 sample for wavelengths from 400 nm (center) to 1000 nm (outer ring). The azimuthal angle increases counter-clockwise and is measured with 5° step. The factor above each element represents the amplitude multiplication factor, for clarity reasons. 83
3.8 L_{m12} element of the differential mean matrix for ordered (top row) and random (bottom row) arrays. The azimuthal angle increases counter-clockwise and the radial component represents wavelength range from 400 nm (center) to 1100 nm (outer ring). 85
3.9 Measurements on the OD10 sample. (a) Normalized azimuthal dependence of unpolarized transmittance spectra using the substrate transmission as a reference. (b) Transmittance of orthogonal polarizations measured at 220° and 130° azimuthal angles α, plotted on a logarithmic scale. (c) Schematic illustration of the nanostructure, where X and Y represent the sample reference frame, r_x and r_y are the major and the minor axes of the nanoparticle, defining particle reference frame, and ϕ is the Euler angle between the two reference frames. (d) Difference in transmittance between orthogonal polarizations measured at different azimuthal angles. 87

3.10 Differential (a) mean L_m and (b) uncertainty L_u matrices of the simulated Mueller matrix obtained from a uniaxial Fresnel model. The wavelengths spawns from 400 nm (center) to 1000 nm (outer ring). The azimuthal angle is counted counterclockwise. 88

3.11 Schematic of the uniaxial Fresnel model with extraordinary optical axis oriented in-plane. The angle Φ represents the Euler angle between the sample and the laboratory reference frames. Imaginary part of dielectric constant extracted from the uniaxial Fresnel model, for ordered (a,c,e) and random (b,d,f) samples. Two Lorentzian oscillators correspond to the LSPR for two orthogonal optical axes denoted as N_o and N_e. 90

3.12 (a) Absorption cross section of the simulated square lattice with particle radii of r_{minor}= 96 nm and r_{major}= 108 nm shown in dashed line. The continuous line represents the imaginary part of dielectric constant extracted from the uniaxial Fresnel model, plotted on the logarithmic scale. (b) Extracted statistical distribution of the minor and major radii of the nanoparticles from the AFM image measured with 5 nm/px resolution. The inset represents the AFM image with the masked regions obtained by value threshold. 92

3.13 (a) The sketch of the sample indicating the illuminated area by the probing beam containing many areas of coherence. The actual scales are exaggerated for clarity. (b) A simplified schematic representing the simulation based on DDA. The illuminated area contains many homogeneous regions, each corresponding to certain particle aspect ratio. The Mueller matrix for each of the regions is calculated separately. The superposition of these matrices results in depolarization. . . 95

3.14 (a) An image representing the coupled dipole approximation model, with single particle represented by a single dipole and the parameters taken for OD10 sample. (b) An image representing the discrete dipole approximation model with periodic boundary conditions (PBC), where each particle is represented as a collection of dipoles. 97
3.15 (a) Resulting regression Mueller matrix (blue) together with the measured Mueller matrix (orange) at azimuthal angle of 0° for OD10 sample. (b) Eigenvalues obtained from Cloude decomposition of the resulting regression matrix (smooth lines) and measured Mueller matrix. (c) Bivariate distribution of the particle size obtained from the fit of the measured spectral Mueller matrix for OD10 sample. 99
3.16 Dispersion of reflected p-polarized (a,c) and s-polarized (b,d) intensity for azimuthal angle 0° and 45° in OD05 sample. The dashed lines represent the Rayleigh lines, where white color represents diffraction emerging from air with refractive index n=1.0 and green from substrate with n=1.49. The labels are the Miller indices of the lattice, where (-1,0) correspond to first Brillouin zone, and (-1,-1) to the second. 102
3.17 Mueller matrix of the OD05 sample measured at azimuthal angle 0° for several AOI. The M_{11} element represents total reflected intensity. The red rectangles mark the off-diagonal block elements which are related to the polarization conversion process. 104
3.18 Azimuthal dependence of the Mueller matrix elements of the OD05 sample measured at 45° AOI. The solid lines depict the Rayleigh-Woods anomalies propagating in air (white) and in substrate (black), emerging from scattering on the first and second Brillouin zones. 105

3.19 Azimuthal dependence of (a) Ψ_{sp} and (b) Ψ_{ps} for OD05 sample measured at 45° AOI. The solid lines represent the RWA according to the previous figures, while the dashed lines are their extended versions. The parts of the figures representing the azimuthal angle above 180°, are symmetric and the RWA would repeat, which is not shown for clarity reasons. 106
3.20 Polarization conversion from p to s polarization normalized by total detected s polarization reflected intensity $\mathrm{R_{ss}}$ measured on OD05 sample at azimuthal angles of (a) 0° and (b) 45° as a function of wavelength and AOI ranging from 20° to 65°. 108
3.21 Azimuthal dependence of the outcoming Stokes vectors S_{out} for different incoming polarizations S_{in} (a) unpolarized light, (b) p-polarized light, (c) $s-$polarized light, (d) 45°-polarized light, (e) -45°-polarized light, (f) right circularly-polarized light and (g) left-circularly polarized light for OD05 sample, measured at 65° AOI. The dashed lines on each element represent the discussed above RWA, black for air and olive for substrate. The RWA are mapped only on the upper part of the graphs, whereas they are symmetric to the lower part. The Stokes parameters $S_1 - S_3$ are normalized by S_0, whereas S_0 represents the total reflected intensity. 110
3.22 Azimuthal dependence of the outcoming polarization ellipse parameters; orientation θ and ellipticity ε for incident p and s polarizations on OD05 sample measured at 65° AOI. . . . 112
3.23 Calculated reflectance based on the Mueller matrix of the OD05 sample measured at 65° AOI, for p and s incident polarizations at azimuthal angles of 0° and 45°. 113

3.24 Differential Mueller matrices L_m and L_u for two honeycomb samples: HC150 (left) and HC190 (right), measured in transmission configuration at normal incidence for wavelengths from 400 to 1000 nm. 115

3.25 Measured optical properties of HC150 (black) and HC190 (red) samples in comparison with the properties of OD10 sample (blue). (a) Depolarization index. (b) Reflected intensity for two orthogonal polarization aligned with the major and minor axes of the nanoparticles (optical axes). (c) Difference between intensities for orthogonal polarizations presented in previous panel. (d) Measured M_{12} Mueller matrix element. . 116

3.26 Measured dispersion relation for *p*- and *s*- polarized light from 20° to 65° AOI with the step of 5° for HC190 sample at azimuthal angles of (a,b) 0° and (c,d) 45°. The wight dashed lines represent the RWA associated with the refractive index of air, n=1.0 and blue lines represent the RWA associated with substrate refractive index n=1.5. The inset in panel (a) represent the scattering of green light, with λ =530 nm, at normal incidence. The inset in (d) represents the scattering, associated with RWA, observed in surface plane of the sample when sample is illuminated at 65° AOI. 118

3.27 Measured Mueller matrix of the HC190 sample for wavelengths from 400 nm to 1690 nm, at azimuthal angle of 45° for AOI from 25° to 65°. The M_{11} element represents the measured total reflected intensity. 119

3.28 Azimuthal dependence of the outcoming polarization ellipse parameters; orientation θ and ellipticity ε for incident *p* and *s* polarizations after interaction with the HC190 sample, measured at 65° AOI, for wavelengths from 400 nm (center) to 1100 nm (outer ring). 120

4.1 VO_2 crystal structure together with a sketch of the band structure around the Fermi level in (a) insulating phase (b) metallic phase. The red spheres represent the Vanadium atoms and blue are the Oxygen atoms. [5] 126

4.2 Temperature-stress phase diagram with deduced monoclinic M_1, M_2 and tetragonal T insulating and rutile R metallic phases. The triple point is estimated to occure at 65 °C for unstrained samples being the value for a bulk single crystal. [6] 127

4.3 Profilometer data recorded on the edge of VO_2 thin films with expected thicknesses of 200, 400, 600, 800 nanometers. . . 132

4.4 Thickness dependence of the evaluated roughness (red symbols) from ellipsometry and AFM data, together with mean grain radius (blue symbols) obtained from AFM. 134

4.5 Temperature-dependent resistivity of VO_2 thin films with thicknesses of 100, 200, 400, 600, 800 nanometers. The inset presents the width of the hysteresis curve versus film thickness. 135

4.6 Derivative of the logarithm of resistivity ρ with respect to temperature T, plotted versus temperature for (a) heating and (b) cooling. The inset in each figure displays a critical temperature versus thickness. 135

4.7 Measured DUV-NIR spectral reflectance as a function of temperature during heating for VO_2 thin films with thickness from 100 nm to 800 nm (a-e). (f) Temperature-dependent reflectance at 1650 nm wavelength as a function of film thickness. 138

4.8 Measured reflectance of the 100 nm VO_2 film at wavelength of 1650, 1050, 780 nm as a function of temperature. The sketches on top demonstrates the increasing volume fraction of the metallic phase, with rise of the temperature. [7] 139

4.9 Fit of the measured ellipsometric parameters (a) Ψ, (b) Δ and (c) reflectance of the insulating phase of 100 nm thick VO_2 film. (d) Schematic representation of an applied isotropic model for the insulating phase of VO_2. The highlighted values are the fitting parameters. 142

4.10 Fit of the measured ellipsometric parameters (a) Ψ, (b) Δ and (c) reflectance of the metallic phase of 100 nm thick VO_2 film.(d) Scheme of the applied isotropic model for the metallic phase of VO_2. The bold highlighted values are the fitting parameters. 144

4.11 Imaginary part of the complex dielectric function for (a) ordinary optical axis in the insulating phase (b) extraordinary optical axis in the insulating phase (d) ordinary optical axis in the metallic phase (e) extraordinary optical axis in the metallic phase of the 100 nm VO_2 film. Blue red and green vertical dashed lines represent the spectral peak position of the interband transitions for ordinary optical axis in the insulating phase (c) Anisotropic difference of optical constants Δn and Δk for insulating phase. (f) Anisotropic difference of optical constants Δn and Δk for metallic phase. 145

4.12 Extracted real and imaginary parts of dielectric constant, for (a,c) insulating phase and (c,d) metallic phase of VO_2 for thickness of 100-800 nm thin films along ordinary optical axes. (e) Spectral position of interband transitions together with the thickness of the roughness layer, as a function of film thickness. (f) Thickness dependence of charge carrier mobility μ and effective mass m* along ordinary optical axis. 146

4.13 Temperature dependence of measured ellipsometric parameter (a)Ψ (b)Δ, together with the resulted fit from BEMA model with a fixed depolarization factor (dotted line) and varying depolarization factor (dashed line), for different wavelengths of 780, 1050, 1650 nm. (c) A closer look on the fit of Ψ at the wavelength of 1650 nm. 151
4.14 Measured ellipsometric parameter Ψ (solid lines) over the IMT, together with the BEMA model fit (dashed lines) at wavelengths of 540, 780, 1050 and 1650 nm for films with thicknesses of 200, 400, 600, 800 nm. 152
4.15 Measured ellipsometric parameter Δ (solid lines) over the IMT, together with the BEMA model fit (dashed lines) at wavelengths of 540, 780, 1050 and 1650 nm for films with thickness of 200, 400, 600, 800 nm. 153
4.16 Temperature dependence of the BEMA parameters for 100 nm thick VO_2 film. (a) depolarization factor $L_{||}$ and (b) corresponding volume fraction f. The inset demonstrates difference in the imaginary part of dielectric function at two critical temperatures T_c^{heat} (red) and T_c^{cool} (blue). 155
4.17 Temperature dependence of the depolarization factor $L_{||}$ for heating (red) and cooling (blue) of VO_2 films with thicknesses of (a) 200 nm (b) 400 nm (c) 600 nm (d) 800 nm. The vertical dashed lines correspond to the insulator-metal transition determined from the dc-resistivity measurements. The horizontal dashed line marks the 0.333 value of the depolarization factor, corresponding to the spherical shape. 156
4.18 Temperature dependence of the roughness layer thickness derived from the BEMA model for samples with thicknesses of 100-800 nm, for heating (red curve) and cooling (blue curve). 158

4.19 Temperature dependence of the roughness determined from ellipsometry (red squares) and AFM (black circles) measurements for (a) 100 nm film, (b) 800 nm film, during heating over the IMT. 158

4.20 Phase-topography AFM measurements on VO_2 thin films with ticknesses of 100, 200, 400, 600, 800 nm. Thickness dependence of the roughness obtained from ellipsometric measurements (red circles), AFM measurements (red triangles) together with the average grain radius (blue squares) obtained from the large scale AFM images. 161

4.21 (a) Temperature dependence of the optical parameters n and k in 600 nm thick VO_2 film, extracted via BEMA model at wavelength of 1100 nm. (b) Corresponding temperature dependence of the dielectric function at the same wavelength. 162

4.22 Temperature and wavelength dependence of the extracted imaginary part of dielectric constant $\varepsilon_2(T,\lambda)$ during heating of VO_2 films with thicknesses of (a) 100, (b) 200, (c) 400, (d) 600 and (e) 800 nm. The value of dielectric constant is normalized to the value of the metallic phase ($T = 90$ °C). . 165

4.23 Signatures of the LSPR in the 100 nm thick VO_2 film. (a) Imaginary part of the temperature-dependent dielectric constant normalized to the value of the metallic phase versus the volume fraction of the metallic phase obtained from the BEMA model. (b) Extinction cross section normalized to maximum extinction cross section versus volume fraction, obtained from CDA simulations of growing VO_2 metallic clusters in the insulating phase with refractive index $n = 3.2$. (c) Obtained extinction cross section from the CDA simulations shown in graph (b), as a function of the cluster in-plane mean radius R. 169

4.24 Temperature dependence of the depolarization index measured in reflectivity configuration for (a) 800 nm thick VO_2 film, (b) 200 nm thick VO_2 film during heating and cooling (curves overlap). 170

4.25 (a) Mueller matrix measured on VASE ellipsometer in transmission as a function of temperature at wavelength of 1550 nm for 400 nm thick VO_2 film. The bottom row is recovered with a two-measurement-regression method. (b) Temperature-dependent depolarization index for the same wavelength derived from the complete Mueller matrix. 172

A.1 (a) Comparison of the Mueller matrices of the OD samples. Intensity for the OD10 sample was not recorded (b) Comparison of the Mueller matrices of RD samples (c) Comparison of the Mueller matrix of OD15 and HC190 samples. The azimuthal angles for each sample are chosen such that the bases of the laboratory and sample frames coincide. 200

A.2 (a) Depolarization index of the OD samples (b) Depolarization index of the RD samples. (c) Depolarization in the OD10 sample at different azimuthal angles measured at 55° AOI. (d) Depolarization index of the RD15 and HC190 sample. . . . 201

A.3 Results of the fit of the known particle size distribution with r_{minor}= 94 nm and r_{major}= 104 nm. (a) The weights, representing different ellipticities of the nanoparticles versus the iterations. (b) Initial (orange) and regressed (blue) Mueller matrices. (c) The eigenvalues of the coherency matrices of the initial and the regression Mueller matrices. (d) The depolarization index of the regression Mueller matrix. 202

A.4 Results of the fit of the known particle size distribution with r_{minor}= 92 nm, r_{major}= 103 nm and r_{minor}= 96 nm, r_{major}= 104 nm. (a) The weights, representing different ellipticities of the nanoparticles versus the iterations (after 40000 iteration). (b) Initial (orange) and regressed (blue) Mueller matrices. (c) The eigenvalues of the coherency matrices of the initial Mueller matrix. (d) The eigenvalues of the coherency matrices of the regression matrix. 203

A.5 (a) Mean square error of fitting with learning rate ε=0.004. The inset shows the depolarization index of the regression matrix, obtained at the minimum of the MSE, in comparison with the measured depolarization index (b) Mean square error of fitting with learning rate ε=0.0004, used for the final fitting. (c) Regression Mueller matrix obtained at the minimum of the MSE with the learning rate ε=0.004. (d) Bivariate size distribution obtained from fitting with learning rate ε=0.004, at the minimal value of MSE. 204

B.1 Depolarization index as a function of wavelength and incident angle measured in 100 nm VO_2 film (a) without suppressing backside reflection, (b) with suppressing the backside reflection by placing the sample on a roughened copper plate. 206

B.2 BEMA fit of the ellipsometric parameter Ψ at λ=1000 nm of 600 nm thick VO_2 film during heating (red) and cooling (blue) cycles with different shape factor (a) $L_{\|}$= 0.333, (b) $L_{\|}$= 0.4 , (c) $L_{\|}$= 0.2 207

B.3 (a) Measured FTIR (black) and simulated ellipsometric (red) reflectivity at normal incidence of the 100 nm VO_2 in the insulating phase. (b) Calculated spectral electrical conductivity of insulating (black) and metallic (red) phases. Δ and Ω indicate interband transitions associated with transition from lower to upper Hubbard band and σ to π^* bands respectively. (c) Measured temperature-dependent far-infrared spectra. . . . 208

B.4 3D topography of the films with 200-800 nm thick films (left column). 2D dimensional representation of the same data (right column) with the red segmentation mask used to extract the grain size properties. 209

B.5 Temperature dependence of the 200 nm thick VO_2 films topography, measured during heating (upper row) and its corresponding auto-correlation function (bottom row). 210

List of Tables

3.1 Optical parameters of the Lorentz oscillators describing nanodisc samples, obtained from the uniaxial Fresnel model of the measured Mueller matrices. A is the amplitude, E is the central energy and Γ is the damping of the Lorentz oscillator. 89

3.2 Physical parameters of the nanodisc samples obtained from fitting optical data presented in table 3.1 by the CDA model as discussed in section 1.4.4. $\Delta\lambda$ is a spectral difference between two resonances. r_{minor} and r_{major} are the radii of the minor and major axes. Δr is the corresponding difference between major and minor radii. e is the particle eccentricity. $\frac{\Delta r}{r}$ is the deviation of the expected radius of 95 nm. Φ represents the Euler angle. 93

4.1 Thickness of the samples derived from modeling ellipsometric data with isotropic and uniaxial models, and from profilometer measurements. μ represents the mean value and σ is the standard deviation. 132

4.2 Sample parameters extracted from the resistivity measurements. Resistivity contrast between insulating R_{i} and metallic R_m phases. Critical temperatures obtained during heating $T_{\mathrm{c}}^{\mathrm{heat}}$ and cooling $T_{\mathrm{c}}^{\mathrm{cool}}$. Transition temperature width during heating ΔT^{heat} and cooling ΔT^{cool}. Hysteresis width ΔH. . . 137

4.3 Optical parameters of the VO_2 thin films, with 100, 200, 400, 600, 800 nm thickness, in the insulating and the metallic phases, derived from the uniaxial Fresnel model. 149

4.4 Aspect ratio $\frac{a}{c}$ of the metallic clusters, calculated according to equation 1.64, at critical temperatures T_c^{heat} and T_c^{cool} . . . 166

Chapter 1

Theory

1.1 Basic concepts of electromagnetism

Historically, electric and magnetic interactions were treated as two separate phenomena. However, in the beginning of the 19th century, scientists of that time have observed the first sign that electric and magnetic field are linked. Hans Christian Ørsted observed, in 1821, that the needle of his compass was deflecting while he turned on and off the current from his battery. This observation induced first attempts to develop mathematical explanation by Andrè-Marie Ampère, resulting in the famous Ampères law. Later, the experimental work of Michael Faraday left no doubts about the relation between electricity and magnetism.

Based on these observation and first mathematical concepts, James Clerk Maxwell developed a mathematical framework which unified the electricity and the magnetism into the electromagnetism. The consequences of his work cannot be overestimated as it brought a first solid understanding that electric and magnetic fields travel as waves, inducing each other. His work is the origin of the progress of the entire 19th and 20th centuries.

The whole classical electrodynamics completely relies on Maxwell equations, which in the most basic form, in SI-units, takes the form [8]:

$$\begin{aligned}
&\nabla\vec{E} = \frac{1}{\varepsilon_0}\rho, \\
&\nabla\vec{B} = 0, \\
&\nabla\times\vec{E} = -\frac{\partial\vec{B}}{\partial t}, \\
&\nabla\times\vec{B} = \mu_0\varepsilon_0\frac{\partial\vec{E}}{\partial t} + \mu_0\vec{J},
\end{aligned} \tag{1.1}$$

where $\vec{E}$ is electric field vector, $\vec{B}$ is magnetic flux density vector, ρ is a charge density, $\vec{J}$ is a current density vector and ε_0, μ_0 are the electric permittivity and magnetic permeability of vacuum respectively. This four equations are the generalization of the discoveries made in the beginning of 19th century in the domains of electricity and magnetism. The first equation is the Gauss law, stating that the source of the electric field is the electric charge. The second equation is an analogue for the magnetic field, showing that there are no magnetic monopoles. The third equation is Faraday law, which tells that changes in electric field induce magnetic field. The fourth equation is the Ampères law with Maxwell correction, stating that the changes in magnetic field induce an electric current and electric field.

In the presence of matter, constitutive equations link the properties of matter and the fields:

$$\begin{aligned}
&\vec{B} = \mu\mu_0\vec{H} = \mu_0\vec{H} + \vec{M}, \\
&\vec{D} = \varepsilon_0\vec{E} + \vec{P}, \\
&\vec{J} = \sigma\vec{E},
\end{aligned} \tag{1.2}$$

where $\vec{H}$ is a magnetic field vector, $\vec{D}$ is electric displacement vector, $\vec{M}$ and $\vec{P}$ are magnetic and electric polarization vectors, ε, μ and σ are relative dielectric constant, relative magnetic permeability and conductivity of matter.

Substituting this into equation 1.1 we obtain Maxwell equations describing light-matter interactions:

$$\begin{aligned}
&\nabla\vec{D} = \rho, \\
&\nabla\vec{B} = 0, \\
&\nabla\times\vec{E} = -\frac{\partial\vec{B}}{\partial t}, \\
&\nabla\times\vec{H} = \frac{\partial\vec{D}}{\partial t} + \vec{J}.
\end{aligned} \tag{1.3}$$

Taking the curl of the curl equations in relation 1.3, we obtain two wave equations which describe the propagation of electromagnetic wave, and its corresponding amplitudes:

$$\nabla\times\nabla\times\vec{E} = \nabla^2\vec{E} = \frac{\varepsilon}{c^2}\frac{\partial^2\vec{E}}{\partial t^2} + \frac{4\pi\sigma}{c^2}\frac{\partial\vec{E}}{\partial t}, \tag{1.4}$$

$$\nabla\times\nabla\times\vec{H} = \nabla^2\vec{H} = \frac{\varepsilon}{c^2}\frac{\partial^2\vec{H}}{\partial t^2} + \frac{4\pi\sigma}{c^2}\frac{\partial\vec{H}}{\partial t}. \tag{1.5}$$

The solution for these equations can be found in a form of plane waves, which are constant frequency waves with infinite plane wavefront:

$$\begin{aligned}
\vec{E}(r,t) &= \vec{E}_0 \exp^{i(\vec{\bar{k}}r - \bar{\omega}t)}, \\
\vec{H}(r,t) &= \vec{H}_0 \exp^{i(\vec{\bar{k}}r - \bar{\omega}t)},
\end{aligned} \tag{1.6}$$

where $\vec{\bar{k}}$ is a complex wavevector and $\bar{\omega}$ is the complex frequency. In this work, I will mainly consider the plane wave solutions of the wave equation. Since at high frequencies of ultraviolet (UV), visible (VIS) and near infrared

(NIR) most of the materials can be assumed as non-magnetic, i.e. μ=1, only equation 1.4 for electric fields would be considered.

1.2 Polarization of electromagnetic waves

As specified in the previous section, electric and magnetic field components in equation 1.6 are vectorial quantities. Thus, more generally, the electric field, for example, can be written as $E(r,t) = [E_x(r,t), E_y(r,t), E_z(r,t)]$. If we assume that an electromagnetic wave propagates along z-axis, then $E_z(r,t) = 0$. The orientation of field variation, or its polarizations then can be represented as a linear combination of the fields in x and y direction [9]:

$$E(z,t) = E_x(z,t) + E_y(z,t) = E_{x0}\exp^{i(kz-\omega t+\delta_x)}\,\hat{\mathbf{x}} + E_{y0}\exp^{i(kz-\omega t+\delta_y)}\,\hat{\mathbf{y}}, \tag{1.7}$$

where $\hat{\mathbf{x}}$ and $\hat{\mathbf{y}}$ are unit vectors along the coordinate axes and δ_x, δ_y are the phases of E_x and E_y.

Notice, that to describe the polarization state it is not required to know the absolute values of δ_x and δ_y, since only relative phase δ_x-δ_y and the amplitude of the fields are taken into account. Based on the relative phase we can obtain linear polarization, where $\delta_x - \delta_y$=0, circular polarization, when $\delta_x - \delta_y$=$\pi/2$, and range of elliptical polarizations, with different ellipticity for other arbitrary relative phases, as visualized in Fig. 1.1. As for linear polarization, the orientation of the field oscillations is fixed, for circular and elliptic polarizations, the resulting field orientation rotates in time. For circular polarization, it is important to note, that the direction of the field rotation, defines the handedness, or chirality, of the electromagnetic wave, resulting in left-circular and right-circular polarizations. The importance of the handedness is related to the investigation of chiral structures and chiral anomaly, possessing the effects of circular dichroism, which would be discussed further in the thesis.

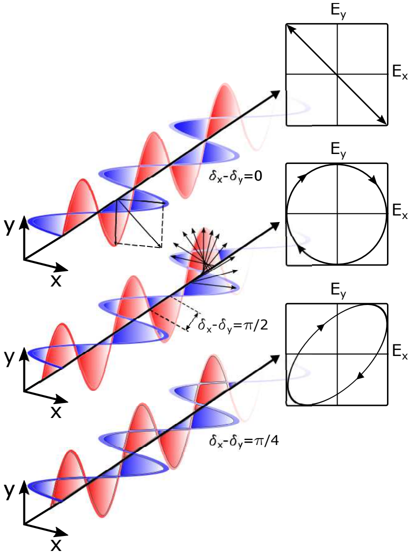

Figure 1.1 (a) Linearly polarized electromagnetic wave, when $\delta_x - \delta_y$=0. (b) Circularly polarized electromagnetic wave, when $\delta_x - \delta_y$=$\pi/2$ and $E_x = E_y$. (c) Elliptically polarized electromagnetic wave, with $\delta_x - \delta_y$=$\pi/4$ and $E_x = E_y$.

The polarization state of electromagnetic wave can be expressed conveniently by the so called Jones vector [10], so the equation 1.7 can be written in the form:

$$E(z,t) = \exp^{i(kz-\omega t)} \begin{bmatrix} E_{x0} \exp^{i\delta_x} \\ E_{y0} \exp^{i\delta_y} \end{bmatrix}. \tag{1.8}$$

When optical measurements are performed, instead of fields, intensities are measured. The total measured intensity of the polarized electromagnetic wave is given by:

$$I = I_x + I_y = E_{x0}^2 + E_{y0}^2 = |E_x|^2 + |E_y|^2 = E_x E_x^* + E_y E_y^*. \tag{1.9}$$

Conventionally, Jones vectors are represented in terms of normalized light intensity, i.e. I=1, so for example, electromagnetic waves polarized along x-axis and along y-axis are represented as:

$$E_{lx} = \begin{bmatrix} 1 \\ 0 \end{bmatrix} \quad \text{and} \quad \mathrm{E_{ly}} = \begin{bmatrix} 0 \\ 1 \end{bmatrix}. \tag{1.10}$$

The Jones vector allows us to conveniently describe any pure polarization state. In nature, however we often deal with partially polarized light, or even unpolarized light; consider the sunlight for example. Depolarization results from field averaging over some random or stochastic parameters, which lead to the loss of field coherence. Further in this thesis, it would become obvious, how depolarization affects the measurement accuracy. It would be shown, that to properly describe an optical system, depolarization effects must be taken into account.

To describe such states, Stokes formalism is used [10]. The Stokes vector represents the polarization state by defining orthonormal basis in polarization space. Typically, Stokes vector looks like:

$$S = \begin{bmatrix} S_0 \\ S_1 \\ S_2 \\ S_3 \end{bmatrix} = \begin{bmatrix} I_x + I_y \\ I_x - I_y \\ I_{+45^\circ} - I_{-45^\circ} \\ I_R - I_L \end{bmatrix} = \begin{bmatrix} 1 \\ \frac{I_x - I_y}{I_x + I_y} \\ \frac{I_{+45^\circ} - I_{-45^\circ}}{I_x + I_y} \\ \frac{I_R - I_L}{I_x + I_y} \end{bmatrix}, \tag{1.11}$$

where S_0 is the total intensity of light, S_1 is the difference of intensity of light polarized along x-axis and y-axis, S_2 is the difference in intensity of light polarized $\pm 45^\circ$ to x-axis, and S_3 is difference between intensity of right and left circularly polarized light. The polarization state can be imaged with the help of Poincare sphere [9], where S_1, S_2 and S_3 are chosen to represent the orthonormal basis of polarization and S_0 represents the radius of the sphere, as shown in Fig. 1.2.

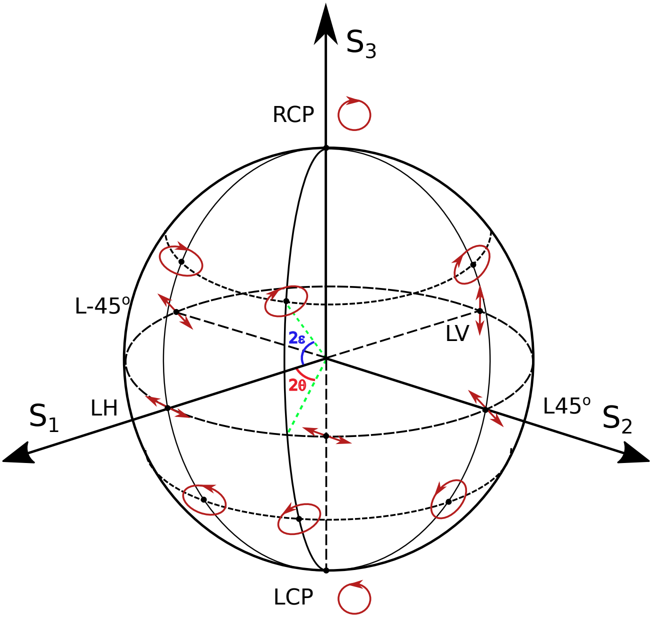

Figure 1.2 Poincare sphere representing polarization states of electromagnetic wave in terms of Stokes S_1, S_2, S_3 unit vectors. LH stands for linear-horizontal polarization, LV represents linear-vertical, L±45° is linear polarization at ±45°, RCP and LCP are right and left circular polarization respectively.

The pure polarization states are represented as points on the sphere surface, whereas the partially polarized states are located within the sphere. The Stokes parameters can be written in new coordinate basis as a function of ellipticity ε and ellipse orientation θ, or in terms of ellipsometric parameters (Ψ, Δ) [9].

$$\begin{aligned} S_1 &= \sin^2\Psi - \cos^2\Psi = -\cos 2\Psi = \cos 2\varepsilon \cos 2\theta, \\ S_2 &= 2\sin\Psi\cos\Psi\cos\Delta = \sin 2\Psi\cos\Delta = \cos 2\varepsilon \sin 2\theta, \\ S_3 &= -2\sin\Psi\cos\Psi\cos\Delta = -\sin 2\Psi\cos\Delta = \sin 2\varepsilon, \end{aligned} \tag{1.12}$$

where $\tan\Psi = E_x^0/E_y^0$ and $\Delta = \delta_x - \delta_y$.

With the Stokes formalism, it is easy then to calculate the degree of polarization p by operating normalized Stokes vector (S_0=1). For partially polarized light, the following inequality holds:

$$S_0^2 > S_1^2 + S_2^2 + S_3^2 \tag{1.13}$$

and the degree of polarization p, as well as depolarization index D, characterizing the amount of depolarization precess, can be determined as:

$$p = (\sqrt{S_1^2 + S_2^2 + S_3^2})/S_0 \qquad D = 1 - p. \tag{1.14}$$

1.3 Dielectric properties of matter

As it has been shown in section 1.1, the constituent equations implement the properties of matter. Consequently, the Maxwell equations, describing the propagation of electromagnetic wave in a medium, are modified accordingly. This underlines the whole principle of optical spectroscopy. By investigating the properties of an electromagnetic wave after interaction with a medium it is possible to extract all the information about the properties of the medium.

Substituting the plane wave equation 1.6, into the wave equation 1.4, we obtain the dispersion relation of the form [11]:

$$\tilde{K}^2 = \frac{\mu\tilde{\omega}^2}{c^2} + \frac{4\pi i\tilde{\sigma}\mu\tilde{\omega}}{c^2}, \tag{1.15}$$

where K is the complex wavevector, ω is the complex radial frequency of the wave,σ is complex electric conductivity and c is the speed of light. Taking into account the losses inside the medium, we can assign a complex dielectric constant, which describes the interaction of EM radiation with the matter:

$$\tilde{\varepsilon} = \varepsilon + \frac{4\pi i\sigma}{\omega} = \varepsilon_1 + i\varepsilon_2. \tag{1.16}$$

In the case of non-magnetic medium, taking into account that μ=1 at optical frequencies, the dispersion relation takes the form:

$$K = \frac{\omega}{c}\sqrt{\tilde{\varepsilon}}. \tag{1.17}$$

To relate the dielectric properties of matter with observables, such as reflectivity for example, it is convenient to introduce a complex refractive index, $\tilde{N}$:

$$K = \frac{\omega}{c}\tilde{N}, \quad \tilde{N} = n + ik, \tag{1.18}$$

where n and k are optical constants of the solid. n is called refractive index and k is an extinction coefficient which describes losses within the material. From the way $\tilde{N}$ is defined we can also write:

$$\begin{aligned} \varepsilon_1 &= n^2 - k^2, \\ \varepsilon_2 &= 2nk, \end{aligned} \tag{1.19}$$

where all quantities are frequency dependent.

The frequency dependence of dielectric properties and optical constants is governed by the finite atomic polarizability and resonant absorption processes. These processes, from a spectroscopic point of view, can be classified according to their resonant energies. Thus, electronic interband transitions, in solids, are usually associated with visible and infrared spectral range, molecular vibrations are observed in the infrared and far-infrared spectral regions, and the response of free electric charge carriers may be probed by frequencies from microwave range up to ultraviolet, dependent on the density and the mobility of the charge carriers in the solid. These interactions separately, as well as combined, have a specific optical response, based on the properties of underlying interactions. Although the models describing underlying physical processes are based on simple physical interpretations, and were established more than a century ago, they are still quite accurately describe the optical response of the majority of the systems and allow to determine its properties.

1.3.1 Models of dielectric function

In this section I will describe a couple of mathematical formulations which are used in this thesis, to extract the dielectric properties of the measured samples. The most simple case, is the solid, where no absorption processes happen in the measured frequency range, as well as in its vicinity. Such medium is transparent in this spectral region and its optical properties are completely governed by the real part of the complex refractive index. To describe the optical properties of such a material empirical models are usually used. The most common choice, is the Cauchy model, which sets the wavelength dependence of the refractive index $n(\lambda)$ as the following expansion:

$$n(\lambda) = A + \frac{B}{\lambda^2} + \frac{C}{\lambda^4}, \tag{1.20}$$

where A, B and C are fitting parameters. If small absorption is present in the vicinity of the modeled spectral region, as in glass substrate in the UV region for example, an Urbach tail can be added to the model:

$$k(\lambda) = A_u e^{B_u\left(\frac{1}{\lambda} - \frac{1}{C_u}\right)}, \tag{1.21}$$

where A_u is amplitude, B_u is width and C_u is a band edge of the absorption tail. Notice however, since n and k are defined separately, one has to be careful when applying this model, in order not to violate the Kramers-Krönig relation.

The first phenomenological model, in the framework of Maxwell equations, describing light-matter interactions, was introduced by Hendrik Lorentz. He proposed that the electron in the atom is bounded to the nucleus by a spring-like force, following the Hooke's law. The applied electric field introduce the displacement of light-weight electrons, making them oscillate due to the restoration force of the atomic nucleus. The oscillation of the electron is described by the Lorentz oscillator model similar to the damped harmonic oscillator:

$$m\frac{d^2\vec{r}}{dt^2} + m\gamma\frac{d\vec{r}}{dt} + m\omega_0^2\vec{r} = -e\vec{E}(t), \tag{1.22}$$

where m, e are electron mass and charge respectively,ω_0 is the resonant frequency, $\vec{r}$ is the displacement vector and $\gamma = \frac{1}{\tau}$ is the damping factor, inversely related to the scattering rate τ. Assuming a harmonic electromagnetic field as in equation 1.17, a frequency dependent expression for complex dielectric constant takes the form:

$$\tilde{\varepsilon}(\omega) = \omega_0 + \frac{\omega_0 \omega_p^2}{\omega_p^2 - \omega^2 - i\gamma\omega}, \tag{1.23}$$

where $\omega_p = \frac{e^2 N}{\varepsilon_0 m_e}$, is the plasma frequency defined by the total number of elementary dipoles N. To separate the real and imaginary part of the dielectric function, the relation is rewritten:

$$\tilde{\varepsilon}(\omega) = \varepsilon_1(\omega) + i\varepsilon_2(\omega) = \frac{\omega_p^2(\omega_0^2 - \omega^2)}{(\omega_0^2 - \omega^2)^2 + \omega^2/\tau^2} + i\frac{\omega_p^2 \omega/\tau}{(\omega_0^2 - \omega^2)^2 + \omega^2/\tau^2}. \tag{1.24}$$

In the case of inhomogeneous distribution of atoms or molecules in the medium, Gaussian oscillator is more relevant:

$$\varepsilon_2(\omega) = Ae^{-(\frac{\omega-\omega_0}{\gamma})^2} - Ae^{-(\frac{\omega+\omega_0}{\gamma})^2}, \tag{1.25}$$

where A is the amplitude of the oscillator. ε_1 is then derived via Kramers-Krönig (KK) relation:

$$\varepsilon_1(\omega) = 1 + \frac{1}{2\pi} P \int_0^\infty \frac{\varepsilon_2(\omega')\omega'}{\omega'^2 - \omega^2} d\omega'. \tag{1.26}$$

The last two oscillator models are also suitable for description of any oscillating phenomena with finite lifetime, such as interband transitions, where an electron is excited to the valence band with higher energy and decays back after some time τ, or localized plasmon oscillations, were electrons dissipate their energy over some time due to scattering.

For the materials, where a band gap is present in the vicinity of the measured spectral range, the Lorentz model must be modified. Following simple logic, that for energies lower than the energy gap, no absorption can occur, due to the absence of free electronic states, the absorption function must be zero; above the energy gap the interaction follows the truncated Lorentz model. Such a model is called Tauc-Lorentz model. The relation for imaginary part of the dielectric constant in this case takes the following form:

$$\begin{aligned} \varepsilon_2(E) &= \frac{AE_0C(E-E_g)^2}{(E^2-E_0^2)^2+C^2E^2}\frac{1}{E} \qquad && \text{for} \quad E > E_g, \\ \varepsilon_2(E) &= 0 && \text{for} \quad E \leq E_g, \end{aligned} \tag{1.27}$$

where $E = \hbar\omega$, $E_0 = \hbar\omega_0$, $C = \hbar\gamma$ and real part of the dielectric constant is again derived from the KK-relation.

In the case of metals, where electrons are not bounded to the nucleus but rather form an electronic cloud, the equation of motion 1.22 must be modified. Paul Drude did this in 1900, by nulling the restoration force, ω_0=0 in the equation, ending up with the differential equation of the form:

$$m\frac{d^2\vec{r}}{dt^2} + m\gamma\frac{d\vec{r}}{dt} = -e\vec{E}(t). \tag{1.28}$$

This yields an expression for the complex dielectric function:

$$\tilde{\varepsilon}(\omega) = 1 - \frac{\omega_p^2}{\omega^2-\tau^{-2}} + i\frac{1}{\omega\tau}\frac{\omega_p^2}{\omega^2+\tau^{-2}}. \tag{1.29}$$

The expression 1.29 takes into account only absorption of the free charge carriers, so-called intraband transitions, and describes well the response of the metals up to IR range. At higher frequencies the interband transitions have strong spectral weight and can dramatically modify the response. Thus, the generalized Lorentz-Drude model is often used, to combine inter- and intraband absorption. The expression for frequency dependent complex dielectric function has the following form:

$$\tilde{\varepsilon}(\omega) = \varepsilon_\infty + \frac{\omega_p^2}{\omega^2 + i\omega/\tau} + \sum_{j=1}^{k} \frac{\omega_{pj}^2}{\omega_{0j}^2 - \omega^2 - i\omega/\tau_j}, \tag{1.30}$$

where the second term represents the superposed contribution of all interband excitations.

1.3.2 Anisotropic materials

So far, the dielectric properties of the material were assumed as scalar values. In nature however, due to the crystal structure, often the properties of matter depend on the direction in the solid. Therefore, the description of the material properties takes the tensor form. The relation between electrical displacement and the electrical field is then generalized to the form of:

$$\begin{bmatrix} D_x \\ D_y \\ D_Z \end{bmatrix} = \varepsilon_0 \begin{bmatrix} \varepsilon_{xx} & \varepsilon_{xy} & \varepsilon_{xz} \\ \varepsilon_{yx} & \varepsilon_{yy} & \varepsilon_{yz} \\ \varepsilon_{zx} & \varepsilon_{zy} & \varepsilon_{zz} \end{bmatrix} \begin{bmatrix} E_x \\ E_y \\ E_z \end{bmatrix}. \tag{1.31}$$

In the case, when optical activity is absent, the dielectric tensor becomes symmetric with $\varepsilon_{ij} = \varepsilon_{ji}$. Moreover, if the coordinate system coincides with the principal axes of the crystal, the tensor is diagonal, with non-diagonal values equal to zero. Materials, where all diagonal elements are different, usually having orthorhombic crystal structure, are called biaxial.

Materials, having two of the diagonal elements equal, tetragonal, hexagonal or trigonal crystal structures, are called uniaxial. In these materials, the direction along z-axis, is usually defined as an extraordinary optical axis, as it breaks the symmetry of the crystal, while two others are called ordinary optical axes, preserving in-plane isotropy. The dielectric tensor of such a material then takes the form:

$$\tilde{\varepsilon} = \begin{bmatrix} \varepsilon_o & 0 & 0 \\ 0 & \varepsilon_o & 0 \\ 0 & 0 & \varepsilon_e \end{bmatrix} = \begin{bmatrix} N_o^2 & 0 & 0 \\ 0 & N_o^2 & 0 \\ 0 & 0 & N_e^2 \end{bmatrix}. \tag{1.32}$$

Whenever the coordinate system of the laboratory frame (lf for laboratory frame) does not coincide with the principal optical axes (sf for sample frame), which is common in ellipsometry measurements, the coordinate system transformation has to be done with the help of the Euler angles α, β, γ. Assuming the transformation between original coordinate frame x, y, z to the rotated coordinate frame X, Y, Z, the angles are defined as follows: α is the angle between x-axis and the intersection line of planes N, β is an angle between z and Z axes, γ is an angle between N and the X axis, as is visualized in Fig. 1.3.

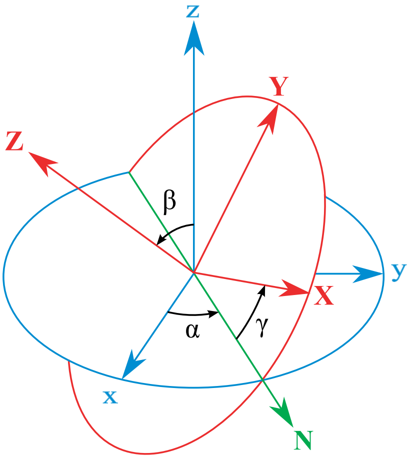

Figure 1.3 Schematic representation of the transformation between two Cartesian coordinate frames, using the Euler angles α, β and γ. The green axis N, represents the intersection of planes xy and XY.

The transformation is expressed as:

$$\varepsilon^{\mathrm{lf}} = \mathbf{A}\varepsilon^{\mathrm{sf}}\mathbf{A}^{-1} = \mathbf{A}\begin{bmatrix} \varepsilon_o^{\mathrm{sf}} & 0 & 0 \\ 0 & \varepsilon_o^{\mathrm{sf}} & 0 \\ 0 & 0 & \varepsilon_e^{\mathrm{sf}} \end{bmatrix}\mathbf{A}^{-1}, \tag{1.33}$$

where **A** is a unitary rotation matrix, defined as:

$$\mathbf{A} = \begin{bmatrix} \cos\alpha\cos\beta - cos\gamma\sin\beta\sin\alpha & \cos\alpha\sin\beta + \cos\gamma\cos\beta\sin\alpha & \sin\gamma\sin\alpha \\ -\sin\alpha\cos\beta - \cos\gamma\sin\beta\cos\alpha & -sin\alpha\sin\beta + \cos\gamma\cos\beta\cos\alpha & \sin\gamma\cos\alpha \\ \sin\gamma\sin\beta & -\sin\gamma\cos\beta & \cos\gamma \end{bmatrix}, \tag{1.34}$$

having the following properties $\mathbf{A}^{-1} = \mathbf{A}^T$ and $\mathbf{A}^{-1}(-\alpha, -\beta, -\gamma) = \mathbf{A}^{-1}$, due to the symmetry of the matrix [10]. This transformation is very general, and is applied many times throughout the thesis.

1.3.3 Optical evaluation of dielectric properties

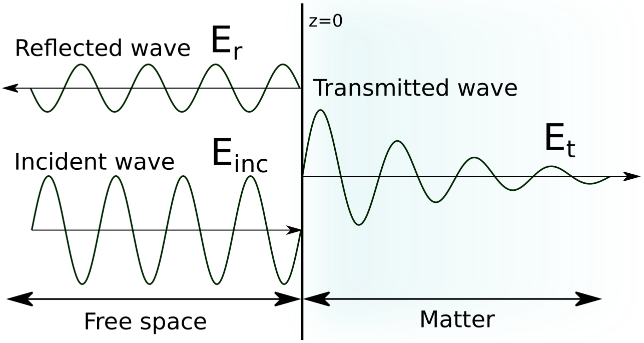

Figure 1.4 Sketch of the electromagnetic wave normal to the interface of two media.

The most common experimental configuration in optical spectroscopy is the normal incidence reflectivity measurement. The sketch of the configuration is shown on Fig. 1.4. With the incident electromagnetic field E_i propagating in free space, along z-axis and oscillating in x-direction, the transmitted field can be written as:

$$E_t = (E_i - E_r) e^{i(Kz - \omega t)}, \tag{1.35}$$

as the continuity equation for the transverse magnetic field H_y requires. This can be also expressed as:

$$(E_i - E_r) = E_t \tilde{N}, \tag{1.36}$$

The continuity equation for the transverse electric filed E_x requires that $E_t = E_i + E_r$. Then, the reflectivity R and the corresponding reflection coefficient r can be expressed as:

$$\begin{aligned} R &= \left| \frac{E_r}{E_i} \right|^2, \\ r &= \frac{E_r}{E_i}. \end{aligned} \tag{1.37}$$

Taking into account both continuity equations for E_x and H_y, we obtain final relations for reflectivity and reflection coefficient in terms of optical constants:

$$R = \left| \frac{1 - \tilde{N}}{1 + \tilde{N}} \right|^2 = \frac{(1-n)^2 + k^2}{(1+n)^2 + k^2}. \tag{1.38}$$

$$r = \frac{1 - n - ik}{1 + n + ik}. \tag{1.39}$$

To relate reflectivity with the transmission measurements, we have to take into account the amount of absorbed power, due to conservation law, which results in:

$$1 = R + A + T. \tag{1.40}$$

Equation 1.39 relates a measurable observable, reflectance, with the optical constants of the material. Since there are two optical constants, n and k, and only one observable, the question arises how to determine both? One common approach is to follow the Kramers-Krönig relation, which is a relation between real and imaginary part of the variable [8]. The problem is, that to apply this relation, the measurement has to be performed over the entire range of frequencies, i.e. up to infinity. Usually, scientists simply extrapolate and interpolate the response at missing frequencies, based on an intelligent guess of the observable behavior. This however, not always leads to satisfactory results.

On the other hand, to determine both, real and imaginary part of the complex refractive index $\tilde{N}$, two independent measurements can be done. One possibility is to perform measurements at different angles of incidence. The other is to measure with different polarizations of the probing electromagnetic wave. In this case, no assumptions about the frequency dependence of the observable outside of the measured range are required. In the next section the equation 1.38 would be generalized for oblique angles of incidence and would be shown to have different outcomes for different polarizations.

1.3.4 Fresnel equations

In section 1.2, the polarization of electromagnetic waves was briefly introduced. The polarization axes were simply denoted according to the spatial axes $\hat{x}$ and $\hat{y}$. In this thesis, however I will stick to the optical convention of denoting polarization according to the plane of incidence. Thus, the two polarizations are referred as p, for field parallel to the plane of incidence (TE) and s, for field perpendicular (senkrecht from German) to the plane of incidence (TM).

In the case of normal incidence, the behavior at the interface for p- and s-polarized wave, is identical. At oblique incidence however, the boundary conditions for both polarizations are different. Fresnel was the first who realized this, although at that time the idea of electromagnetic wave was not yet formulated and the derivations were done entirely on the geometrical basis. He derived two sets of equations, for transmission and for reflection, which relate the observables with the material optical properties, similar to 1.38, but at oblique incidence. Equations for reflection coefficients take the following form:

$$\begin{aligned} r_p &= \frac{n_t \cos(\theta_i) - n_i \cos(\theta_t)}{n_t \cos(\theta_i) + n_i \cos(\theta_t)}, \\ r_s &= \frac{n_i \cos(\theta_i) - n_t \cos(\theta_t)}{n_i \cos(\theta_i) + n_t \cos(\theta_t)}. \end{aligned} \tag{1.41}$$

and for transmission coefficients:

$$\begin{aligned} t_p &= \frac{2n_i \cos(\theta_i)}{n_t \cos(\theta_i) + n_i \cos(\theta_t)}, \\ t_s &= \frac{2n_i \cos(\theta_i)}{n_i \cos(\theta_i) + n_t \cos(\theta_t)}. \end{aligned} \tag{1.42}$$

where n_i and n_t are complex refractive indices of incident and transmitted materials, and θ_i, θ_t are the angle of incidence and angle of refraction, as displayed in Fig. 1.5. Applying the Snell's law, to replace the angle θ_t, the following equations are obtained:

$$\begin{aligned} r_p &= \frac{n_{ti}^2 \cos(\theta_i) - \sqrt{n_{ti}^2 - \sin^2(\theta_i)}}{n_{ti}^2 \cos(\theta_i) + \sqrt{n_{ti}^2 - \sin(\theta_i)}}, \\ r_s &= \frac{\cos(\theta_i) - \sqrt{n_{ti}^2 - \sin^2(\theta_i)}}{\cos(\theta_i) + \sqrt{n_{ti}^2 - \sin^2(\theta_i)}}. \end{aligned} \tag{1.43}$$

where $n_{ti} = n_t / n_i$. The associated transmission coefficients can be obtained from relations $t_p = (r_p + 1)/n_{ti}$ and $t_s = r_s + 1$.

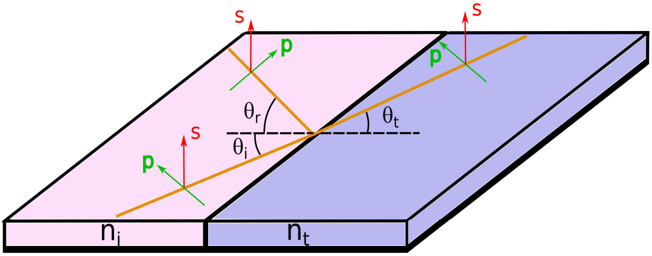

Figure 1.5 Sketch of the oblique incidence of electromagnetic wave on an interface. The angle of incidence is equal to angle of reflection $\theta_i = \theta_r$. θ_t is the refraction angle. n_i and n_t are the complex refractive indices of incident and refracted material.

According to equations 1.43, at oblique incidence the behavior of p and s polarizations are quite different, which is visualized in Fig. 1.6 for an interface of two media with real refractive indices of $n_i = 1.3$ and $n_t = 2.0$. As can be observed, at normal incidence, the amplitude coefficients merge into a single value. The discrepancy rises with the increase of angle of incidence. At some critical angle Θ_B, whose value depends on the ratio of refractive indices, $\tan(\Theta_B) = \frac{n_t}{n_i}$, amplitude coefficient r_p hits zero value, meaning that no reflection occurs for p-polarized light. This angle is called Brewster angle, and is observed for non-absorbing materials. For absorbing materials, r_p never reaches zero value, but it still has a defined minimum, which is referred as pseudo-Brewster angle. For s polarization, the absolute value of r_s is observed to continuously increase with angle of incidence. Since around the Brewster angle the contrast between s and p polarizations is the strongest, ellipsometric measurements are usually performed at these angles, as the highest sensitivity is reached, governed by a relative quantity approach of the technique.

Ellipsometric measurements are performed in different configurations, which are briefly discussed in the next section, but the key principle is to measure the relation between the response of p and s polarizations. In the

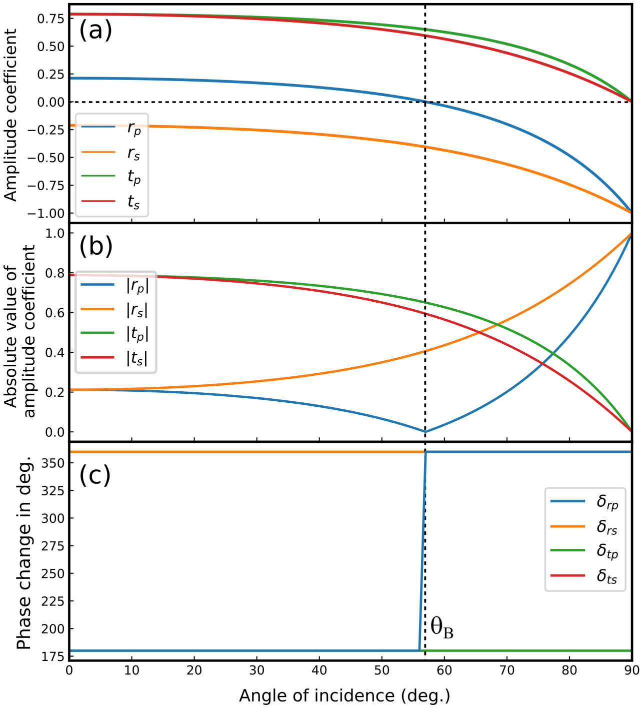

Figure 1.6 Angle of incidence-dependent behavior of (a) amplitude coefficients, (b) absolute value of amplitude coefficients, (c) phase for p and s polarizations of reflected and transmitted waves on the interface of two media with refractive indices of $n_i = 1.3$ and $n_t = 2.0$.

polar form, equation 1.43 takes a more elegant form:

$$\begin{aligned} r_p &= |r_p|e^{i\delta_{rp}}, & r_s &= |r_s|e^{i\delta_{rs}}, \\ t_p &= |t_p|e^{i\delta_{tp}}, & t_s &= |t_s|e^{i\delta_{ts}}, \end{aligned} \tag{1.44}$$

where δ_{rp}, δ_{tp} are the phase terms of reflected and transmitted p-polarized wave respectively and δ_{rs}, δ_{ts} represent the phase of reflected and transmitted

s-polarized wave. This allows us to introduce the main ellipsometric equation as:

$$\begin{gathered}\rho = \frac{r_p}{r_s} = \tan(\Psi)e^{-i\Delta}, \\ \tan(\Psi) = \frac{|r_p|}{|r_s|}, \qquad \Delta = \delta_{rp} - \delta_{rs}.\end{gathered} \tag{1.45}$$

Ψ is the amplitude ratio, whereas Δ is the relative phase between p- and s-polarized waves. It is important to emphasis, that ellipsometry does not recover the absolute phase, but only the relative phase between two polarizations.

The measured transmittance T and reflectance R are expressed simply as:

$$\begin{aligned} R_p &= |r_p|^2, \qquad & R_s &= |r_s|^2, \\ T_p &= Z|t_p|^2, \qquad & T_s &= Z|t_s|^2, \end{aligned} \tag{1.46}$$

where $Z = \frac{n_{ti}\sqrt{1-(1-\cos^2(\theta_i)/n_{ti}^2)}}{\cos(\theta_i)}$. The last equation can be expanded into the case of multilayered system, which is always the case for the samples in this thesis. The expression can be obtained by recursively following the above steps for several layers down to the substrate [9]. Since the expression is quite heavy it is not shown here. In the case of multilayered systems, the secondary beams, reflected from the lower interfaces, are usually also measured, in transparent samples. This not only causes the interference between first and secondary reflections, but also can change the measured polarization state and cause depolarization effect which reduce the sensitivity of the technique. On the other hand, it allows us to determine the thickness of the layer d, with high precision. The total phase variation for the secondary beam α equals 2β, where β is:

$$\beta = \frac{2\pi d}{\lambda}\sqrt{\tilde{N_i}^2 - \tilde{N_t}^2 \sin^2(\theta_1)}. \tag{1.47}$$

This relation allows us to determine the fine thickness of the measured layers, based on the interference, if the complex refractive indices are known.

1.4 Inhomogeneous medium

In the previous section, the anisotropic medium has been discussed, where the properties of matter depend on the orientation of the material. Along a particular direction however, the material was assumed to be homogeneous, meaning that its properties are constant. In reality of course, every material is inhomogeneous, as it consists of atoms with a certain arrangement in space, which results in a periodic potential. The scale of the atomic inhomogeneity is however, very small. As a result, when interacting with the matter on a much larger scale, its properties can be averaged, resulting in a constant response value.

This was first realized by Rudolf Clausius and Ottaviano Mossotti. They where the first, to relate microscopic properties of matter with the macroscopic parameters, such as dielectric constant, for example. The applied electric field E_{inc}, induces the dipole moment p on each lattice site R_i resulting in a dipole distribution:

$$p(r) = \sum_i \alpha E(R_i)\delta(r - R_i), \tag{1.48}$$

where α is the atomic polarizability, $E(R_i)$ is a local field at position R_i and $\delta(r - R_i)$ is a delta function which is equal to unity for $r = R_i$ and 0 elsewhere. The induced dipoles result in a dipolar field E_{dip} which is superposed with the incident filed E_{inc}, resulting in a correction to the local field:

$$E_{loc} = E_{inc} + \sum_i E_{dip}(\alpha E_{loc}, R_i). \tag{1.49}$$

Notice, that the local field is self-consistent, in the sense that it depends on the dipolar field, which itself depends on the local field. The field of an electric dipole is given by :

$$E_{dip}(p, r) = \nabla \frac{1}{4\pi\varepsilon_0} \frac{p\vec{r}}{r^2}. \tag{1.50}$$

Applying the Gauss theorem, integrating this over the volume which encloses the material we obtain the total field induced by all dipoles:

$$E_{dip}(p,r) = -\frac{1}{3\varepsilon_0}P, \tag{1.51}$$

where P is a macroscopic polarization of the material. On the other hand, $P = N\alpha E_{loc}$, where N is the number of dipoles. Combining the last two equations, the total polarization is expressed as:

$$P = N\alpha E_{inc}/(1 - \frac{N\alpha}{3\varepsilon_0}). \tag{1.52}$$

Using the definition of the dielectric constant $\varepsilon = 1 + \frac{P}{\varepsilon_0 E}$, the famous Clausius-Mossotti equation is obtained:

$$\frac{\varepsilon - 1}{\varepsilon + 2} = \frac{N\alpha}{3\varepsilon_0}, \tag{1.53}$$

which in a more general form, assuming dipoles of different types reads as:

$$\frac{\varepsilon - 1}{\varepsilon + 2} = \sum_i \frac{N_i\alpha_i}{3\varepsilon_0}. \tag{1.54}$$

The significance of the last equation is that it provides the relation between the microscopic property α of dipoles and macroscopic dielectric function of the material ε, including dipole-dipole interactions. In addition, as it would be seen in further subsections, it provides the framework for the development of the effective medium theory, often used to describe properties of the composites.

A very similar approach can be applied on the larger scales as long as the size of inhomogeneities is small with respect to the electromagnetic wavelength. The macroscopic response of the medium consisting of several materials can be found by averaging the response of its constituents according to their concentrations. It is reasonable, first to discuss the interactions with only one inhomogeneity embedded into the medium of other type. It is clear that the interaction of the electromagnetic wave with the inhomogeneity would depend on its shape. The simplest case is the interaction with a spherical particle, as it has the highest degree of symmetry; it is discussed in the next subsection.

1.4.1 Mie theory

The interaction of electromagnetic wave with a spherical particles is best described by the Mie theory, giving an exact solution. The incident electromagnetic wave, as in case of atoms, induces polar moments in the spherical particle. Thus, the particle scatters electric field. The relation of incident and scattered field is described by the scattering matrix S [12]:

$$\begin{bmatrix} E_{ss} \\ E_{sp} \end{bmatrix} = \begin{bmatrix} S_2 & S_3 \\ S_4 & S_1 \end{bmatrix} \begin{bmatrix} E_{is} \\ E_{ip} \end{bmatrix} \frac{e^{-ikr+ikz}}{ikr}, \tag{1.55}$$

where E_{ss}, E_{sp} are the scattered field vectors, and E_{is}, E_{ip} are the incidence field vectors for two linear polarizations s and p. The scattering amplitudes S_i are functions of azimuthal and polar angles ϕ and θ [12]. For spherical particles, $S_3 = S_4 = 0$, as the symmetry of the particle allows no polarization conversion. Mie theory provides the solutions for the scattering amplitudes, by solving the scalar Helmholtz equation $\nabla^2\Psi + k^2\Psi = 0$ in the spherical basis. The scattering amplitudes are derived in the form of spherical harmonics expansion, and have the following form:

$$\begin{aligned} S_1(\theta) &= \sum_{n=1}^{\infty} \frac{2n+1}{n(n+1)} \Big(a_n \pi_n\big(\cos(\theta)\big) + b_n \tau_n\big(\cos(\theta)\big) \Big), \\ S_1(\theta) &= \sum_{n=1}^{\infty} \frac{2n+1}{n(n+1)} \Big(b_n \pi_n\big(\cos(\theta)\big) + a_n \tau_n\big(\cos(\theta)\big) \Big). \end{aligned} \tag{1.56}$$

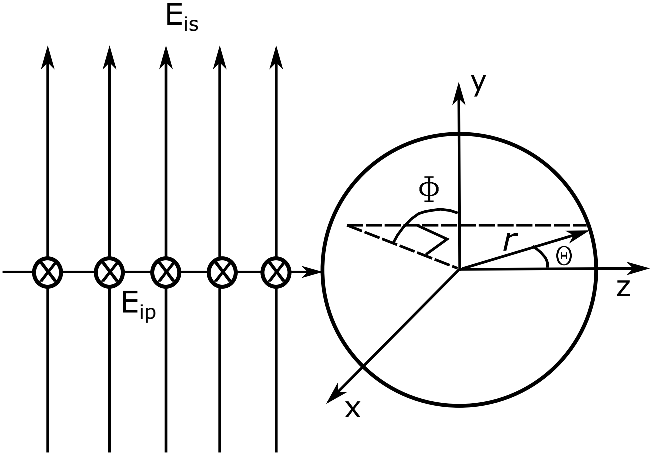

Figure 1.7 Schematic representation of the electromagnetic wave falling on the spherical scatterer. E_{is} and E_{ip} indicate the incident s- and p-polarized electromagnetic waves respectively. r stands for the radius of the sphere. ϕ and θ represent the azimuthal and polar angles respectively.

Here, the angular dependence is governed by the $\pi_n\big(\cos(\theta)\big)$ and $\tau_n\big(\cos(\theta)\big)$ functions which are the Legendre polynomials forming an orthogonal basis:

$$\begin{aligned}\pi_n &= \frac{P_n^1}{\sin\theta},\\ \tau_n &= \frac{dP_n^1}{d\theta}.\end{aligned} \tag{1.57}$$

The Mie scattering coefficients a_n and b_n are determined from the boundary conditions and have the form of:

$$\begin{aligned}a_n &= \frac{m\psi_n(mx)\psi_n'(x) - \psi_n(x)\psi_n'(mx)}{m\psi_n(mx)\xi_n'(x) - \xi_n(x)\psi_n'(mx)},\\ b_n &= \frac{\psi_n(mx)\psi_n'(x) - m\psi_n(x)\psi_n'(mx)}{\psi_n(mx)\xi_n'(x) - m\xi_n(x)\psi_n'(mx)},\end{aligned} \tag{1.58}$$

where m is a relative refractive index N_{sphere}/N, x is a size parameter $x = ka = 2\pi Na/\lambda$, and Ψ_n and ξ_n are the Bessel-Riccati functions. The extinction and scattering cross sections are then expressed as:

$$\begin{aligned}
C_{ext} &= \frac{2\pi}{k^2}\sum_{n=1}^{\infty}(2n+1)(|a_n|^2+|b_n|^2), \\
C_{sca} &= \frac{2\pi}{k^2}\sum_{n=1}^{\infty}(2n+1)\Re(a_n+b_n), \qquad (1.59) \\
C_{abs} &= C_{ext} - C_{sca}.
\end{aligned}$$

Mie theory, can be extended to provide solutions for ellipsoids, however the approach becomes much more complicated, since the spherical symmetry is broken in elliptical particles and additional angular dependence is introduced into the spherical harmonics. Since, in this thesis, mainly non-spherical particles are discussed, another approach to determine the interaction of light with particles is taken. In particular, when the size of the particle is small, the higher modes in expression 1.59, n>1, become vanishingly small. This means that the particles support only dipolar modes, as shown for the gold particle, in Fig. 1.8. This allows us to utilize approximate solutions, in a quasi-static limit, which assume only dipolar interactions. Mie theory provides an information about the validity of the quasi-static approximation. Specifically, the limiting condition can be set as $|\varepsilon x| < 1$, where *epsilon* is a complex dielectric constant of the particle and x is the size parameter, mentioned above. As can be seen from Fig. 1.8, for gold nanoparticles, the quadrupolar moment starts to contribute at the radius of the particle above 60 nm. Although, in comparison to the dipolar term, it is small up to a radius of 100 nm. Above this value, deviations of the results of the quasi-static approximation become considerable and other methods must be used.

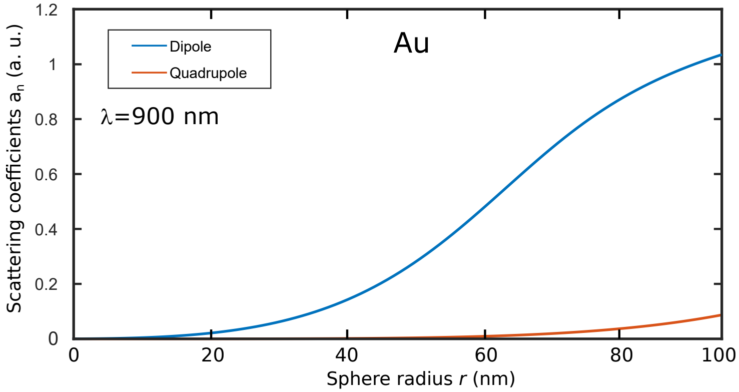

Figure 1.8 Mie scattering coefficients a_n at wavelength λ=900 nm as a function of the Au particle radius r, for dipolar (blue) and quadrupolar (red) modes.

1.4.2 Electrostatic approximation

Let us assume that a small spherical particle is placed in an isotropic homogeneous medium with a different dielectric constant. If a static electric field is applied, the charges accumulate on the surface of the particle, to compensate the field. The separation of charge on a spherical surface results in the dipole moment p, proportional to the applied field:

$$p = 4\pi\varepsilon_m r^3 \frac{\varepsilon - \varepsilon_m}{\varepsilon + 2\varepsilon_m} E_0, \tag{1.60}$$

where ε_m is the dielectric constant of the medium, ε is the dielectric constant of the sphere, and r is its radius. The proportionality constant, which characterizes how easy the dipole moment is induced, is called the polarizability α:

$$\alpha = 4\pi r^3 \frac{\varepsilon - \varepsilon_m}{\varepsilon + 2\varepsilon_m}. \tag{1.61}$$

In general, for an ellipsoid with axes a, b, c, α is a diagonal tensor, where its diagonal elements are determined from:

$$\alpha_i = 4\pi abc \frac{\varepsilon - \varepsilon_m}{3\varepsilon + 3L_i(\varepsilon - \varepsilon_m)}, \tag{1.62}$$

where L_i is a depolarization factor, which depends on the aspect ratio of the ellipsoid, and can be calculated as follows:

$$L_i = \frac{abc}{2} \int_0^\infty \frac{ds}{(s+i^2)\sqrt{(s+a^2)+(s+b^2)+(s+c^2)}}, \tag{1.63}$$

where s is a size parameter having the limits from 0 to ∞. The depolarization factor vector, for any ellipsoid holds the property of $\sum_i L_i$=1. A specific class of ellipsoids are spheroids, with two of the axes equal, is discussed in this thesis. Such shapes leave only one depolarization factor independent. Spheroids are divided into two classes, oblate spheroids having a pancake shape, with $r_a = r_b > r_c$, and prolate spheroids having the cigar-like shape, $r_a = r_b < r_c$, as is visualized in Fig. 1.9.

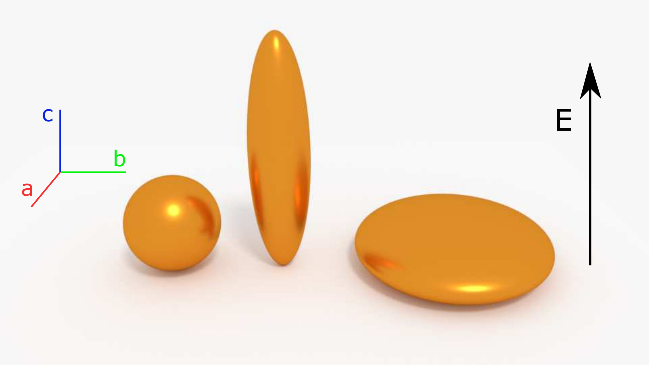

Figure 1.9 Sphere with $r_a = r_b = r_c$, prolate spheroid with $r_a = r_b << r_c$, and oblate spheroid with $r_a = r_b >> r_c$ in respect to the electric field along c-axis.

For spheroids, to determine the depolarization factor, the analytical functions exist, which can be expressed in terms of the particle eccentricity e:

$$\begin{aligned}
&Prolate(a = b < c): \\
&\qquad L_{\perp} = \frac{1-e^2}{e^2}\Big(-1+\frac{1}{2e}\ln(\frac{1+e}{1-e})\Big), \\
&\qquad e^2 = 1-\frac{a^2}{c^2}, \\
&Oblate(a = b > c): \\
&\qquad L_{\perp} = \frac{1+e^2}{e^2}\Big(1-\frac{1}{e}\tan^{-1}(e)\Big), \\
&\qquad e^2 = \frac{a^2}{c^2}-1.
\end{aligned} \tag{1.64}$$

Based on the electrostatic assumptions, a set of simple, yet very powerful techniques have been developed, which are the working tools in this thesis and are discussed in the next subsection.

1.4.3 Discrete dipole approximation

The electrostatic approximation reduces the problem of interaction of electromagnetic wave with a particle down to simple interaction with a dipole, placed in some media. Based on this idea, and taking the inspiration from the Clausius-Mossotti relation 1.54, Purcell and Pennypacker in 1973, developed a method to calculate scattering and absorption of arbitrary shaped particle of interstellar dust [13]. The algorithm represents an arbitrary shape as a collection of point-like dipoles placed on the grid, as depicted in Fig 1.10. Thus, the algorithm has taken the name of discrete dipole approximation (DDA). The dipoles on a grid respond to the excitation from the incident and local fields, and of course interact with each other via their induced electric fields.

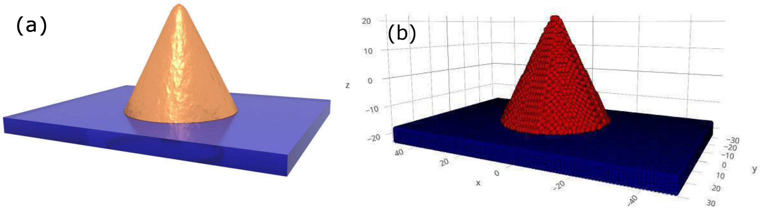

Figure 1.10 (a) A desired shape for a simulation, with two materials. (b) A typical representation of the shapes in Discrete Dipole Approximation algorithm, where each sphere represents a dipole. The color in the visualization encodes the dielectric constant of the material.

Bruce Draine and Piotr Flatau have developed an open source Fortran implementation of this idea [14], which is extensively used in this thesis. The goal of the algorithm is to calculate a system of $3N$ complex linear equations, where N is the number of dipoles:

$$\sum_{k=1}^{N} A_{jk} P_k = E_{inc,j}, \tag{1.65}$$

for given positions of the dipoles r_j, where A_{jk} is $3N$ by $3N$ inverse polarizability matrix, elements of which are defined by:

$$A_{jk} = \frac{\exp^{ikr_{jk}}}{r_{jk}} \times [k^2(\hat{r}_{jk}\hat{r}_{jk} - \mathbf{1}_3) + \frac{ikr_{jk} - 1}{r_{jk}^2}(3\hat{r}_{jk}\hat{r}_{jk} - \mathbf{1}_3)] \qquad j \neq k, \tag{1.66}$$

where $\mathbf{1}_3$ is 3 by 3 identity matrix, $r_{jk} = |r_k - r_j|$, $\hat{r}_{jk} = (r_j - r_k)/r_{jk}$ and $A_{jj}{=}\alpha^{-1}$. The solutions are obtained using complex-conjugate gradient method, as well as fast Fourier transform method, based on the amount of the dipoles N. Once the unknown polarizations P_j are obtained the extinction and absorption cross sections are evaluated as:

$$C_{ext} = \frac{4\pi k}{|E_0|^2}\sum_{j=1}^{N} Im(E^{*}_{inc,j}P_j), \tag{1.67}$$

$$C_{abs} = \frac{4\pi k}{|E_0|^2}\sum_{j=1}^{N} [Im(P_j(\alpha_j^{-1})P_j^{*}) - \frac{2}{3}k^3|P_j|^2]. \tag{1.68}$$

The algorithm was extended by the authors to calculation of the scattering matrix as well as the complete Mueller matrix on the periodic targets [15]. The method however, has a drawback in the sense that the periodic targets can be defined only on the orthorhombic bases, due to the definition of the scattering problem. Thus, it is not a suitable method for systems with more complicated lattice types.

In this thesis, scattering on the nanoparticles, which are at least 5 times smaller than the incident wavelength, is investigated. This validates the quasi-static limit and reduces the problem to dipolar scattering. In addition, the shape of the particles, can always be approximated by the spheroids. This means that particles in the system can be represented by a single dipole and not as their collection. This allows a dramatic improvement of the computation speed, however the approach must be slightly modified to maintain the accuracy. In the following subsection the algorithm of such calculations is discussed.

1.4.4 Coupled dipole approximation

Coupled dipole approximation is a simplified version of the DDA algorithm. The logic is absolutely the same. The main difference is that the particle is now represented with a single dipole instead of their collection. This requires some readjustment of the polarizability term to properly express the particle size in respect to the probing wavelength. The static polarizability α has to be corrected according to the modified long-wavelength approximation

(MLWA) [16]:

$$\alpha_{MLWA} = \frac{\alpha_{static}}{1 - \frac{2}{3} i k^3 \alpha_{static} - \frac{k^2}{r} \alpha_{static}}, \tag{1.69}$$

where $k = nk_0$ is a wave number in the surrounding medium with refractive index n, and r is a particle radius. The second term in the denominator in the equation 1.69 corresponds to the correction due to radiative damping, which grows with the particle volume and corresponds to the linewidth of the resonance. The third term is related to dynamic depolarization on the particle surface, which is responsible for the redshift of the resonance, as the particle increases in size. These two terms define the size range of the particle where the approximation is valid.

The biggest advantage of this algorithm is that it provides the ability to investigate any kind of periodic arrangements in 1, 2 and 3 dimensions. In this thesis I will use my own implementation of the algorithm[1] in python, which provides quite broad capabilities. In particular, it provides a rich library of material dielectric properties, generated based on the Lorentz-Drude equation, with the parameters based on the literature values. A broad class of lattice structures, also including the random arrangements defined by the volume fraction. Finally, it implements calculation and visualization of the near-fields and Mueller matrices based on the precalculated dipoles.

An example of the near-field on the finite hexagonal lattice of gold discs in an effective medium with refractive index $n = 1.25$, is shown in Fig. 1.11. Graph (a), shows the calculated extinction cross section, with the resonance at 632 nm and the inset indicates the parameters of the lattice and particles. The graph (b), shows the projection of the absolute field intensity, in the $x - y$ plane, 100 nm above the lattice, excited with the vertical polarized field. Notice that the field is not equal around different particles. On one hand, this is the consequence of the edge effects on the finite lattice with dimensions of 10 by 10 unit cells, and open boundaries. On the other, the consequence of the diffraction effect, resulting in a formation of new lattice modes. The later is

---

[1] The code of the algorithm is avaliable on github-CDA

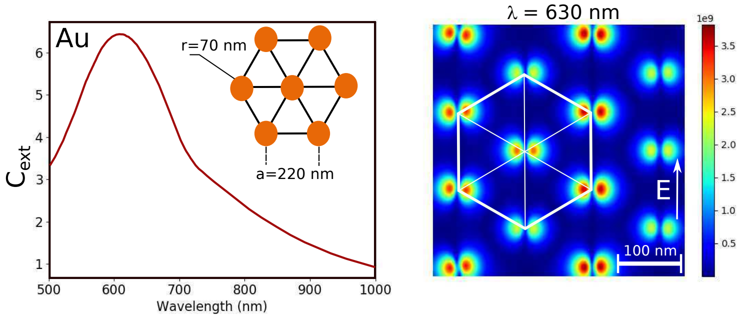

Figure 1.11 (a) Calculated extinction cross section C_{ext} for a hexagonal 10x10 lattice of Au nanodiscs with in-plane radius of 70 nm and height of 46 nm, arranged with the lattice spacing a of 220 nm in the ambient medium with refractive index $n = 1.25$ (b) Absolute value of the electric field around the lattice center, excited with the vertical polarization, measured at the distance of 100 nm above the surface. The white line indicate the hexagon containing triangular unit cells.

very important in the study of artificial plasmonic crystals as the anomalous diffraction can couple to the plasmonic modes and lead to substantial enhancement of the absorption and scattering. The effect is discussed in more details in the subsections, related to the effects of localized plasmon resonances. In the next subsection I will continue the discussion on the medium containing inhomogeneities in the form of particle inclusions, where an analytic expressions can be deduced in order to retrieve the macroscopic response of such a medium.

1.4.5 Effective medium approximation

If the medium contains a lot of scatterers, the macroscopic response of the medium is found by averaging, similar to the Clausius-Mossotti relation. In the simplest case, when the medium with refractive index 1 (air, vacuum) contains spherical inclusions of type a and b, with dielectric constants ε_a and

ε_b, the effective dielectric constant ε_{eff} of the matter can be described by Lorentz-Lorenz equation:

$$\frac{\varepsilon_{eff}-1}{\varepsilon_{eff}+2}=f_a\frac{\varepsilon_a-1}{\varepsilon_a+2}+(1-f_a)\frac{\varepsilon_b-1}{\varepsilon_b+2}, \tag{1.70}$$

where f_a is the volume fraction of the inclusions of type a. In the case, when one type of the inclusions serves as a host, $\varepsilon_b=\varepsilon_h$, enclosing the other material, as shown in Fig. 1.12, the equation 1.70 takes the form of Maxwell-Garnett equation:

$$\frac{\varepsilon_{eff}-\varepsilon_h}{\varepsilon_{eff}+2\varepsilon_h}=f_a\frac{\varepsilon_a-\varepsilon_h}{\varepsilon_a+2\varepsilon_h}. \tag{1.71}$$

This model assumes that the spherical inclusions of type a, are always enclosed only by the dielectric host and cannot be in proximity of the same type of inclusions. As a result the phase transition, in such a model, can be experienced only when the volume fraction of one of the phases reaches 1. The major drawback of this assumption is its asymmetry with respect to the exchange of the host and inclusion material. In reality, it is expected that the only factor which has to influence the averaged composite properties, is a volume fraction of each type of the inclusion. In the case of an equal volume fraction, for example, it is unclear which type of the material serve as a host and which is the inclusion.

The Bruggeman effective medium approximation, shortly BEMA, overcomes this limitation by setting the effective dielectric constant as a host. This approach makes the equation self consistent, in the sense that the presence of the inclusion changes the properties of the host medium, which surrounds it. The equation in this case takes the following form:

$$f_a\frac{\varepsilon_a-\varepsilon_{eff}}{\varepsilon_a+2\varepsilon_{eff}}+(1-f_a)\frac{\varepsilon_b-\varepsilon_{eff}}{\varepsilon_b+2\varepsilon_{eff}}=0. \tag{1.72}$$

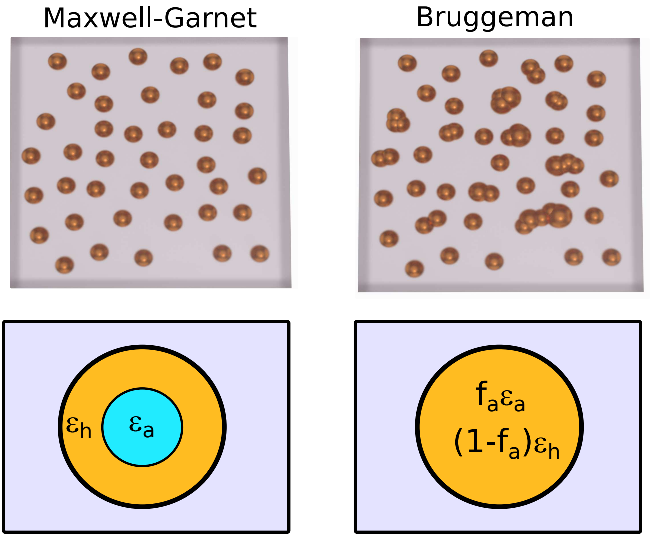

Figure 1.12 Schematic representation of the Maxwell-Garnett and the Bruggeman models. The images on the bottom represent the simplified sketch of the boundaries between two constituent media.

The BEMA model assumes each inclusion to have the dielectric constant of a particular type with some probability, dependent on the volume fraction and independent on the values taken by its neighboring sites. As a result, at high volume fractions, aggregated clusters of the inclusions can be formed, which can result in the phase transition at volume fractions much smaller than 1.

The shape of the inclusions, although they are much smaller than the wavelength, plays an important role in the establishment of an average response of the composite, its anisotropy and phase transition. The above equation, is valid only for the spherical inclusions. To account for other shapes, namely a class of ellipsoids, the equation has to be rewritten in the form:

$$f_a \frac{\varepsilon_a - \varepsilon_{eff}}{\varepsilon_{eff} + L_i(\varepsilon_a - \varepsilon_{eff})} + (1 - f_a) \frac{\varepsilon_b - \varepsilon_{eff}}{\varepsilon_{eff} - L_i(\varepsilon_b - \varepsilon_{eff})} = 0, \tag{1.73}$$

where the L_i is a depolarization factor accounting the polarizability of the particle in a specific direction $i = x, y, z$ defined by the axes of ellipsoid, as introduced in the previous section.

To find the solution for the effective medium dielectric constant, an explicit form of the equation is used:

$$\varepsilon_{eff} = \frac{\varepsilon_a(1-f_b-L_i)+\varepsilon_b(f_b-L)}{2(1-L_i)} \pm \frac{\sqrt{(\varepsilon_a(1-f_b-L_i)+\varepsilon_b(f_b-L))^2-4\varepsilon_a\varepsilon_b L_i(L_i-1)}}{2(1-L_i)}, \tag{1.74}$$

where the minus sign is chosen unless the result is non-physical (negative absorption). An example of shape dependence of the mixing model, based on equation 1.74 is shown in Fig. 1.13(a). Again, two limiting cases, of needles and discs where $L = (0, 0.5, 0.5)$ and $L = (1, 0, 0)$ respectively, can be highlighted. In the first case, the screening factor $L_\perp$ is zero, meaning there is no interaction between two phases, similar to the parallel capacitor in the electric circuit. In such a case the effective dielectric constant is expressed by a simple linear combination:

$$\varepsilon_{eff} = f_a\varepsilon_a + f_b\varepsilon_b. \tag{1.75}$$

In the second case, analogous to the parallel capacitors, with screening factor set to 1, the effective dielectric constant is defined as:

$$\varepsilon_{eff} = \frac{\varepsilon_a\varepsilon_b}{f_a\varepsilon_b + f_b\varepsilon_a}. \tag{1.76}$$

The most commonly used case of the BEMA model in ellipsometry, is modelling of the roughness layer. The roughness layer is expressed as an equal mixture (f= 0.5) of the material and the air, or some other ambient medium encapsulated in form of spheres (L_i= 0.333). The other, is to determine the volume fractions of the composites and porous media, when the dielectric

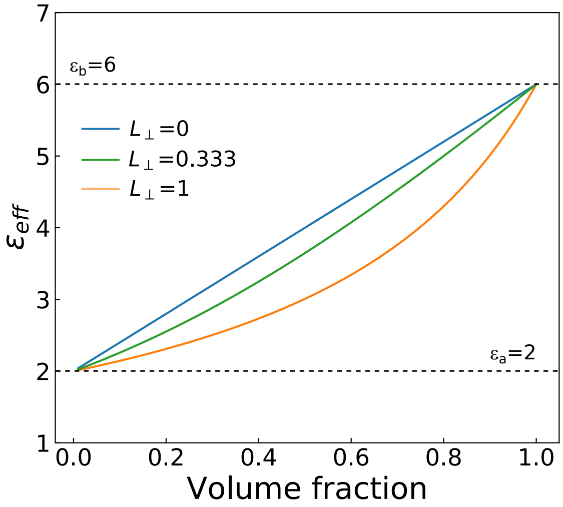

Figure 1.13 Effective dielectric constant as a function of volume fraction of two materials with dielectric constants $\varepsilon_a = 2 + 0.01i, \varepsilon_b = 6 + 0.01i$ for different value of depolarization factor $L_\perp$=0, 0.333, 1.

properties of its constituents are known. The knowledge of the exact volume fraction is very important in certain cases, as the properties of the composites, usually drastically change at certain volume fractions, known as critical volume fraction, or percolation threshold. When mixing dielectric and metallic particles, for example, it is clear that at some volume fraction a metal-insulator transition must occur.

From the definition of the BEMA model, the critical volume fraction f_c is related to the shape of the particle and for spherical particles f_c=L=0.33. The problem is that the predictions of the critical volume fractions from the BEMA model, are inconsistent with theory and experimental results, which is assumed as a major drawback of the model. The percolation theory, predicts a percolation threshold to be independent on the shape, in the case of periodic lattices. In the case of aggregates, where the overlap of the particles is possible, the dependence on the shape appears. Nevertheless, for a 3-dimensional case, the theoretical predictions of the percolation theory is always smaller then one from the BEMA model, and are $f_c = 16\%$ for non-overlapping, and $f_c = 29\%$ for spherical particles. In two- dimensions, the performance of the BEMA model is better, with a common prediction of 50%.

1.4.6 Percolation theory

Percolation theory, aims to study the percolation processes in the mixture compounds. In other words, the theory addresses the question of the connectivity of the objects, placed randomly on a N-dimensional lattice. In particular, starting with an empty lattice, the initial filling fraction $p = 0$. By occupying the lattice site, the filling fraction increases, and clusters are formed, which increase in size with increase of p. At certain filling fraction, called the percolation threshold p_c, a continuous path, connecting the system boundaries emerge. Mathematically, below p_c the probability of percolation is 0, while for $p > p_c$ the probability increase according to the power-law $P \propto (p - p_c)^{\beta}$, with β being a parameter dependent on the dimensionality of the system. The power of the theory is its scale-invariance and its underlying fractal nature.

The exact evaluation of the percolation threshold is of great importance since at this specific filling fraction the physical properties of such a systems show very unique properties. In particular, in systems consisting of metallic inclusions in the dielectric matrix, which is the topic of this thesis, the real part of the effective dielectric constant is expected to diverge in the static limit, $\omega = 0$. The divergence is governed by the divergence of the capacitive coupling, between the metallic clusters, since the intercluster distance approaches zero as $p \rightarrow p_c$. At finite frequency, the real part of the dielectric constant is described by:

$$\varepsilon_1^{eff}(\omega, p_c) = \varepsilon_{1d} \left(\frac{\sigma_m}{\omega \varepsilon_0 \varepsilon_{1d}} \right)^{1-u}, \tag{1.77}$$

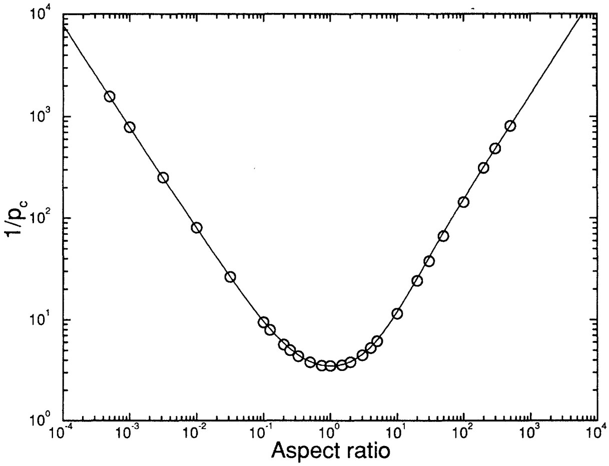

Figure 1.14 Dependence of the critical volume fraction on the aspect ratio a/b,where a is axis of symmetry of ellipsoid, obtained with the Monte-Carlo simulations [4]

where σ_m is the conductivity of the metallic phase, ε_{1d} is the real part of the dielectric constant of the dielectric phase, and u is a critical exponent dependent on the dimensionality, which takes value of 0.62 in 3-dimensional case. After the peak values, the effective dielectric constant rapidly decreases, crossing the zero value, ε_{eff}=0, where the properties of the composite become metallic.

In the case of non-overlapping particles, the percolation threshold is known to be shape independent. The volume fraction, occupied by particles is simply described as $p = nV_p$, where n is a total number of particles and V_p is the volume of one particle. In the overlapping case, the volume fraction is rather defined by $p = 1 - e^{-nV_p}$. Since the excluded volume depends on the shape of the particle and is minimized for the sphere, the critical volume fractions are expected to have lower values for any other finite geometries of the particles. Indeed, as shown in Fig. 1.14 [4], for both oblate and prolate spheroids, $1/p_c$ takes larger values than in the case of a sphere.

For overlapping spheres the calculations yield a percolation threshold of 0.285. For oblate and prolate inclusion the value of p_c decreases, however with different rate, dying off faster for prolate shapes. In the analysis of the experimental results, I would refer to the results obtained in this study, as they are more general and reliable compared to the values extracted from the BEMA model.

1.5 Plasmonic effects

In section 1.3, the dielectric model for metals was introduced. The Drude model, describes the response of free charge carriers to the electromagnetic wave. Plasmon-polariton is the term describing collective oscillations of free charge carrier density in the material coupled to the EM field and is associated with the notion of plasma frequency ω_p. Based on the Drude model 1.29, the dispersion of such oscillations, with the momentum k, in the lossy medium, combined with the equations 1.17 , has to satisfy the condition [11]:

$$k = k_0\sqrt{1-\frac{\omega_p^2}{\omega^2}}, \tag{1.78}$$

resulting in dispersion relation for bulk plasmon-polaritons:

$$\omega^2 k_0^2 = \omega^2 k^2 - \omega_p^2 k_0^2. \tag{1.79}$$

The dispersion equation states that the bulk plasmon-polaritons below the plasma frequency cannot propagate in plasma, as they get screened out. They propagate with frequencies above the plasma frequency and at higher momentum are asymptotic to the light-line, as depicted further in Fig 1.15(a).

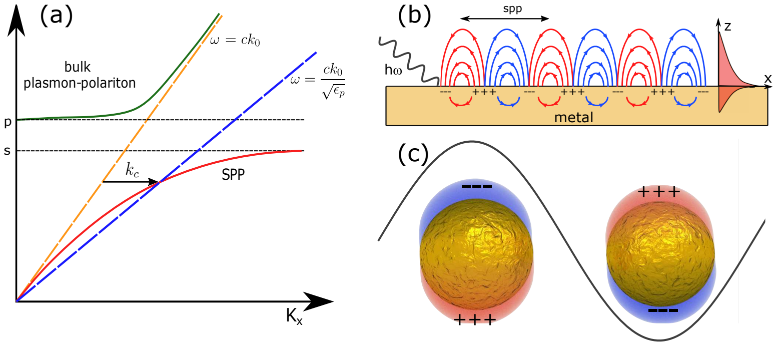

Figure 1.15 (a) Dispersion diagram of bulk plasmon-polariton (green) and surface plasmon-polariton (red). The horizontal dashed lines show asymptotic values of ω_p and ω_s. The dashed straight lines represent the light lines in air (orange) and in the prism with permittivity ε_p (blue). (b) Schematic diagram of the SPP excited on the metal-dielectric interface. (c) Schematic diagram of the LSPP on the spherical nanoparticles.

1.5.1 Surface plasmon-polaritons

The significance of the plasmon-polaritons arises from the fact that they can exist as surface waves propagating along the boundary of dielectric and conductor. Such waves are called surface plasmon-polaritons (SPP). The condition of existence of such waves arises from the continuity properties of the tangential components of electric and magnetic fields at the interface. In general, the conditions for existence of the surface modes propagating in arbitrary direction x along the interface between two media with dielectric constants ε_d and ε_m are [11]:

$$\varepsilon_d \varepsilon_m < 0, \quad \varepsilon_d + \varepsilon_m < 0, \tag{1.80}$$

which ensures that the signs of the dielectric constants ε_d, ε_m are opposite, and:

$$k_x = k_0 \sqrt{\frac{\varepsilon_d \varepsilon_m}{\varepsilon_d + \varepsilon_m}}, \tag{1.81}$$

ensuring that the momentum of the wave is real. As one of the materials is metallic, its dielectric constant is complex, consequently k_x is complex valued. Separating the real and imaginary part, the equation above takes the form:

$$k_x = k_{1x} + k_{2x} = k_0 \left(\frac{\varepsilon_{1m}\varepsilon_d}{\varepsilon_{1m} + \varepsilon_d} \right)^{1/2} + k_0 \left(\frac{\varepsilon_{1m}\varepsilon_d}{\varepsilon_{1m} + \varepsilon_d} \right)^{3/2} \frac{i\varepsilon_{2m}}{2\varepsilon_{1m}^2}. \tag{1.82}$$

As the losses are present in the above equation, the SPP exponentially decays while propagating along the interface according to the exponent $e^{-2k_{2x}x}$, which defines the propagation length of the SPP L_{spp} as :

$$L_{spp} = \frac{1}{2k_{2x}}. \tag{1.83}$$

Normal to the interface the field of the SPP decays exponentially $e^{-k_z \dot{z}}$. As two materials on the interface have different dielectric properties, the penetration depth, or more commonly the skin depth $\delta = 1/2k_{2z}$, is different, as the normal momentum for both media is:

$$k_{zd} = \sqrt{\varepsilon_{1d}k_0^2 - k_x^2}, \quad k_{zm} = \sqrt{\varepsilon_{1m}k_0^2 - k_x^2}. \tag{1.84}$$

The sketch of the field distribution on the interface of two media is displayed in Fig 1.15(b). The dispersion relation of the SPP is displayed in Fig 1.15(a). At low frequencies the waves follow the light line and has light-like properties. As the frequency increases the mode deviates and approaches the saturation value of ω_s which is defined as [11]:

$$\omega_s = \frac{\omega_p}{\sqrt{1 + \varepsilon_{1d}}}. \tag{1.85}$$

It is clear that the dispersion line of the SPP is located outside of the light cone. Thus to excite it, an additional in-plane momentum has to be provided. This is commonly done with the help of an optical prism with high refractive index according to Otto or Kretschmann configurations [17]. On the other hand additional momentum to the coupling electromagnetic wave can be provided by scattering or diffraction. If, for instance, a diffraction grating, with some periodicity P is formed on the surface of the metal, the diffracted electromagnetic waves would obtain an additional in-plane momentum $k_c = \frac{n2\pi}{P}$, by reflecting on the unit cell boundaries [18–20]. If $k_0 + k_c = k_{spp}$ the electromagnetic wave would excite a surface plasmon-polariton.

When SPP is exited its wavelength is much smaller than the wavelengths of light and the field density close to the interface is very large[21–24]. These are the key physical phenomena which make plasmonics very attractive for applied physics. The small wavelength of the SPP allows us to achieve sub diffraction limit imaging, and the large surface fields provide stronger coupling, leading to enhanced sensitivity in different spectroscopic methods. The hindrance of the direct excitation of the SPP is however introducing many limitations for the practical use of the effect.

1.5.2 Localized plasmon-polariton

Luckily, oscillations of plasma also exist in the isolated particles containing free charge carriers. If particles are small in comparison to the excitation wavelength, the interactions are well described within the quasistatic limit, as described in section 1.4. According to the equation 1.61, the resonance of the polarizability occurs when the denominator $\varepsilon_p + 2\varepsilon_m$ equals zero:

$$\Re(\varepsilon_p(\omega)) = -2\varepsilon_m(\omega), \tag{1.86}$$

where ε_p is the dielectric constant of the particle and ε_m is the dielectric constant of the surrounding medium. This is known as Fröhlich condition, resulting in the excitation of localized surface plasmon resonance LSPR [25]. As the polarizability depends not only on the dielectric properties but also on the shape of the nanoparticle, expressed in terms of depolarization factor, in equation 1.62, the resonance can also be tuned by the shape of the nanoparticles. This is illustrated in Fig. 1.16, where the resonance of

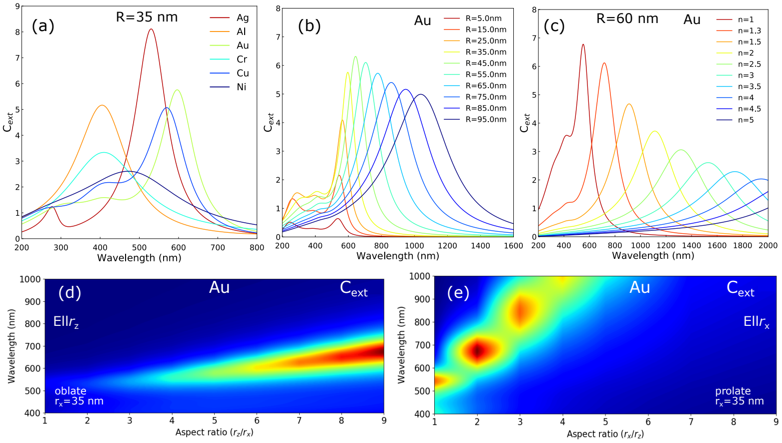

Figure 1.16 (a) LSPR for spherical nanoparticles with radius 35 nm, composed of different materials; Ag, Al, Au, Cr, Cu, Ni. (b) Spectral response of the gold particles, with radius ranging from 5 to 95 nanometers. (c) Spectral response of the gold nanoparticles with radius of 60 nm emerged in the medium with refractive index n, ranging from 1 to 5. (d) Spectral position of the LSPR as a function of the aspect ratio r_z/r_x for a Au oblate particle. (e) Spectral position of the LSPR as a function of the aspect ratio r_x/r_z for a Au prolate particle.

nanoparticles is calculated with different parameters, using the CDA algorithm. As can be seen the spectral position of the LSPR can be effectively tuned by changing the composite, size, surrounding medium, or the aspect ratio and shape of the nanoparticle. What is more important, is the fact that LSPR directly couples to the incident electromagnetic field, due to the geometry of the particles, which satisfies the boundary conditions for the excitation.

LSPR by its nature is different from the SPP, as the oscillations are bound to the particles and cannot propagate. When dealing with the collection of the particles however, the generated dipole fields on one particle can induce the fields on its neighbours, if the particles are close enough. Thus the particles interact with each other and the plasma oscillations can still propagate along the chains of nanoparticles [26, 27]. In general the response field of the nanoparticle is described by the expansion [8]

$$E = -\nabla\Phi = \frac{1}{4\pi\varepsilon_0}\left(\frac{q\vec{n}}{|r-r_0|^2} - \frac{3\vec{n}(p\vec{n})-p}{|r-r_0|^3} + ...\right), \tag{1.87}$$

where r is the particle position, $\vec{n}$ is the unit vector in the direction of $r - r_0$ and p is the dipole moment. The second term in the expansion represents the dipole contribution. In the quasistatic limit dipolar term is dominant, i.e. all the higher orders can be neglected. To fulfill the quasistatic limit the interparticle distance a has to fulfill the condition $a = 3r$, where r is the particle radius [27]. In such a case the interaction between two particles i, j can be considered as simple dipole-dipole interaction and can be expressed as:

$$W = \frac{p_i p_j - 3(p_i\vec{n})(p_j\vec{n})}{|r_i - r_j|^3}. \tag{1.88}$$

Such interaction results in the phenomena called collective LSPR, the plasmonic oscillations which can extend far beyond single nanoparticle. The collective plasmon oscillations are dependent not only on the interparticle distance but also on their arrangement. For instance, Fig. 1.17 (a) shows extinction cross section associated with the collective plasmon resonance calculated for different gold nanoparticle arrangements. It is clear that the amplitude, as well as the spectral position of the LSPR varies, especially compared to the single particle resonance.

The propagation of the collective modes in plasmonic metacrystals, can be treated in analogy with light propagation in photonic crystals. The scattering on the periodic lattice results in constructive and destructive interference, which leads to the formation of bands and bandgaps. In particular, when the periodicity of the arrangement is of the order of plasmon resonance wavelength, the grazing diffraction orders, known as Rayleigh-Woods anomalies (RWA), may couple to the LSPR and form so-called surface lattice resonance

(SLR). SLR can yield very sharp resonances, and have interesting dispersion properties [28–30] as demonstrated for example in Fig. 1.17 (b).

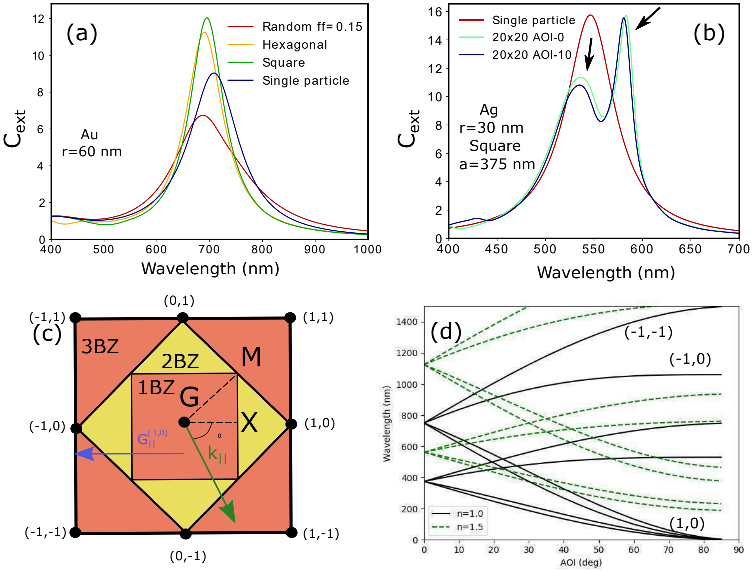

Figure 1.17 (a) Extinction cross-section attributed to the collective plasmon resonance for Au spherical nanoparticles arranged in a hexagonal, random and square arrays in comparison to the single particle LSPR. (b) Coupling of the LSPR to the RWA for square arrangements of cylindrical Ag particles with lattice constant of 375 nm, simulated at 0° (green) and 10° (blue) AOI, compared to the single particle LSPR. (c) Schematic diagram of the reciprocal space of the square lattice. (d) Degenerate diffraction orders along Γ-X direction of the reciprocal square lattice as a function of the AOI. The black lines represent grazing diffraction orders emerging from air, and green lines from medium with refractive index n=1.5, calculated according to the equation 1.89 .

The spectral position of the RWA can be best explained by looking into the momentum space, where the momentum of the scattered order k is described by the quadratic equation [31]:

$$k^2 - \frac{2k\sin(\theta_0)G_{\parallel}^{m}\cos(\phi_m - \phi_0)}{n_i^2 - \sin^2(\theta_0)} - \frac{(G_{\parallel}^{m})^2}{n_i^2 - \sin^2(\theta_0)} = 0, \tag{1.89}$$

where $G_{\parallel}^{m}$ is the reciprocal lattice vector of the m^{th} order, n_i is the refractive index of the medium, from which the diffraction order emerges, θ_0 is the angle of incidence, ϕ_0 is the azimuthal angle, and ϕ_m is the referral angle for the m^{th} scattering plane. To understand the equation the scheme of the reciprocal space for the square lattice is included in the Fig. 1.17 (c). Considering the symmetry of the square lattice, the reciprocal lattice vector $G_{\parallel}^{m} = \frac{2\pi}{a}[m_1^2 + m_2^2]^{1/2}$, where m_i are the indices of the scattering plane. Thus, $G_{\parallel}^{(-1,0)}$ represents the boundary of the 1st Brillouin zone and $G_{\parallel}^{(-1,-1)}$ the boundary of the second Brillouin zone.

If the structure is placed on a substrate, but not emerged in the index matching medium, the diffraction orders degenerate, due to the presence of two media, air and substrate, with two refractive indices. In this case, the dispersion diagram of such a structure obtains very rich dispersion properties as displayed in panel d of the Fig. 1.17.

1.6 Mueller matrix formalism

In the section 1.2 the polarization state of an electromagnetic wave was introduced first in the form of Jones vector and later generalized in the form of the Stokes vector. Another useful representation of the polarization state is based on the variance of the electric fields contained in so-called field coherence vector C [18]:

$$C = (\langle E_p E_p^* \rangle, \langle E_p E_s^* \rangle, \langle E_s E_p^* \rangle, \langle E_s E_s^* \rangle), \tag{1.90}$$

which is related to the Stokes vector as $S = AC$, where A is:

$$A = \begin{bmatrix} 1 & 0 & 0 & 1 \\ 1 & 0 & 0 & -1 \\ 0 & 1 & 1 & 0 \\ 0 & i & -i & 0 \end{bmatrix}. \tag{1.91}$$

While the Stokes vector is handy for direct analysis of optical measurements, as it contains measured intensities, the coherence vector is useful for derivation and decomposition of the Mueller matrices, as is demonstrated further.

When light interacts with matter, usually its polarization state is altered. Thus, interaction with matter, and a consequent transition from one polarization state into another can be represented in the matrix form. In cases where the Jones formalism is applicable, interaction with the non-depolarizing media, the conversion is represented by the Jones matrix:

$$\begin{bmatrix} E_{op} \\ E_{os} \end{bmatrix} = \begin{bmatrix} J_{pp} & J_{sp} \\ J_{ps} & J_{ss} \end{bmatrix} \begin{bmatrix} E_{ip} \\ E_{is} \end{bmatrix} = (J_{ik} J_{jl}^*)(E_k E_l^*)^{in}, \tag{1.92}$$

where i, k, j, l are permutations of the p, s indices. If the electromagnetic wave interacts with a sample, where some of its properties are averaged over the beam area, the depolarization process may take place. In other words, averaging of light- matter interactions leads to the averaging of the field properties and as a result ill defined polarization states. In such cases, the above equation takes the form with averaged quantities [18]:

$$\langle E_i E_j^* \rangle^{out} = \sum_{k,l} \langle J_{ik} J_{jl}^* \rangle \langle E_k E_l^* \rangle^{in} \quad \text{or} \quad C^{out} = F C^{in}, \tag{1.93}$$

where matrix F can be conveniently expressed with the help of Kronecker product $\otimes$:

$$F = \langle J \otimes J^* \rangle, \tag{1.94}$$

where J is a Jones matrix. In such a way the matrix M, describing transformation from one Stokes vector to the other can be expressed in a condensed form as:

$$M = A\langle J \otimes J^{*} \rangle A^{-1} = \begin{bmatrix} M_{11} & M_{12} & M_{13} & M_{14} \\ M_{21} & M_{22} & M_{23} & M_{24} \\ M_{31} & M_{32} & M_{33} & M_{34} \\ M_{41} & M_{42} & M_{43} & M_{44} \end{bmatrix}. \tag{1.95}$$

The Mueller matrix can represent any optical element or sample, which interacts with the electromagnetic radiation. The above equation provides a direct relation between Jones and Mueller matrices, where in the case of non-depolarizing interactions, the averaging of the Jones matrices is replaced by the fixed values which simplifies the Mueller matrix, reducing it to only seven independent terms. On the other hand, if the sample described by a Mueller matrix is depolarizing, a direct Jones matrix cannot be found. The degree of depolarization, or conventionally the depolarization index Di is found as:

$$Di = \sqrt{\frac{tr(M^{T}M) - 1}{3}}, \tag{1.96}$$

for a normalized Mueller matrix. Di takes value between 0 and 1, where 1 refers to a non-depolarizing Mueller matrix and 0 for a perfect depolarizer.

As a Mueller matrix, in general, represents a subset of all possible 4x4 matrices, to be physically realizable a Mueller matrix has to satisfy at least four conditions. These conditions are governed by a common sense that after interaction with the sample, the degree of polarization has to be smaller or equal to 1 and greater than or equal to zero. The conditions are summarized as follows [32]:

$$
\begin{aligned}
&tr(M^T M) \leq 4m_{11}^2,\\
&m_{11} \geq |m_{ij}|,\\
&m_{11}^2 \geq b^2,\\
&(m_{11}-b)^2 \geq \sum_{j=2}^{4}\left(m_{1,j} - \sum_{k=2}^{4} m_{j,k}a_k\right),
\end{aligned}
\tag{1.97}
$$

where $b = \sqrt{m_{12}^2 + m_{13}^2 + m_{14}^2}$ and $a_j = m_{1j}/b$. Other conditions have been studied, however there is no condensed list of all derived necessary conditions.

The elements of the Mueller matrix cannot be directly related to any physical properties, as they effectively represent linear combinations of polarization transformation effects. To determine the pure properties of matter which cause these transformations, a proper decomposition of the matrix is required. The decomposition method of choice heavily depends on the symmetry of the sample and measurement configurations at which Mueller matrix was acquired. In the next sections several decomposition methods, used in this thesis, are discussed.

1.6.1 Sum decomposition

One of the main properties of depolarizing Mueller matrices is that they can be represented as a linear combination of non-depolarizing matrices. Cloude has shown that any physically realizable Mueller matrix can be decomposed into a combination of up to four non-depolarizing Mueller matrices [33]:

$$
M = \lambda_1 M_1 + \lambda_2 M_2 + \lambda_3 M_3 + \lambda_4 M_4. \tag{1.98}
$$

The goal of such decomposition is to find the eigenvalues λ_i and non-depolarizing matrices M_i. This can be done by transforming the Mueller matrix M into the coherency matrix C as follows:

$$C = \sum_{i,j} m_{i,j}(\sigma_i \times \sigma_j^*), \tag{1.99}$$

where σ_i are the Pauli spin-matrices. For a physically realizable Mueller matrix, its coherency matrix is Hermitian, positive semi-definite and thus has real and positive eigenvalues. So the coherency matrix C can be decomposed into the form as in equation 1.98, with eigenvalues λ_i and matrices $c_i = e_i e_i^\dagger$. Once all four matrices are found, they can be transformed back into Mueller matrices with:

$$m_{ij} = \frac{1}{4} tr\left(c_{ij}(\sigma_i \times \sigma_j^*) \right), \tag{1.100}$$

and the eigenvalues λ_i are the eigenvalues of the coherency matrix C, holding the condition of $0 \leq \lambda_4 \leq \lambda_3 \leq \lambda_2 \leq \lambda_1 \leq 1$. The eigenvalues contain information about the depolarization of the system. In particular, if λ_2 is non-zero, the system is depolarizing. A specific case of such a decomposition is Le Roy-Bréhonnet decomposition, where Mueller matrix is decomposed into two matrices, one non-depolarizing and the other containing all the information about the depolarization of differently polarized light [34].

1.6.2 Regression sum decomposition

Similar to the Cloude decomposition, the regression sum decomposition represents the depolarizing Mueller matrix as a linear combination of non-depolarizing Mueller matrices. The main difference is that the form of non-depolarizing Mueller matrices is predefined, and can represent any perfect optical element.

$$M = \sum_i w_i M_i. \tag{1.101}$$

In such a way the problem is reduced to finding the normalized weight coefficients w_i, to determine the contribution of each element. In general this is done by minimization of the root-mean-square of all elements and can be generalized as a minimization of Frobenius norm F [10]:

$$F = \| M - \vec{M}_{fit}\vec{W} \|, \tag{1.102}$$

where $\vec{W}$ is a weight vector and M_{fit} is a set of predefined Mueller-Jones matrices. In general this approach has non-singular solutions, as Cloude has demonstrated that for a bistatic scattering problem the maximum required amount of the coefficients is four. However, if multi-frequency scattering information is treated this way, the implicit bounds provided by the Kramers-Krönig relation can grant a singular solution for the coefficients, even if their amount exceeds four. This approach is important for this thesis and would be applied to show that the measured depolarization contains a useful information about the entropy of the measured sample.

1.6.3 Differential decomposition

Differential decomposition is applicable when the sample can be seen as a homogeneous matter with constant physical parameters along the propagation direction of an electromagnetic wave. Such a medium can be imagined as a set of infinitesimal layers, with equal parameters described by a differential Mueller matrix m, which accumulate with distance into Mueller matrix M, as demonstrated in Fig. 1.18(a). Mathematically this is formulated as [35]:

$$\frac{dM}{dz} = mM. \tag{1.103}$$

By integrating over the whole thickness of the sample d, taking into account that m is independent on the thickness, it is easy to obtain the solution for m:

$$md = ln(M) \qquad \text{or} \qquad L = ln(M), \tag{1.104}$$

which reduces simply to the logarithm of the measured Mueller matrix M. Refering back to the sum decomposition, the L matrix can be further decom-

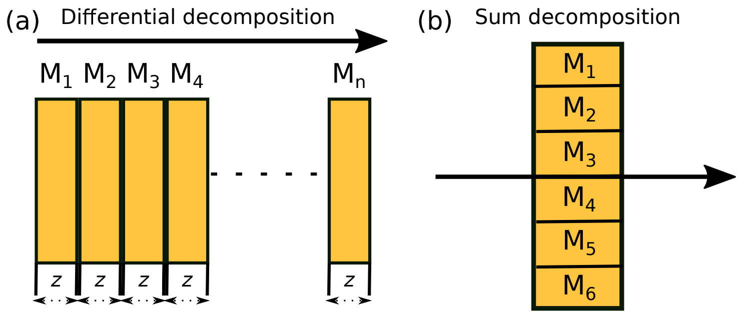

Figure 1.18 (a) A scheme representing the concept of the differential decomposition. The method allows us to separate optical contributions from infinitesimal slices with differential thickness z, along the propagation of the electromagnetic wave. (b) A scheme representing the concept of the Sum decomposition. The method allows us to separate the optical contributions from different regions in-plane, perpendicular to the propagation direction.

posed into mean L_m and uncertainty L_u matrices:

$$\begin{aligned} L_m &= \frac{1}{2}(L - GL^T G), \\ L_u &= \frac{1}{2}(L + GL^T G), \end{aligned} \tag{1.105}$$

where G is a diagonal matrix, $G = \mathrm{diag}(1, -1, -1, -1)$. The mean matrix contains all the information about polarization properties of the sample. In particular about linear dichroism ($LD = 2d\pi(k_y - k_x)/\lambda$), linear birefringence ($LB = 2d\pi(n_y - n_x)/\lambda$) and circular dichroism and birefringence, ($CD = 2d\pi(k_l - k_r)/\lambda$), ($CB = 2d\pi(n_l - n_r)/\lambda$), which take their place as follows [36]:

$$L_m = \begin{bmatrix} 0 & LD & LD' & CD \\ LD & 0 & CB & -LB' \\ LD' & -CB & 0 & LB \\ CD & LB' & -LB & 0 \end{bmatrix}, \tag{1.106}$$

where prime refers to the values measured at ±45°. The uncertainty matrix contains the information about depolarization as diagonal elements and the uncertainties of the mean values on the off-diagonal elements:

$$L_u = \begin{bmatrix} 0 & \Delta p_1 & \Delta p_2 & \Delta p_3 \\ \Delta p_1 & -LDP & \Delta p_4 & \Delta p_5 \\ \Delta p_2 & \Delta p_4 & -LDP' & \Delta p_6 \\ \Delta p_3 & \Delta p_5 & \Delta p_6 & -CDP \end{bmatrix}, \tag{1.107}$$

where *LDP* is depolarization of linearly polarized light, *LDP′* depolarization of linearly polarized light at 45°, and *CDP* is depolarization of circularly polarized light.

The differential decomposition is useful in the case of transmission measurements at normal incidence, and sometimes, dependent on the symmetry of the sample, at oblique incidence. In reflectivity measurement configuration, however the method is not applicable, although there exist some attempts to adapt the method for the backscattering direction [37], which is not always accessible in ellipsometry measurements.

In next chapter I will discuss in details how ellipsometric measurements are performed, which configurations are possible and which instrumentation is required in order to extract a complete Mueller matrix of the sample.

Chapter 2

Experimental techniques and instrumentation

2.1 Ellipsometry

The main investigation technique for this thesis is ellipsometry. In general, there is a variety of experimental configurations, in order to perform ellipsometric measurements. All of them however, have an optical source, polarization state generator (PSG), polarization state analyser (PSA) and the detection system. Some of the configurations allow to retrieve the Mueller matrix partially, while the others provide an access to a complete Mueller matrix. Although the concept of ellipsometry is very old, introduced by Paul Drude back in 1888 [38], only recently, instruments utilizing the full capability of the technique have been developed. Modern ellipsometers provide an access to the full Mueller matrix of the measured material over a broad range of optical frequencies, recorded simultaneously, governed by the advances in the material research, resulting in broadband polarization state generators and analysers. In this thesis two configurations of ellipsometry are used, both having its advantages and disadvantages, which are discussed in details in the following subsections.

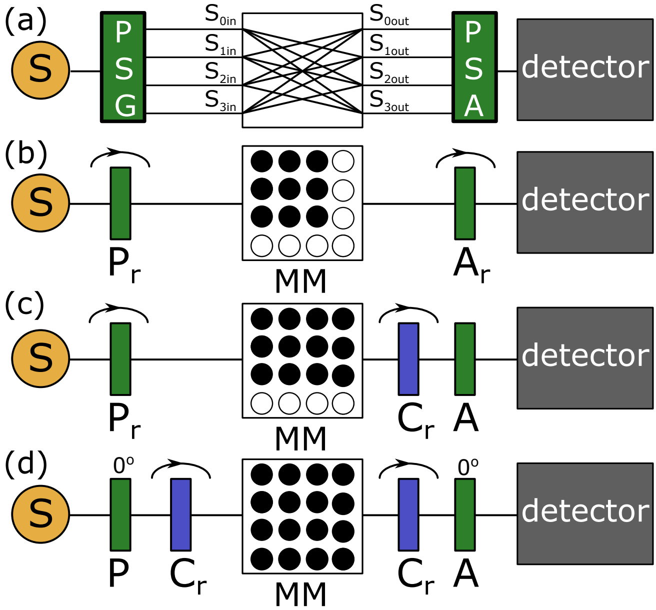
(a)
S
PSG
S_{0in}
S_{1in}
S_{2in}
S_{3in}
S_{0out}
S_{1out}
S_{2out}
S_{3out}
PSA
detector
(b)
S
P_r
MM
A_r
detector
(c)
S
P_r
MM
C_r
A
detector
(d)
S
0°
P
C_r
MM
C_r
0°
A
detector

Figure 2.1 Schematic diagram of several ellipsometric configurations. (a) General consideration of Stokes vector transformation. (b) Rotating analyser ellipsometer (RAE). (c) Rotating compensator ellipsometer (RCE). (d) Dual rotating compensator ellipsometer (RC2). The subscript r of the elements denote that the element is rotating.

2.1.1 Rotating analyser ellipsometer

Rotating analyser ellipsometer is one of the simplest configuration of the automated ellipsometer which consists of a polarizer, fixed to some angle P, for polarization state generation and an analyser rotating at a constant frequency ω. This results in a harmonic modulation of the detected intensity, expressed as:

$$S(t) = S_0(1 + \alpha \cos(2\omega t) + \beta \sin(2\omega t)), \tag{2.1}$$

where α and β are the Fourier coefficients. The Fourier coefficients can be expressed in terms of ellipsometric parameters Ψ, Δ and polarizer orientation P:

$$\alpha = \frac{\tan^2\Psi - \tan^2 P}{\tan^2\Psi + \tan^2 P}, \quad \beta = \frac{2\tan\Psi\cos\Delta}{\tan^2\Psi + \tan^2 P}, \tag{2.2}$$

from which ellipsometric parameters can be derived:

$$\tan\Psi = \sqrt{\frac{1+\alpha}{1-\alpha}}|\tan P|, \quad \cos\Delta = \frac{\beta}{\sqrt{1-\alpha^2}}\frac{\tan P}{|\tan P|}. \tag{2.3}$$

As a result Ψ is determined unambiguously, while only the absolute value of Δ is retrieved which lies between 0° and 180°. Thus, the distinction between left and right circular polarization is impossible. This means that only S_0-S_2 Stokes parameters are retrieved, while S_3 cannot be measured. In terms of Mueller matrix consequently, the information contained in the fourth row is not accessible. In addition, for only linear incidence polarizations, the information of transforming the circular polarization, contained in the fourth column of the Mueller matrix is also not available. Nevertheless, the cross-polarization terms r_{ps} and r_{sp} of the Jones matrix are measured. As a result, the upper 3 by 3 block of the Mueller matrix is can only be measured, as visualized on the Fig. 2.1(b).

The configuration can be extended by inserting a compensator element, to provide access to a complete Stokes vector. The compensator, which is commonly a quarter-waveplate, has to be aligned with its fast axis parallel to the s-polarization axis. The presence of a compensator does not influence the Ψ parameter, but introduces additional phase shift in measured Δ, $\delta' = \Delta - \delta$, where δ is the phase shift of the compensator. As a result, the intensity measured in this configuration, is expressed as:

$$I = I_0(1 - \cos 2\Psi \cos 2A + \sin 2\Psi \cos(\Delta - \delta) \sin 2A), \tag{2.4}$$

where A is the angle of the analyser. The equation can be written in terms of the Stokes parameters [9]:

$$I = I_0(1 - S_1 \cos 2A + (S_2 \cos \delta - S_3 \sin \delta) \sin 2A), \tag{2.5}$$

which are derived as Fourier coefficients. It is clear that in these configuration S_1 and $(S_2 \cos \delta - S_3 \sin \delta)$ are measured simultaneously. To obtain all elements of the Stokes vector separately, at least two measurements have to be performed with different orientations δ of the compensator.

Such an ellipsometric configuration is used in the Variable Angle Spectroscopic Ellipsometer (VASE) system provided by J. A. Woollam company, which was used for some specific measurements. An image of the system is presented in Fig. 2.2.The system utilizes the Xenon lamp as a source, covering a broad spectral range from 230 nm up to 2300 nm wavelength, embedded in the monochromator, with adjustable aperture width. The maximum spectral resolution of 1 nm is achieved with the 100 μm slit width. The outcoming light is guided with an optical fibre into the polarization generation chamber, where a rotating polarizer together with the adjustable compensator are situated.

The sample holder is placed on the high precision goniometer, which allows us to perform measurements in transmission and reflection, with adjustable angle of incidence, with the resolution of 0.5°. After interacting with the sample the light enters the detection tube, containing the analyzer. As the measurements are performed wavelength by wavelength over a broad spectral range, the system utilizes two semiconducting detectors. For UV-VIS range from 200 nm to 1400 nm Si is used, while for range above 1400 nm InGaAs serves as a detector. The induced voltage on the detectors as a function of polarizer and compensator orientation is fitted, and the Fourier coefficients are derived, which are further converted into the eliipsometric parameters.

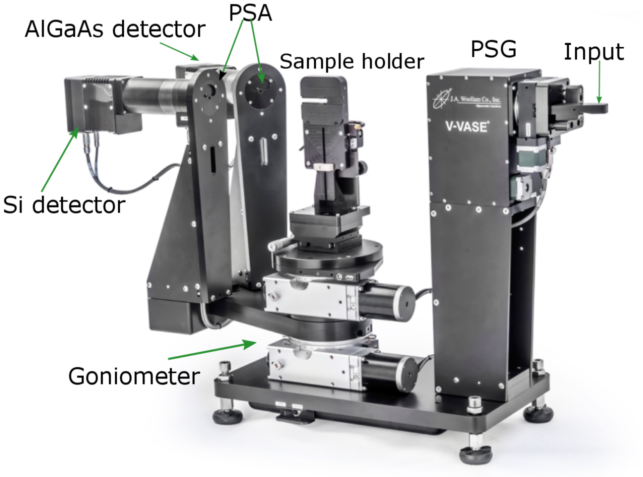

Figure 2.2 An image of the VASE ellipsometer from the J. A. Woollam company.

The system has two main disadvantages. The first is that only monochromatic light can be measured, which results in large measurement time for a complete spectra. The second is its inability to measure a complete Mueller matrix, as only one compensator is utilized. Nevertheless, the first argument can also be considered as an advantage. The design of the system allows the use of external light sources, such as laser diodes for example, for the measurements. In this case the intensity of the external source has to be synchronized with the modulations of the internal source of the monochromator. This can be easily done with the help of photomultiplier and the pulse generator. The ability to use high power sources, combined with relatively large sensitivity of the semiconducting detectors allows us to perform measurements of the samples with high extinction.

The second limitation can be overcome with the help of additional quarter-waveplate, placed in front of the PSA. By performing two sets of measurements, with different orientations of the additional compensator, in total 24 equations are acquired, describing polarization state transformation, which are enough to recover the complete Mueller matrix. This custom approach, however results in the increase of the uncertainty of the Mueller elements, but allows us to determine the depolarizing properties of the sample, as will be shown in the end of chapter 4.

2.1.2 Rotating compensator ellipsometer

Other possible configuration of the ellipsometer is stationary polarizer and analyser combined with compensator rotating at frequency ω with an instantaneous angle $C = \omega t$. The measured intensity for such a configurations takes the form [9]:

$$\begin{aligned} I &= I_0(2 - \cos 2\Psi + 2\sin 2\Psi \sin\Delta \sin 2C - \cos 2\Psi \cos 4C + \sin 2\Psi \cos\Delta \sin 4C) \\ &= I_0(2 + S_1 - 2S_3 \sin 2C + S_1 \cos 4C + S_2 \sin 4C). \end{aligned} \tag{2.6}$$

It is apparent that if the compensator angle C is changed, all three stokes parameters $S_1 - S_3$ can be determined as normalized coefficients from the Fourier analysis. As a result, dependent on the where the compensator is placed, the fourth row (in the case of compensator in PSA), or the fourth column (in the case of compensator in PSG), of the Mueller matrix can be obtained, as displayed in Fig. 2.1(c).

To get access to the full Mueller matrix, however two compensators both in PSG and in PSA has to be implemented. Such a configuration is called Dual-rotating compensator, and is the latest commercially available type of ellipsometer. Two compensators are rotated simultaneously, with synchronized frequencies $\omega_1 = p\omega$ and $\omega_2 = q\omega$, where ω is the base fundamental angular frequency, p and q are integers. p and q can be arbitrary chosen, nevertheless they determine the accuracy of the system and its base acquisition time, so a careful consideration of this parameters has to be done. On one hand the choice of *p*:*q* must provide enough independent Fourier coefficients, to reduce them to 15 independent Mueller elements. On the other, the operational frequency must not exceed the acquisition frequency of the detecting system. As a result, systems of such form usually utilize frequency ratio of 5:3, which results in 32 independent Fourier coefficients, 8 from which are zero, and optimized operation base frequency, close to the frequency of modern detection systems.

The expression of measured intensity, in such a system becomes rather complicated and is expressed as [39]:

$$\begin{aligned} I = I_0(K_1 &+ [c_2 \cos 2A' + s_2 \cos(4C'_s - 2A')]K_2 \\ &+ [c_2 \sin 2A' + s_2 \sin(4C'_2 - 2A')]K_3 \\ &- [\sin\delta_2 \sin(2C'_2 - 2A']K_4), \end{aligned} \tag{2.7}$$

where K_j is:

$$\begin{aligned} K_j = M_{j1} &+ [c_1 \cos 2P' + s_1 \cos(4C'_1 - 2P')]M_{j2} \\ &+ [c_1 \sin 2P' + s_1 \sin(4C'_1 - 2P')]M_{j3} \\ &+ [\sin\delta_1 \sin(2C'_1 - 2P')]M_{j4}. \end{aligned} \tag{2.8}$$

Here, $c_j = \cos^2(\delta_j/2)$ and $s_j = \sin^2(\delta_j/2)$. M_{jk} are the elements of the Mueller matrix. P' and A' are the true angles of the polarizer and analyser. Analogously C'_1 and C'_2 are the true angles of the fast axes of the compensators. Substituting the frequency ratio, results in $C'_1 = 5(C - C_{s1})$ and $C'_2 = 3(C - C_{s2})$, the measured intensity can be expressed in terms of dc-normalized Fourier coefficients (α_{2n}, β_{2n}) as:

$$I(t) = I_0\left(1 + \sum_{n=1}^{16} [\alpha_{2n} \cos(2nC - \phi_{2n}) + \beta_{2n} \sin(2nC - \phi_{2n})]\right), \tag{2.9}$$

where $2n$ ranges from 2 to 32, where coefficients with index *n*=9, 12, 14, 15 are zero and ϕ_{2n} are the phase terms. From the coefficients Mueller elements can be expressed. The equations are however very bulky and are not provided here, they can be found in [40].

Such a system, with dual rotating compensators, is the workhorse in this thesis. Figure 2.3 demonstrates the image of the setup, RC-2 UI from the J. A. Woollam manufacturer. As the source, the system utilises a combination of the Hydrogen and Xenon lamps, which together cover the spectral range from 190 nm to 2300 nm. The accessible measurement range is, however 210-1690 nm governed by the spectral response of the broadband compensators. The incident light is well collimated, with the beam diameter of 5 mm, which can be reduced with the help of focusing probes down to 500 μm. The probes however, introduce the offset of Δ parameter, due to the presence of the lens in the beam path. This effect is numerically compensated during the calibration procedure.

The sample holder is mounted on the goniometers similar to the one used in the VASE system, providing an angular resolution of 0.5°. For a sample holder different stages are available. The standard stage, shown in Figure 2.3, allows only to adjust the sample tilt. Rotational stage, contains a stepper motor with high angular resolution, which allows a control of the azimuthal orientation of the sample, during the measurement. Finally, the heating stage is available, which allows us to perform in-situ temperature-dependent measurements up to 300° Celsius. The sample holder consists of the metallic plate, on which sample is mounted, and the temperature is controlled with the external temperature controller, also provided by the Woollam company, with a temperature resolution of 0.1 °C. For the in-situ measurements, the acquisition time and the heating time can be adjusted to reach required measurement resolution.

As a detector, two CCD array spectrometers are used. One covers the wavelength range up to 1000 nm, with the resolution of 1 nm, the other one detects NIR wavelengths with the resolution of 2.5 nm. The configuration of the system, allows us to collect full Mueller matrix of the measured sample, for a complete accessible spectral range in the fraction of a second, i.e. 25

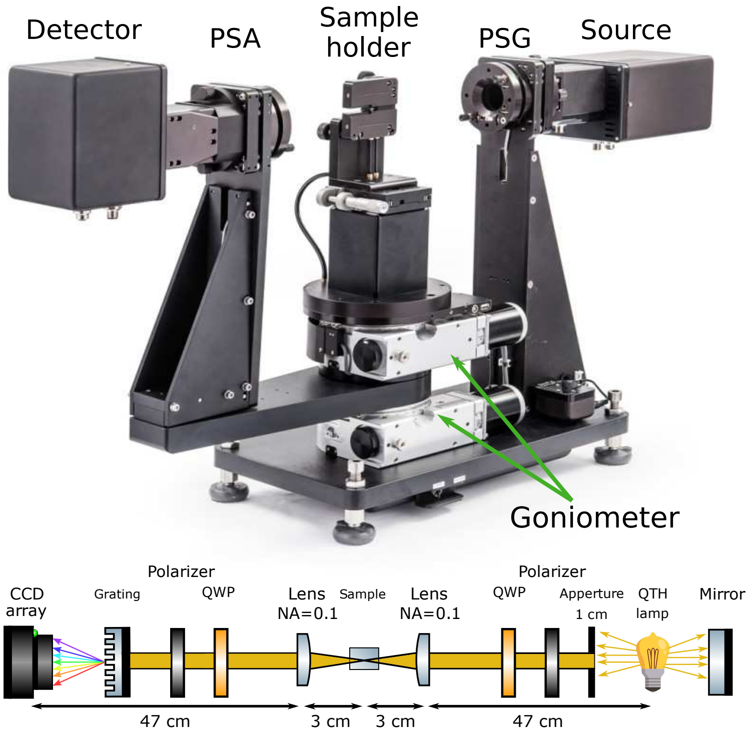
Detector
PSA
Sample holder
PSG
Source
Goniometer
CCD array
Grating
Polarizer
QWP
Lens NA=0.1
Sample
Lens NA=0.1
Polarizer
QWP
Apperture 1 cm
QTH lamp
Mirror
47 cm
3 cm
3 cm
47 cm

Figure 2.3 An image of the RC2-UI ellipsometer from the J. A. Woollam company. The schematics bellow display the optical beam path with focusing probes of numerical aperture NA=0.1 installed. In the schematics, the Hydrogen lamp is omitted, QWP stands for quarter-wave plate.

ms defined by the rotational base frequency of the compensators. The disadvantage of the system, is the usage of relatively low intensity light sources (75 W lamp), and low sensitivity of of the CCD arrays in comparison to the semiconductor detectors. Thus, samples with high extinction cannot be measured precisely on this setup.

2.2 Atomic force microscope

Atomic force microscopy (AFM) is a standard technique for surface topography characterization. The underlying principle is to measure the deflection of the cantilever which interacts with the surface. The cantilever has an atomically thin pyramid on its edge (see Fig. 2.4), which is brought to the proximity with the surface of the sample, where their mutual interaction can be approximated with the Lennard-Jones potential. The deflection of the cantilever is detected with an optical subsystem. The laser is pointed on the cantilever, where it is reflected onto the photo diode array, consisting of four parts. The deflection of the cantilever, caused by interaction with the surface, are thus transferred into the deviation of the reflected laser light from the center of the detector. To obtain the topography, the system has to correct this deviations, which is done with the help of the feedback loop. The feedback loop basically consist from the PID controller and the set of the piezo elements, which control either the cantilever or a stage. The PID controller estimates the exact voltage to be applied to the piezo element to correct the deflection, which allows us to avoid overshooting, preventing the damage of the sample, cantilever and increasing accuracy of the measurement. The applied voltage is than converted into distance based on the Lenard-Jones potential and preceding calibration of the system. The sketch of the measurement scheme is presented in Fig. 2.4(a).

For AFM measurements of the samples in this thesis, Bruker Dimension Icon atomic force microscope was used, which is displayed in Fig. 2.4(b). The measurements were mainly performed in the tapping mode, meaning the cantilever was driven close to its resonating frequency and the measurements were performed at the distance corresponding to the attractive part of the Lennard-Jones potential, down to the equilibrium distance r_0. The resolution of the obtained images is not pushed to the limits of the technique but is rather governed by the requirements to scan relatively large surface areas. So, in the

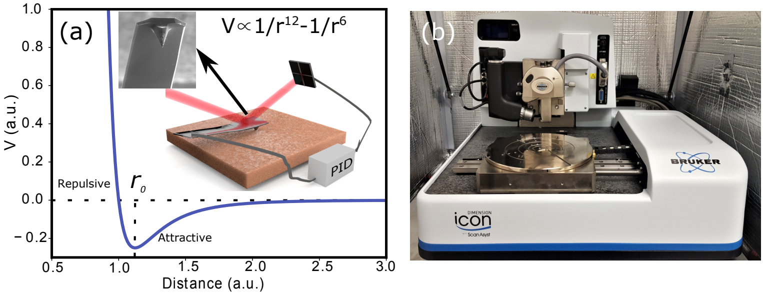

Figure 2.4 (a) Interaction potential as a function of distance to the surface, described be Lenard-Jones equation. The inset demonstrates the scheme of the AFM measurement. (b) Bruker Dimension Icon atomic force microscope, used for measurements in this thesis.

end the resolution is picked to compromise between large surface area and imposed time constraints for the experiments.

Temperature dependent AFM measurements were performed with the help of a custom heating stage, with the Peltier heating element. The temperature was controlled with the help of the commercial Lakeshore temperature controller. As heating above ambient temperature results in temperature gradient on the surface, the measurements cannot be performed in-situ, due to high thermal noise. Thus temperature-dependent AFM measurements have been performed in discrete steps, with some stabilization time from 1 up to 10 minutes, resulting in good quality of obtained results. The visualization and quantitative analysis of the topography of the sample is done with the help of an open-source Gwyddion software.

2.3 Resistivity measurements

To determine the electrical conductivity of thin films, temperature-dependent dc-resistivity measurements have been performed. Although the samples were of square shape, the measurements were performed in the van der Pauw configuration, i.e. with four contacts placed in corners of the sample [41]. As a current source Keithly 6221 was used and as a temperature controller the Lakeshore device was utilized.

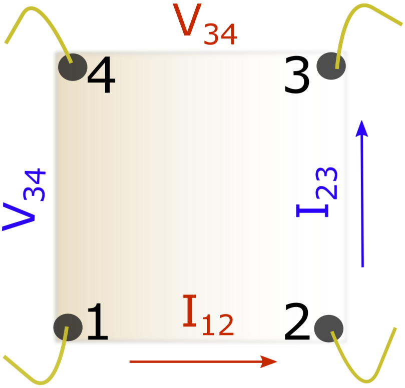

Figure 2.5 Scheme of the van der Pauw dc-measurement configuration.

The advantage of the method is governed by its accuracy. To perform the measurement the current is applied along one edge of the sample and the voltage is measured along the other. After, the second measurement is performed, with applied current and measured voltage along the edges, perpendicular to the edges used in the first measurement. Referring to the scheme shown on Fig. 2.5, two resistances are obtained:

$$R_{12,34} = \frac{V_{34}}{I_{12}}, \quad R_{23,41} = \frac{V_{23}}{I_{41}} \tag{2.10}$$

In addition, to achieve higher accuracy, the polarity of the current source and voltmeter can be switched to measured the reverse resistance. As a result two measured resistances can be assigned as:

$$\begin{aligned} R_{vertical} &= \frac{R_{12,34}+R_{21,43}}{2}, \\ R_{horizontal} &= \frac{R_{23,41}+R_{32,41}}{2} \end{aligned} \tag{2.11}$$

The relation with the average sheet resistance R_s is expressed in terms:

$$e^{-\pi R_{vertical}/R_s} + e^{-\pi R_{horizontal}/R_s} = 1 \tag{2.12}$$

In general, from Eqn. 2.12, the R_s can be recovered using numerical methods. In the case when $R_{vertical}$=$R_{horizontal} = R$, however the sheet resistance can be expressed with an analytical function:

$$R_s = \frac{\pi R}{\ln 2}, \tag{2.13}$$

and the resistivity of the material ρ, composing the film is:

$$\rho = R_s \frac{A}{L}, \tag{2.14}$$

where L is the distance between the contacts and A is an area of the sample cross section.

Chapter 3

Results on plasmonic nanostructures

The field of plasmonics dates back to the middle of the previous century, when the surface plasma waves have been theoretically predicted by Ritchie [42]. Since then, the research field has only been growing, as new aspects of plasmonics emerged. During last decades the study of plasmonics went through a substantial boost, governed by the advances in the nanopaterning techniques. The demand of producing smaller transistors for the semiconductor industry induced a better control and higher resolution for the lithographic techniques. As a result, electron-beam lithography emerged, and evolved from first machines based on the SEM apparatus to fully functional independent devices capable of nano patterning. This opened the door for the experimental investigations of plasmonic effects at the nanometer scale.

The potential of the field was fast recognized, and the amount of research directions based on the plasmonic effects on the nano scale increased exponentially. This includes development of new spectroscopic methods as well as improving standard ones [43, 44]. Efficient and fast modulation of light intensity and polarization state [45–47]. Metamaterials with remarkable optical properties, not accesible in natural materials [48, 27, 49]. Quantum optical devices, providing an access for significant device miniaturization [50, 51] and many more.

All these technologies and applications are based on the crucial property of the plasmonic nanoparticles, namely the field enhancement. It was demonstrated, that the near-field around the nanoparticles, in specific cases can be enhanced up to an order of 10^3, limited by Landau damping [23]. Such strong local field enhances near-field interactions and appears to be advantageous for photovoltaics [52] arguably increasing the absorption efficiency of the active layer. For spectroscopy [43], by enhancing the coupling to molecular vibrations. For imaging [53, 54], providing sub-diffraction limit resolution. And even for cancer treatment [55, 56], burning the cancer cells with strong local fields.

Another prominent phenomenon is observed in the plasmonic lattice arrangements. The near-field interaction between the LSPR on lattice sites results in an emergence of the collective oscillations [57]. The propagation of collective plasmon oscillations can be viewed in analogy to the light propagating in a photonic crystals, where scattering on spatial inhomogeneities results in superposition and consequently in the formation of the new eigenmodes of the system [58]. These collective oscillations can propagate along the lattice, and be either non-dispersive or display very strong dispersion, dependent on the lattice arrangement. The geometry of the nanoparticles define the base properties of the oscillations, but the lattice spacing and arrangements define the eigenmodes of the collective oscillations. As a result, it is possible to engineer non-trivial optical properties in the plasmonic crystals. It was demonstrated theoretically, that honeycomb arrangements of gold nanoparticles, under certain conditions can result in propagation properties of collective plasmons governed by Dirac equation with all associated properties such as linear dispersion and resistance to backscattering [27]. Other studies have demonstrated topologically protected states in quasi-2d crystals [59, 60] giving rise to edge-bounded propagation modes. A remarkable concequence of this effect is the associated topologically protected complete polarization conversion [61] with 100 % efficiency.

Plasmonic crystals can serve as model systems to investigate properties of the systems beyond natural occurrence. As there are no limits on the structural lattice arrangements it is possible to produce artificial crystals of any kind. A great example is the family of theoretical allotropes of carbon atoms, called graphyne [62]. These structures have not been found in nature, nor synthesized yet, but its properties have already been theoretically investigated. It appears that these structures might have phenomenal optical properties, useful for all-optical modulation [63]. With plasmonic crystals these properties can be translated to VIS-IR range, used for optical communications.

As a matter of fact, all these advanced technologies rely on the fabrication of critical dimensions with a precision from nanometers down to the atomic level. At these scales the modern lithographic techniques reach their limitations due to the focusing optics and the backscattering effect governed by the interactions of electrons with the matter [64]. Paradoxically, today not many metrology techniques exist, that can provide both, the sensitivity on this scale and the agility to characterize large surface areas. In addition, for the industrial production of the nanoscale devices it is crucial to obtain a non-destructive and in-line compatible method. Few microscopic techniques such as AFM or SEM, provide a necessary resolution but have limited acquisition speed, are not suitable for large area characterizations and even can result in sample degradation. On top of that, these techniques are really hard to implement into an automated industrial production line. On the other hand, optical techniques such as through focus microscopy [65], solve the problem of the integrability and sample degradation, but still appear to be quite time consuming for characterization of large surfaces. Thus, the quality assurance process bottlenecks the production time, and increases the production cost. Today, a lot of research aims to develop a robust, reliable and fast method for nanostructure characterization, which potentially could eliminate the bottleneck [66–68]. Specifically, the goal is to better understand the light-matter interactions on the nanoscale and utilize its features for fast and precise critical dimension analysis.

The first part of this chapter is dedicated to the characterization of plasmonic nanostructures with the help of ellipsometry. In particular, it is demonstrated how Mueller matrix ellipsometry can be utilized as a metrology tool achieving nanometer precision in critical dimension and defect analysis of plasmonic nanostructures on a potentially unlimited area. The depolarization extracted from the measured Mueller matrices, serves as a direct signature of the spatial inhomogeneity of the sample. It is shown that the detected depolarization can be related with the variance of the critical parameter of the nanostructure which can be evaluated by the regression sum-decomposition. Being sensitive to structural inhomogeneities beyond the coherence length of the source, the method appears to be complementary to the microscopic techniques, which are limited only to small areas.

The second part of the chapter is related to the phenomena of polarization conversion in the nanostructures. Mainly, I investigate the influence of the surface lattice resonance on the amplitude of polarization conversion. It is demonstrated that s and p polarizations couple differently to the grazing diffraction orders, which results in polarization conversion. The properties of polarization conversion are investigated as a function of azimuthal rotation. The spectral proximity of the degenerate grazing diffraction lines, can result in narrow LSPR response and enhanced polarization conversion effects. Although, the observed polarization conversion effects are weak, a detailed investigation of the phenomena provides the understanding on how to reach higher efficiency in future.

3.1 Investigated samples

The samples were prepared by Marcus Rommel, a former PhD student in the nanostructure lab, headed by professor doctor Jürgen Weis, in the

Max Planck Institute for solid state research (MPI FKF), in Stuttgart. For the production, Jeol JBX6300FS electron beam lithography system was used. The arrays of nanodiscs were fabricated on a fused silica substrate with a refractive index n=1.5. Two layers of PMMA with different sensitivity were spin coated on the substrate to obtain a resist mask with undercut, which improves the lift-off of the Au film. First PMMA 200k 3.5% was spin coated at 6000 rpm for 35 s and then prebaked on a hot plate for 4 minutes at 160 °C. In the same way PMMA 950k 1.5% was spun on the sample and baked. The patterns, consisting of 500 μm by 500 μm super cells were repeatedly exposed into the resist to cover an area of 1.5x1.5 mm^2. The discs are fractured into trapezoids for the exposure. The exposure parameters were 100 kV of acceleration voltage, 1 nA of beam current, shot pitch of 4 nm and a dose of 1300 μC/cm^2. During the exposure the auto-focus was active, with depth of focus of the order of 6 μm. Astigmatism correction as well as correction for the distortion of the main field, subfield and writing field was performed before exposure. The sample was developed in a Methylisobutylketone (MIBK) and Isopropanol (IPA) mixture of 1:3 for 15 seconds at 22 °C. The development was stopped by putting the sample for 15 s in IPA and blown-dry with N$_2$ gas. Thermal evaporation was then used to deposit a 1-nm-thick adhesion layer of Ti with an evaporation rate of 1 /s and 30 nm of Au with an evaporation rate of 2 /s. Finally, a 3 hour-lasting N-Ethyl-2-pyrrolidone (NEP) bath at 80 °C as well as followed by ultrasonic agitation applied at low power for few seconds at the end of the lift-off process. The sample was rinsed in acetone and isopropanol and then dried with N$_2$. The large area is divided in smaller zones, thus allowing parallelization of the generation process.

The samples can be divided into two groups. The first group is a set of six samples, arranged either in periodic square lattices with different particle density, or randomly arranged with the same particle density. The initial aim to study these samples was to investigate the optical response as a function of the particle density, and the role of the lattice structure. This was done in the work of Stefano de Zuani [69], where the exact particle distribution

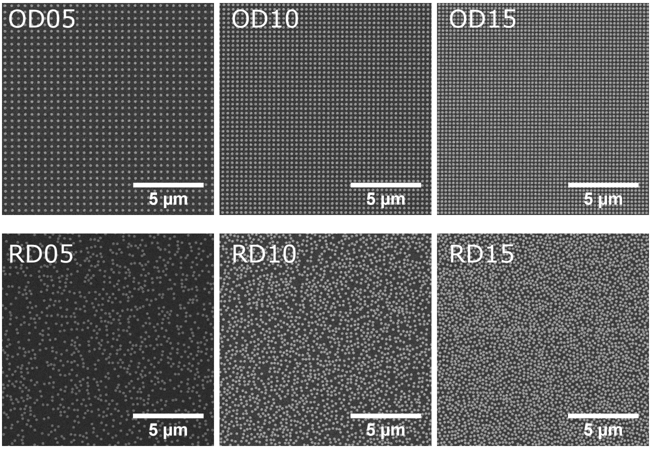

Figure 3.1 SEM images of the samples with the particle densities of 5, 10 and 15 per $\mu\mathrm{m}^2$. The upper row corresponds to the square lattice arrangements with periodicity of 439 nm for OD05, 312 nm for OD10 and 262 nm for OD15. The bottom row shows the arrangements of the random samples RD05, RD10 and RD15.

functions are presented. Here, I further investigate the samples to address the question of polarimetric response of the structures deduced from a complete Mueller matrix. In particular, I will demonstrate that the complete Mueller matrix provide all the necessary information to perform the precise estimation of the critical dimensions of the nanoparticles, as well as the evaluation of the statistical distribution of these parameters.

The nanodiscs, in all six samples have a height $h = 30$ nm and a radius $r = 95$ nm. The samples have the particle densities of 5, 10 and 15 nanodiscs/$\mu\mathrm{m}^2$. In the case of square lattice samples this results in the lattice constants of 439, 312 and 262 nm respectively. These samples are further referred as OD05, OD10 and OD15, while the random samples are RD05, RD10 and RD15. The SEM images of the samples are presented in Fig. 3.1.

Notice that the random samples are produced in the way to avoid overlapping of the nanoparticles by fixing minimal interparticle distance $d = 2r + 20$ nm. The pattern is then exposed by randomly choosing the position of the particle if the minimal distance condition is satisfied. Nevertheless, for the RD15 sample, it is clearly observed from Fig. 3.1 that in some regions the particles do overlap. This overlapping is a result of stitching of the writing field areas (super cells), governed by the production method. In any case the area of such regions is negligible in comparison to the total area of the sample, and hardly influences the optical properties of the sample.

The second set of samples consist of two samples which are the honeycomb arrays of gold nanodiscs. The nanodiscs have again the height $h = 30$ nm and the radius $r = 60$ nm for the first sample and $r = 80$ nm for the second sample. The distance between the surfaces of the nanoparticles is constant and is equal to 30 nm. Thus, the interparticle distance for these samples is equal to $2r + 30$ nm and the samples are further referred as HC190 and HC150, according to the lattice constant. The small interparticle distance is chosen to go beyond the electrostatic approximation and maximize the coupling between the particles. The AFM image of the structures with 80 nm base radius is shown in Fig. 3.2. The motivation to investigate such samples originally lies in the confirmation of the results obtained for square arrays and further investigation of coupling of lattice effects to the plasmonic modes and subsequent polarization conversion.

The samples, discussed in this section, have been extensively measured both in transmission and reflection ellipsometric configurations, with varying angle of incidence as well as function of azimuthal orientation. For these measurements, a complete Mueller matrices were obtained, which are discussed in details in the following sections.

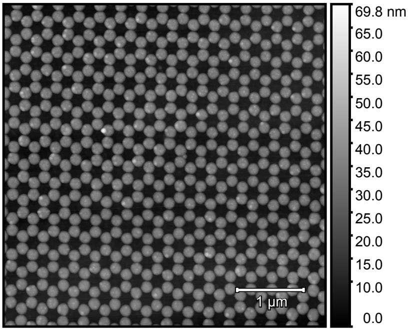

Figure 3.2 5x5 μm AFM image of the honeycomb arrangement of Au nanoparticles with radius $r = 80$ nm, height $h = 30$ nm, arranged with a lattice constant a= 190 nm, measured with 4.5 nm/px resolution.

3.2 Square and random arrays

3.2.1 Critical dimension analysis with Mueller matrix ellipsometry

The transmission intensity as a function of angle of incidence was previously investigated [69], where two important things were observed. First of all, the ordered arrays display higher extinction than the random ones. This, in fact is explained by the scattering/beaming effects of the lattice [69–71]. The superposition of the scattered fields from periodically arranged nanoparticles leads to a sharper scattering peaks with respect to polar angle. The ratio of the extinction for ordered and random samples is shown in Fig. 3.3. In such a way it is observed that the lattice effects lead to 11, 13 and 21 times larger forward extinction in ordered samples than in their random counterparts.

Secondly, the OD05 sample has shown rather special extinction properties at normal incidence. The presence of the periodic lattice leads to diffraction. The periodicity of the OD05 sample results in the grazing diffraction order, the RWA, which alters the properties of the LSPR mode. While at higher

AOI, RWA couples with LSPR for all the samples, in the OD05 sample the coupling is observed already at normal incidence. This results in the azimuthal dependence of the transmission. Due to the four-fold symmetry of the lattice, the RWA line can be described by the equation 1.89, where the angle ϕ_0 is taken from 0° to 45°. Figure 3.4(b) displays the azimuthal dependence of the intensity, measured at 16° AOI, where the black dashed line represent the RWA line from the first Brillouin zone, emerging from the substrate $(1,0)_{sub}$. At low AOI the coupling effect is minor, since RWA does not match the LSPR. Nevertheless, the spectral position of the LSPR is still affected by the presence of the RWA, which is observed by comparing with LSPR in RD05 [69]. At large oblique angles of incidence the coupling effect would become crucial for the discussion of the polarization conversion phenomena.

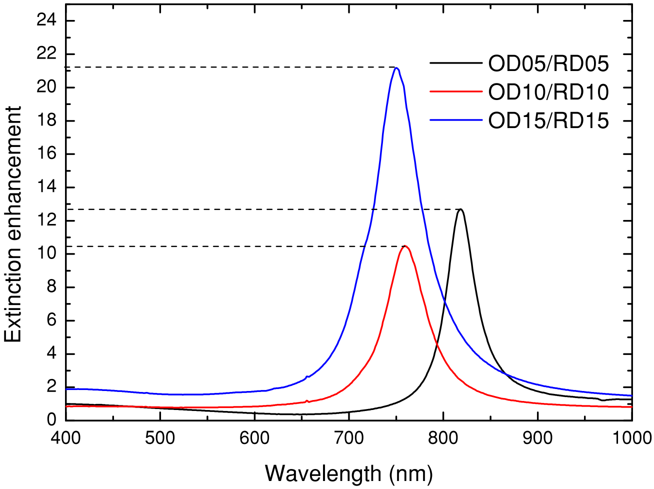

Figure 3.3 Ratio of the measured extinction of ordered and random samples with the same particle density.

For now it is reasonable to forget about the oblique angles of incidence and concentrate on the ellipsometric properties at normal incidence. In this configuration it is very convenient to interpret the ellipsometric measurements

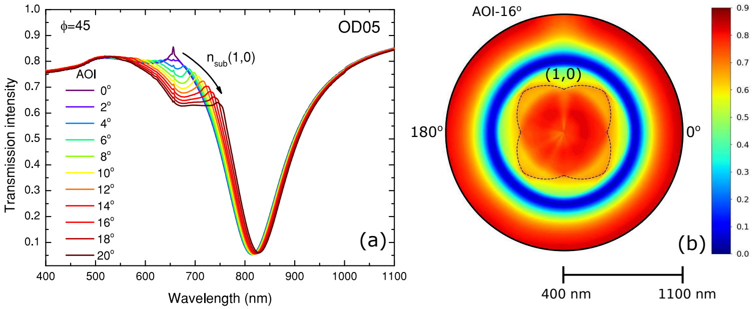

Figure 3.4 (a) Measured transmission intensity of the OD05 sample measured at azimuthal angle ϕ=0°, for AOI= 0°-20°. The dispersion of the LSPR is observed due to the RWA with the substrate refractive index $n_{sub} = 1.49$. (b) Azimuthal rotation polar plot of the transmission intensity measured at 16° AOI for wavelength from 400 nm (center) to 1100 nm (outer ring). The dashed line indicates the (1,0) RWA.

and to relate them with the in-plane anisotropy of the sample, as at normal incidence both p and s polarizations are indistinguishable. Referring to ellispometric parameter $\Psi = \tan^{-1}|r_p|/|r_s|$, it is reasonable to expect $\Psi = 45°$ for our samples, indicating equal orthogonal polarization response, as well as wavelength independent phase shift $\Delta = 0$.

In the measurements, a different picture is observed, which is shown in Fig 3.5. A strong resonance is present around LSPR frequencies. Ψ shows a bimodal behavior, where at lower wavelengths, it drops down below the unperturbed value, and above certain wavelength a crossover is observed with Ψ values above 45°. Δ shows a slightly asymmetric Lorentzian behavior, where maximum is reached at the wavelength of the crossover. It is interesting to note, that resonances, observed in ellipsometric parameters, do not exactly coincide with the LSPR determined from the transmission measurements. In the random samples the observed effect is of the order of 10 weaker than in arranged samples. This is related to the above mentioned differences in extinction properties of the two types of the samples.

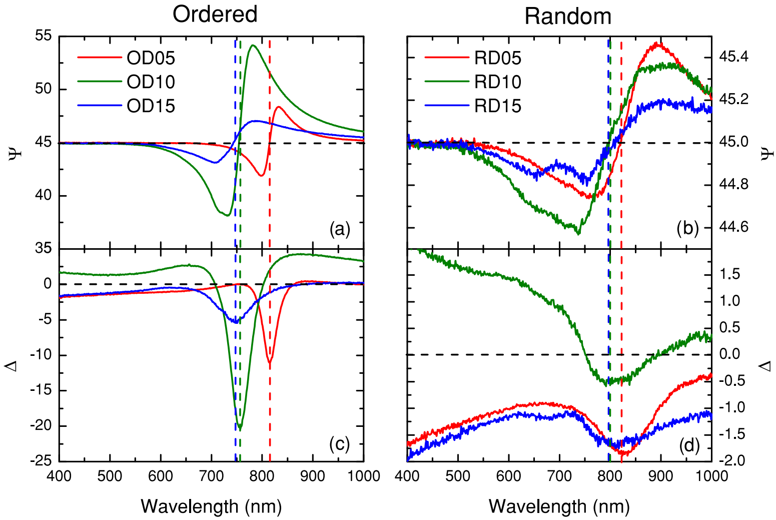

Figure 3.5 Measured ellipsometric parameters (a-b) Ψ and (c-d) Δ, for ordered (left column) and random (right column) samples, with the disc densities of 5 disc/μm^2 (red curve), 10 disc/μm^2 (olive curve) and 15 disc/μm^2 (blue curve). The vertical dashed lines denote the wavelength where Ψ changes sign (crossover) for each of the samples. Horizontal black dashed lines are the guideline for the expected values for an isotropic sample.

From Fig. 3.5 several conclusions can be made. First of all, all the samples show similar features, with much stronger amplitude in the ordered samples. Secondly, the spectral region of the anisotropy is broader in the case of random samples. Finally, OD10 sample shows the strongest deviation from an isotropic response, with observed asymmetry with respect to the crossover point. Because of this fact, OD10 sample is investigated further in order to determine the origin of the anisotropy. Other samples will be used further only for comparison.

The observed anisotropy in the samples is unexpected. With the intended cylindrical shape of the particles with the circular base, the scattering response is expected to be isotropic. On the other hand, the imperfections of the lattice arrangement can be the origin of the observed anisotropy. However, the fact that the anisotropic response is also observed in the random samples, contradicts the assumption of the lattice origin.

3.2.1.1 Measured Mueller matrices

Mueller matrix is a powerful tool to investigate different kinds of anisotropies. Basically, Mueller matrix contains the same information as standard ellipsometric parameters, but in addition stores information about polarization conversion and depolarization. From the measurements of Ψ and Δ, a strong azimuthal dependence was observed. Thus, it is reasonable to study the Mueller matrix response also as a function of azimuthal angle. The normalized measured data for OD10 sample is presented in Fig. 3.6, where the first element M_{11} is the unpolarized transmission intensity data.

Very interesting conclusions can be drawn from this Mueller matrix. First of all, while the transmission intensity is invariant with respect to azimuthal rotation, from M_{12} and M_{21} elements it is clear that the sample carry a two-fold symmetry, with two well-defined orthogonal optical axes. Secondly, the off-diagonal blocks of the matrix are non-zero, which is a direct evidence of the anisotropy of the sample and related polarization conversion. Thirdly, the matrix looks to be almost symmetric, if not considering M_{14} and M_{41}, which have much smaller amplitudes in comparison to the other elements. The symmetry of the Mueller matrix tells a lot about the system [72]. In particular, in the measured Mueller matrix $M_{12} = M_{21}$, $M_{13} = M_{31}$, $M_{24} = -M_{42}$ and $M_{34} = -M_{43}$. This type of symmetry correspond to a system in which the diattenuation and retardation effects are aligned. Such systems have non-reciprocal symmetry and do not contain any circular anisotropy. On the other hand, although the M_{14} and M_{41} are small, they are not equal, giving a hint that depolarization process is involved during the interaction with the sample.

The elements of the main diagonal are non identity, which is another evidence of depolarization (at normal incidence). M_{22} and M_{33} have azimuthal

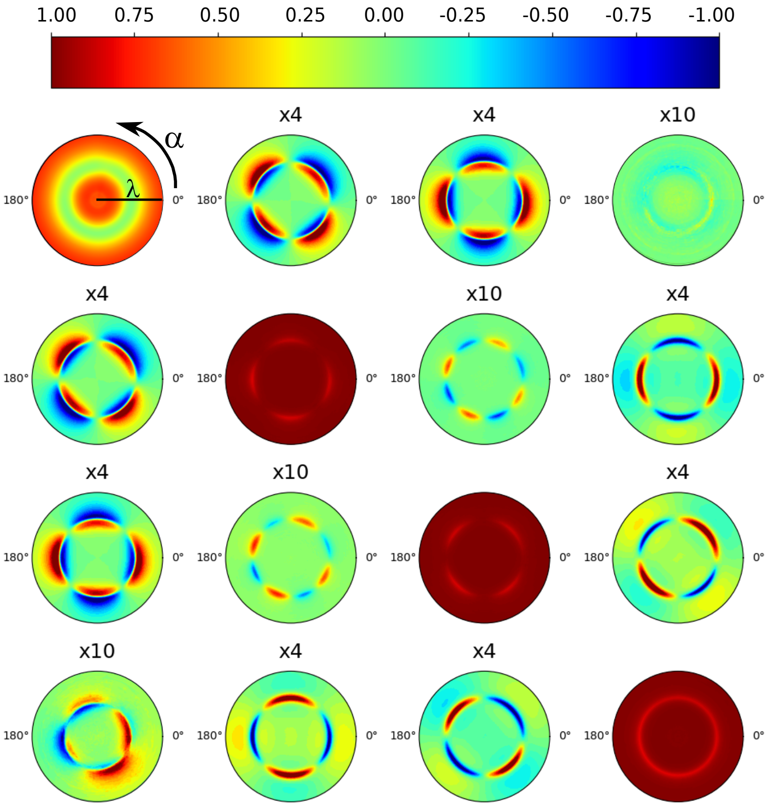

Figure 3.6 Measured normalized Mueller matrix for OD10 sample. The first element M_{11} represents the unpolarized transmission intensity. Radially, the data spans from 400 nm (center) to 1000 nm (outer ring) wavelength, and the azimuthal angle increases in counter-clockwise direction. The factor, above each element, represents the amplitude multiplication factor, for clarity reasons.

dependence, with four-fold symmetry while M_{44} is rotational invariant. The elements of the secondary diagonal deserve a separate discussion, as in general, they are related to the circular effects. M_{14} and M_{41}, related to CD, are non-zero and non-equal between each other. The M_{32} and M_{23} elements, related to the CB, have an enhanced four-fold symmetry, and have the same sign. Nevertheless, to gain access to the pure physical properties of the sample, a decomposition of the matrix has to be performed. In the case of normal incidence transmission measurements, differential decomposition is a method of choice, as it provides a direct access to all the properties, together with their associated uncertainties. The decomposed mean L_m and uncertainty L_u matrices for OD10 sample are presented in Fig. 3.7.

From the mean values matrix L_m it is clearly observed that the elements M_{12}, M_{21}, M_{13}, M_{31}, M_{24}, M_{42}, M_{34}, M_{43} remain effectively unchanged, signalizing that the depolarization effects are not strong. Uncertainty values of the above-mentioned elements, from the L_u matrix are negligible. The mean values can now be considered as the values representing pure linear dichroism and birefringence effects, which are easy to understand. As was mentioned above, the sample has well defined optical axes, which is governed by the anisotropy of the absorption process, causing observed LD and LD' and associated retardance, contained in LB and LB' elements.

The elements associated with the CB and CB' are absent in the mean-value matrix, and the values observed in the measurements are completely covered with uncertainty values. The elements of circular dichroism, remain small, equal between each other, and their amplitude is in the uncertainty range. These are clear signs that the circular elements, observed in the measurements, are originating from the combinations of linear dichroism and linear birefringence. Elements M_{14} and M_{41} in the measured matrix, usually display the apparent circular dichroism which is defined as $CD_{app} = CD + 1/2(LBLD' - LB'LD)$. The same effect is related to the apparent circular birefringence, where $CB_{app} = CB + 1/2(LBLB' - LDLD')$. The combination of elements with an offset of 45° explains the resulting increase

(a) L_m plot at 0° AOI for 400-1000 nm wavelength

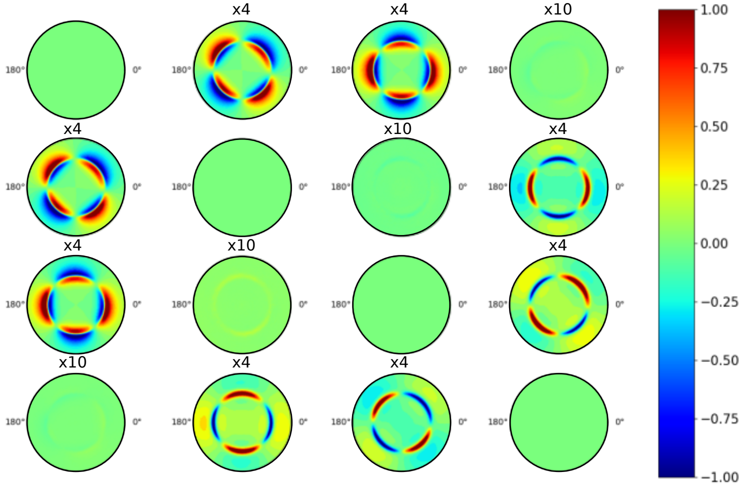

(b) L_u plot at 0° AOI for 400-1000 nm wavelength

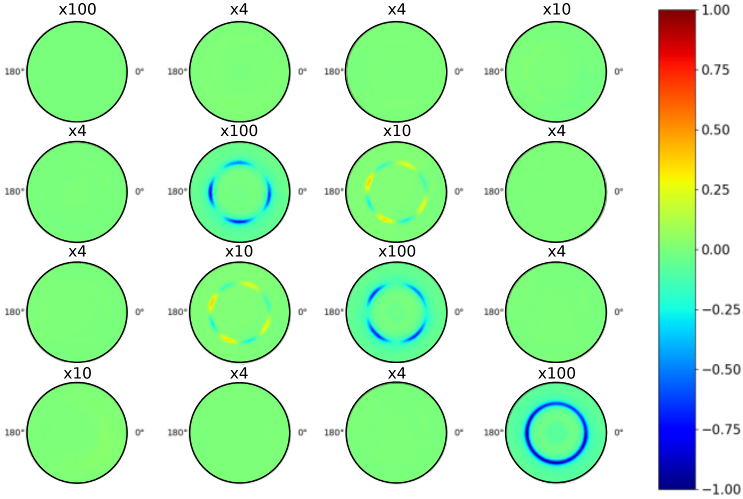

Figure 3.7 Differential (a) mean L_m and (b) uncertainty L_u matrices of OD10 sample for wavelengths from 400 nm (center) to 1000 nm (outer ring). The azimuthal angle increases counter-clockwise and is measured with 5° step. The factor above each element represents the amplitude multiplication factor, for clarity reasons.

in the rotational symmetry of apparent circular dichroism in the measured matrix. The differential decomposition allows extraction of the real intrinsic *CD* and *CB*. In the end, it is apparent that the sample shows no intrinsic circular effects, which is reasonable, as it only occurs in the systems which lack mirror symmetry, which is not the case here.

The uncertainty matrix L_u contains more information about the sample. The depolarization occurring during the interaction with the sample, is stored in the diagonal elements of the matrix. Interestingly, for circular polarization the depolarization is invariant with respect to azimuthal rotation, while for linear polarizations it has a four-fold symmetry and appears to be related to the observed dichroic effects with a 45° offset. The depolarization of linearly polarized light takes its maximum when the polarization bases are not aligned with the sample optical axes, and is minimum when both reference frames are aligned. The total depolarization index of the system, which is an average of three diagonal terms, remains rotational invariant, since L_{u22} takes its maximum where L_{u33} takes its minimum values and *vice versa*.

For all the other samples, very similar matrices are obtained. However, certain differences are prominent and the comparison for all the systems gives additional information about the underlying anisotropies of the samples. The comparison of the M_{12} element for all six samples is shown in Fig. 3.8. In fact, several key features, which define the future path of the investigation of the samples, can be noticed. Firstly, it is clear that the observed Mueller matrix features are related to the LSPR. Comparing elements of OD05 and OD10 samples, for example, the difference in width as well as the spectral position of the features is observed. Same is observed for the position and the width of the LSPR deduced from simple transmission measurements [69]. Secondly, the amplitude of the features in the random samples is approximately by a factor of 10 smaller than in the ordered structures, which is of the same order as the extinction ratio shown in Fig. 3.3. Finally, it is clear that the orientation of the observed optical axes, with respect to the sample reference frame, is different for all the samples.

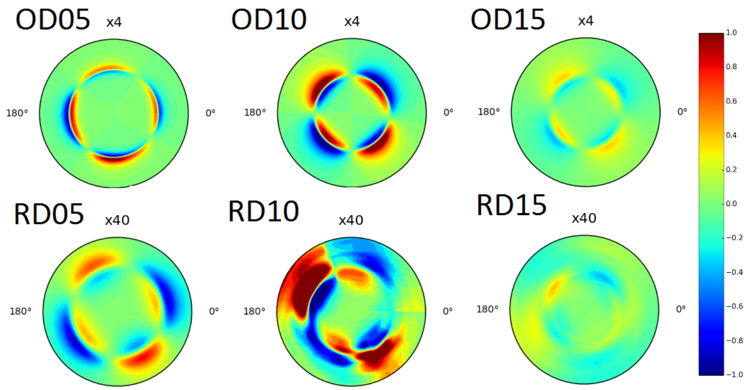

Figure 3.8 L_{m12} element of the differential mean matrix for ordered (top row) and random (bottom row) arrays. The azimuthal angle increases counter-clockwise and the radial component represents wavelength range from 400 nm (center) to 1100 nm (outer ring).

All together these give a hint about the origin of the observed anisotropy. The anisotropy originates from the differential absorption due to the presence of the anisotropic LSPR. Due to the symmetry of observed anisotropy, it is reasonable first to assume that the anisotropy is induced by the lattice imperfections, i.e. deviations from the square lattice, where $a_x \neq a_y$. As already mentioned, the fact that the same anisotropy is observed in the random samples, as well as different orientation of the optical axes, which are not alligned with the lattice axes, completely refutes this assumption. As a matter of fact, it can be concluded, that the observed anisotropy is attributed to the asymmetry of the particles themselves, rather than their arrangement.

3.2.1.2 Simulation of optical properties

As discussed in the theory part, the LSPR of the nanoparticle is governed by the polarizability of the particle, which depends on the particle geometry. While the spherical particle supports only one LSPR, the asymmetry of the particle lifts the degeneracy of the LSPR, resulting in the polarizability tensor. From the observations made from the measured Mueller matrices, it is reasonable to assume that the base of the cylindrical nanoparticles deviates from a circle and is slightly elliptical. To test this assumption, first a simple uniaxial Fresnel model with in-plane extraordinary optical axes can be utilized. Each axis is represented simply by the Lorentzian oscillator, describing LSPR, having three parameters: Amplitude A, resonant energy E and damping Γ. In addition, an Euler angle ϕ is introduced to relate the laboratory reference frame, defined by the orientation of the electric fields of two orthogonal polarizations (parallel to the sample edges), to the reference frame of the sample, oriented along the minor and major radii of the ellipsoidal nanoparticles. To better understand the reference frame relation, it is sketched in Fig. 3.9(c). Additionally, the figure demonstrates intensity information. While unpolarizaed transmission intensity, on panel (a), is rotation invariant, polarized intensity, presented on panel (b), demonstrates a difference in transmittance. Panel (d) visualizes the difference in transmission intensities for orthogonal polarization measured at different azimuthal angles. This allows us to better understand the azimuthal dependence of the elements of the differential Mueller matrix.

At normal incidence the out-of-plane optical axes has no contribution into the optical response. Thus, the model contains effectively, only seven fitting parameters. This simple model results in the Mueller matrix, whose differential matrix is presented in Fig. 3.10. The model perfectly reproduces the mean-value matrix, where the circular elements CB and CD are zero. The uncertainty matrix, however shows no depolarization and no uncertainty for the off-diagonal elements. This is expected, as the depolarization arises from either spatial or temporal averaging, and is a consequence of loss of coherence. In the uniaxial Fresnel model, both optical axes are excited coherently, and there are no sources of decoherence. Very often, in the ellipsometric measurements the detected depolarization is related to the intrinsic imperfections of the apparatus, such as finite-bandwidth of the spectrometer, or angular spread

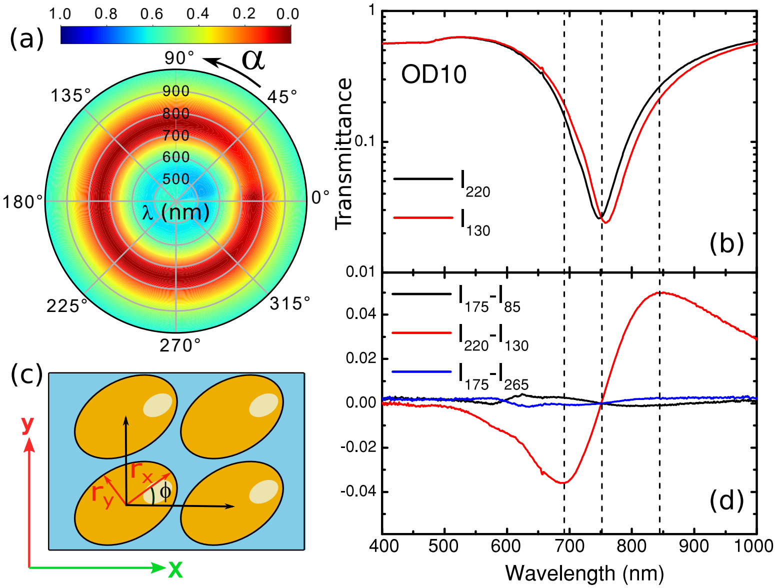

Figure 3.9 Measurements on the OD10 sample. (a) Normalized azimuthal dependence of unpolarized transmittance spectra using the substrate transmission as a reference. (b) Transmittance of orthogonal polarizations measured at 220° and 130° azimuthal angles α, plotted on a logarithmic scale. (c) Schematic illustration of the nanostructure, where X and Y represent the sample reference frame, r_x and r_y are the major and the minor axes of the nanoparticle, defining particle reference frame, and ϕ is the Euler angle between the two reference frames. (d) Difference in transmittance between orthogonal polarizations measured at different azimuthal angles.

caused by focusing optics. On the other hand, depolarization can be caused by very large roughness of the sample or its thickness inhomogeneity.

Numerical implementation of these effects can be done by averaging over these parameters. Combining all these possible sources of depolarization and implementing it into the model, does not result in amplitudes of the depolarization compared to measured ones. Thus, it can be concluded that

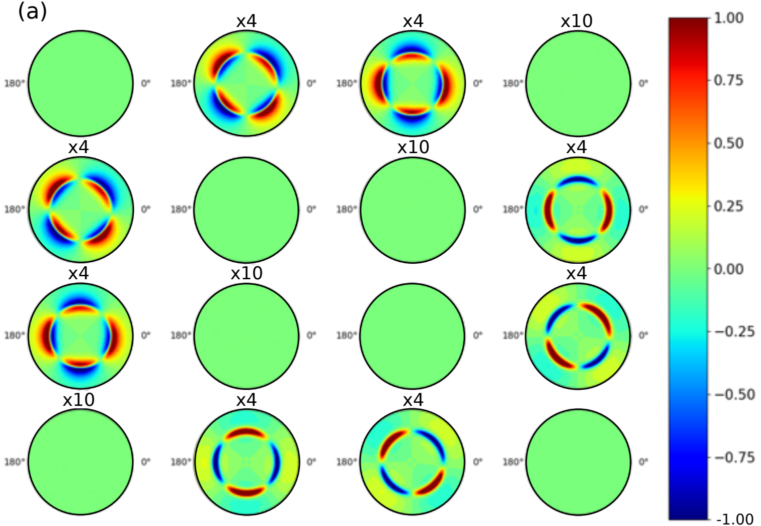

(a) Simulated L_m plot at 0° AOI for 400-1000 nm wavelength

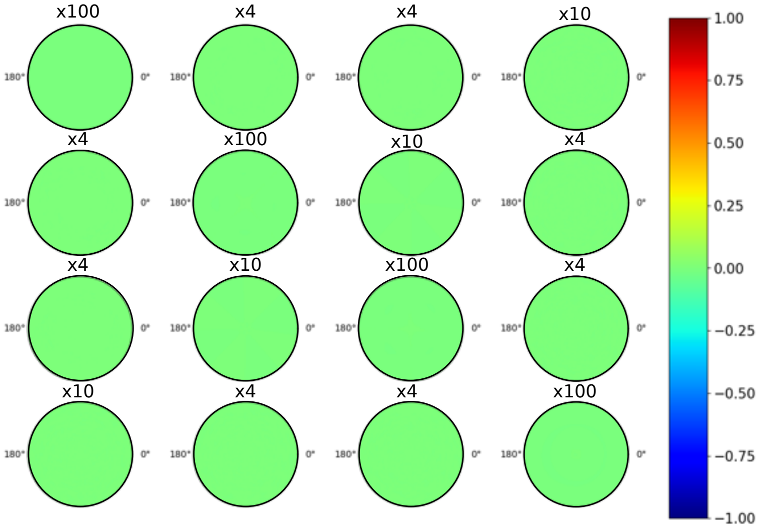

(b) Simulated L_u plot at 0° AOI for 400-1000 nm wavelength

Figure 3.10 Differential (a) mean L_m and (b) uncertainty L_u matrices of the simulated Mueller matrix obtained from a uniaxial Fresnel model. The wavelengths spawns from 400 nm (center) to 1000 nm (outer ring). The azimuthal angle is counted counter-clockwise.

Table 3.1 Optical parameters of the Lorentz oscillators describing nanodisc samples, obtained from the uniaxial Fresnel model of the measured Mueller matrices. A is the amplitude, E is the central energy and Γ is the damping of the Lorentz oscillator.

Sample	OD05	OD10	OD15	RD05	RD10	RD15
Lorentz minor axes (eV)	A=24.1	A=29.8	A=20.9	A=4.7	A=4.5	A=3.9
	E=1.51	E=1.61	E=1.63	E=1.48	E=1.50	E=1.53
	Γ=0.08	Γ=0.15	Γ=0.27	Γ=0.34	Γ=0.53	Γ=0.6
Lorentz major axes (eV)	A=23.5	A=28.0	A=20.0	A=4.5	A=4.6	A=4.0
	E=1.52	E=1.65	E=1.65	E=1.5	E=1.53	E=1.57
	Γ=0.08	Γ=0.15	Γ=0.27	Γ=0.34	Γ=0.55	Γ=0.61

measured depolarization has a different source which is directly related to the properties of the sample. In addition, it becomes clear that observed, small but non-zero circular elements *CB* and *CD*, are related to the depolarization effects together with the limitations of the setup. In fact, the depolarized light intensity, which is detected, is misinterpreted as circular. This effect is absent in the simulations.

The model provides some quantitative information about the properties of the sample. After fitting, all seven parameters mentioned above are extracted. These parameters are presented in the table 3.1. Figure 3.11, demonstrates the imaginary part of dielectric constant extracted from the model for all the six samples. For each sample a pair of Lorentzians represent the absorption associated with two LSPR in orthogonal optical directions.

It is observed that OD10 sample has highest spectral distance $\Delta\lambda$ between localized plasmon resonances, which reaches 20 nm wavelength difference. This is the origin of the strongest amplitude in the Mueller matrix elements for this sample. Other samples show smaller degree of optical anisotropy however, non-zero. For samples RD10 and RD15 only azimuthal angles, where anisotropy is well defined, were used, since information on the other regions is corrupted due to the quality degradation of the samples. Nevertheless, this information is enough to capture the main features of the samples.

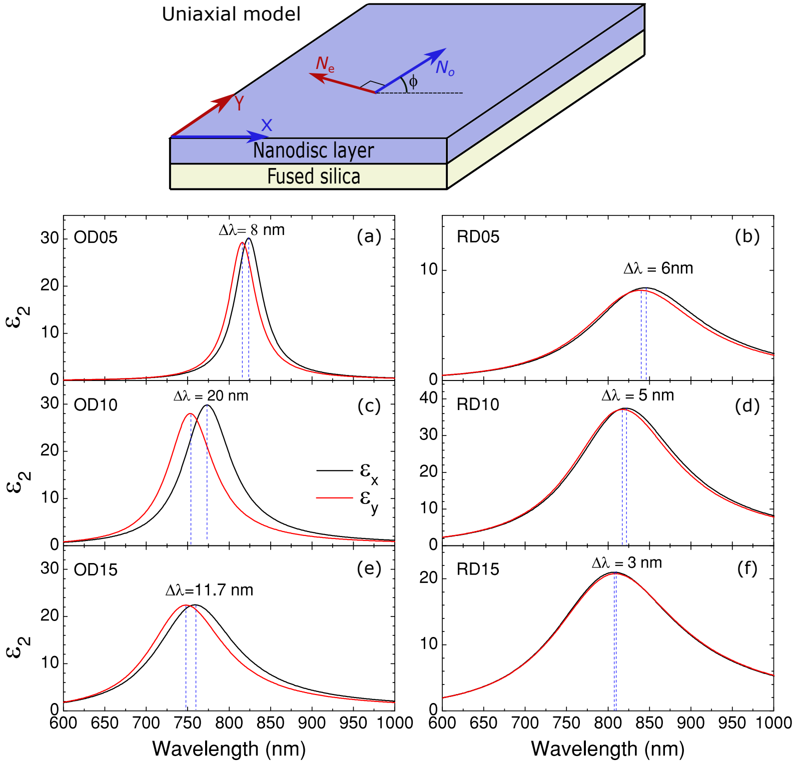

Figure 3.11 Schematic of the uniaxial Fresnel model with extraordinary optical axis oriented in-plane. The angle Φ represents the Euler angle between the sample and the laboratory reference frames. Imaginary part of dielectric constant extracted from the uniaxial Fresnel model, for ordered (a,c,e) and random (b,d,f) samples. Two Lorentzian oscillators correspond to the LSPR for two orthogonal optical axes denoted as N_o and N_e.

The obtained results show that the nanodiscs in the sample actually deviate from the circular shape in-plane and rather have elliptical shape. From this data the observed dichroism can be well understood. At a specific azimuthal angles, when the basis of two orthogonal polarizations are aligned with the minor and major axes of the ellipsoid, each polarization excite the two LSPR separately. The absorption along minor axis is larger at lower wavelengths, and absorption along major axis is higher at larger wavelengths, due to the redshift with increasing size. This results in the bimodal spectral behavior observed in M_{12} for example, which is proportional to the difference of the extinction along two optical directions, as indicated in Fig. 3.9 (b,d). Rotating the sample by ninety degrees, swaps the major and minor axes, resulting in the change of the sign of the observed features.

It is interesting that for each sample, the amplitude as well as the direction of deviation from the circular shape is different, despite the fact that the samples are produced on the same substrate, with the same procedure. In fact the observed asymmetry can be related to the production algorithm. The nanodiscs are produced with the exposure fracturing algorithm [73, 74] with dynamic focus. This means that the particles are effectively divided into trapezoidal mesh, where exposure is applied and the focus of the electron beam is adjusted according to the current position of exposure. Apparently, such an approach introduces some imperfections of the shape.

Based on the ellipsometric data it is possible to quantify these imperfections. The goal now is to relate the optical response, observed in the measured Mueller matrices to the morphology of the nanoparticles. While the uniaxial layer model is in fact a two-dimensional model, the particles are defined within a three-dimensional space. As introduced in the theory part, Coupled Dipole Approximation method relates the LSPR and the size of the nanoparticles. So it can be used to extract the nanoparticle shape and size based on available information.

The spectral position of the two degenerate plasmon resonances is known from the Fresnel model simulations. CDA is used to calculate the scattering,

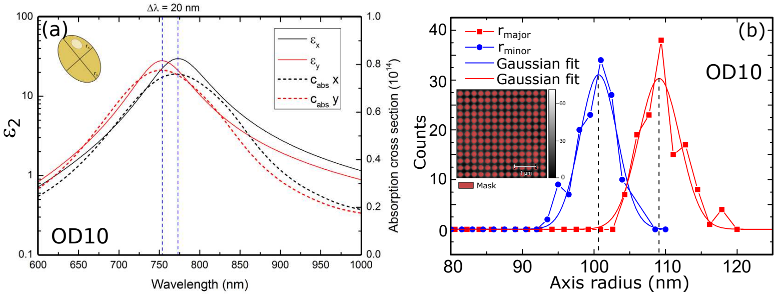

Figure 3.12 (a) Absorption cross section of the simulated square lattice with particle radii of r_{minor}= 96 nm and r_{major}= 108 nm shown in dashed line. The continuous line represents the imaginary part of dielectric constant extracted from the uniaxial Fresnel model, plotted on the logarithmic scale. (b) Extracted statistical distribution of the minor and major radii of the nanoparticles from the AFM image measured with 5 nm/px resolution. The inset represents the AFM image with the masked regions obtained by value threshold.

absorption and extinction cross sections of the corresponding arrays. The position of the peak of the absorption cross-section can be adjusted by changing the initial particle size and aspect ratio. Since the orthogonal plasmon resonances in the single particle are coupled and are defined by the aspect ratio of the particle, there is only one combination of minor and major radii, which results in two fixed resonant frequencies, given that the third axis (height) is fixed. So, the particle radii are adjusted during the fit procedure to match the spectral position of the LSPRs obtained from the Fresnel model. A comparison of the resulting absorption cross section and the imaginary part of the dielectric constant for the OD10 sample is shown in Fig. 3.12(a).

For OD10 sample, r_{minor}= 96 nm and r_{major}= 108 nm are obtained. Parameters for the other samples are condensed in the table 3.2. While the minor axis appears to be close to the expected value of 95 nm, the major axis deviates a lot. In order to validate the results, AFM is used. The images are obtained with 5 nm resolution ($5\mu m/1024$ px). To extract the ellipticity of the nanopar-

Table 3.2 Physical parameters of the nanodisc samples obtained from fitting optical data presented in table 3.1 by the CDA model as discussed in section 1.4.4. $\Delta\lambda$ is a spectral difference between two resonances. r_{minor} and r_{major} are the radii of the minor and major axes. Δr is the corresponding difference between major and minor radii. e is the particle eccentricity. $\frac{\Delta r}{r}$ is the deviation of the expected radius of 95 nm. Φ represents the Euler angle.

Sample	OD05	OD10	OD15	RD05	RD10	RD15
$\Delta\lambda$	8 nm	20 nm	11 nm	6 nm	5 nm	3 nm
r_{minor}	97 nm	96 nm	91 nm	93 nm	92 nm	93 nm
r_{major}	102 nm	108 nm	97 nm	98 nm	97 nm	95 nm
Δr	5 nm	14 nm	6 nm	5 nm	5 nm	2 nm
e	0.31	0.46	0.35	0.31	0.32	0.2
$\frac{\Delta r}{r}$	5.2%	14.7%	6.3%	5.2%	5.2%	2.1%
ϕ	-11°	-38.6°	-36.6°	20.2°	-14°	-47°

ticles, several preprocessing steps are performed with the help of Gwydion software. The measured quasi-three-dimensional image is first filtered in the Fourier space, to get rid of the unwanted residuals and dust particles left after the production. As the sample contain periodic arrangement of nanoparticles, it is easy to remove unwanted contributions in the spatial-frequency space. After, the segmentation is performed by a height threshold of 30 nm, which corresponds to the height of the gold layer. The statistical distribution of the nanoparticles minor and major radii are extracted by analyzing each masked region by fitting an ellipsoid, function available in Gwydion. The obtained result is presented in Fig. 3.12(b).

From the AFM analysis the nanoparticle radii of r_{minor}= 100± 2.74 nm and r_{major}= 109± 3.21 nm are extracted. While the value for a major axis is in perfect agreement with the value extracted from optical measurements, there is a slight discrepancy for the minor axis. This discrepancy may originate from the fact that the area investigated by AFM is 200 000 times smaller than in the ellipsometric measurement and thus may not represent the complete statistics over the whole sample. On the other hand the CDA approach simplifies the structure a lot, negating the effects of roughness, particle edges, and substrate related effects. Nevertheless, for other samples, the consistency of the results is much better, with not more than 1.5 nm difference.

3.2.1.3 Regression analysis

The analysis of the AFM images provides an additional important information about the distribution of the parameters. This information can also be obtained from ellipsometry measurements. It is accessible from the analysis of depolarization contained in the measured Mueller matrices. As discussed above, depolarization always arises from spatial or temporal averaging. From differential decomposition of the Mueller matrix, it is observed that the OD10 sample has depolarizing properties, which cannot be explained by roughness or setup imperfections. In addition, the depolarization of the linearly polarized light has a certain azimuthal angle dependence. The depolarization is maximum when both eigen LSPR modes are excited simultaneously, and has its minimum value when they are excited separately, i.e. the basis of laboratory frame coincide with the orientation of particle optical axes. Commonly, the depolarization caused by nanoparticles, whose shape deviates from spherical, is explained by the interference of the two eigen-LSPR [75, 76] within the particle. While the explanation is consistent with experimental results, it is wrong to assume that absorption or scattering on a single particle would lead to depolarization process. With a continuous wave, as in our experiment, the excitation of both modes is coherent. Thus, the scattered light may have different polarization state but this difference is stationary and does not lead to depolarization. Moreover, it was theoretically demonstrated, that inhomogeneities within the coherence range of the source do not result in decoherence and thus no depolarization can be observed [77].

In the experiment, however a broadband thermal light source is used, specifically a Quartz-Tungsten-Halogen lamp, in the spectral range of interest. Such a source is known to have low lateral coherence. The coherence length l_c of our optical system can be estimated using the van Cittert-Zernike theorem

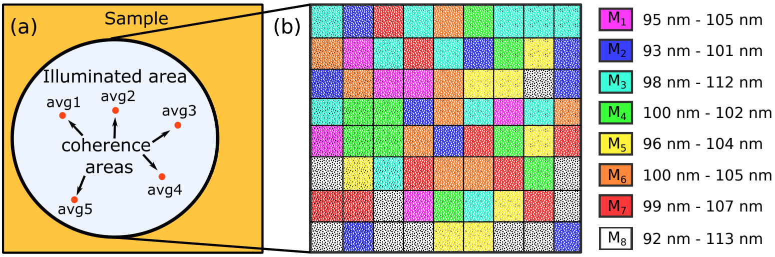
(a)
Sample
Illuminated area
avg1
avg2
avg3
coherence areas
avg4
avg5
(b)
M_1 95 nm - 105 nm
M_2 93 nm - 101 nm
M_3 98 nm - 112 nm
M_4 100 nm - 102 nm
M_5 96 nm - 104 nm
M_6 100 nm - 105 nm
M_7 99 nm - 107 nm
M_8 92 nm - 113 nm

Figure 3.13 (a) The sketch of the sample indicating the illuminated area by the probing beam containing many areas of coherence. The actual scales are exaggerated for clarity. (b) A simplified schematic representing the simulation based on DDA. The illuminated area contains many homogeneous regions, each corresponding to certain particle aspect ratio. The Mueller matrix for each of the regions is calculated separately. The superposition of these matrices results in depolarization.

[78]:

$$l_c = 0.16\frac{l\lambda}{d/2}, \tag{3.1}$$

where l is the distance between the source and the sample, λ is a wavelength of interest and d is the diameter of the source. Plugging the parameters of the system l= 50 cm, λ= 400 nm , d= 1 cm, into the above equation a coherence length of 12.8 μm is obtained. Theoretically the coherence length is a constant of the optical system and condensing lenses must not influence the initial degree of coherence. Practically, the lens imperfections and some possible misalignment can further reduce the degree of coherence.

The diameter of the probing beam is 500 μm, when focusing probes are used. Thus, the illuminated area $A_{ill} \approx 200000\ \mu\text{m}^2$, while the area of coherence A_{coh} is only 129 μm^2. The measurements are done beyond the coherence area and the observed depolarization can be attributed to the spacial inhomogeneity, as is sketched in Fig. 3.13(a). When many particles with slightly different sizes are excited simultaneously, the dipolar field of the particles, separated by distance more than coherence length, can lead to incoherent superposition of the fields. As a result, interacting with a system of particles, any variation of their parameters, such as shape, dimensions, roughness, orientation *etc.* would lead to a depolarization. This can be viewed as the relation of the structural entropy of the sample to the variance of light polarization properties. Based on this logic, it is possible to extract structural entropy from the measured depolarization.

While differential decomposition is useful to separate physical properties of the sample, sum decomposition is a perfect method to represent the sample with in-plane variation of its properties, Fig. 1.18. In this framework, the sample can be simulated as a set of patches with different particle sizes, with associated Mueller matrices, which are combined together. As discussed in the theory part 1.6, the Cloude decomposition allows us to represent any depolarizing Mueller matrix with up to four trace orthonormal non-depolarizing Mueller matrices, derived from the coherency matrix. The sum-decomposition relaxes the restriction on the type and the number of the chosen Mueller matrices. As a result the depolarizing Mueller matrix can be represented as a sum of predefined non-orthonormal matrices. This can lead to non-unique solutions, however if the spectral response is considered, the unique solution can be recovered.

Following this logic I utilize Discrete Dipole Approximation to generate the Mueller matrices associated with different ellipticities. The method is analogous to the CDA, however more accurate by accounting the real shape of the particles. Patches are generated with the minor and major axes centered around the values extracted from CDA, 96 nm and 108 nm, and a variation of ± 10 nm, with a step of 1 nm. This results in 441 separate patch models. The dipolar resolution for particles in this model is 1 nm, which results in 100 000 dipoles on average. To reduce the computation time, the presence of the substrate is again accounted by the effective refractive index of n= 1.25. The Mueller-Jones matrices for each patch are calculated separately, using periodic boundary conditions with appropriate periodicity and lattice constant

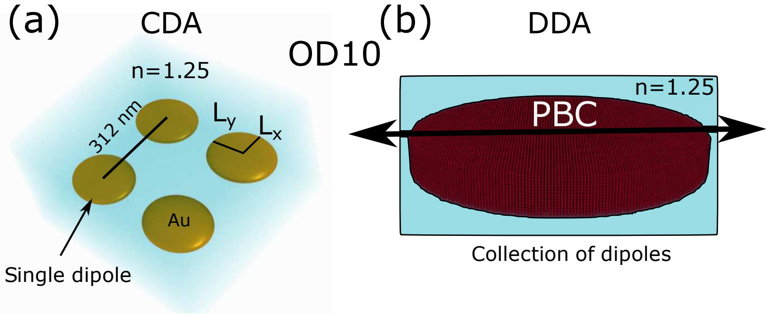

Figure 3.14 (a) An image representing the coupled dipole approximation model, with single particle represented by a single dipole and the parameters taken for OD10 sample. (b) An image representing the discrete dipole approximation model with periodic boundary conditions (PBC), where each particle is represented as a collection of dipoles.

of 312 nm. The evaluation of these 441 spectral Mueller matrices, in the wavelength range between 400 to 1000 nm, takes approximately four days on the 3.2 GHz 32 core Intel Xeon processor. Once the Mueller-Jones matrices are obtained, the problem reduces to simple least square regression problem.

The calculated matrices are linearly superposed with normalized weights $\vec{w}_i$, which are initialized according to the normal distribution. The weights are adjusted according to the minimization of the MSE function:

$$MSE = \sum_{\lambda} \sum_{i,j=1}^{4} \left(M_{\text{exp}}(\lambda, i, j) - \sum_{k=1}^{441} w(k) M_{\text{sim}}(\lambda, i, j, k) \right)^2, \tag{3.2}$$

using simple gradient descent algorithm [79]. With learning rate $\varepsilon = 10^{-4}$, which is obtained empirically, around 40000 steps are required to achieve convergence. After regression, out of 441 weights, only 54 have a non-zero value, resulting in the parameter space reduction. As each matrix in the linear combination represents a certain size and aspect ratio of the particle, the statistical size distribution is obtained from the resulted weights for each axis separately. The result of this fit is depicted in Fig. 3.15.

Panel (a) presents a comparison of the Mueller matrix measured at azimuthal angle of 0°, where depolarization hits its maximum, together with the simulated regression Mueller matrix for OD10 sample. The dichroic and birefringent effects, associated with the corresponding LSPR are well recovered. The discrepancy in the elements with small amplitudes, M_{12}, M_{21}, M_{34}, M_{43} and M_{33} are related to the angular resolution of the measurements. The measurements are performed with the resolution of 5 degrees, and the Euler angle ϕ is determined to be -38.6° for OD10 sample. While the simulations are done with the 0° offset, in the measurements there is a 6.4° mismatch between the laboratory and the sample reference frames. This results in non-zero values of the above mentioned Mueller matrix elements, opposed to the case of simulation, where the reference frames match at this angle. In principle this descripancy could be overcome by applying the rotation matrix R, as described in Appendix A. Nevertheless, the discrepancy is small and this was not done. The main elements, M_{13},M_{31},M_{24},M_{42},M_{11},M_{44}, in the regression matrix appear to have a broader resulting resonance.

As the assumptions inducing this discussion are based on the observation of depolarization effects, it is reasonable to compare the depolarization properties of two matrices. This information is introduced in panel (b), where the eigenvalues of the coherence matrices, both for measured and regression matrices are shown. The eigenvalue λ_1, which indicate the total amount of depolarization in the system, of the regression matrix matches both the spectral position and the amplitude of the eigenvalue of the measured matrix. It also covers a slightly broader spectrum, as well as the features in Mueller matrix, governed by broader resonance in the simulations. This is a sign that the total depolarization in both matrices is comparable. It is interesting to note that for the regression matrix only λ_2 is non zero, meaning that all the depolarization is lumped into one source of depolarization and the resulting matrix can be represented by only two non-depolarizing Mueller matrices.

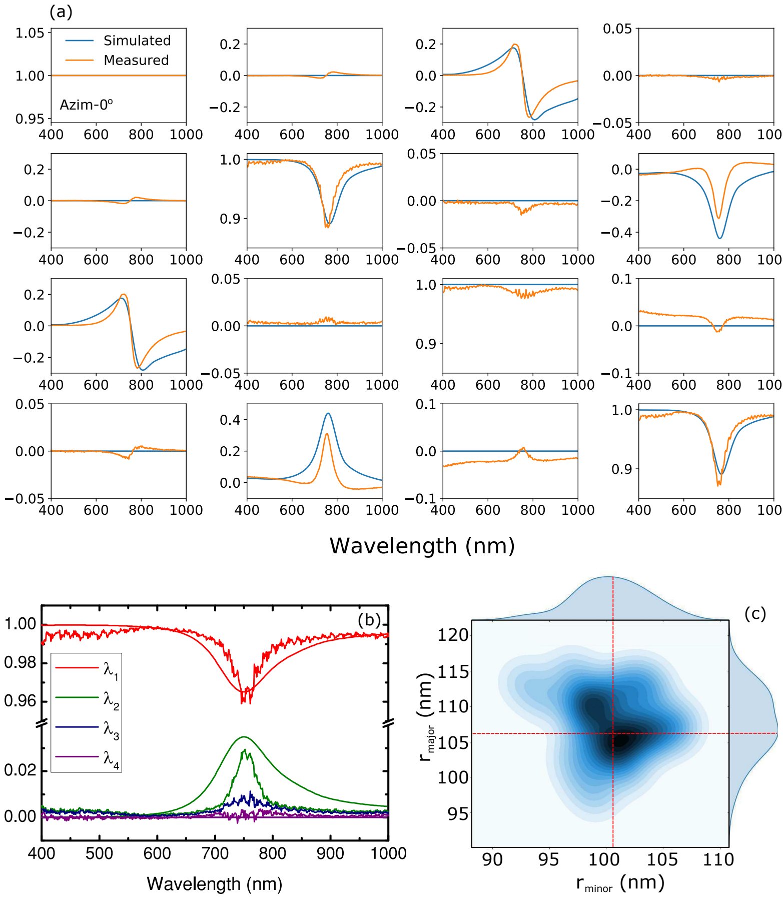

Figure 3.15 (a) Resulting regression Mueller matrix (blue) together with the measured Mueller matrix (orange) at azimuthal angle of 0° for OD10 sample. (b) Eigenvalues obtained from Cloude decomposition of the resulting regression matrix (smooth lines) and measured Mueller matrix. (c) Bivariate distribution of the particle size obtained from the fit of the measured spectral Mueller matrix for OD10 sample.

For the measured Mueller matrix, small but non-zero eigenvalue λ_3 can be observed around plasmon resonance. This is a clear indication that there is an additional source of depolarization, which is not accounted in the simulations. The sum of all eigenvalues of the measured matrix, perfectly matches the λ_2 of the regression matrix. In general the additional source of depolarization can be a variance of any other physical parameter of the nanoparticles such as height, tilt, orientation etc.

The discrepancy in resonance width is governed by the simplifications made during the simulation process. The first and the most contributing reason is the usage of the effective refractive index instead of the substrate in the simulations. In OD10 sample at normal incidence the grazing diffraction order, associated with the refractive index of substrate n=1.49, is in the proximity of the LSPR, at 930 nm according to the equation 1.89. Although its spectral position is relatively far from LSPR to achieve coupling, its presence still modifies the width of the LSPR, resulting in a narrower resonance. In the simulations the refractive index of the substrate is absent, and the associated RWA does not reduce the width of the resonance, which results in a broader spectral width in comparison to the measured spectra. The second simplification is related to the simulation approach. While in reality the size of the particles is distributed over the whole sample, we simulate the different ellipticities separately, on a perfect lattice. Thus, the variation of the surface-to-surface particle distance, which also influences the resonance position and width, is not accounted in the simulations. Finally, the distribution of the particles size is continuous within the sample, while we model it in discrete steps. It was observed that decreasing the step size from 2 nm to 1 nm dramatically improves the quality of the fit. Further decrease of size discretization is expected to provide even more improvement. Nevertheless, the particle size step was chosen to be 1 nm, being a trade-off between accuracy and computational complexity. What is important in this case, is that the obtained regression matrix matches the resonance position and the amplitude of the elements observed in the measurements.

Finally, panel (c) shows the derived mutual distribution of the minor and major axes of the particles, obtained from weights w_i. The distribution slightly deviates from a bivariate normal distribution and is centred around r_{minor}= 100.5±4.3 nm and r_{major}= 106.5 ±5.2 nm. The obtained mean values are in a perfect agreement with the AFM results presented in Fig. 3.12(b). The variance, obtained with optical technique is slightly larger. This can be governed by the fact that the investigated area, in the case of optical measurement is three orders of magnitude larger than the one probed by AFM, thus, it better captures the statistics of the whole sample. The main advantage of the method is an ability to characterize large surface areas, whereas the microscopic techniques are suitable for characterization below the coherence area. The good agreement of both techniques proves the good performance and robustness of the optical method, which can be used as a complementary technique, when large area characterization is required.

3.2.2 Polarization conversion properties

As observed in the transmission measurements at normal incidence, the samples have decent polarization conversion properties, which are concealed in the off-diagonal blocks of the Mueller matrix. It is known from various studies, that the lattice modes can couple to the plasmonic modes and result in substantial enhancement of the plasmonic modes [80, 81, 57, 82]. In this section, I investigate the influence of the lattice modes on the polarization conversion properties of the samples. To achieve better coupling of the lattice modes to the LSPR, it is necessary to perform measurements at higher angles of incidence. Taking into account the limitations of the ellipsometer, measurements at high AOI are more convenient to perform in the reflectivity configuration.

Reflectivity measurements are performed only at oblique angles of incidence, since the configuration of the RC2 ellipsometer does not support reflectivity at normal incidence. At larger AOI, in the periodic samples, diffraction starts to play an important role. In particular the emergence of Rayleigh-Woods anomalies. The grazing diffraction orders couple to the LSPR, leading to an extreme enhancement of the plasmon mode, spectral shift and drastic changes in the propagation direction [28]. Such coupling is known as surface lattice resonance (SLR) [81]. This effect is best observed in the OD05 sample due to its lattice constant. The measured dispersion relation for the sample at 0° and 45° azimuthal angles is shown in Fig. 3.16

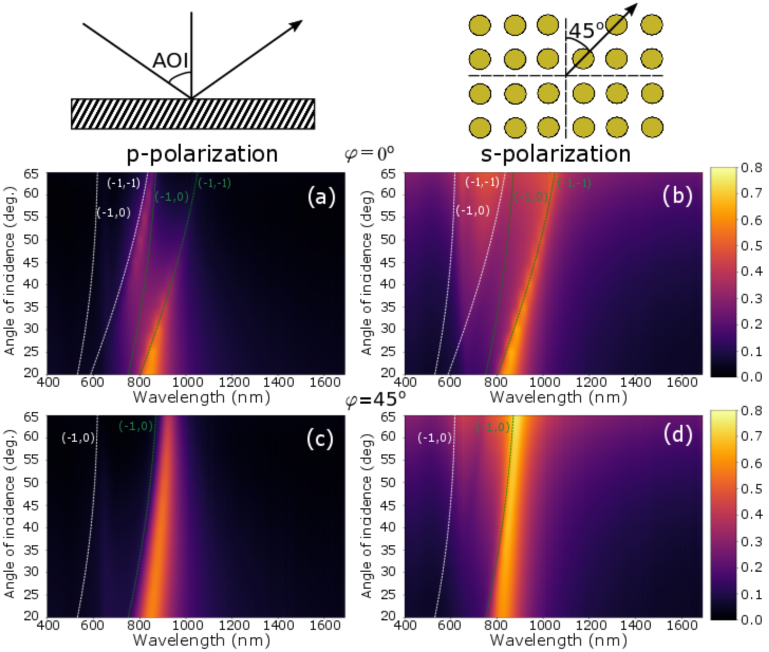

Figure 3.16 Dispersion of reflected *p*-polarized (a,c) and *s*-polarized (b,d) intensity for azimuthal angle 0° and 45° in OD05 sample. The dashed lines represent the Rayleigh lines, where white color represents diffraction emerging from air with refractive index n=1.0 and green from substrate with n=1.49. The labels are the Miller indices of the lattice, where (-1,0) correspond to first Brillouin zone, and (-1,-1) to the second.

At azimuthal angle of 0° the LSPR is distorted by four Rayleigh lines. According to equation 1.89 the diffraction is governed by the scattering on the first and second Brillouin zone, labelled by Miller indices (-1,0) and (-1,-1) respectively. Due to the presence of the substrate with refractive index n=1.49, the degeneracy of diffraction lines is lifted. As can be observed, for *p* polarization this results in splitting of the LSPR into two modes. The mode at higher wavelength, is coupled to the the $(-1,-1)_{\text{sub}}$ diffraction mode causing a red shift. This mode has higher intensity at lower AOI and decays with an increase of AOI. The second mode, at lower wavelength, on the contrary, increases in intensity at higher AOI, as it is spectrally "squeezed" between two Rayleigh lines, resulting in a narrow spectral response. This shows an interesting effect of energy redistribution between two modes for *p* polarization. *S* polarization, on the contrary does not display such an effect. The mode at larger wavelength is coupled to the $(-1,1)_{\text{sub}}$ order and remains dominant for the whole range of measured AOI. Other lattice modes result in decrease of the LSPR intensity.

Rotating the sample by 45° leads to a swap of the lattice momentum of first and second Brillouin zones, and the dispersion is affected only by two Rayleigh lines, the other two do not couple. For the *p* polarization, all the intensity of the LSPR is now guided along a single Rayleigh line, resulting in a spectral shift of approximately 100 nm. The same is observed for the *s* polarization.

Since the *p* and *s* polarizations are effected differently, in the case of the 0° azimuthal angle, it is reasonable to expect interesting features in the Mueller matrix. Indeed, as can be seen from Fig. 3.17, the off-diagonal blocks, marked by red rectangles are non-zero. This points out that the sample has polarization conversion effects. As discussed in previous section, the asymmetry of the nanoparticles results in this effect, which is observed at normal incidence. From the dispersion of the Mueller matrix effects however, we can see that the effect is enhanced at higher AOI, attributed with sharp peaks, where the LSPR couples to the diffraction modes. Moreover, at oblique

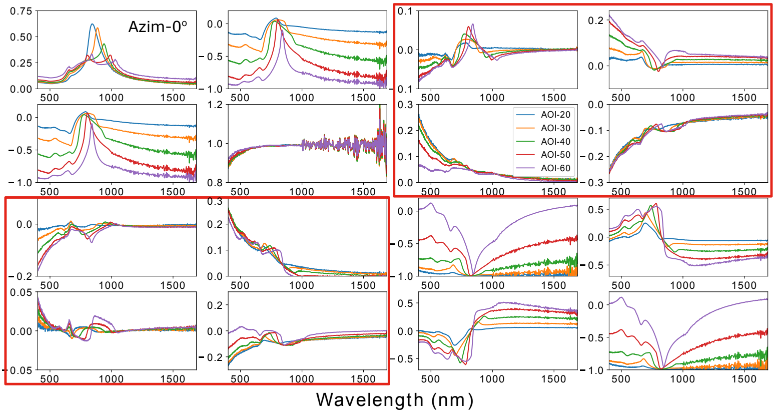

Figure 3.17 Mueller matrix of the OD05 sample measured at azimuthal angle 0° for several AOI. The M_{11} element represents total reflected intensity. The red rectangles mark the off-diagonal block elements which are related to the polarization conversion process.

incidence the symmetry of the system is lost, which is observed from the asymmetry of the off-diagonal elements of the Mueller matrix.

Before transferring directly to the polarization conversion, it is reasonable first to investigate the azimuthal dependence of the Mueller matrix elements, to get a better idea about the symmetry of the system. The measured complete azimuthal Mueller matrix at incidence angle of 45° is presented in Fig. 3.18. As discussed above, four Rayleigh lines are coupled to the LSPR with the azimuthal angle dependency. An interesting phenomena is observed in the off-diagonal block elements. Each time the LSPR matches the Rayleigh anomaly, the phase change occurs. This results in a higher four-fold symmetry of the crystal, opposed to the observations at normal incidence.

To investigate polarization conversion it is convenient to address the generalized ellipsometry terms. In general, the equation 1.45 is valid only for isotropic samples. Anisotropic samples can be described by a set of complex

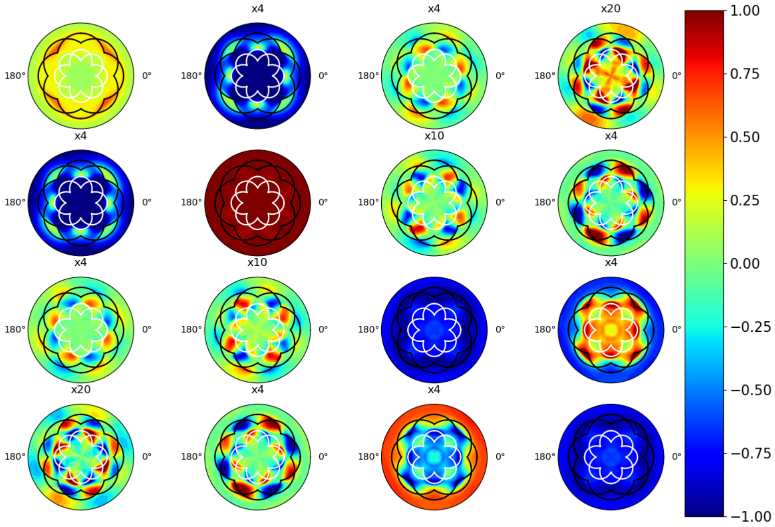

Figure 3.18 Azimuthal dependence of the Mueller matrix elements of the OD05 sample measured at 45° AOI. The solid lines depict the Rayleigh-Woods anomalies propagating in air (white) and in substrate (black), emerging from scattering on the first and second Brillouin zones.

reflection coefficients [10]:

$$
\begin{aligned}
\rho_{pp} &= \frac{r_{pp}}{r_{ss}} = \tan\Psi_{pp} e^{i\Delta_{pp}}, \\
\rho_{ps} &= \frac{r_{ps}}{r_{ss}} = \tan\Psi_{ps} e^{i\Delta_{ps}}, \\
\rho_{sp} &= \frac{r_{sp}}{r_{ss}} = \tan\Psi_{sp} e^{i\Delta_{sp}},
\end{aligned}
\tag{3.3}
$$

where r_{pp} represents the amplitude of reflected p polarization induced by incidence p polarization, and r_{ps}, r_{sp} represent the amplitudes induced by orthogonal polarizations, i.e. measured in cross-polarizers configuration. For an isotropic sample ρ_{pp} is equal to ρ, while in the case of anisotropic sample,

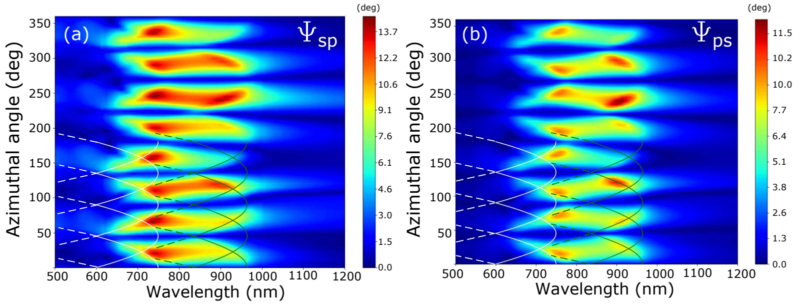

Figure 3.19 Azimuthal dependence of (a) Ψ_{sp} and (b) Ψ_{ps} for OD05 sample measured at 45° AOI. The solid lines represent the RWA according to the previous figures, while the dashed lines are their extended versions. The parts of the figures representing the azimuthal angle above 180°, are symmetric and the RWA would repeat, which is not shown for clarity reasons.

all three parameters describe the polarization conversion process from *s* to *p* and *vice versa*. Since, the depolarization measured in OD05 sample does not exceed 2% [1], it is possible to switch to generalized ellipsometric parameters, without loss of generality. Parameters Ψ_{sp} and Ψ_{ps}, representing polarization conversion amplitudes, are presented in Fig. 3.19 as a function of azimuthal angle. The solid lines represent the RWA calculated according to Eqn. 1.89, as in previous figures. The dashed lines show their extensions if an azimuthal angle ϕ_m is considered in range of 0°-180°.

Polarization conversion extends over the whole LSPR spectral width, from 700 nm to 1000 nm, emphasising its plasmonic origin. It is clear that the RWA enhances the effect and induces dispersion. The enhancement is, however different for two incident polarizations. For incident *p* polarization, Fig. 3.19(a), in general, the conversion is stronger and more homogeneous over the whole LSPR range. The conversion amplitude is enhanced stronger, at lower wavelength, where the mode couples to the surface modes emerging from air (white lines). For incident *s* polarization, the overall polarization conversion amplitude is weaker, but it is enhanced stronger by coupling to the surface modes. This observations are consistent with the dispersion relation from the Fig. 3.16.

---

[1] The depolarization data is presented in the Appendix *A*

It is interesting to note, that the azimuthal dependence of the polarization conversion displays regions with no polarization conversion, i.e. at around $\frac{n\pi}{4}$, where n is integer. This highlights the origin of the effect, the asymmetry of the nanoparticles. As was evaluated in previous section, the particles are slightly elongated, which breaks the rotational symmetry of the crystal. The results suggest that symmetric particles, result in no polarization conversion, even when coupled to lattice modes, in good agreement with the theory. Thus, the observed polarization conversion and its azimuthal dependence, may be another parameters to investigate the quality of the cylindrical particles, even at oblique angles of incidence. The procedure is however, more tedious and the analysis, in this case would be less straight-forward. Nevertheless, the dispersion of the polarization conversion allows us to investigate the quality of the lattice arrangements. Using the equation 1.89, with lattice constant as a fit parameter it is possible to evaluate the lattice constant precisely. In the case of OD05 sample, the lattice constant perfectly matches the intended 439 nm.

The parameters Ψ_{ps} and Ψ_{sp} alone, provide the information about polarization conversion amplitude, but it is unknown what is the conversion efficiency, i.e. how much of incident light is converted, and into exactly which polarization state. To obtain this information also the relative phases Δ_{ps} and Δ_{sp} has to be considered. It is convenient then to investigate the direct reflectance R_{pp} and R_{ss} and crossed-polarisers reflectance R_{sp} and R_{ps}. The polarization conversion has a prominent AOI dependence. Dependent on the azimuthal angle the conversion can increase or decrease with rise of the AOI. This is displayed in Fig. 3.20 for polarization conversion from p to s normalized by total detected s intensity at azimuthal angles 0° and 45°.

At this azimuthal angles the polarization conversion is low, reaching only 1-2% of total detected s-intensity, whereas at azimuthal angles between these two angles it can reach upto 20%. Nevertheless, the figure nicely demonstrates

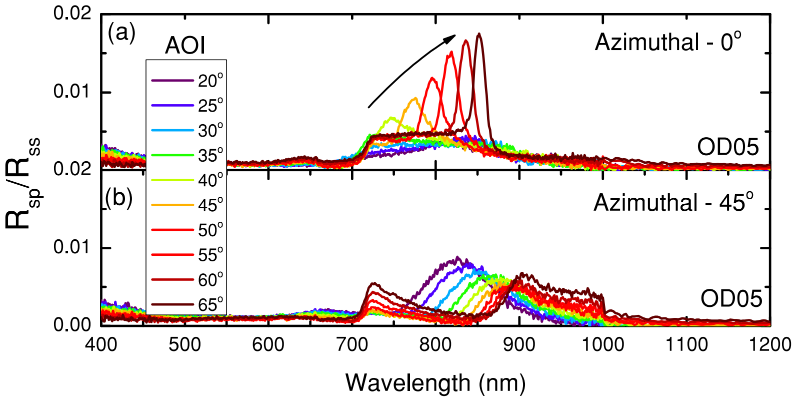

Figure 3.20 Polarization conversion from *p* to *s* polarization normalized by total detected *s* polarization reflected intensity R_{ss} measured on OD05 sample at azimuthal angles of (a) 0° and (b) 45° as a function of wavelength and AOI ranging from 20° to 65°.

how the polarization conversion can either be enhanced or reduced based on the RWA. Panel (a) demonstrates that the increase of the quality factor of LSPR results in a stronger polarization conversion and provides a narrow spectral control of the process. Panel (b), on the other hand, demonstrates how the polarization conversion can be suppressed in a desired spectral region.

A more convenient way to investigate the polarization conversion is to evaluate resulting Stokes vectors, from the measured Mueller matrices for different incident polarizations. This has an advantage, since the obtained three Stokes parameters, can be easily reduced into two parameters of the polarization ellipse according to equation 1.12, granting a direct access to the polarization state of light, after interaction with the sample. In addition, it is possible to conveniently investigate how different incident polarizations are converted after the interaction. As the polarization conversion effects, on average, are stronger at highest measured AOI of 65°, I concentrate on the analysis of data obtained at this angle. The azimuthal dependence of the outcoming Stokes vectors for different incident polarizations is presented in Fig. 3.21.

As the measurements are done at large oblique incidence, the reflectance of the s polarization is prevalent. With unpolarized incident light, the reflected polarization is mainly s, determined by dominant values of S_1 parameter with negative sign. At some azimuthal angles however, polarization rotation is observed, expressed in larger values of S_2, induced by the diffraction. At the same time, weak intensities of the circular polarization emerge in the S_3 parameter. For azimuthal angles of $\frac{n\pi}{4}$, $n = 1,3,5,7$, where the reflected intensity has its maximum, the polarization state remains unpolarized, observed from negligible amplitudes of $S_1 - S_3$ elements.

For incident p polarization an interesting phenomena is observed. While most of the light is transmitted through the structure, observed as white areas with low intensity values, at specific angles of $\frac{n\pi}{4}$, $n = 1,3,5,7$ and wavelengths around 900 nm, the coupling to the surface modes results in a strong enhancement of reflection. Moreover the reflected light has a strong p polarization character, as other Stokes parameters in these regions are close to zero. At lower wavelengths and angles of $\frac{n\pi}{2}$, the RWA result in weaker reflected intensity, and stronger polarization conversion, as observed from non-zero S_2 and S_3. The enhanced reflection of the p polarization on the RWA, in particular, explains the observed dispersion presented in the Fig. 3.16, where strong contribution of p polarization is observed even at large angles of incidence.

Incident s polarization show the strongest polarization conversion efficiency. Notice, while all the rows in Fig. 3.21, are multiplied by a factor of two, the row for incident s polarization is not modified. The coupling to the $(-1,0)_{\mathrm{air}}$ and $(-1,-1)_{\mathrm{air}}$ RWA, at lower wavelength results in polarization rotation by 45°. The coupling to the $(-1,-1)_{\mathrm{air}}$ and $(-1,-1)_{\mathrm{sub}}$ results in emergence of circular polarization at larger wavelengths. It is interesting that different properties of coupling, determine the properties of the emergent polarization. Most probably the spectral proximity of two surface modes,

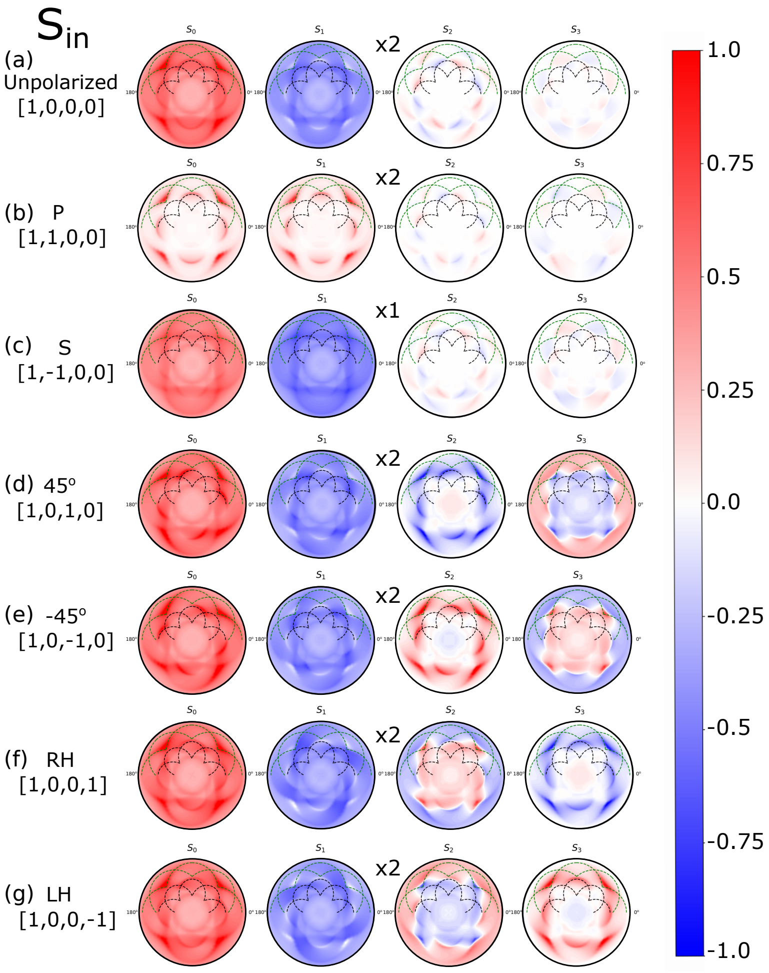

Figure 3.21 Azimuthal dependence of the outcoming Stokes vectors S_{out} for different incoming polarizations S_{in} (a) unpolarized light, (b) *p*-polarized light, (c) $s-$polarized light, (d) 45°-polarized light, (e) -45°-polarized light, (f) right circularly-polarized light and (g) left-circularly polarized light for OD05 sample, measured at 65° AOI. The dashed lines on each element represent the discussed above RWA, black for air and olive for substrate. The RWA are mapped only on the upper part of the graphs, whereas they are symmetric to the lower part. The Stokes parameters $S_1 - S_3$ are normalized by S_0, whereas S_0 represents the total reflected intensity.

which determine the quality factor of the surface lattice resonance is a key factor which leads to different polarization properties.

For ±45° incident polarizations, at the edges of the Brillouin zone, where LSPR coupling occurs, a 180° flip of polarization upon reflection occurs. This is concluded from the dominant values of S_2 at these azimuthal angles, with opposite sign with respect to the incidence. Outside of these regions, conversion to s polarization as well as to circular polarization is observed, which in combination results in elliptical polarization. It is interesting to note, that the helicity of resulting elliptical polarization depends on the choice of the incident polarization. Similar, but reversed in terms of elements, conversion properties are observed for incident circular polarization. It may seem that at specific azimuthal angles, where the spectral proximity of two RWA is the highest, quite efficient conversion of the left circular polarization to the right circular polarization is achieved. However, such conclusions are easier to perform from the reduced polarization state, or even by investigating the total reflected intensity in terms of specific polarization.

The Stokes vectors can be easily reduced into the parameters characterizing the polarization ellipse, orientation θ and ellipticity ε [9]:

$$\theta = \frac{1}{2}\arctan(\frac{S_2}{S_1}) \quad \varepsilon = \frac{1}{2}\arcsin(S_3) \tag{3.4}$$

The obtained azimuthal and spectral dependence of the emerging polarization parameters for the incident p and s polarizations are presented in Fig. 3.22. Apart from the polarization conversion induced by the asymmetry of the nanoparticles, the additional polarization conversion is induced by different coupling efficiency of the LSPR to surface modes for p and s polarization. Also, Fig. 3.22 demonstrates that there is no direct ps and sp conversion, rather some ellipticity is always induced. P polarization undergoes stronger polarization rotation, by around 25°, with weaker induced ellipticity, of around 2°. So in general, it is possible to achieve perfect polarization rotation by this type of the nanostructure.

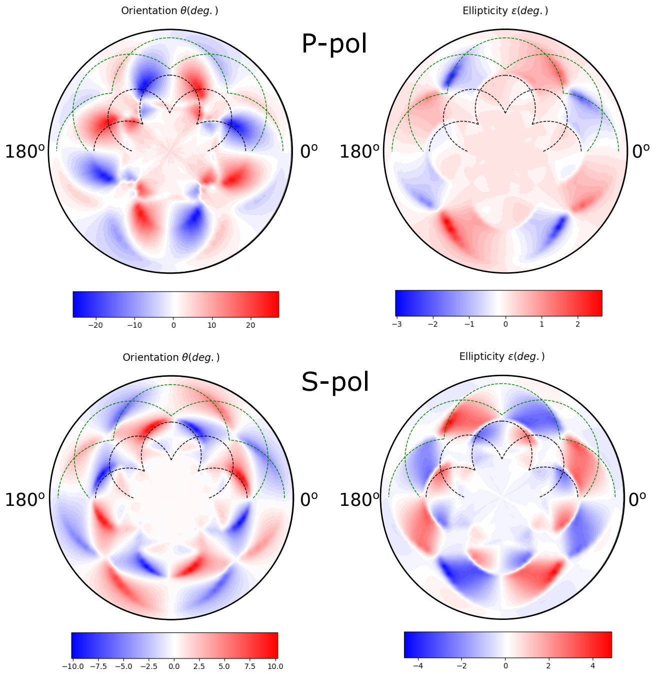

Figure 3.22 Azimuthal dependence of the outcoming polarization ellipse parameters; orientation θ and ellipticity ε for incident p and s polarizations on OD05 sample measured at 65° AOI.

Figure 3.23 displays the normalized intensities for different polarizations after the reflection of incident p and s polarized light, presented by a Stokes vector $\mathrm{S_{in}} = [1,1,0,0]$ and $\mathrm{S_{in}} = [1,-1,0,0]$ respectively. No direct conversion from p to s and *vice versa* is observed. The detected intensity for ±45° as well as for left and right circular polarizations, are comparable but not equal, which results in low values of S_2 and S_3 Stokes parameters.

Note, that by rotating the sample by 45° the RWA of the first and second Brillouin zones swap in wavelength. As a result the coupling for both

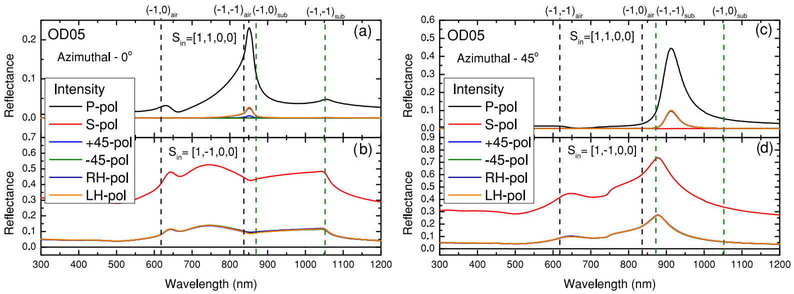

Figure 3.23 Calculated reflectance based on the Mueller matrix of the OD05 sample measured at 65° AOI, for *p* and *s* incident polarizations at azimuthal angles of 0° and 45°.

polarizations is affected. The LSPR for *p* polarization is observed to red shift, while the LSPR for *s* polarized light is blue shifted. This is governed by the asymmetry of the particles. As a result, the spectral distance between the LSPR and the RWA changes, which causes strong variations in the the coupling efficiency and significant changes in the polarization conversion for both incident polarizations.

It can be concluded, that the orientation of the particle asymmetry with respect to the lattice axes, in combination with the lattice period, provide a rich playground for polarization conversion control. By properly tuning these parameters a sample with a broad functionality can be obtained. In particular one can think about the device, which provide different polarization states upon interaction, dependent on the chosen azimuthal angle. Moreover, by tuning the asymmetry of the nanoparticles even further, it is in principle possible to suppress and enhance distinct polarizations in different direction, in order to achieve pure circular polarizations, without introducing chiral materials for example.

3.3 Honeycomb structures

In previous section, it was demonstrated that the asymmetry of the arranged nanoparticles results in an optical anisotropy, which consequently leads to polarization conversion. On top of that, the coupling of plasmonic modes to the surface diffraction modes resulted in an increase of quality factor of the plasmon resonance and as a result to the enhancement of the polarization conversion. With honeycomb structures, the azimuthal rotation symmetry is decreased and new surface modes are introduced. This allows us to further investigate the effect of the polarization conversion enhancement by the lattice modes, due to a better coupling to the LSPR.

3.3.1 Particle symmetry

The Mueller matrices for the honeycomb samples in transmission at normal incidence, show similar behavior as in square and random arrays. As the method of production of the structures is the same, all the previous assumptions about the sample are applicable. The asymmetry of the particles is not intended, rather is governed by the limitation of the fracturing method used for production. On the other hand, the reduced interparticle distance, different lattice arrangement and smaller particle sizes, result in the LSPR at higher frequency (lower wavelength) and broader spectral width, covering the whole VIS-NIR spectrum. For HC150 sample, the central wavelength of the LSPR is around 688 nm and for HC190 the central wavelength is at 790 nm. Thus, the four-fold anisotropy in the differential Mueller matrices are observed around these wavelengths, as demonstrated in Fig. 3.24.

The anisotropy of both samples show again similar two-fold symmetry, as for previous samples. The amplitude of the anisotropy is comparable with the square arrays, but the features are asymmetric with respect to their phase inversion. This asymmetry is governed by the weaker LSPR extinction at lower wavelength, close to the interband transition of gold, in comparison the

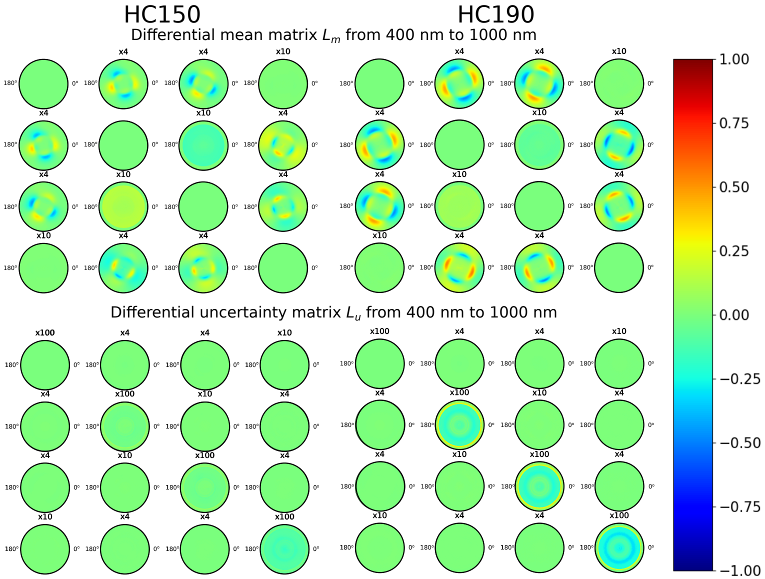

Figure 3.24 Differential Mueller matrices L_m and L_u for two honeycomb samples: HC150 (left) and HC190 (right), measured in transmission configuration at normal incidence for wavelengths from 400 to 1000 nm.

the LSPR at larger wavelength. Nevertheless, it is clear that the origin of the anisotropy is the same as in samples from previous section.

What is more important, is that these two samples result in almost no depolarization. As can be observed from the L_u matrices in the Fig. 3.24, the HC150 sample shows no depolarization, while the HC190 sample has very weak amplitudes of the diagonal elements. This gives a nice perspective on the quality of these samples and provides a possibility to compare it with the results obtained in the previous section, as shown in the Fig. 3.25. Panel (a) demonstrates the significant difference between the depolarization index in the square and honeycomb samples. The anisotropy of the particles is however, present in the honeycomb samples, and is comparable with the one observed in the square array sample, which is demonstrated through panels (b-d). The absence of the depolarization, is a direct sign that the variance of the particle size is very low. In addition, this emphasizes that the depolarization rises from the parameter variation rather than from the LSPR interference on asymmetric nanoparticle, as claimed by some studies. It can be concluded that the particles in the sample are asymmetric, however there is no variance of the minor and major axes over the entire sample area.

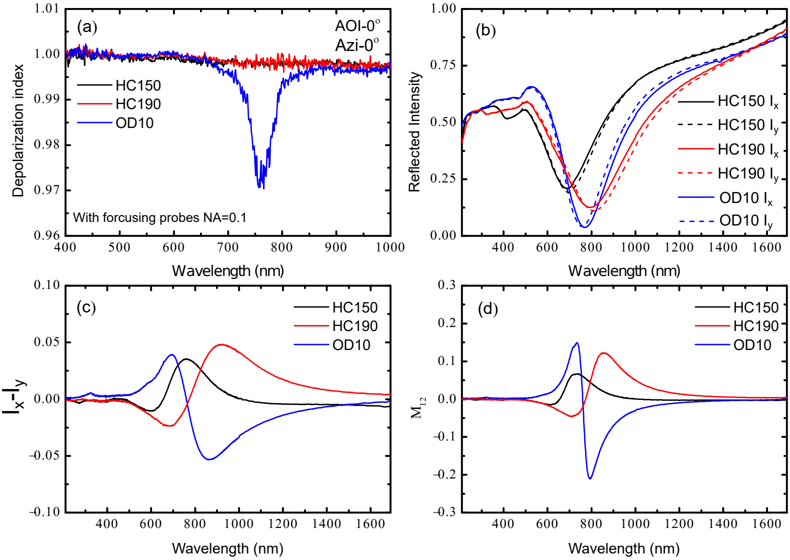

Figure 3.25 Measured optical properties of HC150 (black) and HC190 (red) samples in comparison with the properties of OD10 sample (blue). (a) Depolarization index. (b) Reflected intensity for two orthogonal polarization aligned with the major and minor axes of the nanoparticles (optical axes). (c) Difference between intensities for orthogonal polarizations presented in previous panel. (d) Measured M_{12} Mueller matrix element.

The further analysis of the structures quality is not done here as the results do not yield any new information. The broader spectral width of the LSPR results in lower extinction amplitude and consequently in less polarization conversion. In the next section the possibility to enhance the process with the RWA is investigated.

3.3.2 Polarization conversion properties

The honeycomb arrangement of inhomogeneities is famous for its extraordinary scattering properties. The dispersion relation for electrons in graphene, for example, displays Dirac quasi-particle regime, where the electrons follow the relativistic equations [83]. Beyond graphene it was demonstrated that, honeycomb arrangement of holes on the plasmonic surface, on the larger scale, results in similar phenomena for the propagation of the plasmon-polariton quasi-particles [84]. The associated effects of suppressed backscattering and topologically protected states have been also observed. According to the Babinet principle, the honeycomb arrangements of the plasmonic scatterers should also provide an interesting dispersion diagram.

In particular, the HC190 sample is interesting, as it contains the lattice resonances which couple well with LSPR. The dispersion of incident *p*- and *s*-polarized light for the HC190 sample is presented in the Fig. 3.26. The modes represent the eigenmodes of the lattice (the grazing diffraction orders) and the yellow region highlights the collective plasmon resonance of the lattice. In comparison to the OD10 sample, the dispersion of the HC190 sample is a bit more complicated. The scattering from second and third Brillouin zones couple to the plasmon resonance (from substrate) as well as the scattering from the fourth and fifth Brillouin zones (from air), for both azimuthal angles at 0° and 45°. It is prominent that the RWA at middle wavelengths couple well to the plasmon resonance and split it into two modes. Even at normal incidence, it is possible to observe the in-plane RW scattering for the green wavelengths, as demonstrated in the inset of panel (a). The coupling is however not so strong and enhancement is observed, as in the square arrays, since the plasmon mode itself is broader in honeycomb samples. On the other hand, the RWA in the vicinity of the plasmon resonance can be even observed with the naked eye, as demonstrated in the inset of the pallet (d) of the Fig. 3.26. The blue and red dots on the image are the in-plane propagating modes at associated wavelengths related to the RWA. It is interesting to note that both colors are spatially well separated and guided into different directions.

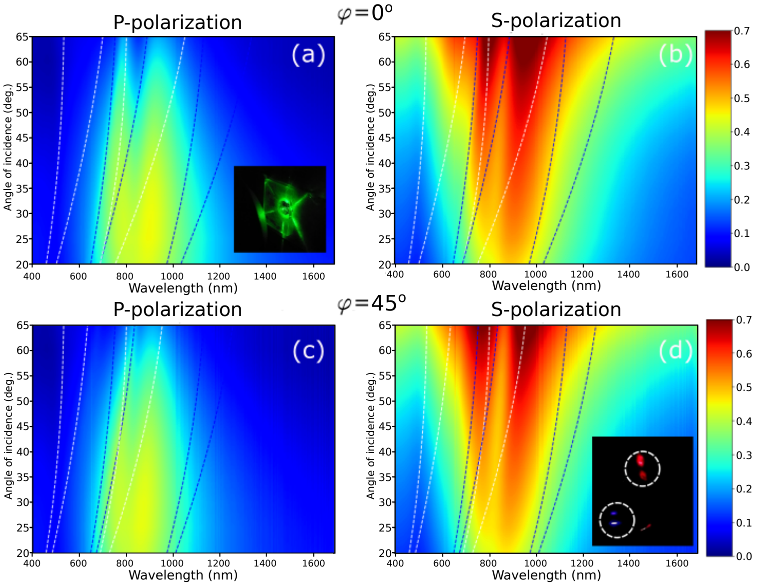

Figure 3.26 Measured dispersion relation for p- and s- polarized light from 20° to 65° AOI with the step of 5° for HC190 sample at azimuthal angles of (a,b) 0° and (c,d) 45°. The wight dashed lines represent the RWA associated with the refractive index of air, n=1.0 and blue lines represent the RWA associated with substrate refractive index n=1.5. The inset in panel (a) represent the scattering of green light, with λ =530 nm, at normal incidence. The inset in (d) represents the scattering, associated with RWA, observed in surface plane of the sample when sample is illuminated at 65° AOI.

These phenomena are well observed in the Mueller matrix, measured at the corresponding azimuthal angle of 45°, presented in Fig. 3.27. In comparison to the data of OD05 sample, demonstrated in Fig. 3.17, it becomes clear that the effect of the lattice resonance modes is stronger, which should contribute to stronger polarization conversion effects, displayed in the off diagonal blocks. The M_{13} element shows two resonant peaks, resulting from the splitting of the plasmon mode, with larger amplitudes than in OD05 sample. Moreover, the M_{24} element demonstrates larger intensities around the modes, which signifies the larger induced ellipticity upon polarization conversion.

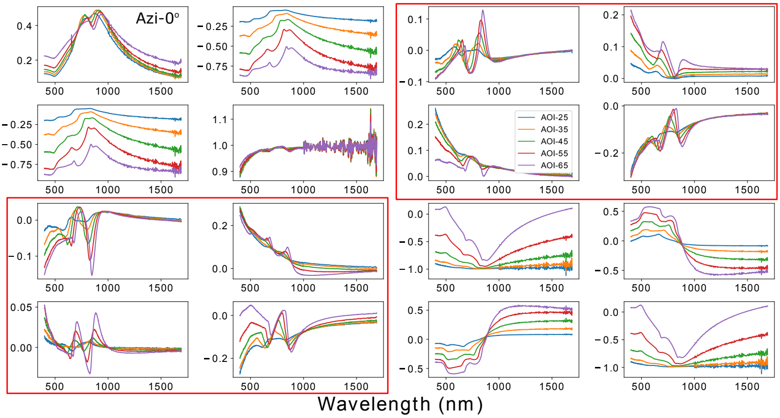

Figure 3.27 Measured Mueller matrix of the HC190 sample for wavelengths from 400 nm to 1690 nm, at azimuthal angle of 45° for AOI from 25° to 65°. The M_{11} element represents the measured total reflected intensity.

On the other hand, as mentioned, it is hard to deduce the properties of the polarization conversion from the Mueller matrix itself. Instead, it is reasonable to look again on the orientation and the ellipticity of the outcoming electromagnetic wave, after interaction with the sample. This information is presented in Fig. 3.28 for p and s incident polarizations. It is prominent that the symmetry of the polarization conversion effects is lifted due to higher symmetry of the crystal. Again, in comparison to the amplitudes at normal incidence, the values for p-polarized light display a stronger polarization rotation, up to 8° (almost 3 times larger) and almost the same amplitude for induced ellipticity, up to 1°. For *s* polarization, on the contrary, the polarization rotation amplitude increases only by around 30%, but the ellipticity is observed to increase by almost 5 times, up to 2°. Nevertheless, by a direct comparison to the results for the OD05 sample, presented in Fig. 3.22, it becomes clear that the effects of polarization conversion are actually weaker in the HC190 sample.

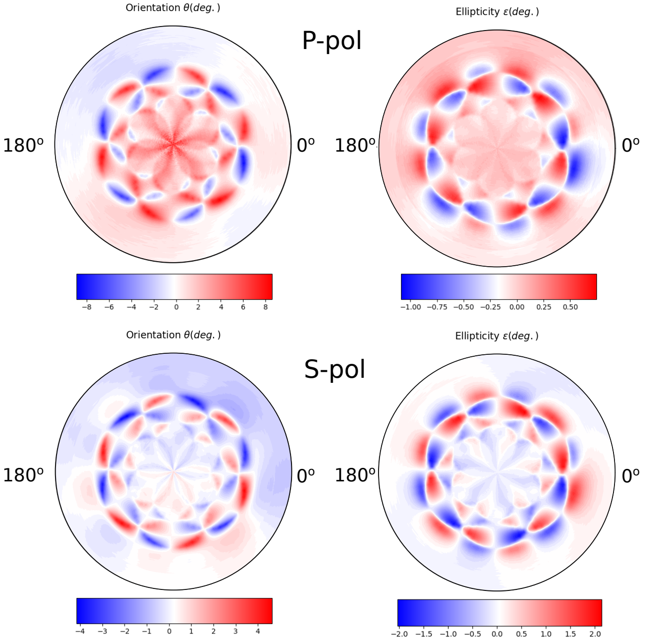

Figure 3.28 Azimuthal dependence of the outcoming polarization ellipse parameters; orientation θ and ellipticity ε for incident *p* and *s* polarizations after interaction with the HC190 sample, measured at 65° AOI, for wavelengths from 400 nm (center) to 1100 nm (outer ring).

For HC150 sample, where there is no coupling of RWA to the LSPR, such an enhancement is not observed and the amplitudes for θ and ε remain immutable while increasing AOI. In addition, for samples with low particle anisotropy, RD15 sample for example, no polarization conversion is observed at any angle of incidence. As a summary, it can be concluded that better coupling of the LSPR and RWA, leads to a dramatic polarization conversion enhancement nevertheless, the amplitude of the polarization conversion is firstly defined by the quality factor of the LSPR. So to achieve strong polarization conversion properties, for nanometer-thick waveplates for example, many factors have to be accounted. First, the particles have to be asymmetric, large ellipticity is beneficial. Second, both resonance modes, have to lie far from the band gap, to achieve larger amplitudes. This, already settles some limitations on the particle ellipticity. Finally, the lattice structure has to be adjusted in such a way that two RWA match both operating LSPR.

3.4 Conclusion

In the first part of the chapter it was demonstrated, on the example of nanostructures consisting from gold nanodiscs, that structural asymmetries as small as several nanometers can be well detected with the Mueller matrix ellipsometry. Mueller matrix measurements, combined with appropriate simulation techniques, allows quantification of these imperfections and precise determination of the quality of the sample. In particular, gold disc nanostructures were observed to posses optical anisotropy. This anisotropy is related to the nanodisc asymmetry, arising as a consequence of the e-beam lithography production method. The depolarization, contained in the measured Mueller matrices, serve as an indication of structural entropy over the entire sample area. Using the Discrete Dipole Approximation algorithm, the Mueller matrices were calculated as bases for the regression analysis. Performing least squares regression, the mean and the standard deviation of nanoparticles major and minor axes were recovered. Some discrepancies between measured and regressed data were observed, however they are completely justified by the model simplifications done during the simulation procedure. The extracted size and its distribution, utilizing this method, are in good agreement with the topographical methods such as AFM. As a result, a new optical, non-destructive method for critical dimension analysis is demonstrated, capable to perform fast analysis on a potentially unlimited area. This makes it an attractive alternative method to other microscopic techniques, which are limited only to the analysis on the smaller scales.

Further investigations are required to study the full potential of the method. In this study, only one critical parameter was quantified. From the Cloude decomposition of the measured Mueller matrices it was observed that there are multiple independent sources of depolarization. It would be interesting to apply the method, in order to recover the variation of several critical parameter simultaneously. For that, however it is reasonable to apply different simulation techniques, such as finite difference time domain (FDTD) or rigorous coupled wave analysis (RCWA), which might be beneficial in terms of accuracy and time.

In the second part of the chapter the polarization conversion properties of the nanostructures, containing asymmetric metallic nanoparticles were investigated. In particular the question of polarization conversion enhancement with the lattice modes was addressed. The particle asymmetry results in the polarization conversion, which is observed at normal incidence. Periodic arrangements of the particles lead to the diffraction phenomena. Increasing the angle of incidence, the eigenmodes of the particles couple to the grazing diffraction orders, which can significantly modify the properties of LSPR. The coupling of p and s polarizations is, however different. For p-polarized light it was observed that the polarization rotation angle θ can be increased by more than 3 times, without influencing the resulting ellipticity ε. For s-polarized light an opposite effect was observed; the resulting ellipticity dramatically increases by coupling to the lattice resonances, while the polarization rotation increases only slightly. The effects are investigated on two types of lattices, namely the square and the honeycomb arrays. The effect is observed for both types, where the coupling is strong, while in samples with weak or no coupling the effect is absent.

As a result, by properly tuning the particle shape and asymmetry, combined with smart particle arrangement it is possible to control and generate the polarization state on demand with nanometer thick metacrystals. While in this study, the asymmetry of the particles is not intended and is, in general rather small, for future investigations it is interesting to study the arrangements of the particles with different shapes and larger degree of asymmetry, such as nanorods for example. In addition to that, the arrangement has to be defined in the way to achieve the strongest coupling, already at normal incidence. This can be done if the coupling between the neighboring particle is not a concern. Finally, one can introduce the periodic variation of the asymmetry in the nanostructure, which would result in additional phase shift, in order to study if the observed ellipticity enhancement can be pushed further to achieve a single layer circular polarizer.

Chapter 4

Results on metal-insulator transition in VO_2

4.1 Introduction to VO_2 properties

V-O systems are invoking interest of scientist for many decades as strong correlated electron systems. Vanadium, with many oxidation states, form a huge family of allotropes, VO, VO_2, V_2O_3, V_2O_5, V_3O_5,V_4O_7, V_5O_9, V_6O_{11} etc. [85]. Many of them undergo insulator-metal transition (IMT) at different temperatures. VO_2 however, has obtained special attention, since in this compound the transition falls just above room temperature, making this material very promising for a variety of applications.

Historically, the insulator-to-metal transition in VO_2 was first reported by Morin [86] in 1959, where a sharp drop of resistivity, of four orders of magnitude was observed. Later, an associated structural transition was detected [87], from M_1 monoclinic lattice with $P2_1/c$ space group in the insulating phase, to rutile R lattice with a space group of $P4_2/$ mnm in the metallic phase. In rutile phase the vanadium V^{4+} atoms occupy the body center and the lattice vertices of the tetragonal structure. Undergoing the structural transition from rutile to monoclinic phase, the vertex atoms shift from its positions, lowering the symmetry of the crystal and resulting in two sets of vanadium dimers with a zig-zag pattern and two different bond lengths, as is sketched in Fig. 4.1. The transition is accompanied with the unit cell doubling along c-axis and around 1% expansion in the same direction.

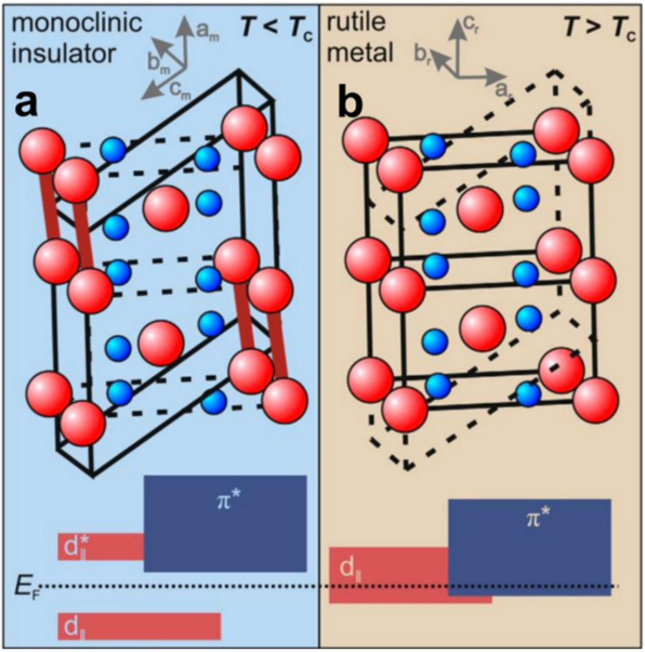

Figure 4.1 VO_2 crystal structure together with a sketch of the band structure around the Fermi level in (a) insulating phase (b) metallic phase. The red spheres represent the Vanadium atoms and blue are the Oxygen atoms. [5]

In addition, the insulating phase was observed to exist in other structural arrangements. In samples, where tensile stress is present, a second monoclinic phase M_2 stabilizes between M_1 and R phases, forming a triple point, where three phases coexist [88, 6]. In M_2, only half of the Vanadium chains form a zig-zag pattern, while the other half remains in linear chains. While the existence of intermediate insulating phase does not influence much on the spectral properties of the material, in the VIS-IR range, the electronic phase transition itself as well as its critical temperature are affected. The phase diagram obtained for VO_2 single crystals as a function of tensile strain is presented in Fig. 4.2.

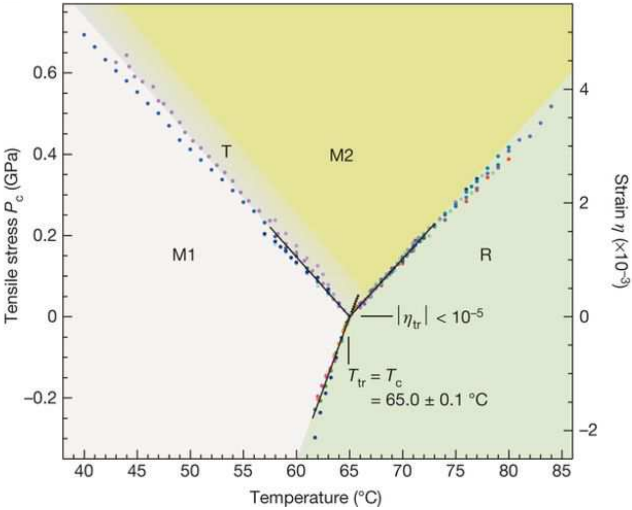

Figure 4.2 Temperature-stress phase diagram with deduced monoclinic M_1, M_2 and tetragonal T insulating and rutile R metallic phases. The triple point is estimated to occure at 65 °C for unstrained samples being the value for a bulk single crystal. [6]

The coincidence of electronic and structural transitions, gave birth to the debates about the origin of the metal-insulator transition, which continue even today. On one hand, the dimerization of vanadium atoms points towards Peierls distortion, which occurs in the chains of conducting atoms. Indeed, from the band formation perspective, the crystal field splits the 3d band of

Vanadium into t_{2g} (Π^* bonding) and e_g ($\sigma\ d_{||}$ bonding). The t_{2g} band is further split into a_{1g} and e_g^π, due to symmetry braking of non-cubic lattice structure [89]. The Vanadium atom has 5 electrons on the outer shell, four of which are shared to form bonds with oxygen atoms. Thus, in a rutile phase the atom is left with one valence electron which partially occupies a_{1g} band, and the systems is metallic. The structural transition into M_1 phase leads to hybridization of a_{1g} band, due to formation of Vanadium dimmers, leaving completely filled a_{1g} band. This introduces an energy gap between a_{1g} and unoccupied e_g^π. This behavior, is confirmed with the *ab-initio* calculations [90] with one important remark. The a_{1g} and e_g^π bands are observed to overlap, resulting in the metallic state.

On the other hand, for transition metal oxides, Mott has shown that electron-electron correlations can induce the band splitting of partially filled d orbitals, causing the formation of the band gap around the Fermi level [91]. Indeed, the implementation of electronic correlations in the *ab-initio* calculations results in the shift of e_g^π band and a consequent formation of the band gap in accord with the experimental observations [92]. The exact value of the band gap is however, different from experimental observations. After decades of theoretical and experimental studies, the question is still unresolved, whether the insulator-metal transition in VO_2 is purely due to electron-electron correlations, or due to the lattice distortions. Latest results suggest the importance of both phenomena. Several studies has demonstrated that the structural and electronic transitions can be decoupled by external or internal strain effects [93–95], which puts the above statement under the question mark.

Additional complexity is introduced by the hysteretic nature of the transition, observed for example in resistivity [96, 97] and Hall measurements [98, 99], optical spectroscopy in different frequency ranges [100–102], and structural investigations [103, 104]. The width of hysteresis depends on the sample production method [105], the substrate and its orientation [106–108]. In particular, the width and the sharpness of the transition is linked to the quality of the material, with thinner and steeper transitions for higher quality samples [105]. Moreover, an asymmetric hysteresis is observed both in single crystals and thin films, with a steeper transition from the metallic to the insulating phase than *vice versa* [109–111]. Although *ab-initio* calculations can reproduce the main characteristics of the IMT in VO_2 [92, 112, 113], they neither include the hysteretic nature nor its asymmetry, which is governed by microscopic and thermodynamic processes in the samples [114].

Many potential applications involving IMT in VO_2 rely on its hysteretic nature. This includes memory devices [115, 116], optical switches [117], plasmonic modulators [118] etc. Thus, the ability to understand the origin of hysteresis and develop a model reproducing it, is vital for high quality realization of these applications. To do so, it is reasonable to step one level up from the atomic scale and investigate microscopic nature of the transition.

The hysteretic nature of the observed transition implies that the transition is of the first-order. This means that the transition is not abrupt and overgoes a coexistence region of two or several phases, forming the domain structure. Very recently, it has been confirmed by several microscopic techniques, such as nanoscale x-ray microscopy [119, 120], near-field optical microscopy [120], and conducting atomic force microscopy [121]. The metallic phase is observed to develop as clusters, within the insulating matrix, with rising temperature. At certain temperature the fraction of metallic phase in the composite reaches the critical value, at which a long-range conducting cluster is built and the properties of the composite are governed by the properties of the biggest cluster. Such transition is known as percolation transition and is well described by the percollation theory [122], based on some critical parameter, as described in section 1.3.3.

As was discussed in the theory section, the macroscopic properties of intermediate states of such a transition can be well described via effective medium approximation. In particular, the Bruggeman approach is most suitable to discuss the evolution of aggregated metallic clusters in VO_2 thin films, due to its polycrystalline grainy topography. Previously, some attempts were done to apply different EMA models to data, measured over the transition in VO_2 compound. In particular, Kim *et. al*, back in 1996, has applied a 2-dimensional BEMA model [123], to describe IR measurements over the transition. Later, 2d BEMA as well as Maxwell-Garnet models were applied to describe the resistivity measurements [96, 124, 98]. These works however, are all based on several assumptions of parameters, such as the dimensionality of the percolation process and the value of the depolarization factor, or the shape of the clusters. As a result, only the inconsistency of the measured data and the model was reported.

Reasonable approach was taken by Qazilbash *et. al*, for applying BEMA model to treat mid-IR and far-IR optical response of the VO_2 over the transition [125]. In this work, instead of assuming static depolarization factor of the developing metallic inclusions, authors have treated it as a fitting parameter. The filling fraction was determined from SNOM data and the dielectric properties of constituents from optical measurements. This model resulted in satisfactory outcomes and was shown to be applicable for extraction of dielectric properties of the VO_2 material over IMT above 800 cm^{-1}. Nevertheless, the study omits several important points. First, the scarcity of data points at different temperatures around IMT restricts from obtaining of the temperature-dependent function of the depolarization factor over the IMT. Secondly, the study completely omits the hysteretic nature of the transition and origins of its asymmetry.

This chapter summarizes an extensive study of the optical properties in the UV-NIR range of VO_2 thin films produced by radio frequency sputtering. The ellipsometric measurements on films with different thicknesses are analyzed in the framework of the anisotropic dynamic Bruggeman effective medium approximation. It is demonstrated that the model is not only capable to accurately describe optical properties over the complete transition region, but also provides valuable insights about the microscopic nature of the transition. In particular, the extracted temperature dependence of the depolarization factor, describing the shape of the metallic clusters, display a non-linear behavior.

Additionally, it is responsible for the observed asymmetry of the transition during heating and cooling cycles. This interesting behavior is further related to the structural transformation and the associated strain relaxation effects, deduced from the roughness data, extracted with the help of the same model and confirmed with the AFM measurements. Finally, localized surface plasmon resonance, associated with the metallic clusters, is detected in the percolation regime. Based on the parameters of the resonance an attempt to estimate the average cluster size is made, which provides additional information about the development of the transition.

4.2 Preliminary characterization of the samples

The vanadium dioxide thin films were deposited by radio frequency sputtering using a metallic V target in a reactive process with an Ar/O_2 gas mixture on an Al_2O_3 substrate of 510 μm thickness, with the *c*-axis (0001) perpendicular to the plane. During deposition, the gas pressure was about 3.4×10^3 mbar and the ratio of the mass flows O_2/Ar was adjusted to 3.1%. The growth temperature was kept at 550 °C over the full deposition period of 60 minutes [126]. In total 5 samples are produced with expected thickness of 100, 200, 400, 600 and 800 nm.

To characterize the samples, their exact thickness, roughness, critical temperatures and optical properties has to be determined. The rough estimation of thickness is done from the profilometer data, obtained after sample preparation and is presented in Fig. 4.3. The profilometer data for the 100 nm sample is unfortunately not recorded. The average thicknesses are determined to be 203± 2.4, 404± 3.3, 589± 13.7 and 819 ± 5.2 nm. For the 600 nm sample the layer height is not stabilized in the accessible region, thus the determined thickness is not accurate enough.

The derived thicknesses can be compared to the results obtained from standard ellipsometric measurements, where the thickness is derived from the created optical model, fitting complete Mueller matrices. The model

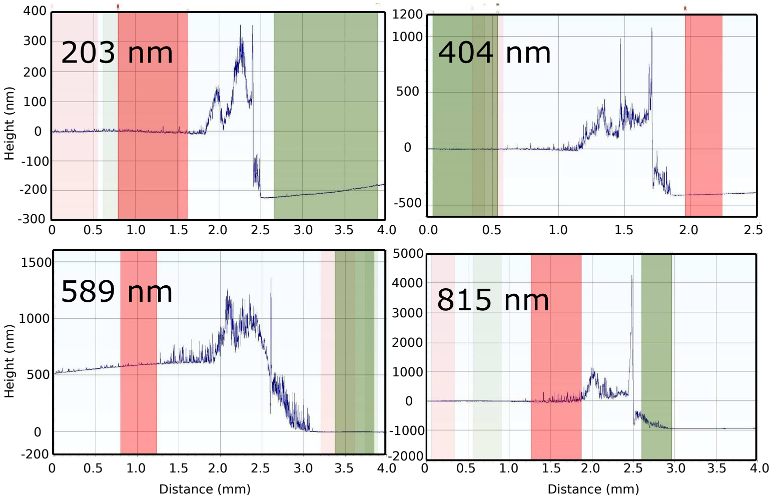

Figure 4.3 Profilometer data recorded on the edge of VO_2 thin films with expected thicknesses of 200, 400, 600, 800 nanometers.

parameters are discussed in the next section. Based on the two approaches, with isotropic and uniaxial models, the derived thicknesses are presented in the table 4.1.

Table 4.1 Thickness of the samples derived from modeling ellipsometric data with isotropic and uniaxial models, and from profilometer measurements. μ represents the mean value and σ is the standard deviation.

Sample	Isotropic		Uniaxial		Profilometer	
	$\mu(nm)$	$\sigma(nm)$	$\mu(nm)$	$\sigma(nm)$	$\mu(nm)$	$\sigma(nm)$
Sample 1	102	0.4	101	0.3	-	-
Sample 2	227	0.7	198	0.4	203	2.4
Sample 3	465	1.63	406	0.8	404	3.3
Sample 4	664	0.8	602	0.7	589	13.7
Sample 5	810	1.1	810	1.1	819	5.2

The values obtained from isotropic model are 10-13 % larger then expected values for 200 and 400 nm samples. The reason for that is the anisotropy in the thinner films, which is not accounted in the isotropic model. The uniaxial model, on the other hand, accounts the anisotropy along the out-of-plane direction of the film, parallel to the c-axis of the substrate and results in more precise values of the film thickness. The origin of the anisotropy in the samples is discussed further in the text. Despite the actual thicknesses, in the text, I will continue to refer to the samples according to their expected thicknesses.

Roughness can also be derived from the ellipsometric model, and validated with the AFM data. For the samples, independent on the model, roughness values of 17.5, 15, 21, 12, 10.5 nm are obtained. This is in a good agreement with the values extracted from large scale (50 μm by 50 μm) AFM measurements. Ellipsometric values represent the total thickness of a rough layer, which is modeled via BEMA mixing model with 50% volume fraction of air. The AFM data represent the root-mean-square (rms) values. To compare both values, ellipsometric data is divided by $\sqrt{2}$ to convert it into rms [127]. The derived root-mean-square values are presented in Fig. 4.4. In addition, the average grain size is extracted from the AFM images by estimating the average radius of approximate circle inscribing the grain, available in Gwydion software. The large scale AFM images are presented in the Appendix B. The thicker films are smoother than thinner ones. The 400 nm thick film however is an outlier. The mean grain radius correlates with roughness and increases form 65 nm in 100 nm thick film to 75 nm in 800 nm thick film . It is reasonable to mention that the roughness changes over the transition into the metallic state. The temperature dependence of the roughness, as well as the comparison with the AFM data are discussed further in the section 4.4.

To characterize the quality of the films and to determine the critical temperatures of the IMT, temperature-dependent dc-resistivity measurements are performed. The measurements are done in the van der Pauw configuration from 300 K to 370 K. The resistivity is derived according to the procedure

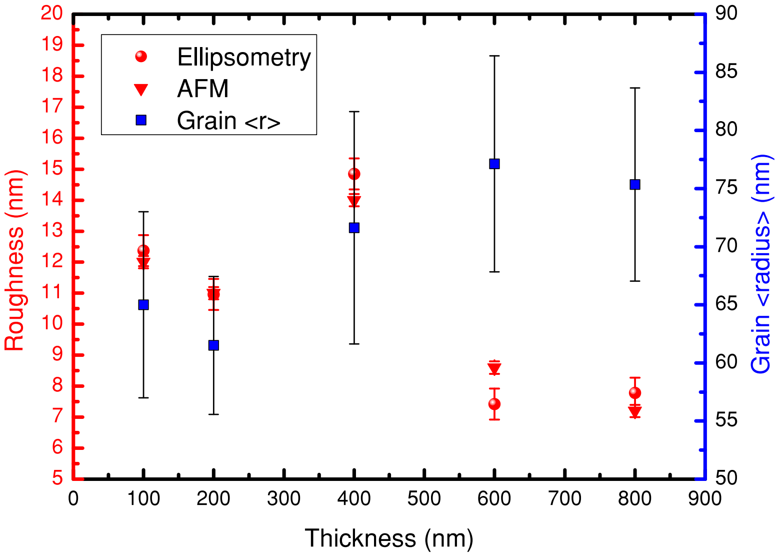

Figure 4.4 Thickness dependence of the evaluated roughness (red symbols) from ellipsometry and AFM data, together with mean grain radius (blue symbols) obtained from AFM.

described in the section 2.3 and is displayed in Fig. 4.5. All the five samples have a comparable resistivity for both phases. The insulating phase settles around 6 Ω·cm at ambient temperature, for all samples except 600 nm with a slightly higher 8 Ω·cm. Reaching critical point, an abrupt decrease of resistivity is observed, of almost 4 orders of magnitude, down to 1.2×10^{-3} Ω·cm. The 600 nm thick sample, again has a different resistivity in the metallic phase, of 1.0×10^{-3} Ω·cm, making 600 nm sample to have the highest resistivity contrast among the others. Such a contrast of resistivity corresponds to the samples of the highest quality and is almost reaching the resisitivity difference of single crystals [128]. All the samples show a well-defined hysteretic behavior of the transition, but with different onset temperatures and different hysteresis width, as demonstrated in the inset of the Fig. 4.5. 200

nm thick sample, has the broadest hysteresis width of ΔT= 6.7 °C, while other samples have a width in the range between 5 and 6 degrees.

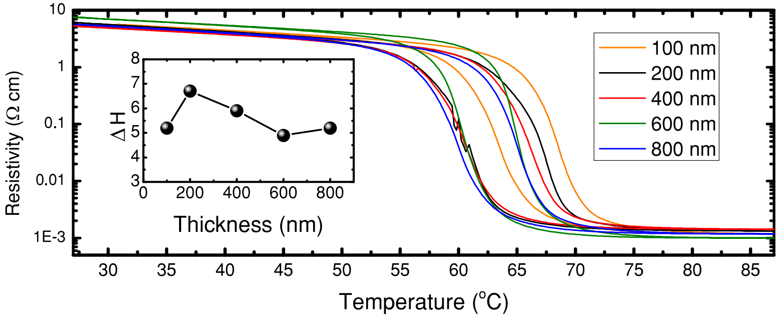

Figure 4.5 Temperature-dependent resistivity of VO_2 thin films with thicknesses of 100, 200, 400, 600, 800 nanometers. The inset presents the width of the hysteresis curve versus film thickness.

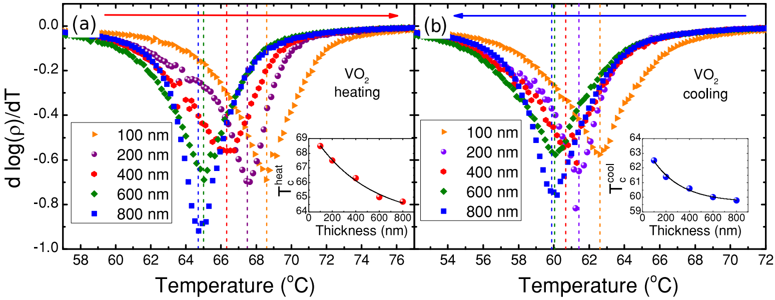

Figure 4.6 Derivative of the logarithm of resistivity ρ with respect to temperature T, plotted versus temperature for (a) heating and (b) cooling. The inset in each figure displays a critical temperature versus thickness.

Notice a negative correlation of the width of the hysteresis, shown in the inset of Fig. 4.5 and the determined grain size, presented in Fig. 4.4. Interestingly, the larger the grains the lower the width of the hysteresis ΔH. Apparently, this correlation must be a result of an interplay between surface topography and superheating/supercooling effects associated with the amount of defect states. It has been shown that the hysteresis and its asymmetry is related with coupling of structural and electronic transitions, and is defined by nucleation on the defect states [114]. While heating, the metallic phase can nucleate on generated twin wall domains of the insulating state, which reduces superheating effect. During cooling, the nucleation of the insulating phase is restricted only to the point-like defects, as the metallic rutile phase symmetry does not allow the existence of twin walls, resulting in a supercooling. With larger grains, the grain separation as well as the grain boundary density is reduced and the geometrical constraints for structural transition on the upper layer are lowered. These effects take a key role in determining the properties of IMT and are discussed in more details in the discussion section.

From the resistivity data, the critical temperature of the electronic transition can be precisely determined. The slope of the logarithm of resistivity displays a well defined extremum at the transition temperature, as the absolute rate of change has its maximum at this temperature. This is displayed in Fig. 4.6 (a) for heating, and (b) for cooling, separately. The critical temperature decreases with increasing film thickness, both for heating and cooling cycle. The rate of change is however, different for heating and cooling, which is displayed in the inset of the Fig. 4.6(a,b). For heating the T_c^{heat} changes by almost four degrees in total, from 68.5 °C down to 64.7 °C. For cooling T_c^{cool} decrease by 2.7 degrees, from 62.6 °C down to 59.9 °C. The critical temperature together with the hysteresis width ΔH and transition width for all the samples is condensed in Table 4.2.

The decrease of critical temperature with thickness is puzzling, since sometimes the inverse thickness-temperature relation is observed [129, 130]. Nevertheless, some studies point out that the substrate induced anisotropy plays a major role in the temperature dependence of the critical temperature, and the reverse behavior, as in this case, is observed [131].

The changes in the width of hysteresis are mainly governed by the shift of IMT in the heating regime, while the cooling curve shifts slower to lower

Table 4.2 Sample parameters extracted from the resistivity measurements. Resistivity contrast between insulating R_i and metallic R_m phases. Critical temperatures obtained during heating $T_\mathrm{c}^\mathrm{heat}$ and cooling $T_\mathrm{c}^\mathrm{cool}$. Transition temperature width during heating ΔT^heat and cooling ΔT^cool. Hysteresis width ΔH.

Thickness (nm)	$R_\mathrm{i}/R_\mathrm{m}$	T_c^{heat} (°C)	$T_\mathrm{c}^\mathrm{cool}$ (°C)	ΔT^heat (°C)	ΔT^cool (°C)	ΔH (°C)
100	$4.65{\cdot}10^3$	68.5	62.5	24.1	26.16	5.21
200	$4.61{\cdot}10^3$	67.5	61.4	23.92	30.63	6.76
400	$3.78{\cdot}10^3$	66.3	60.6	24.96	27.22	6.12
600	$7.66{\cdot}10^3$	65.0	60.0	20.6	23.48	5.11
800	$4.71{\cdot}10^3$	64.8	59.9	24.76	26.74	4.83

temperatures. This may be related to film roughness and average grain size. Both would have an influence on the process of twin wall formation within a film. With higher roughness the formation of twin walls decreases as the separation between grains with different crystallographic orientations, on the surface layer, increases. This reduces the nucleation probability and enhances the superheating effect. The same effect is expected for decreasing grain boundary density.

According to the phase diagram displayed in Fig. 4.2, based on the critical temperatures for heating cycle, the samples must cover the range between positive tensile strain, with an emergence of M_2 phase, down to no strain around triple critical point. This phase diagram is however, valid only for the single crystal samples, whereas for thin films, with relatively large grains, the critical temperatures may be shifted. It is unclear however, how to treat the reverse transition, from metallic to insulating phase, were the critical temperatures are lower. The different rate of change of the critical temperatures for heating and cooling, confirms nonequivalence in processes involved in the transition from insulator to metal and *vice versa*. This also points towards relation of electronic and structural degrees of freedom, and

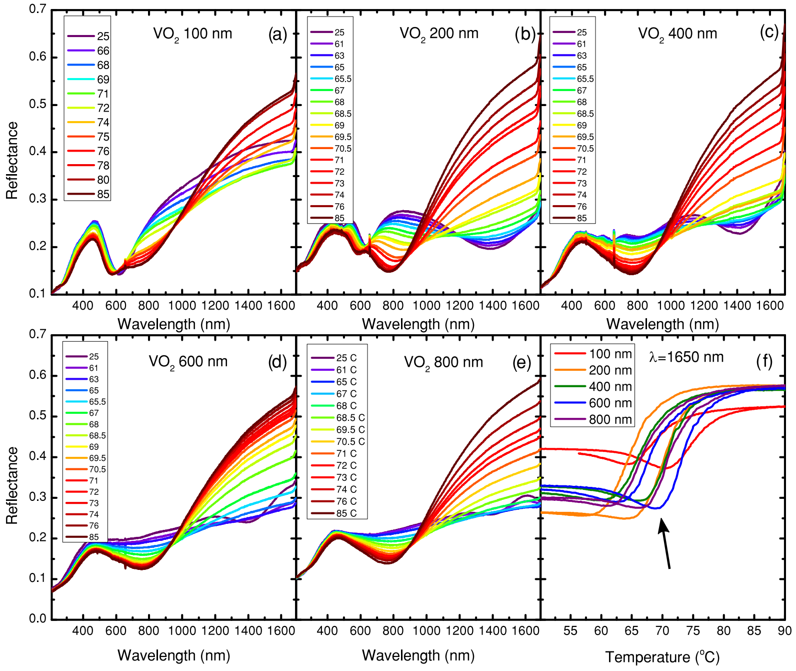

Figure 4.7 Measured DUV-NIR spectral reflectance as a function of temperature during heating for VO_2 thin films with thickness from 100 nm to 800 nm (a-e). (f) Temperature-dependent reflectance at 1650 nm wavelength as a function of film thickness.

highlights the importance of the heterojunction properties as well as the topographical properties of the films. This is discussed in more details in relation to ellipsometric measurements in the following sections.

The temperature-dependent reflectivity was measured from 210 nm (5.9 eV) up to 1690 nm (0.73 eV) with the RC2-UI ellipsometer at oblique angles of incidence of 55 degrees. Later, based on the Fresnel models, I derive the reflectivity at normal incidence. The results are compared with the extended range of IR measurements, performed under the microscope attached to Bruker 66 FTIR spectrometer, from 1000 nm (1.24 eV) to 10000 nm (0.124 eV) for some temperatures, which is partially provided in Appendix *B*. Figure 4.7 shows the wavelength-dependent reflectivity measured at different temperatures on the ellipsometer, for all the samples.

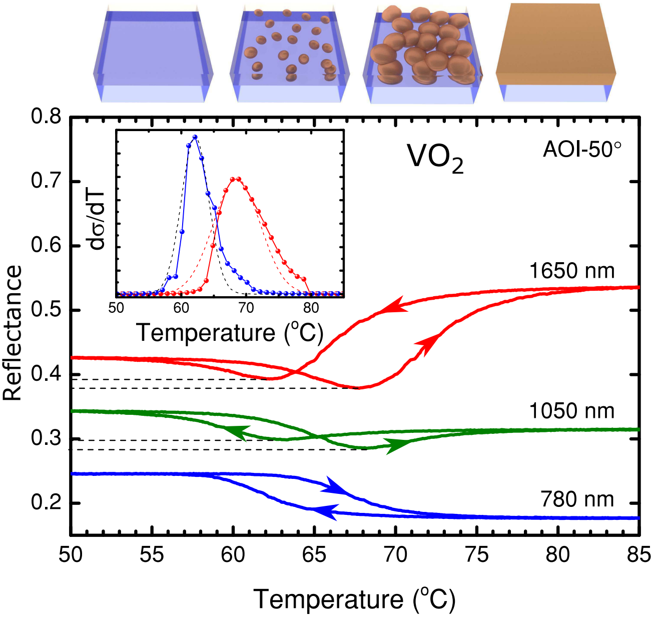

Figure 4.8 Measured reflectance of the 100 nm VO$_2$ film at wavelength of 1650, 1050, 780 nm as a function of temperature. The sketches on top demonstrates the increasing volume fraction of the metallic phase, with rise of the temperature. [7]

With increase of temperature, the reflectance changes. The visible range (400-700 nm) is not affected much, with maximum of 5% decrease in reflectivity. In the NIR range, above 800 nm, a strong increase in reflectance is observed, associated with the emergence of free charge carriers in the sample and consequently a transition into the metallic state. As presented on the panel (f) of the Fig. 4.7 , the strongest change of the reflectance at 1650 nm is observed for the 200 nm sample, from 0.27 in the insulating to 0.57 in the metallic phase. This is related to the presence of Fabry-Perrot resonance at this wavelength for 200 nm thick film. In the metallic phase the reflectance for all the samples, except 100 nm sample is the same, as the thickness of the samples is larger than the skin-depth. This is consistent with the results of dc-resistivity data, where the resistivity is almost the same for all the 5 samples.

It is important to note that a decrease in reflectance for all the samples is observed, before the intensity increases upon transition into the metallic phase, as demonstrated in Fig. 4.7(f). The drop in reflectivity depends on the film thickness and is wavelength- and temperature-dependent. For more clarity, the temperature-dependent reflectivity of the 100 nm film is presented in Fig. 4.8. It is prominent that the sample has different optical properties during heating and cooling cycles. The larger wavelengths, which are affected by an emergence of free charge carriers, show a strong asymmetry at minimal values, located in the vicinity of the critical temperatures T_c^{heat} and T_c^{cool}. The relative decrease for all the samples is different. The origin of this phenomena is investigated and discussed in details in the section 4.4.

4.3 Properties of the insulating and the metallic phases

To be able to apply the mixing formula of the BEMA model according to the equation 1.73, it is necessary first to determine the properties of the constituent phases, based on the optical measurements. The measurements are performed at oblique angles of incidence from 20° to 65° with the angular resolution of 5°. Measurements at oblique incidence allow to probe not only in-plane properties but also out-of-plane contributions by measuring both, s and p polarizations. The angular dependence measurements provide the dispersion information in a material and allow to precisely model and determine the in- and out-of-plane optical properties. The properties of the substrate are determined from the separate measurement, and result in a birefringent Cauchy model with very weak absorption in the UV region, below 300 nm, modelled by the Urbach tail.

In general, the crystal structure of VO_2 suggests strong anisotropy of the insulating phase due to its monoclinic structure. Thin films however, are polycrystalline and thus, its properties are governed by the average of three crystallographic axes, and is similar in all directions (isotropic). In reality, for thin film samples it is often observed, that some degree of anisotropy is still present [132]. This can originate from many sources based on the growth method and conditions, type of the substrate and purity of the films. Here, in the investigated samples, anisotropy is also observed. It is deduced from the better performance of the uniaxial anisotropic model in comparison to the isotropic one. The significance of the anisotropy decreases with the film thickness, especially for metallic phase. Films of 600 and 800 nm thickness are observed to be optically isotropic. For clarity reason and space economy, here the isotropic model is introduced, which served as a base for the anisotropic model, used for final evaluations. The results of isotropic model are further compared with the results of the anisotropic model.

The insulating phase of VO_2 is known, from experimental data, to have an optical band gap in the range between 0.6-0.75 eV dependent on the film quality [133, 104, 134]. This implies that the use of a model, incorporating a band gap is necessary. For semiconductors with a direct band gap, a common solution is to use Tauc-Lorentz oscillator model, to describe the spectral response. Combined with three Gaussian oscillators, the model which adequately describes optical properties of the insulating phase of VO_2 is obtained. The results of the fit of the ellipsometric parameters Ψ and Δ together with reflectance for 100 nm film are displayed in Fig. 4.9. Panel (d) represents the schematics of the model together with the values of the fitting parameters.

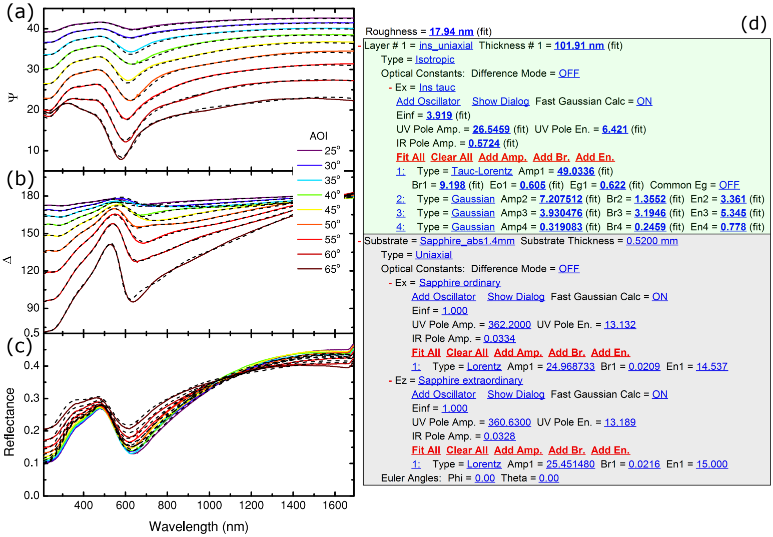

```
Roughness = 17.94 nm (fit)
- Layer # 1 = ins_uniaxial  Thickness # 1 = 101.91 nm (fit)
    Type = Isotropic
    Optical Constants:  Difference Mode = OFF
      - Ex = Ins tauc
        Add Oscillator   Show Dialog  Fast Gaussian Calc = ON
        Einf = 3.919 (fit)
        UV Pole Amp. = 26.5459 (fit)  UV Pole En. = 6.421 (fit)
        IR Pole Amp. = 0.5724 (fit)
        Fit All  Clear All  Add Amp.  Add Br.  Add En.
        1:   Type = Tauc-Lorentz  Amp1 = 49.0336 (fit)
           Br1 = 9.198 (fit)  Eo1 = 0.605 (fit)  Eg1 = 0.622 (fit)  Common Eg = OFF
        2:   Type = Gaussian  Amp2 = 7.207512 (fit)  Br2 = 1.3552 (fit)  En2 = 3.361 (fit)
        3:   Type = Gaussian  Amp3 = 3.930476 (fit)  Br3 = 3.1946 (fit)  En3 = 5.345 (fit)
        4:   Type = Gaussian  Amp4 = 0.319083 (fit)  Br4 = 0.2459 (fit)  En4 = 0.778 (fit)
- Substrate = Sapphire_abs1.4mm  Substrate Thickness = 0.5200 mm
    Type = Uniaxial
    Optical Constants:  Difference Mode = OFF
      - Ex = Sapphire ordinary
           Add Oscillator   Show Dialog  Fast Gaussian Calc = ON
           Einf = 1.000
           UV Pole Amp. = 362.2000  UV Pole En. = 13.132
           IR Pole Amp. = 0.0334
           Fit All  Clear All  Add Amp.  Add Br.  Add En.
           1:   Type = Lorentz  Amp1 = 24.968733  Br1 = 0.0209  En1 = 14.537
      - Ez = Sapphire extraordinary
           Add Oscillator   Show Dialog  Fast Gaussian Calc = ON
           Einf = 1.000
           UV Pole Amp. = 360.6300  UV Pole En. = 13.189
           IR Pole Amp. = 0.0328
           Fit All  Clear All  Add Amp.  Add Br.  Add En.
           1:   Type = Lorentz  Amp1 = 25.451480  Br1 = 0.0216  En1 = 15.000
    Euler Angles:  Phi = 0.00  Theta = 0.00
```

Figure 4.9 Fit of the measured ellipsometric parameters (a) Ψ, (b) Δ and (c) reflectance of the insulating phase of 100 nm thick VO_2 film. (d) Schematic representation of an applied isotropic model for the insulating phase of VO_2. The highlighted values are the fitting parameters.

As already mentioned, the isotropic fit does not ideally reproduce the measurement. For 100 nm thick film this is most prominent. The strongest deviation is observed in the range between 600 and 800 nm at higher angles of incidence. For thicker films the effect is less prominent and the performance of the isotropic model is much better. In addition, the measurements on thinner films are more affected by depolarization related to the backside reflection on the birefringent substrate. The treatment and the reduction of this effect is discussed in the Appendix *B*.

From the parameters of the oscillators the band gap and the properties of the interband transitions are determined. For 100 nm film the band gap occurs at 0.62 eV, as expected. The first interband transition appear at 3.36 eV corresponding to transition from O_{2p} band to Vanadium empty band. Second observed transitions is at 5.34 eV and corresponds to transition from lowest Hubbards band to the empty e_g^σ band. Finally, the last interband transition is at 0.778 eV and is transition from the lower Hubbard band to the upper Hubbard band in the Mott-picture [134]. The obtained parameters are in good agreement with previous theoretical and experimental reports [135, 136].

In addition, the thickness of the roughness layer of the films is obtained. It is determined to be 18±0.5 nm for 100 nm sample. Note, that roughness determined by ellipsometry, is a total thickness of the rough layer which can be connected to the root-mean-square value determined from AFM by factor of $1/\sqrt{2}$. The film thickness is determined to be 102±0.1 nm, close to the demanded 100 nm. As discussed in previous section, the isotropic model fails to provide an accurate film thickness, resulting in higher values for 200 and 400 nm films. Since the insulating phase exhibits less absorption, which is more suitable for thickness estimation [9], it is reasonable to determine the thickness from insulating model and fix determined thickness in metallic phase.

This model serves as the starting point for the uniaxial model where, for extraordinary axis the parameters are duplicated. Throughout the fit each optical axis is left only with two Gaussians and one Tauc-Lorentz terms. The spectral position of the optical band gap remains equal for both optical axes. The spectral positions and the amplitudes of Gaussians, at higher frequencies are observed to be slightly different. Both interband transitions blue-shift for extraordinary axis. Also, a spectral weight redistribution form interband at higher frequency to the interband at lower frequency is observed.

For metallic phase the model is very similar to the insulating model and differs just by one additional Drude term, to account free charge carriers contribution. The isotropic fit of the metallic phase of VO_2 100 nm film is shown in Fig. 4.10. As expected, the Tauc-Lorentz band gap closes (equals to 0) and the total amplitude of the oscillator approaches 0. The interband transitions shift to lower frequency, which is visualized in Fig. 4.11. From the Drude term the properties of the charge carriers are determined; the density n=

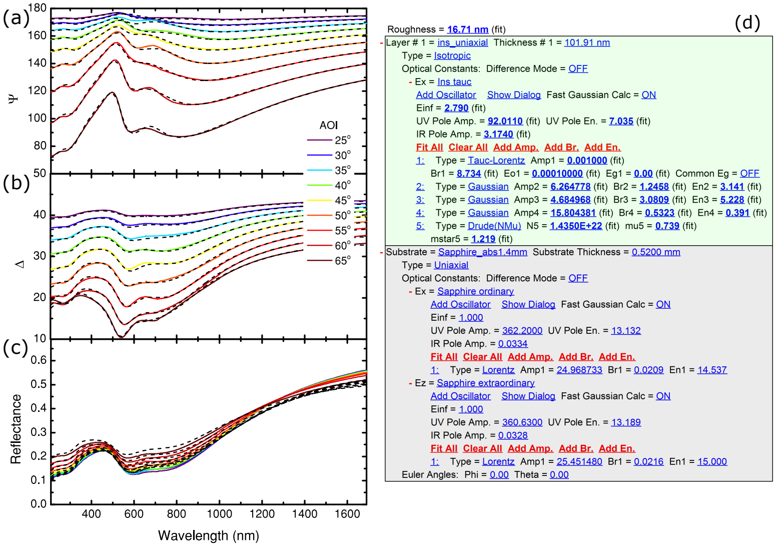

```
Roughness = 16.71 nm (fit)
- Layer # 1 = ins_uniaxial  Thickness # 1 = 101.91 nm
    Type = Isotropic
    Optical Constants:  Difference Mode = OFF
      - Ex = Ins tauc
        Add Oscillator   Show Dialog  Fast Gaussian Calc = ON
        Einf = 2.790 (fit)
        UV Pole Amp. = 92.0110 (fit)  UV Pole En. = 7.035 (fit)
        IR Pole Amp. = 3.1740 (fit)
        Fit All  Clear All  Add Amp.  Add Br.  Add En.
        1:   Type = Tauc-Lorentz  Amp1 = 0.001000 (fit)
          Br1 = 8.734 (fit)  Eo1 = 0.00010000 (fit)  Eg1 = 0.00 (fit)  Common Eg = OFF
        2:   Type = Gaussian  Amp2 = 6.264778 (fit)  Br2 = 1.2458 (fit)  En2 = 3.141 (fit)
        3:   Type = Gaussian  Amp3 = 4.684968 (fit)  Br3 = 3.0809 (fit)  En3 = 5.228 (fit)
        4:   Type = Gaussian  Amp4 = 15.804381 (fit)  Br4 = 0.5323 (fit)  En4 = 0.391 (fit)
        5:   Type = Drude(NMu)  N5 = 1.4350E+22 (fit)  mu5 = 0.739 (fit)
          mstar5 = 1.219 (fit)
- Substrate = Sapphire_abs1.4mm  Substrate Thickness = 0.5200 mm
    Type = Uniaxial
    Optical Constants:  Difference Mode = OFF
      - Ex = Sapphire ordinary
          Add Oscillator   Show Dialog  Fast Gaussian Calc = ON
          Einf = 1.000
          UV Pole Amp. = 362.2000  UV Pole En. = 13.132
          IR Pole Amp. = 0.0334
          Fit All  Clear All  Add Amp.  Add Br.  Add En.
          1:   Type = Lorentz  Amp1 = 24.968733  Br1 = 0.0209  En1 = 14.537
      - Ez = Sapphire extraordinary
          Add Oscillator   Show Dialog  Fast Gaussian Calc = ON
          Einf = 1.000
          UV Pole Amp. = 360.6300  UV Pole En. = 13.189
          IR Pole Amp. = 0.0328
          Fit All  Clear All  Add Amp.  Add Br.  Add En.
          1:   Type = Lorentz  Amp1 = 25.451480  Br1 = 0.0216  En1 = 15.000
    Euler Angles:  Phi = 0.00  Theta = 0.00
```

Figure 4.10 Fit of the measured ellipsometric parameters (a) Ψ, (b) Δ and (c) reflectance of the metallic phase of 100 nm thick VO_2 film.(d) Scheme of the applied isotropic model for the metallic phase of VO_2. The bold highlighted values are the fitting parameters.

$1.32 \cdot 10^{21}$ 1/cm^3, the mobility $\mu = 0.66$ cm^2/Vs and the effective mass $m_{\mathrm{eff}} = 1.22 \cdot m_e$, which are in accord with the previous studies [99, 134].

Again, the isotropic model is taken as a starting point for the uniaxial model. The interband transitions are slightly shifted with respect to isotropic model. What is more interesting is that the Drude properties are also slightly different for in- and out-of-plane axes. The charge carrier density is slightly different, $n_o = 1.41 \cdot 10^{21}$ 1/cm^3 for ordinary and $n_e = 1.26 \cdot 10^{21}$ 1/cm^3 for extraordinary axis, which results in slightly different plasma frequency. The effective mass for the out-of-plane axis is slightly lower then in the in-plane direction, with $m_o^* = 1.22$ and $m_e^* = 1.17$ and hence, the mobility is slightly higher.

The comparison of the in-plane and out-of plane dielectric properties of the insulating and metallic phases for 100 nm VO_2 film is presented in Fig. 4.11. The transition in- and out-of plain has pretty different temperature dependence. The interband transition around 5 eV shifts to higher energies, for both axes, while the interband at around 3 eV shifts to lower energies, over the transition. The spectral shift is however, stronger for the out-of-plane direction, which might be related to the difference in the lattice relaxation along two crystallographic directions.

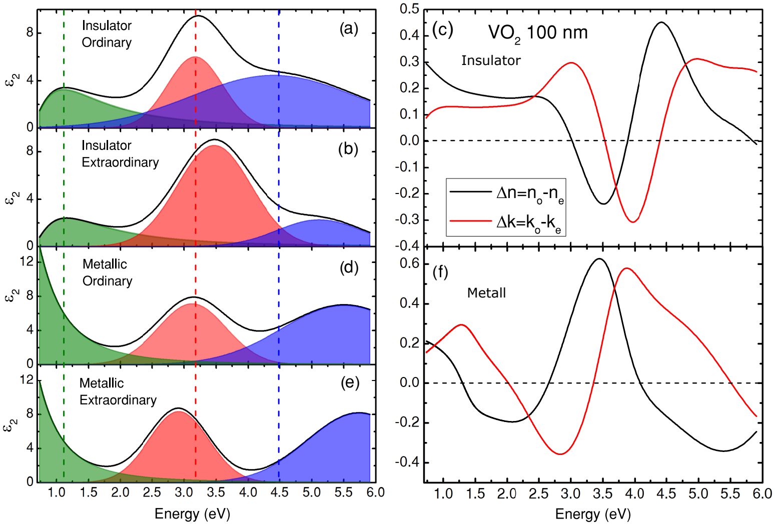

Figure 4.11 Imaginary part of the complex dielectric function for (a) ordinary optical axis in the insulating phase (b) extraordinary optical axis in the insulating phase (d) ordinary optical axis in the metallic phase (e) extraordinary optical axis in the metallic phase of the 100 nm VO_2 film. Blue red and green vertical dashed lines represent the spectral peak position of the interband transitions for ordinary optical axis in the insulating phase (c) Anisotropic difference of optical constants Δn and Δk for insulating phase. (f) Anisotropic difference of optical constants Δn and Δk for metallic phase.

An interesting behavior, in terms of optical anisotropy, is observed around the interband transitions. As shown in the Fig. 4.11(c,f), the interband transition around 3 eV results in swapping of the fast and slow optical axes for the dedicated spectral range. Since the observed birefringence changes its sign and is frequency dependent, to estimate the degree of anisotropy for both phases, the spectral sum root-mean-square value of optical difference is taken. So for insulating phase, degree of anisotropy is A_{ins}= 0.205, and for metallic phase, A_{met}= 0.213, which exceeds the anisotropy of the substrate by an order of magnitude.

Over the transition, the decrease in roughness for 100 nm film is observed by almost 1.5 nm. This phenomena is related to the structural transformations. A detailed analysis of the temperature dependence of roughness would be discussed in further sections.

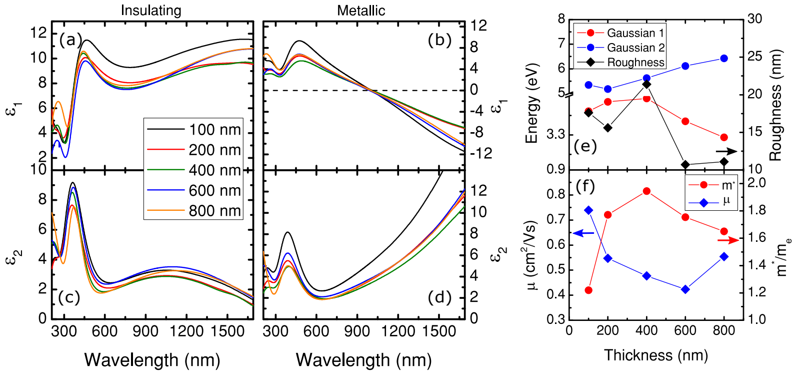

Figure 4.12 Extracted real and imaginary parts of dielectric constant, for (a,c) insulating phase and (c,d) metallic phase of VO_2 for thickness of 100-800 nm thin films along ordinary optical axes. (e) Spectral position of interband transitions together with the thickness of the roughness layer, as a function of film thickness. (f) Thickness dependence of charge carrier mobility μ and effective mass m^* along ordinary optical axis.

The same model is applied to the thicker films. Ideally, only tuning of the thickness is required to reproduce properties of the thicker films. In reality, the properties of the films also depend on their purity, grain size and topography. In addition, the degree of anisotropy gradually decreases with the film thickness, where 600 and 800 films are observed to be isotropic. Also, the films with thicknesses 200-800 nm belong to different batch with slightly different manufacturing parameters. Thus, the parameters of the interband transition has to be adjusted accordingly.

The obtained real and imaginary parts of dielectric functions of ordinary optical axis for all thicknesses are presented in Fig. 4.12(a-d), the extraordinary axes can be found in Appendix *B*. As can be observed, the 100 nm film has slightly different physical properties compared to the other films. In the insulating phase, we can observe a correlation between film thickness and the position of the interband transitions. While the interband transition at 3.34 eV shows a red-shift, with increase of thickness, the transition at 5.5 eV show a blue-shift, as shown in Fig. 4.12(e). In the metallic phase the energies of the interband transitions show almost no dependency on the thickness of the films, while the roughness show similar trend to the insulating phase.

The overall charge carrier density remains constant of n_o=1.41$\cdot 10^{21}$ 1/cm^3 for all the films, which results in a common plasma frequency of around 1.24 eV or 1000 nm, clearly observed from ε_2 in Fig. 4.12(b), crossing of the zero value. The extracted charge carrier density, is in the range of usually reported values, which again confirms the high quality of the films. The dc-mobility and the effective mass of charge carriers however, show a thickness dependence. As the mobility is inversely related to the effective mass, and a clear negative correlation in 4.12(f) is observed, it can be deduced that the scattering rate remains relatively constant for all the sample. This is in a good agreement with the resistivity measurements, where in the metallic phase, resistivity is almost independent on the sample thickness. The thickness dependence for the extraordinary axis shows a very similar picture as for ordinary axis. The summary of extracted parameters for ordinary and extraordinary, as well as the sample roughness and degree of anisotropy is provided in the Table 4.3.

4.4 Temperature dependence of the VO_2 thin films

As the properties of the insulating and metallic phases are determined, the BEMA model can be implemented to derive the properties of the thin films over the IMT. It is assumed that the metallic clusters are seeding, relatively far apart, and gradually expand, with rise of temperature, until they percolate, forming a macroscopic conducting path. Such an image is already confirmed by some microscopic experimental techniques such as SNOM and CAFM [119–121]. This techniques however, are surface techniques and do not provide information about the bulk. In other words, it is not clear how the metallic clusters develop in out-of-plane direction. Does structural anisotropy influence the cluster development? Does structural transition trigger variation of cluster shape and size? Ellipsometric measurements at oblique incidence are sensitive to the out-of plane contribution, and will provide answer to these questions. Although the material may be assumed isotropic, it may become anisotropic in strongly-correlated regime, due to anisotropic development of the metallic clusters ($L \neq 0.333$). The goal here, is to determine the exact cluster shape and the shape dynamics in all directions over the IMT.

In the previous chapter it was demonstrated, how much the aspect ratio of the scatterer may influence the spectral properties of a composite medium. In general, there are no reasons to assume the shape factor of developing VO_2 metallic clusters to be temperature independent. The structural transition for instance, leads to changes in size of the unit cell, and these changes are dramatic. In monoclinic M_1 phase, the crystal lattice parameters are $a = 0.572$ nm, $b = 0.452$ nm and $c = 0.538$ nm with two distances between Vanadium atoms $d_{V-V} = 0.265$, 0.313 nm, which change to $a = b = 0.455$ nm and $c =$

Thickness / Oscillator	100 nm	200 nm	400 nm	600 nm	800 nm
	Insulating phase				
Ordinary optical axis					
Gaussian 1	A=7.2	A=6.8	A=6.92	A=7.02	A=7.1
	Γ=1.35 eV	Γ=1.47 eV	Γ=1.33 eV	Γ=1.32 eV	Γ=1.36 eV
	E=3.36 eV	E=3.38 eV	E=3.4 eV	E=3.32 eV	E=3.29 eV
Gaussian 2	A=3.93	A=3.84	A=3.82	A=3.90	A=3.85
	Γ=3.2 eV	Γ=2.81eV	Γ=2.71eV	Γ=2.74 eV	Γ=2.77 eV
	E=4.5 eV	E=5.36 eV	E=5.52 eV	E=5.8 eV	E=6.1 eV
Tauc-Lorentz	A=49.0	A=52.5	A=48.2	A=49.2	A=49.3
	Γ=9.1 eV	Γ=8.6 eV	Γ=8.7eV	Γ=9.1 eV	Γ=9.1 eV
	E_g=0.622 eV	E_g=0.622 eV	E_g=0.622 eV	E_g=0.622 eV	E_g=0.622 eV
Extraordinary optical axis					
Gaussian 1	A=9.3	A=7.0	A=7.1	A=7.02	A=7.1
	Γ=2.23 eV	Γ=1.37 eV	Γ=1.4 eV	Γ=1.32 eV	Γ=1.36 eV
	E=3.51 eV	E=3.36 eV	E=3.36 eV	E=3.32 eV	E=3.29 eV
Gaussian 2	A=1.4	A=3.93	A=3.93	A=3.93	A=3.85
	Γ=1.6 eV	Γ=3.21 eV	Γ=3.2 eV	Γ=2.74 eV	Γ=2.77 eV
	E=5.32 eV	E=5.4 eV	E=5.4 eV	E=5.8 eV	E=6.1 eV
Tauc-Lorentz	A=43.0	A=52.3	A=48.3	A=49.2	A=49.3
	Γ=8.9 eV	Γ=8.2eV	Γ=8.1 eV	Γ=9.1 eV	Γ=9.1 eV
	E_g=0.622 eV	E_g=0.622 eV	E_g=0.622 eV	E_g=0.622 eV	E_g=0.622 eV
Rougness	17.5 nm	15.5 nm	21.2 nm	10.5 nm	11 nm
Degree of Anisotropy	0.2	0.17	0.07	0	0
	Metallic phase				
Ordinary optical axis					
Gaussian 1	A=7.5	A=7.1	A=6.9	A=6.5	A=6.6
	Γ=1.47 eV	Γ=2.27 eV	Γ=2.23 eV	Γ=2.13 eV	Γ=2.17 eV
	E=3.12 eV	E=3.05 eV	E=3.42 eV	E=3.51 eV	E=3.51 eV
Gaussian 2	A=4.1	A=9.3	A=5.4	A=9.3	A=9.3
	Γ=2.23 eV	Γ=2.24 eV	Γ=2.23 eV	Γ=2.23 eV	Γ=2.23 eV
	E=3.4 eV	E=3.51 eV	E=5.34 eV	E=3.51 eV	E=3.51 eV
Drude	n=1.41x10^{21}	n=1.41x10^{21}	n=1.41x10^{21}	n=1.41x10^{21}	n=1.41x10^{21}
	μ=0.74	μ=0.53	μ=0.48	μ=0.42	μ=0.55
	m*=1.22	m*=1.75	m*=1.93	m*=1.71	m*=1.65
Extraordinary optical axis					
Gaussian 1	A=6.8	A=6.6	A=6.7	A=6.5	A=6.6
	Γ=2.08 eV	Γ=2.11 eV	Γ=2.19 eV	Γ=2.13 eV	Γ=2.17 eV
	E=2.85 eV	E=3.51 eV	E=3.51 eV	E=3.51 eV	E=3.51 eV
Gaussian 2	A=9.4	A=7.5	A=7.7	A=6.5	A=6.6
	Γ=2.23 eV	Γ=2.32 eV	Γ=2.23 eV	Γ=2.13 eV	Γ=2.17 eV
	E=3.51 eV	E=3.51 eV	E=3.51 eV	E=3.51 eV	E=3.51 eV
Drude	n=1.26x10^{21}	n=1.26x10^{21}	n=1.26x10^{21}	n=1.26x10^{21}	n=1.26x10^{21}
	μ=0.89	μ=0.63	μ=0.52	μ=0.42	μ=0.55
	m*=1.17	m*=1.73	m*=1.89	m*=1.71	m*=1.65
Rougness	16 nm	14.3 nm	19.5 nm	13.4 nm	12.5 nm
Degree of Anisotropy	0.21	0.18	0.07	0	0

Table 4.3 Optical parameters of the VO$_2$ thin films, with 100, 200, 400, 600, 800 nm thickness, in the insulating and the metallic phases, derived from the uniaxial Fresnel model.

0.286 nm in the rutile phase [137]. The unit cell along c-axis doubles, upon the transition to monoclinic structure, due to the formation of the Vanadium dimers, followed by the increase of the average distance between Vanadium atoms by around 1%. This, in principle, might influence the cluster aspect ratio and its volume.

$$f_m \frac{\varepsilon_m - \varepsilon_{eff}}{\varepsilon_{eff} - L_i(\varepsilon_m - \varepsilon_{eff})} + (1 - f_m) \frac{\varepsilon_d - \varepsilon_{eff}}{\varepsilon_{eff} - L_i(\varepsilon_d - \varepsilon_{eff})} = 0 \tag{4.1}$$

In the following analysis only three fitting parameters for the BEMA mixing model are utilized. One of them, is roughness, an extrinsic parameter, the limits of which are already known from the fitting of the constituent phases, provided in table 4.3. The other two, are BEMA major parameters, the volume fraction f_m and the depolarization factor L_i in equation 4.1. As discussed in the theory part, the BEMA model is symmetric with respect to increase of the inclusion volume fraction and its decrease. This means that the BEMA model with a constant depolarization factor is not able to reproduce the observed asymmetry of the optical parameters over the transition. To emphasize this fact, a comparison of a fit of temperature-dependent ellipsometric parameters in 100 nm VO_2 film with constant depolarization factor $L = 0.333$, and fit with varying depolarization factor is shown in Fig. 4.13 [1].

Notice, in Fig. 4.13(a), for heating curve, which has higher transition temperature, the fit with constant L_i is relatively acceptable, but for cooling curve, this value results in stronger deviations. The reached minimum, takes much smaller value than measured and is exactly the same as observed during the heating cycle. Interesting to note, that while Δ is not very sensitive to the cluster shape, at high wavelength a non-negligible deviation is observed with the constant BEMA model. Moreover, the temperature range where the model deviates is pretty wide, starting from 75 °C down to 60 °C, which is more

---

[1] Although the fitting is performed on a complete Mueller matrix, to include possible depolarization effects, plus intensity information, for reasons of better visualization and space economy, the fit of ellipsometric parameters is shown.

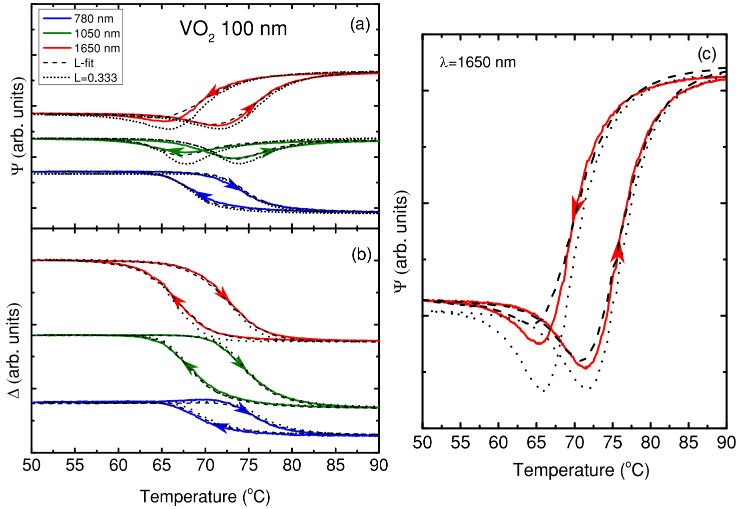

Figure 4.13 Temperature dependence of measured ellipsometric parameter (a)Ψ (b)Δ, together with the resulted fit from BEMA model with a fixed depolarization factor (dotted line) and varying depolarization factor (dashed line), for different wavelengths of 780, 1050, 1650 nm. (c) A closer look on the fit of Ψ at the wavelength of 1650 nm.

clearly observed in Fig. 4.13(c). This means that even if the depolarization factor for heating is adjusted properly, for cooling value it takes different value. More details are provided in the Appendix *B*. The performance of the model with varying depolarization factor is much better. Although, this model still deviates in the percolation region, the temperature range of deviations is reduced, and the absolute values better reproduce the measurements.

Before discussing derived parameters of the model, it is reasonable to discuss its performance in more details. A good performance is observed for all the other samples with decrease of MSE in range of 20-40% dependent on the sample, in comparison to the static shape factor model. The fit of ellipsometric parameters is presented in Fig. 4.14 for Ψ and Fig. 4.15 for Δ respectively. It is interesting to note, that 200 nm sample, in comparison to the other samples, shows an asymmetry in Δ at high wavelengths, with rising value at critical temperatures. This observation points toward percolation transition, and variation in the anisotropy, as Δ is directly related to observed birefringence in the anisotropic samples.

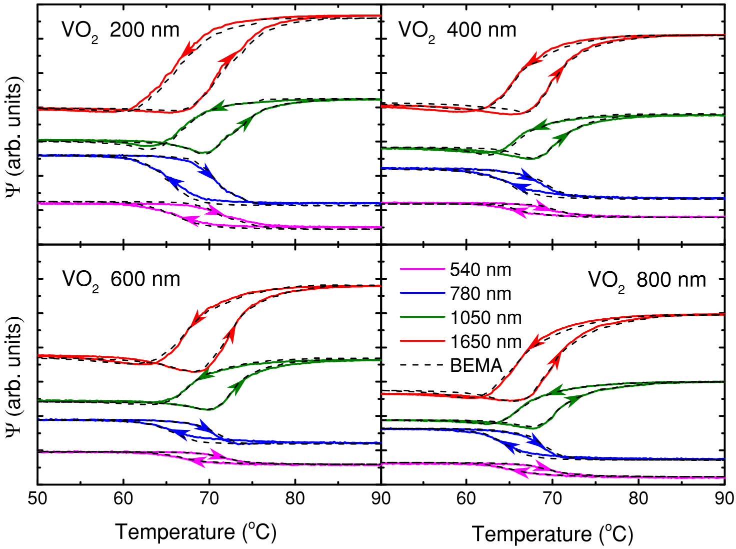

Figure 4.14 Measured ellipsometric parameter Ψ (solid lines) over the IMT, together with the BEMA model fit (dashed lines) at wavelengths of 540, 780, 1050 and 1650 nm for films with thicknesses of 200, 400, 600, 800 nm.

From literature, it is known that around the percolation threshold the performance of EMA models is poor. This is explained by the violation of homogeneity assumption, which obviously breaks down close to the percolation threshold, where long-range correlations become important. On the other hand, BEMA model includes the interaction between the particles in the mean-field approximation. Thus, the model must hold as long as the dipolar approximation holds. In other words, as long as the clusters remain small compared to the probing wavelength. From field expansion coefficients derived in

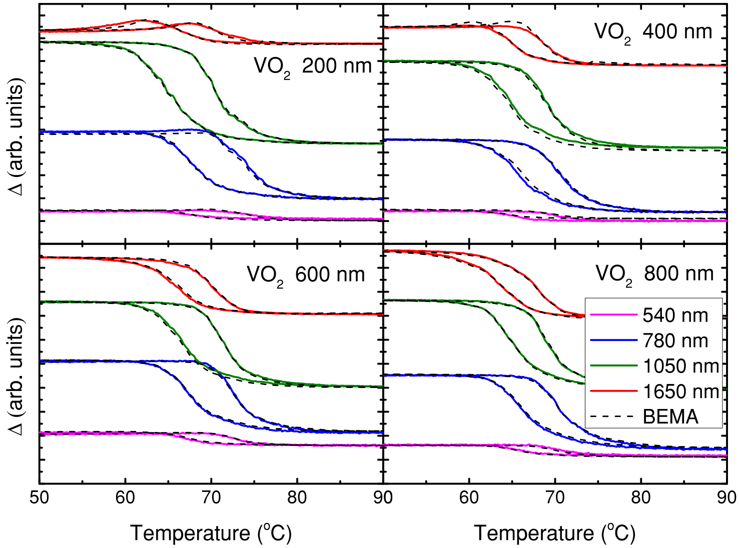

Figure 4.15 Measured ellipsometric parameter Δ (solid lines) over the IMT, together with the BEMA model fit (dashed lines) at wavelengths of 540, 780, 1050 and 1650 nm for films with thickness of 200, 400, 600, 800 nm.

the framework of Mie theory, this range is upto around 200 nm in diameter of the particles and spacing down to 20 nm. Since a good performance of the BEMA model is observed, with MSE value peaks around the transition temperatures, the configuration of the metallic clusters in the sample must satisfy these conditions before percolation. This provides a first estimate of the average cluster size at the transition. A more precise estimation of the average cluster size is done later in the next section.

Since the measured optical properties along the IMT are nicely reproduced, the assessment of the fitting parametershas can be done. As was reported in the [7], the extracted shape factor for the 100 nm film, displays an interesting temperature behavior, which is shown in Fig. 4.16(a). The errorbars of the parameter, increase further away from the critical temperatures. This is governed by the parameters sensitivity, which drops rapidly with filling fraction approaching its boundary values of 0% or 100 %. It is important to emphasize that the development of the clusters for all the samples are assumed to be isotropic in-plane, having the shape factor $L_x = L_y = L_{||}$ and shape factor $L_{\perp}$ oriented out-of-plane. This simplification is reasoned by negligible difference of L_x and L_y, when the biaxial BEMA model is applied. The displayed behavior is a result of the averaging for seven measurements, on different regions, for each sample, to validate the consistency of the values. No significant differences in the results were observed, apart from thermal shifts, in some measurements, due to the bad thermal coupling of the sample to the heating stage.

The in-plane depolarization factor, declines from the value of 0.333, for spherical shape, approaching the critical temperature. It is interesting to note, that the minima in the shape factor do not coincide with the critical temperatures, but rather appear at higher temperature. The decrease of the shape factor $L_{||}$, according to the equation 1.64, means an in-plane expansion and the oblate disk-like shape of the developing metallic inclusions. It is clear that the shape factor $L_{||}$ reaches different minima values during heating and cooling cycles. This, together with slightly different volume fraction, explains well the asymmetry of the hysteresis and an observed differences in the optical properties during the heating and cooling transitions. The difference in cluster shape at critical temperatures T_c^{heat} and T_c^{cool} induces a strong difference in the dielectric properties, even when the volume fraction is the same, which is displayed in the inset of Fig. 4.19(b). Minor difference in depolarization factor, as small as 0.05 in this case, lead to a strong difference in the dielectric properties in the NIR regime, as demonstrated by the inset.

The obtained percolation threshold, marked by blue and red dots in Fig. 4.16(b), display the value of the volume fraction, determined at the critical temperatures for this film. The values are f_c^{cool}=0.27 and f_c^{heat}=0.28, which is in a perfect agreement with the prediction of the percolation theory. For aggregated ellipsoids of the corresponding aspect ratio of 1.5 and 1.8 respectively,

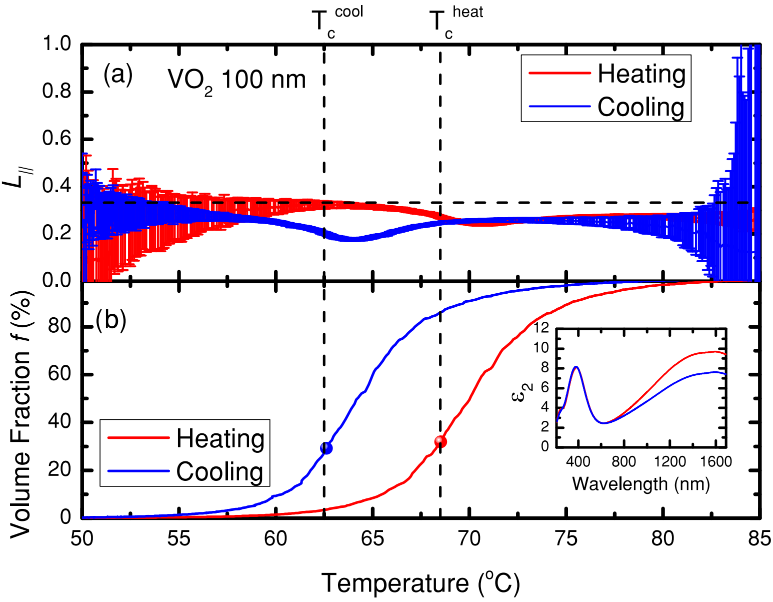

Figure 4.16 Temperature dependence of the BEMA parameters for 100 nm thick VO_2 film. (a) depolarization factor $L_{||}$ and (b) corresponding volume fraction f. The inset demonstrates difference in the imaginary part of dielectric function at two critical temperatures T_c^{heat} (red) and T_c^{cool} (blue).

percolation theory predicts critical fractions of 26 and 28 percent, which can be derived form Fig. 1.14 [4]. The perfect matching of the critical fraction not only explains the effectiveness of the BEMA model in this case, but also gives an understanding of the underlying properties of the transition. The evolving metallic clusters aggregate rather than form independently, which gives the hint that several clusters can exist within a single grain. This reduces an upper boundary of the cluster size to the value of a grain size.

The determined depolarization factor for the thicker films is presented in Fig. 4.17. Different behavior is observed. While approaching critical temperature during heating, the depolarization factor still decreases and is in the oblate regime. Close to the critical temperature, however instead of well-pronounced dip, the shape factor displays a peak. For the 200 nm film, the jump in the shape factor is so dramatic, that a transition from oblate to prolate shape is reached, which is depicted as crossing of the spherical shape value of 0.333. After, the value approaches the spherical shape limit, although the uncertainty of the value rises rapidly. During cooling, for this sample, the transition is less abrupt and the cluster shape remains in the oblate configuration over the whole temperature range.

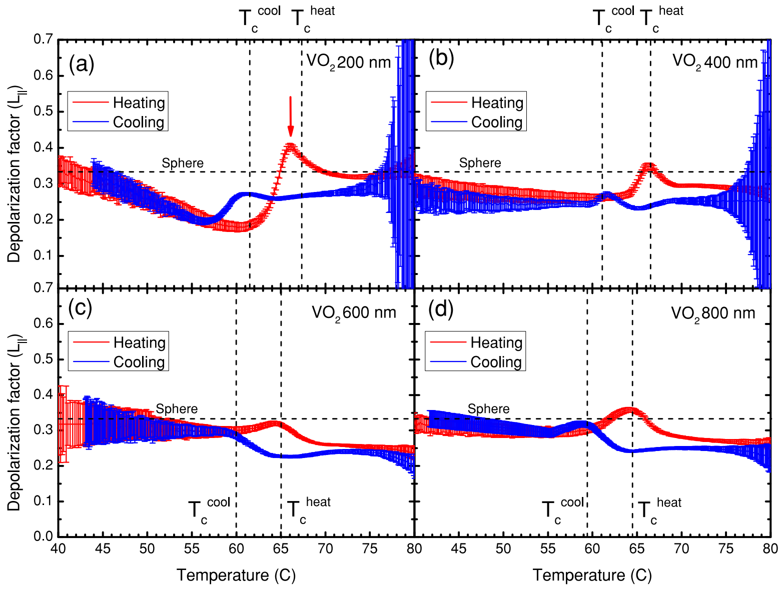

Figure 4.17 Temperature dependence of the depolarization factor $L_{||}$ for heating (red) and cooling (blue) of VO_2 films with thicknesses of (a) 200 nm (b) 400 nm (c) 600 nm (d) 800 nm. The vertical dashed lines correspond to the insulator-metal transition determined from the dc-resistivity measurements. The horizontal dashed line marks the 0.333 value of the depolarization factor, corresponding to the spherical shape.

As the thickness of the film increases, the deviation from the spherical shape smoothens, meaning that the shape of the particle tends to remain spherical. In other words, the development of the metallic clusters is more isotropic. The peaks are however, still observed, but the maximum value during heating remains close to the spherical limit. Interesting observation can be done. For thin films, 100 nm 200 nm, the abrupt changes in the shape does not exactly coincide with the measured critical temperatures. While for 100 nm sample, the observed dips are above critical temperature, for 200 nm sample the peaks are located at temperatures below the critical values. For the 400 nm film the peaks are observed in the proximity of the critical temperatures, but still, not exactly at the same temperature. For the 600 nm and 800 nm samples, position of the peaks is observed to coincide with the critical temperatures. For all the samples, the changes of the shape factor are more pronounced during the heating cycle.

To understand the origin of such alternation of the shape of the metallic clusters it is important to address another extracted parameter, the roughness. The derived temperature dependence of the roughness layer thickness is presented in Fig. 4.19. For thickness of 100 nm, roughness decreases during IMT by almost 1.5 nm. During the transition, peaks are observed, where roughness slightly increases. Similar behavior is observed for 200 nm thick film, however with less prominent jumps in roughness. It is important to note that the peaks do not coincide with the critical temperature, but rather with the observed rapid changes of the shape factor. For 400 nm film, no peaks are observed, while the roughness still decreases over IMT. For films with 600 and 800 nm the situation is reversed. The thickness increases by around 2.5 nm upon entering into the metallic state. Changes in the roughness, for the films with thicknesses below 600 nm, show very narrow hysteresis, meaning that the changes during heating and cooling cycles happen almost at the same temperature. For thicker films of 600 and 800 nm, a hysteresis is observed with much sharper and abrupt changes in the roughness.

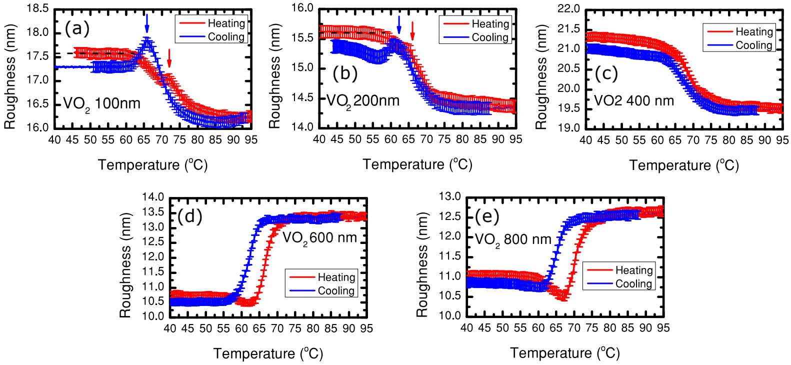

Figure 4.18 Temperature dependence of the roughness layer thickness derived from the BEMA model for samples with thicknesses of 100-800 nm, for heating (red curve) and cooling (blue curve).

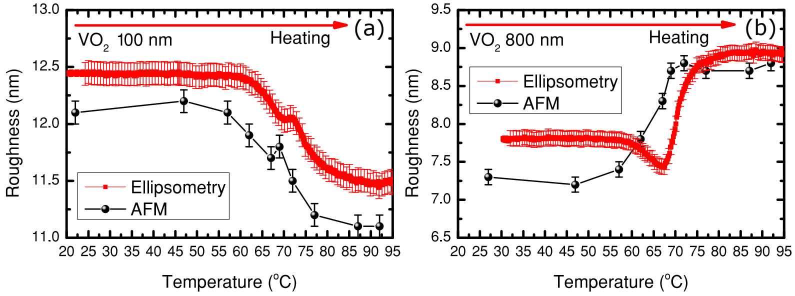

Figure 4.19 Temperature dependence of the roughness determined from ellipsometry (red squares) and AFM (black circles) measurements for (a) 100 nm film, (b) 800 nm film, during heating over the IMT.

From the first glance, this dependence may seem random, and the observed peaks around the transition temperatures can be assumed as numerical artifacts, but the behavior is well supported with results from the AFM measurements. For samples with 100 and 800 nm thickness, temperature-dependent AFM measurements are shown in Fig. 4.19. On the graph, the values extracted from the ellipsometry measurements are adapted to the root-mean-square values. The small increase in the film roughness is also observed from the AFM data for 100 nm thick film. For 800 nm film, however, some discrepancy is observed. While the ellipsometry data shows a decrease in roughness before the increase, the AFM data points towards continuous increase of the roughness. Nevertheless, the overall behavior from the two complementary experimental techniques is consistent.

The two derived parameters, $L_{||}$ and roughness, show a very complex thickness and temperature dependence. To reveal the underlying processes, which govern the observed behavior, it is important to take a closer look on the relation of the obtained data with the initial properties of the films, which is done in the next section.

4.5 Discussion

To continue with the discussion it is necessary to summarize the experimental results, in order to identify the open questions. The optical data has to be juxtaposed with the results from AFM and resistivity measurements. The dc-resistivity measurement display a tendency of decrease of the critical temperature with rising thickness. On the other hand, optical measurements suggest that the degree of anisotropy decreases with increasing film thickness, leaving 600 and 800 nm films optically isotropic. Combining these, a conclusion can be made that with the film thickness, the strain, imposed on the films, is effectively controlled. In [138], it was demonstrated that the lattice mismatch between the monoclinic VO_2 phase, in all possible growth configurations, and Al_2O_3 (0001) substrate, effectively leads to the formation of the interface layer of V_2O_3, which spans over several monolayers, up to around 3-4 nm. The presence of another, well-defined crystallographic phase nicely explains the observed decrease of the anisotropy with film thickness increase, as the proportion of the interface layer decreases.

Nevertheless, V_2O_3 has a lower transition temperature, so its presence would result in the decrease of the critical temperature in thinner films. In contradiction, 100 nm sample has the highest T_c. In the studies discussed in this thesis, the measurements are performed on the polycrystalline thin films produced by sputtering. This means that the interface layer, close to the substrate is inhomogeneous, in contrast to epitaxially grown films. Moreover, due to its polycrystalline nature, the strain on the substrate/film interface is expected to decrease, due to possible drift diffusion. Thus, the effective strain in the films must originate from other effects.

The nature of strain in the thin films is quite complex, as it can combine effects from substrate-film interface, thermal strain and strain induced by grain boundaries. As each particular strain effect can be both tensile or compressive, it is extremeley hard to deduce the underalaying origins of the effective strain. In polycrystalline films however, the thermal and grain boudary strain dominate [139]. It has been reported that the grain boundaries induce internal strain, whose magnitude depends on the grain orientation, their surface area and density [140]. As well, the influence of grain size on the critical temperature of VO_2, thought produced by pulsed laser deposition, were conducted [141, 142]. In addition, strong strain relaxation, induced by structural transition in VO_2 films was reported [143]. It was concluded that the relaxation is related to the substrate type and grain morphology. VO_2, in general, has anisotropic thermal expansion coefficient [144]. Combined with random orientation of grains in polycrystalline films, the strain within the grains/domains during the structural transition is significantly enhanced [145]. The overall conclusion of this studies can be formulated as follows, the stress magnitude as well as the consequent stress relaxation processes are proportional to the grain boundary density. As can be deduced from the thickness evolution of the surface topography of the films, obtained by AFM and presented in Fig. 4.20, the grain boundary density decreases with the sample thickness as the grain size increases. Thus, the lower grain boundary density can be associated with lower strain effects, which explains the decrease of the critical temperature with sample thickness.

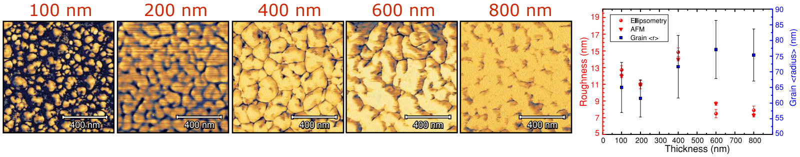

Figure 4.20 Phase-topography AFM measurements on VO_2 thin films with ticknesses of 100, 200, 400, 600, 800 nm. Thickness dependence of the roughness obtained from ellipsometric measurements (red circles), AFM measurements (red triangles) together with the average grain radius (blue squares) obtained from the large scale AFM images.

The obtained experimental results suggest that with the measured films a certain range of the phase diagram, similar to the one presented in Fig. 4.2 is covered. Starting with the 100 nm film, the critical temperature, during heating, hits 68.5 °C, indicating presence of the tensile strain. As a result the transition in this film is expected to pass additional structural transformation involving M_2 phase. Nevertheless, no signatures of the structural transitions from M_1 to M_2 phases was observed in the far infrared measurements (See Appendix *B*). However, to confirm the absence of the additional insulator-insulator transition, x-ray or Raman measurements are required as they are more sensitive to such a structural transition.

On the other hand, the observed peaks in the temperature-dependent roughness data suggest an abrupt strain relaxation, which may be associated with the above mentioned structural transformation. In thinner films, 100 and 200 nm, a small additional peak is observed in the intermediate state. This may be a signature of the insulator-insulator transition. In thicker films this feature is absent. As the films get thicker, the critical temperature decreases, approaching the bulk critical temperature at the triple point. Thus, the contribution of the M_2 insulating phase is expected to decay, which is consistent with the experimental data, both from AFM and ellipsometry.

Regardless of the presence or absence of the additional structural transformation, the roughness profile is observed to change during the IMT transition, in all the films. Combined with the temperature-dependent shape factor data, it becomes clear that it is the structural transition which triggers the changes in the shape factor. A direct correlation between grain boundary density and the variation of the shape factor can be established. In fact, although the electronic and structural transition can be decoupled, pointing towards electronic correlation origin of the IMT transition, the structural transformation can still influence the electronic properties of the material. This happens due to macroscopic variation of the metallic cluster shape via transformation of the crystal lattice. The shape and size of the metallic nanoparticle defines the properties of the associated LSPR, which defines the optical properties in the corresponding frequency range.

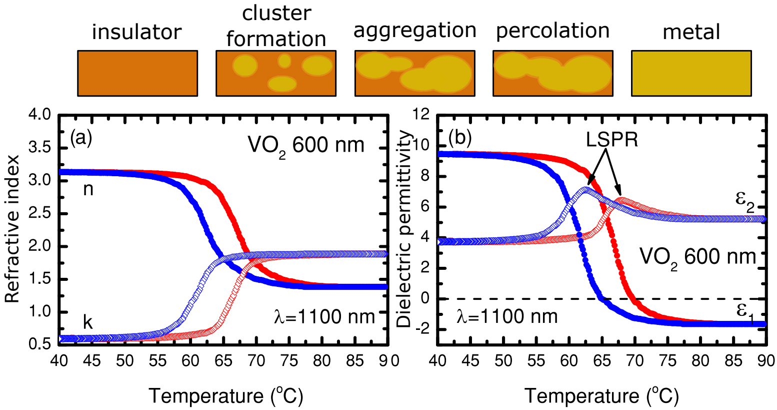

Figure 4.21 (a) Temperature dependence of the optical parameters *n* and *k* in 600 nm thick VO_2 film, extracted via BEMA model at wavelength of 1100 nm. (b) Corresponding temperature dependence of the dielectric function at the same wavelength.

The second open question concerns the observed decrease in optical reflectivity in the vicinity of the critical temperature, with the subsequent increase in the metallic phase. The origin of such a behavior was not yet addressed, although this is basically the first experimental observation made from temperature-dependent measurements. Having now a model, which describes the properties of the films over the transition it is reasonable to investigate the optical properties as a function of temperature, in order to understand the origin of this effect. This information is presented in Fig. 4.21. The extracted optical constants n, k evolve smoothly over the transition. At high wavelength in the NIR range, the refractive index goes down and the absorption coefficient goes up. The corresponding real part of the dielectric constant also evolves smoothly, displaying a zero-crossing, which indicates emergence of the metallic properties. One might expect to observe a divergence of the real part of the dielectric constant, as a hallmark of the percolation transition. This effect is however, observed only at much lower frequencies, where the inclusions display well established metallic properties. At the frequencies close to the plasma frequency the contrast between the dielectric constants of the insulating and the metallic phases is still low to observe such an effect. Nevertheless, the divergence is observed by extrapolating the BEMA model to low frequencies.

The imaginary part, on the contrary, displays an increase in absorption, peak in ε_2, both during heating and cooling. Thus, the absorption in the intermediate state is larger than in the metallic phase, in certain wavelength range. This is a direct evidence of the LSPR absorption of the metallic clusters. Indeed, as was introduced in previous chapter, the sub-wavelength Au nanoparticles support a LSPR, resulting in the strong absorption in VIS-NIR wavelength range. Here, metallic clusters of VO_2 continuously increase in size, tuning the resonance, until they percolate, and form a macroscopic conducting path. Since VO_2 in the metallic phase has lower charge carrier density, compared to Au, its plasma frequency is lower, and consequently the LSPR of particles with the same size must be observed at higher wavelengths. In addition, the clusters are developing in the insulating matrix with an average refractive index $n = 3.2$, which further shifts the resonance to lower frequencies. It is clear that the absorption rises with an increase of the cluster size, as temperature grows. At the point where the films become metallic, the LSPR absorption rapidly decays, as the proximity of the metallic clusters lead to quenching of the LSPR. Such a behavior explains well the observed decrease in the reflectivity data, previously presented in Fig. 4.7(f) and Fig. 4.8. As a result, the asymmetry of the reflectivity with respect to heating and cooling, is associated with the asymmetry of the metallic cluster shape, deduced from the ellipsometric measurement. To the current knowledge of the author, this is a first report of the observations of the formation of the LSPR during IMT in VO_2 thin films. Although, studies of the LSPR in VO_2 material have been already conducted on separate nano-islands of VO_2 material [146, 147].

The resulting imaginary part of the dielectric constant for all the five samples is shown in Fig. 4.22. The figure represent the temperature and wavelength dependence of the imaginary part of the evaluated dielectric constant, normalized to the values of the metallic phase. It is apparent that the central wavelength of the LSPR in all samples is approximately the same and is 1200 nm. The amplitude, damping and temperature relations is, however different between the samples. Most prominent is the LSPR in 200 nm sample which has the lowest amplitude and highest damping rate, vanishing already at 1400 nm wavelength. The 100 nm sample, on the other hand, has the largest amplitude and also largest spectral width. In terms of temperature, samples with 100 nm and 800 nm thickness has to be highlighted. The contribution of the LSPR in these samples is still observed above 75 °C, which is far beyond their critical temperatures. In other samples, already at 70 °C, the peak decays. In 600 nm sample, the LSPR contribution extends to larger wavelengths, while in 400 nm sample, the LSPR is centered around 1200 nm. In general, all the samples, except the 200 nm sample, are comparable, in terms of their absorption features.

To confirm the LSPR contribution during the IMT, Fröhlich condition can be calculated, according to the equation 1.86, using the extracted dielectric properties of the VO_2 in both phases. A more general approach would be to

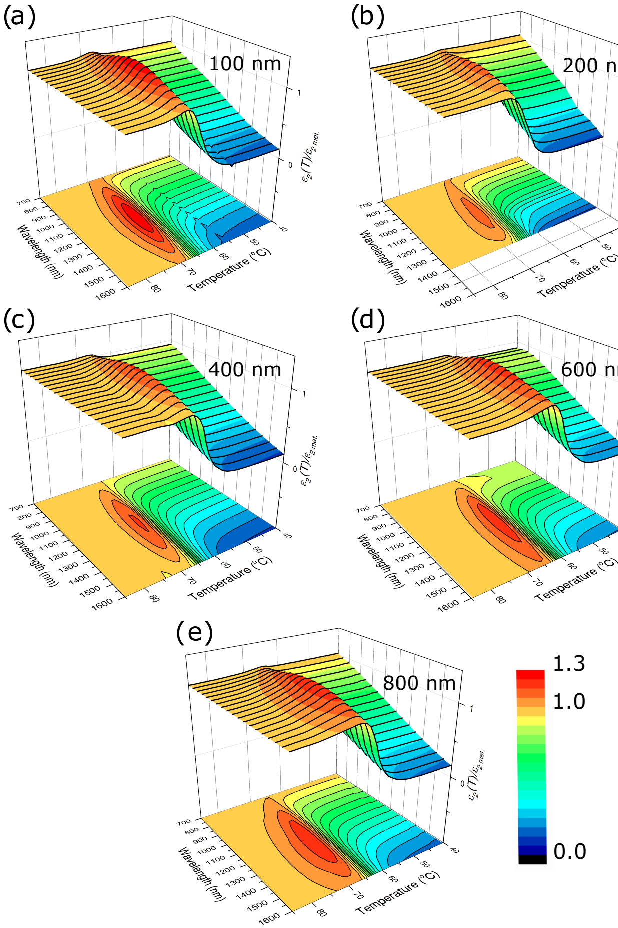

Figure 4.22 Temperature and wavelength dependence of the extracted imaginary part of dielectric constant $\varepsilon_2(T,\lambda)$ during heating of VO_2 films with thicknesses of (a) 100, (b) 200, (c) 400, (d) 600 and (e) 800 nm. The value of dielectric constant is normalized to the value of the metallic phase ($T = 90$ °C).

Table 4.4 Aspect ratio $\frac{a}{c}$ of the metallic clusters, calculated according to equation 1.64, at critical temperatures T_c^{heat} and T_c^{cool}

Thickness	(T_c^{heat})	(T_c^{cool})	δ
100 nm	1.49	1.85	0.36
200 nm	0.61	1.39	0.78
400 nm	1	1.49	0.49
600 nm	1.1	1.34	0.24
800 nm	1.17	1.1	0.07

perform a similar procedure, as in the previous chapter. Utilizing the CDA algorithm, it would be possible to investigate the pure LSPR response, without additional dielectric background coming from the interband transitions. As a result, an insight about the cluster size can be obtained. In the case of VO_2, the shape of the metallic inclusions is already known. The BEMA model however, does not provide a relation between the optical response and the cluster size. CDA on the contrary does. The goal is to estimate the average size of the clusters.

To perform CDA simulations, the depolarization factor, obtained from temperature dependent measurements has to be converted into an aspect ratio first. The obtained aspect ratio of the metallic clusters, for all the samples, according to the equation 1.64, are presented in the table 4.4. The aspect ratio represents the ratio of the in-plane axis a to the rotational axis c, calculated at critical temperatures T_c^{heat} and T_c^{cool}, as well a their difference δ at these critical temperatures.

To determine the particle size, the aspect ratio is fixed. To reproduce the percolation transition, random nucleation spots within a certain volume are generated with a fixed average cluster distance d. The cluster size is iteratively increased. Growing particles eventually increases the total volume fraction, occupied by the metallic phase in the simulated volume. During the growth, the particle may overlap and form irregular cluster shapes. At each iteration the extinction cross-section C_{ext} is evaluated according to the equation 1.67.

The obtained extinction cross section is compared to the observed absorption, the cluster nucleation distance d is adjusted accordingly, to obtain a better fit and the size sweep is performed again.

As observed from the measurements, the LSPR must have its maximum above the percolation threshold for all the samples. For 100 nm sample, the volume fraction where LSPR has its maximum is around 50%. It is reasonable to concentrate only on the transition during heating cycle. With the total thickness of of 100 nm, it is clear that the out-of plane radius of the cluster cannot exceed 50 nm. This, together with the known aspect ratio of 1.49, gives a limiting value for the in-plane radius of 75 nm. The starting intercluster distance is thus set to 150 nm in-plane. The index of refraction of the surrounding medium is taken from the insulating model, with no absorption included, resulting in an average constant value $n = 3.2$. The dielectric properties of the clusters, are taken from the metallic phase model. The fitting of the maximum of the LSPR is done as a function of the wavelength and the volume fraction.

The results of the fit for 100 nm thick sample are presented in Fig. 4.23. Plot (a), presents the data shown in Fig. 4.23(a), but as a function of the volume fraction. The LSPR starts to contribute already above 20 % of the volume fraction. The peak of the absorption amplitude is however, between 50-55 %, and between 1000 and 1300 nm in wavelength. With increase of the volume fraction, the intercluster surface distance decreases, resulting in quenching of the LSPR, observed as a decrease in resonance amplitude and its substantial broadening and red-shifting. The result of the fit is presented in the plot (b), where the extinction cross section, normalized to the maximum extinction value is presented. The accuracy of the data below 30 % of the volume fraction is low, governed by the small particle size, thus the data is not presented. Very similar behavior is observed, as on a plot (a), with slight differences. The fit resulted in the maximum of the LSPR contribution at a slightly lower volume fractions of around 45 %, with a faster decay with respect to the volume fraction increase. The wavelength dependence is however, in good agreement with the experimental data. The discrepancy observed in terms of volume fraction can be explained by the fact that in the CDA simulations, a static depolarization factor is used for simplicity, while in reality, it varies over the whole temperature range. In addition, the hosting material in the simulation is lossless, while in reality interband absorptions, which also depend on the wavelength, are present in the insulating phase. Moreover, in general the CDA is based on the same assumptions as made in the BEMA model, thus its accuracy around the percolation threshold is doubtful.

The fitting, results in the cluster radius of 40±2 nm in-plane, at LSPR maximum, as presented in Fig. 4.23(c). The value corresponds to only 27 nm diameter of the clusters in out-of-plane direction. The estimated size of metallic VO_2 clusters scales in a good agreement with the previous measurements of VO_2 nanodiscs in the ambient medium [146, 147]. This clarifies, that the observed changes in the aspect ratio of the particles, are not governed by the limited thickness of the film, but rather attributed to the structural transformations. Although the accuracy of the simulations does not allow to determine the cluster size exactly, it gives an estimate of the average cluster size, contributing into the optical wavelength range. The size appears to be well below the resolution of standard microscopic techniques. It has to be mentioned, that the determined cluster size is only the size of the clusters which contribute to the LSPR absorption. As has been mentioned, with increasing the volume fraction of the metallic phase, the clusters start to overlap and form the irregular shapes. As a consequence the size distribution of the metallic clusters must be treated in terms of the fractals. Indeed, as IMT transition in VO_2 is effectively the percolation transition, its properties are described by the critical exponent, which is linked to the fractal dimension of the transition, explaining the self similarity of the evolving clusters. Determination of the fractal dimension of the system, in this case is an interesting but rather complicated task, which is out of the scope of this work.

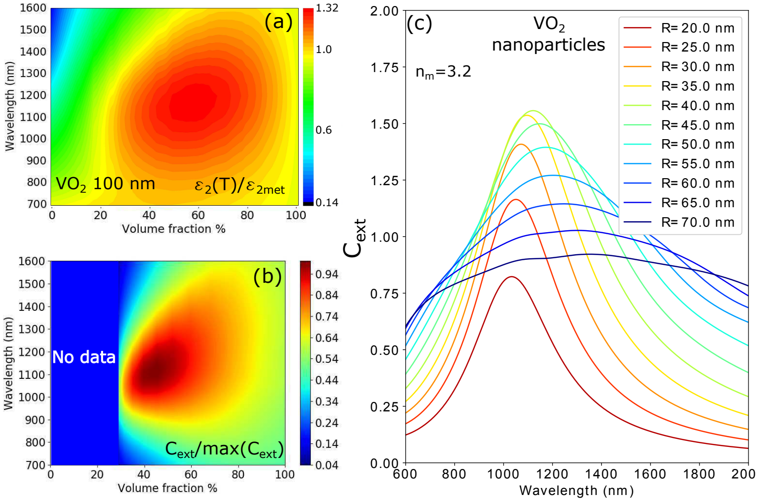

Figure 4.23 Signatures of the LSPR in the 100 nm thick VO_2 film. (a) Imaginary part of the temperature-dependent dielectric constant normalized to the value of the metallic phase versus the volume fraction of the metallic phase obtained from the BEMA model. (b) Extinction cross section normalized to maximum extinction cross section versus volume fraction, obtained from CDA simulations of growing VO_2 metallic clusters in the insulating phase with refractive index $n = 3.2$. (c) Obtained extinction cross section from the CDA simulations shown in graph (b), as a function of the cluster in-plane mean radius R.

Some attempt to estimate the cluster size distribution can still be performed. As discussed in previous chapter, the distribution of the size parameter of the clusters is related to the measured depolarization. If the distribution is spatially inhomogeneous, beyond the coherence length scale, depolarization effects are expected. In reflectivity, however the changes in depolarization index are not observed, even for the thickest film. This is demonstrated in Fig. 4.24, together with the depolarization index for wavelength below the

LSPR, for comparison. Over the complete thermal cycle the depolarization is observed to be constant.

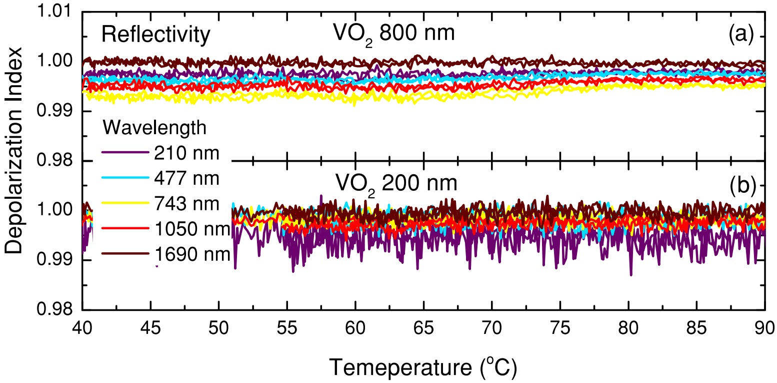

Figure 4.24 Temperature dependence of the depolarization index measured in reflectivity configuration for (a) 800 nm thick VO_2 film, (b) 200 nm thick VO_2 film during heating and cooling (curves overlap).

To observe depolarization it is required to switch to the transmission configuration, where forward scattering is measured, thus the sensitivity to polarization loss is higher. In transmission however, the high absorbance of the films in the metallic phase restricts from the accurate measurement of the depolarization index, as the signal intensity is close to the threshold sensitivity of the detector. To perform such a measurement, it is necessary to utilize a more powerful source and more sensitive detector. This is done on the VASE setup, where a diode laser of 1550 wavelength is used as a source. The probing wavelength does not coincide with the peak wavelength of the plasmon resonance, but still falls in the spectral width of the LSPR, which is enough to detect changes in depolarization index. On the one hand, it is favorable to measure the thickest films, as the amount of scattering events is expected to be the highest. On the other, the thinnest film has highest transmittance and gives the most accurate results. Thus, the measurements are performed on the 400 nm thick film. The VASE configuration does not provide an access to the fourth row of the Mueller matrix. Nevertheless, implementing an additional external compensator in front of the detector, and conducting two sets of measurements, allows us to determine all the elements of the Mueller matrix and consequently to calculate the depolarization index. The resulting Mueller matrix is displayed in Fig. 4.25(a).

As can be seen from panel (a), the measured Mueller matrix elements M_{22} and M_{33}, are not equal, which serves as a sign of the anisotropic scattering. As the measurements are performed at normal incidence, this is a sign that the clusters develop in some preferential orientation, in contradiction to the assumption taken during BEMA model analysis, that in-plane the anisotropy is absent. Nevertheless, the difference between M_{22} and M_{33} is very small, which justifies the isotropic approximation. Another signature of inhomogeneity is the non-zero values of the off-diagonal elements, although, this can be attributed to fluctuations within the errorbars. Close to the critical temperature, where the LSPR contribution is observed for this sample, the depolarization index shows a week deep, demonstrated in panel (b). The variation of the depolarization factor is minor and is within the errorbars. Nevertheless, it is apparent that the changes of the depolarization mean value coincide with the expected temperature for the LSPR absorption. Moreover, after the percolation region, the depolarization index mean value is again around 1, which corresponds to absence of the depolarization effects.

Although, the detected depolarization is very weak, much weaker than for gold nanoparticles, its rise in the percolation region serves as a signature of the stochastic scattering within the film, due to the formation of the metallic clusters. As the film thickness is 400 nm, which is far below the coherence length of the probing beam (around 12 μm), forward scattering is responsible for the observed depolarization. Thus, it can be concluded, that the depolarization originates from the lateral inhomogeneity of the insulator-metal transition.

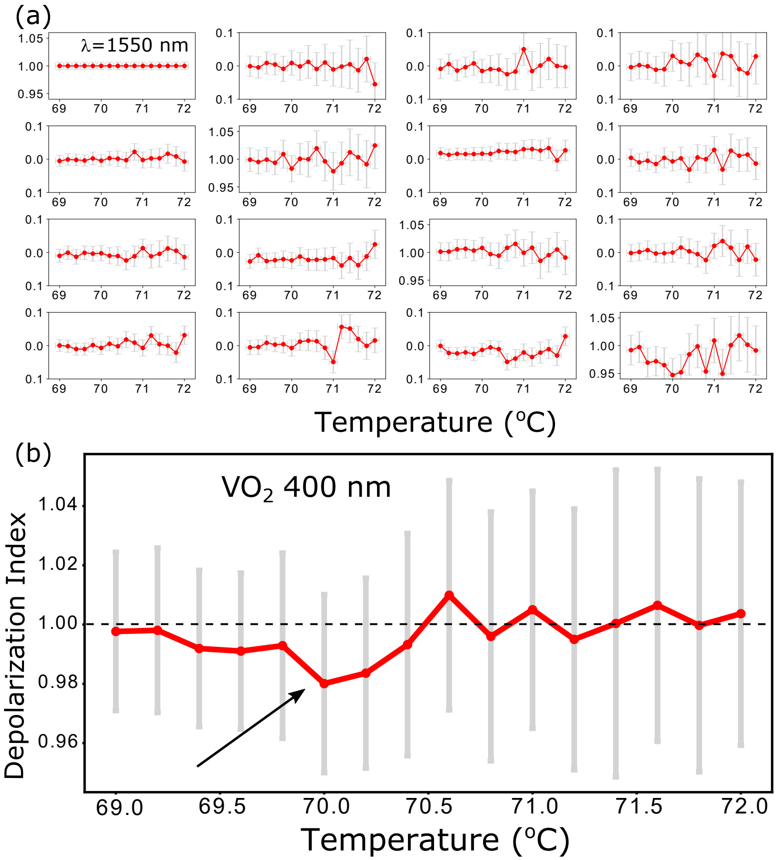

Figure 4.25 (a) Mueller matrix measured on VASE ellipsometer in transmission as a function of temperature at wavelength of 1550 nm for 400 nm thick VO_2 film. The bottom row is recovered with a two-measurement-regression method. (b) Temperature-dependent depolarization index for the same wavelength derived from the complete Mueller matrix.

With these results, the LSPR origin of the enhanced absorption is confirmed. Unfortunately, the depolarization effects in the films are very weak, to obtain any quantitative information about the size distribution of the clusters. In principle, at the resonance wavelength of 1200 nm, the observed effect can be stronger and information about size distribution can still be extracted. Nevertheless, at this point the information about presence of inhomogeneity has been extracted, which can be related to the presence of local defects within the film. Combining this with the observed variation of the shape factor, it becomes clear why the optical response is different during cooling and heating cycles, as changes in shape of the plasmonic particles, triggered by the structural transformations, dramatically tune its resonance frequency.

4.6 Conclusion

In this chapter the insulator-metal transition in polycrystalline VO_2 thin films was investigated as a function of the film thickness. To obtain a deeper understanding of the complex process of the transition, results from several experimental techniques were correlated. The dc-resistivity measurements revealed a thickness-dependent critical temperature. Both, for heating and cooling, the transition temperatures increase while film thickness decreases. On the other hand, from the standard ellipsometric measurements of the insulating and metallic phases, it was concluded that the optical anisotropy of the films increases towards thinner films. Finally, from the AFM measurements it was observed that the grain boundary density decreases towards thicker films, as the average size of the grains increases. Combining the information from these three independent sources, it is concluded that a certain amount of internal strain accumulates in thinner films. The main origin of the strain is attributed to the larger grain boundary density in thinner films. As a result, a set of the investigated samples cover a certain range of the strain-temperature phase diagram, where the properties of the insulator-metal transition are altered.

To investigate the transition in more details, temperature-dependent ellipsometric measurements were performed. Several interesting features were observed from this measurements. One, is a substantial drop in reflectivity at larger wavelength, close to the transition temperatures. The properties of the phenomena are frequency- and thickness-dependent. The other, is an asymmetry of the transition with respect to heating and cooling. The asymmetry is most prominent in the vicinity of the critical temperate, where the decreased reflectivity is observed.

To understand the origin of these observations, an effective medium approximation is used to obtain the temperature-dependent optical properties of the films. The most suitable type of the effective medium model, for the particular problem, is the Bruggeman model. As a first step however, it was demonstrated that the standard static Bruggeman effective medium approximation fails to reproduce the optical properties of the films over the complete thermodynamic cycle. Instead, the anisotropic Bruggeman model, with a varying cluster shape is used. The model not only successfully reproduces the measurements over the complete thermodynamic cycle, but also provides an incite into the nature of the transition. In particular, the shape of the developing metallic phase clusters appears to be temperature-dependent. While in the thinnest film, of 100 nm, the clusters extend in-plane, for thicker films, they tend to grow more out-of-plane. In the thickest films, of 600 and 800 nm, where strain is the lowest, the development is observed to be more homogeneous. Moreover, the asymmetry of the hysteresis, is completely described by minor differences in the cluster shape.

The origin of such cluster shape variation is related to the structural transformations, deduced from the roughness data, obtained from ellipsometry and confirmed by AFM. In thinner films, 100, 200 and 400 nm, roughness decreases during the transition into the metallic state, with almost no hysteresis. The changes in roughness are associated with the structural transformations. Two thinnest films, also posses some anomalies in roughness data, which might be related to the abrupt strain relaxation process. As a results, the variation of the cluster size can be related to the structural transformations. This highlights the interplay between electronic and structural transition in VO_2.

On the one hand, two transitions can be decoupled by strain effects, which highlights the electron-correlation origin of the insulator-metal transition. On the other, the structural transformations still influences the microscopic geometry, and as a result the macroscopic electronic response.

In the final part of the chapter, some attempt to estimate the size of the clusters is performed. This is done by using the properties of the localized plasmon resonance of the metallic clusters. The Bruggeman model provides an evidence of the plasmon absorption, together with its spectral properties. Unfortunately, it does not link these properties with the size. The size of the clusters is retrieved via Coupled Dipole Approximation, which allows relation of the extinction spectral properties with the particle size. The extracted size of the clusters appears to be four times smaller than the thickness of the thinnest film. Nevertheless, the percolation transition is expected to have a fractal nature, thus the extracted size, is only the size of the clusters contributing the the observed plasmon resonance. The particle size distribution may be extracted from the depolarization spectra, similar to the previous chapter. Unfortunately, the measured depolarization signal is weak, governed by strong absorbing properties of the films in the metallic phase. The variation of the depolarization factor is still observed however, within the errorbars. So no quantitative information about the distribution could be extracted.

To further investigate the nature of the percolation transition in VO_2 additional measurements are required. In particular, it is reasonable to concentrate on the measurements, sensitive to the structural transition, x-ray or Raman. These measurements have to be juxtaposed with the results obtained from ellipsometric measurements, the cluster shape variation and the electronic transition critical temperature. Such a study would allow us to establish an exact relation between structural and electronic transition and provide more information about their interplay. Additional depolarization index measurements, at wavelengths matching the localized plasmon resonance would be also beneficial. They can provide the information about the spatial inhomogeneity of the percolation transition, which can be further correlated with the amount of stress in the thin films.

Bibliography

[1] E. Armstrong and C. O'Dwyer, "Artificial opal photonic crystals and inverse opal structures – fundamentals and applications from optics to energy storage," *J. Mater. Chem. C*, vol. 3, pp. 6109–6143, 2015.

[2] E. D. Finlayson, L. T. McDonald, and P. Vukusic, "Optically ambidextrous circularly polarized reflection from the chiral cuticle of the scarab beetle Chrysina resplendens," *Journal of The Royal Society Interface*, vol. 14, p. 20170129, 2017.

[3] W. Cai, U. K. Chettiar, A. V. Kildishev, and V. M. Shalaev, "Optical cloaking with metamaterials," *Nature Photonics*, vol. 1, p. 224, 2007.

[4] E. J. Garboczi, K. A. Snyder, J. F. Douglas, and M. F. Thorpe, "Geometrical percolation threshold of overlapping ellipsoids," *Phys. Rev. E*, vol. 52, pp. 819–828, 1995.

[5] D. Wegkamp and J. Stähler, "Ultrafast dynamics during the photoinduced phase transition in VO_2," *Progress in Surface Science*, vol. 90, pp. 464 – 502, 2015.

[6] J. H. Park, J. M. Coy, T. S. Kasirga, C. Huang, Z. Fei, S. Hunter, and D. H. Cobden, "Measurement of a solid-state triple point at the metal-insulator transition in VO_2," *Nature*, vol. 500, p. 431, 2013.

[7] I. Voloshenko, F. Kuhl, B. Gompf, A. Polity, G. Schnoering, A. Berrier, and M. Dressel, "Microscopic nature of the asymmetric hysteresis in the insulator-metal transition of VO_2 revealed by spectroscopic ellipsometry," *Applied Physics Letters*, vol. 113, p. 201906, 2018.

[8] J. Jackson, *Classical electrodynamics*. John-Wiley & Sons, 1998.

[9] H. Fujiwara, *Spectroscopic ellipsometry: principles and applications*. John-Wiley & Sons, 2007.

[10] H. Arwin, *Thin film optics and polarized light*. Private publisher: H. Arwin, 2016.

[11] E. S. Laszlo Solymar, *Waves in metamaterials*. Oxford university press, 2010.

[12] C. F. Bohren and D. R. Huffman, *Absorption and scattering of light by small particles*. Wiley-VCH Verlag GmbH, 2017.

[13] E. M. Purcell and C. R. Pennypacker, "Scattering and Absorption of Light by Nonspherical Dielectric Grains," *Astrophysical Journal*, vol. 186, pp. 705–714, 1973.

[14] B. T. Draine and P. J. Flatau, "Discrete-dipole approximation for scattering calculations," *J. Opt. Soc. Am. A*, vol. 11, pp. 1491–1499, 1994.

[15] B. T. Draine and P. J. Flatau, "Discrete-dipole approximation for periodic targets: theory and tests," *J. Opt. Soc. Am. A*, vol. 25, pp. 2693–2703, 2008.

[16] T. Jensen, L. Kelly, A. Lazarides, and G. C. Schatz, "Electrodynamics of noble metal nanoparticles and nanoparticle clusters," *Journal of Cluster Science*, vol. 10, pp. 295–317, 1999.

[17] E. Kretschmann and H. Raether, "Notizen: Radiative Decay of Non Radiative Surface Plasmons Excited by Light," *Zeitschrift Naturforschung Teil A*, vol. 23, pp. 2135–2136, 1968.

[18] M. Losurdo and K. Hingerl, *Ellipsometry at the nanoscale*. Springer-Verlag Berlin Heidelberg, 2013.

[19] M. Seo, J. Lee, and M. Lee, "Grating-coupled surface plasmon resonance on bulk stainless steel," *Opt. Express*, vol. 25, pp. 26939–26949, 2017.

[20] M. Wang, *Revealing plasmonic effects of one-dimensional periodic structures through Mueller matrix spectroscopic ellipsometry*. PhD thesis, Universität Stuttgart, 2018.

[21] P. G. Kik and M. L. Brongersma, *Surface plasmon nanophotonics*. Springer Netherlands, 2007.

[22] J. B. Khurgin, “Ultimate limit of field confinement by surface plasmon polaritons,” *Faraday Discuss.*, vol. 178, pp. 109–122, 2015.

[23] J. Khurgin, W.-Y. Tsai, D. P. Tsai, and G. Sun, “Landau Damping and Limit to Field Confinement and Enhancement in Plasmonic Dimers,” *ACS Photonics*, vol. 4, pp. 2871–2880, 2017.

[24] J. R. Krenn, H. Ditlbacher, G. Schider, A. Hohenau, A. Leitner, and F. R. Aussenegg, “Surface plasmon micro- and nano-optics,” *Journal of Microscopy*, vol. 209, pp. 167–172, 2003.

[25] S. A. Maier, *Plasmonics: Fundamentals and Applications*. Springer-Verlag US, 2007.

[26] G. Weick, C. Woollacott, W. L. Barnes, O. Hess, and E. Mariani, “Dirac-like plasmons in honeycomb lattices of metallic nanoparticles,” *Phys. Rev. Lett.*, vol. 110, p. 106801, 2013.

[27] T. J. Sturges, C. Woollacott, G. Weick, and E. Mariani, “Dirac plasmons in bipartite lattices of metallic nanoparticles,” *2D Materials*, vol. 2, p. 014008, 2015.

[28] H. T. Rekola, T. K. Hakala, and P. Törmä, “One-dimensional plasmonic nanoparticle chain lasers,” *ACS Photonics*, vol. 5, pp. 1822–1826, 2018.

[29] W. Wang, M. Ramezani, A. I. Väkeväinen, P. Törmä, J. G. Rivas, and T. W. Odom, “The rich photonic world of plasmonic nanoparticle arrays,” *Materials Today*, vol. 21, pp. 303 – 314, 2018.

[30] R. Guo, M. Nečada, T. K. Hakala, A. I. Väkeväinen, and P. Törmä, “Lasing at k points of a honeycomb plasmonic lattice,” *Phys. Rev. Lett.*, vol. 122, p. 013901, 2019.

[31] T. Brakstad, M. Kildemo, Z. Ghadyani, and I. Simonsen, “Dispersion of polarization coupling, localized and collective plasmon modes in a metallic photonic crystal mapped by mueller matrix ellipsometry,” *Opt. Express*, vol. 23, pp. 22800–22815, 2015.

[32] M. Bass, C. DeCusatis, J. Enoch, V. Lakshminarayanan, G. Li, C. Macdonald, V. Mahajan, and E. Van Stryland, *Handbook of Optics, Third Edition Volume I: Geometrical and Physical Optics, Polarized Light, Components and Instruments*. McGraw-Hill, Inc., 3 ed., 2010.

[33] S. R. Cloude and E. Pottier, “A review of target decomposition theorems in radar polarimetry,” *IEEE Transactions on Geoscience and Remote Sensing*, vol. 34, pp. 498–518, 1996.

[34] F. L. Roy-Bréhonnet, B. L. Jeune, P. Eliès, J. Cariou, and J. Lotrian, “Optical media and target characterization by mueller matrix decomposition,” *Journal of Physics D: Applied Physics*, vol. 29, pp. 34–38, 1996.

[35] N. Agarwal, J. Yoon, E. Garcia-Caurel, T. Novikova, J.-C. Vanel, A. Pierangelo, A. Bykov, A. Popov, I. Meglinski, and R. Ossikovski, “Spatial evolution of depolarization in homogeneous turbid media within the differential mueller matrix formalism,” *Opt. Lett.*, vol. 40, pp. 5634–5637, 2015.

[36] R. Ossikovski, “Differential matrix formalism for depolarizing anisotropic media,” *Opt. Lett.*, vol. 36, pp. 2330–2332, 2011.

[37] N. Ortega-Quijano and J. L. Arce-Diego, “Mueller matrix differential decomposition for direction reversal: application to samples measured in reflection and backscattering,” *Opt. Express*, vol. 19, pp. 14348–14353, 2011.

[38] P. Drude, “Über Oberflächenschichten. I. Theil,” *Annalen der Physik*, vol. 272, pp. 532–560, 1889.

[39] R. W. Collins and J. Koh, “Dual rotating-compensator multichannel ellipsometer:instrument design for real-time Mueller matrix spectroscopy of surfaces and films,” *J. Opt. Soc. Am. A*, vol. 16, pp. 1997–2006, 1999.

[40] J. Li, B. Ramanujam, and R. Collins, “Dual rotating compensator ellipsometry: Theory and simulations,” *Thin Solid Films*, vol. 519, pp. 2725 – 2729, 2011.

[41] L. J. van der Pauw, “A method of measuring specific resistivity and Hall effect of disc of arbitrary shape,” *Philips Technical Review*, vol. 20, pp. 220–224, 1958.

[42] R. H. Ritchie, “Plasma losses by fast electrons in thin films,” *Phys. Rev.*, vol. 106, pp. 874–881, 1957.

[43] R. F. Aroca, “Plasmon enhanced spectroscopy,” *Phys. Chem. Chem. Phys.*, vol. 15, pp. 5355–5363, 2013.

[44] P. G. Etchegoin, “Plasmonics and spectroscopy,” *Phys. Chem. Chem. Phys.*, vol. 15, pp. 5261–5261, 2013.

[45] D. Li and D. Pacifici, “Strong amplitude and phase modulation of optical spatial coherence with surface plasmon polaritons,” *Science Advances*, vol. 3, pp. 324–328, 2017.

[46] C. Hoessbacher, A. Josten, B. Baeuerle, Y. Fedoryshyn, H. Hettrich, Y. Salamin, W. Heni, C. Haffner, C. Kaiser, R. Schmid, D. L. Elder, D. Hillerkuss, M. Möller, L. R. Dalton, and J. Leuthold, “Plasmonic modulator with >170 GHz bandwidth demonstrated at 100 GBd NRZ,” *Opt. Express*, vol. 25, pp. 1762–1768, 2017.

[47] R. Djabery, M. Naser-Moghaddasi, and A. Andalib, “Design and analysis of a polarization modulator based on surface plasmons,” *Appl. Opt.*, vol. 56, pp. 8793–8796, 2017.

[48] D. Wu, Y. Liu, L. Yu, Z. Yu, L. Chen, R. Li, R. Ma, C. Liu, J. Zhang, and H. Ye, “Plasmonic metamaterial for electromagnetically induced transparency analogue and ultra-high figure of merit sensor,” *Scientific Reports*, vol. 7, p. 45210, 2017.

[49] L. Lei, S. Li, H. Huang, K. Tao, and P. Xu, “Ultra-broadband absorber from visible to near-infrared using plasmonic metamaterial,” *Opt. Express*, vol. 26, pp. 5686–5693, 2018.

[50] Y.-H. Chou, K.-B. Hong, C.-T. Chang, T.-C. Chang, Z.-T. Huang, P.-J. Cheng, J.-H. Yang, M.-H. Lin, T.-R. Lin, K.-P. Chen, S. Gwo, and T.-C. Lu, “Ultracompact pseudowedge plasmonic lasers and laser arrays,” *Nano Letters*, vol. 18, pp. 747–753, 2018.

[51] J. M. Fitzgerald, S. Azadi, and V. Giannini, “Quantum plasmonic nanoantennas,” *Phys. Rev. B*, vol. 95, p. 235414, 2017.

[52] K. Ueno, T. Oshikiri, Q. Sun, X. Shi, and H. Misawa, “Solid-state plasmonic solar cells,” *Chemical Reviews*, vol. 118, pp. 2955–2993, 2018.

[53] B. Hou, M. Xie, R. He, M. Ji, S. Trummer, R. H. Fink, and L. Zhang, “Microsphere assisted super-resolution optical imaging of plasmonic interaction between gold nanoparticles,” *Scientific Reports*, vol. 7, p. 13789, 2017.

[54] H. Cang, A. Salandrino, Y. Wang, and X. Zhang, “Adiabatic far-field sub-diffraction imaging,” *Nature Communications*, vol. 6, p. 7942, 2015.

[55] J. T. Jørgensen, K. Norregaard, P. Tian, P. M. Bendix, A. Kjaer, and L. B. Oddershede, “Single Particle and PET-based Platform for Identifying Optimal Plasmonic Nano-Heaters for Photothermal Cancer Therapy,” *Scientific Reports*, vol. 6, p. 30076, 2016.

[56] K. Turcheniuk, T. Dumych, R. Bilyy, V. Turcheniuk, J. Bouckaert, V. Vovk, V. Chopyak, V. Zaitsev, P. Mariot, N. Prevarskaya, R. Boukherroub, and S. Szunerits, “Plasmonic photothermal cancer therapy with gold nanorods/reduced graphene oxide core/shell nanocomposites,” *RSC Adv.*, vol. 6, pp. 1600–1610, 2016.

[57] B. Auguié and W. L. Barnes, “Collective resonances in gold nanoparticle arrays,” *Phys. Rev. Lett.*, vol. 101, p. 143902, 2008.

[58] S.-P. Yu, J. A. Muniz, C.-L. Hung, and H. J. Kimble, “Two-dimensional photonic crystals for engineering atom-light interactions,” *Proceedings of the National Academy of Sciences*, vol. 116, pp. 12743–12751, 2019.

[59] D. Pan, R. Yu, H. Xu, and F. J. García de Abajo, “Topologically protected Dirac plasmons in a graphene superlattice,” *Nature Communications*, vol. 8, p. 1243, 2017.

[60] F. Bleckmann, Z. Cherpakova, S. Linden, and A. Alberti, “Spectral imaging of topological edge states in plasmonic waveguide arrays,” *Phys. Rev. B*, vol. 96, p. 045417, 2017.

[61] Y. Guo, M. Xiao, and S. Fan, “Topologically protected complete polarization conversion,” *Phys. Rev. Lett.*, vol. 119, p. 167401, 2017.

[62] J. Kang, Z. Wei, and J. Li, “Graphyne and its family: Recent theoretical advances,” *ACS Applied Materials & Interfaces*, vol. 11, pp. 2692–2706, 2019.

[63] Z. Liu, G. Yu, H. Yao, L. Liu, L. Jiang, and Y. Zheng, “A simple tight-binding model for typical graphyne structures,” *New Journal of Physics*, vol. 14, p. 113007, 2012.

[64] H. Levinson, *Principles of Lithography*. SPIE Press, 2005.

[65] S.-W. Park, G. Park, Y. Kim, J. H. Cho, J. Lee, and H. Kim, "Through-focus scanning optical microscopy with the Fourier modal method," *Opt. Express*, vol. 26, pp. 11649–11657, 2018.

[66] J. S. Madsen, L. H. Thamdrup, I. Czolkos, P. E. Hansen, A. Johansson, J. Garnaes, J. Nygård, and M. H. Madsen, "In-line characterization of nanostructured mass-produced polymer components using scatterometry," *Journal of Micromechanics and Microengineering*, vol. 27, p. 085004, 2017.

[67] E. Bugnicourt, T. Kehoe, M. Latorre, C. Serrano, S. Philippe, and M. Schmid, "Recent Prospects in the Inline Monitoring of Nanocomposites and Nanocoatings by Optical Technologies," *Nanomaterials*, vol. 6, p. 150, 2016.

[68] R. Haight, F. M. Ross, and J. B. Hannon, *Handbook of Instrumentation and Techniques for Semiconductor Nanostructure Characterization*. World Scientific Publishing Company, 2011.

[69] S. De Zuani, M. Rommel, R. Vogelgesang, J. Weis, B. Gompf, M. Dressel, and A. Berrier, "Large-area two-dimensional plasmonic meta-glasses and meta-crystals: a comparative study," *Plasmonics*, vol. 12, pp. 1381–1390, 2017.

[70] W. H. Kummer, "Basic array theory," *Proceedings of the IEEE*, vol. 80, pp. 127–140, 1992.

[71] J. Qi, T. Kaiser, R. Peuker, T. Pertsch, F. Lederer, and C. Rockstuhl, "Highly resonant and directional optical nanoantennas," *J. Opt. Soc. Am. A*, vol. 31, pp. 388–393, 2014.

[72] E. Kuntman and O. Arteaga, "Decomposition of a depolarizing Mueller matrix into its nondepolarizing components by using symmetry conditions," *Appl. Opt.*, vol. 55, pp. 2543–2550, 2016.

[73] S.-Y. Lee, F. Hu, and J. Ji, "Representation of nonrectangular features for exposure estimation and proximity effect correction in electron-beam lithography," *Journal of Vacuum Science & Technology B*, vol. 22, pp. 2929–2935, 2004.

[74] G. G. Lopez, S. A. Wood, M. G. Metzler, S. J. H. Stammberger, and R. S. McCay, "Shape positional accuracy optimization via writing order correction," *Journal of Vacuum Science & Technology B*, vol. 34, p. 06K601, 2016.

[75] J. C. Heckel and G. Chumanov, "Depolarized light scattering from single silver nanoparticles," *The Journal of Physical Chemistry C*, vol. 115, pp. 7261–7269, 2011.

[76] S. Chandel, J. Soni, S. k. Ray, A. Das, A. Ghosh, S. Raj, and N. Ghosh, "Complete polarization characterization of single plasmonic nanoparticle enabled by a novel dark-field mueller matrix spectroscopy system," *Scientific Reports*, vol. 6, p. 26466, 2016.

[77] R. Ossikovski and K. Hingerl, "General formalism for partial spatial coherence in reflection Mueller matrix polarimetry," *Opt. Lett.*, vol. 41, pp. 4044–4047, 2016.

[78] M. Born and E. Wolf, *Principles of Optics*. Pergamon, 1980.

[79] X. Dong and D.-X. Zhou, "Learning gradients by a gradient descent algorithm," *Journal of Mathematical Analysis and Applications*, vol. 341, pp. 1018 – 1027, 2008.

[80] V. G. Kravets, A. V. Kabashin, W. L. Barnes, and A. N. Grigorenko, "Plasmonic surface lattice resonances: A review of properties and applications," *Chemical Reviews*, vol. 118, pp. 5912–5951, 2018.

[81] A. D. Humphrey and W. L. Barnes, "Plasmonic surface lattice resonances on arrays of different lattice symmetry," *Phys. Rev. B*, vol. 90, p. 075404, 2014.

[82] P. Törmä and W. L. Barnes, "Strong coupling between surface plasmon polaritons and emitters: a review," *Reports on Progress in Physics*, vol. 78, p. 013901, 2014.

[83] N. M. R. Peres, J. N. B. Rodrigues, T. Stauber, and J. M. B. L. dos Santos, "Dirac electrons in graphene-based quantum wires and quantum dots," *Journal of Physics: Condensed Matter*, vol. 21, p. 344202, 2009.

[84] V. T. Tenner, M. J. A. de Dood, and M. P. van Exter, "Surface plasmon dispersion in hexagonal, honeycomb and kagome plasmonic crystals," *Opt. Express*, vol. 24, pp. 29624–29633, 2016.

[85] J. Goodenough, "Metallic oxides," *Progress in Solid State Chemistry*, vol. 5, pp. 145–399, 1971.

[86] F. J. Morin, "Oxides Which Show a Metal-to-Insulator Transition at the Néel Temperature," *Phys. Rev. Lett.*, vol. 3, pp. 34–36, 1959.

[87] T. Mitsuishi, “On the Phase Transformation of VO_2,” *Japanese Journal of Applied Physics*, vol. 6, p. 1060, 1967.

[88] N. F. Quackenbush, H. Paik, M. J. Wahila, S. Sallis, M. E. Holtz, X. Huang, A. Ganose, B. J. Morgan, D. O. Scanlon, Y. Gu, F. Xue, L.-Q. Chen, G. E. Sterbinsky, C. Schlueter, T.-L. Lee, J. C. Woicik, J.-H. Guo, J. D. Brock, D. A. Muller, D. A. Arena, D. G. Schlom, and L. F. J. Piper, “Stability of the M2 phase of vanadium dioxide induced by coherent epitaxial strain,” *Phys. Rev. B*, vol. 94, p. 085105, 2016.

[89] S. Lee, T. L. Meyer, C. Sohn, D. Lee, J. Nichols, D. Lee, S. S. A. Seo, J. W. Freeland, T. W. Noh, and H. N. Lee, “Electronic structure and insulating gap in epitaxial VO_2 polymorphs,” *APL Materials*, vol. 3, p. 126109, 2015.

[90] R. M. Wentzcovitch, W. W. Schulz, and P. B. Allen, “VO_2: Peierls or Mott-Hubbard? A view from band theory,” *Phys. Rev. Lett.*, vol. 72, pp. 3389–3392, 1994.

[91] N. F. Mott, “The basis of the electron theory of metals, with special reference to the transition metals,” *Proceedings of the Physical Society. Section A*, vol. 62, p. 416, 1949.

[92] M. Gatti, F. Bruneval, V. Olevano, and L. Reining, “Understanding correlations in vanadium dioxide from first principles,” *Phys. Rev. Lett.*, vol. 99, p. 266402, 2007.

[93] Z. Tao, T.-R. T. Han, S. D. Mahanti, P. M. Duxbury, F. Yuan, C.-Y. Ruan, K. Wang, and J. Wu, “Decoupling of Structural and Electronic Phase Transitions in VO_2,” *Phys. Rev. Lett.*, vol. 109, p. 166406, 2012.

[94] J. Laverock, S. Kittiwatanakul, A. A. Zakharov, Y. R. Niu, B. Chen, S. A. Wolf, J. W. Lu, and K. E. Smith, “Direct Observation of Decoupled Structural and Electronic Transitions and an Ambient Pressure Monocliniclike Metallic Phase of VO_2,” *Phys. Rev. Lett.*, vol. 113, p. 216402, 2014.

[95] M. Yang, Y. Yang, B. Hong, L. Wang, K. Hu, Y. Dong, H. Xu, H. Huang, J. Zhao, H. Chen, L. Song, H. Ju, J. Zhu, J. Bao, X. Li, Y. Gu, T. Yang, X. Gao, Z. Luo, and C. Gao, “Suppression of Structural Phase Transition in VO_2 by Epitaxial Strain in Vicinity of Metal-insulator Transition,” *Scientific Reports*, vol. 6, p. 23119, 2016.

[96] J. Rozen, R. Lopez, R. F. Haglund, and L. C. Feldman, "Two-dimensional current percolation in nanocrystalline vanadium dioxide films," *Appl. Phys. Lett.*, vol. 88, p. 081902, 2006.

[97] A. Sharoni, J. G. Ramírez, and I. K. Schuller, "Multiple avalanches across the metal-insulator transition of vanadium oxide nanoscaled junctions," *Phys. Rev. Lett.*, vol. 101, p. 026404, 2008.

[98] T. Yamin, Y. Strelniker, and A. Sharoni., "High resolution Hall measurements across the VO_2 metal-insulator transition reveal impact of spatial phase separation," *Sci. Rep.*, vol. 6, pp. 128–132, 2016.

[99] D. Ruzmetov, D. Heiman, B. B. Claflin, V. Narayanamurti, and S. Ramanathan, "Hall carrier density and magnetoresistance measurements in thin-film vanadium dioxide across the metal-insulator transition," *Phys. Rev. B*, vol. 79, p. 153107, 2009.

[100] A. S. Barker, H. W. Verleur, and H. J. Guggenheim, "Infrared optical properties of vanadium dioxide above and below the transition temperature," *Phys. Rev. Lett.*, vol. 17, pp. 1286–1289, 1966.

[101] P. J. Hood and J. F. DeNatale, "Millimeter-wave dielectric properties of epitaxial vanadium dioxide thin films," *J. Appl. Phys.*, vol. 70, pp. 376–381, 1991.

[102] H. Zhan, V. Astley, M. Hvasta, J. A. Deibel, D. M. Mittleman, and Y.-S. Lim, "The metal-insulator transition in VO_2 studied using terahertz apertureless near-field microscopy," *Appl. Phys. Lett.*, vol. 91, pp. 21–24, 2007.

[103] T. Yao, X. Zhang, Z. Sun, S. Liu, Y. Huang, Y. Xie, C. Wu, X. Yuan, W. Zhang, Z. Wu, G. Pan, F. Hu, L. Wu, Q. Liu, and S. Wei, "Understanding the Nature of the Kinetic Process in a VO_2 Metal-Insulator Transition," *Phys. Rev. Lett.*, vol. 105, p. 226405, 2010.

[104] T. C. Koethe, Z. Hu, M. W. Haverkort, C. Schüßler-Langeheine, F. Venturini, N. B. Brookes, O. Tjernberg, W. Reichelt, H. H. Hsieh, H.-J. Lin, C. T. Chen, and L. H. Tjeng, "Transfer of spectral weight and symmetry across the metal-insulator transition in VO_2," *Phys. Rev. Lett.*, vol. 97, p. 116402, 2006.

[105] X. Xu, X. He, H. Wang, Q. Gu, S. Shi, H. Xing, C. Wang, J. Zhang, X. Chen, and J. Chu, "The extremely narrow hysteresis width of phase transition in nanocrystallineVO_2 thin films with the flake grain structures," *Appl. Surf. Sci.*, vol. 261, pp. 83 – 87, 2012.

[106] G. J. Kovacs, D. Burger, I. Skorupa, H. Reuther, R. Heller, and H. Schmidt, “Effect of the substrate on the insulator–metal transition of vanadium dioxide films,” *J. Appl. Phys.*, vol. 109, p. 063708, 2011.

[107] J. Li and J. Dho, “Characteristics of phase transition of VO_2 films grown on TiO_2 substrates with different crystal orientations,” *J. Cryst. Growth*, vol. 404, pp. 84 – 88, 2014.

[108] Y. Zhu, Y. Zhao, M. Holtz, Z. Fan, and A. A. Bernussi, “Effect of substrate orientation on terahertz optical transmission through VO_2 thin films and application to functional antireflection coatings,” *J. Opt. Soc. Am. B*, vol. 29, pp. 2373–2378, 2012.

[109] T. Peterseim, M. Dressel, M. Dietrich, and A. Polity, “Optical properties of VO_2 films at the phase transition: Influence of substrate and electronic correlations,” *J. Appl. Phys.*, vol. 120, p. 075102, 2016.

[110] Y. D. Ji, T. S. Pan, Z. Bi, W. Z. Liang, Y. Zhang, H. Z. Zeng, Q. Y. Wen, H. W. Zhang, C. L. Chen, Q. X. Jia, and Y. Lin, “Epitaxial growth and metal-insulator transition of vanadium oxide thin films with controllable phases,” *Appl. Phys. Lett.*, vol. 101, p. 071902, 2012.

[111] Y. Xiong, Q.-Y. Wen, Z. Chen, W. Tian, T.-L. Wen, Y.-L. Jing, Q.-H. Yang, and H.-W. Zhang, “Tuning the phase transitions of VO_2 thin films on silicon substrates using ultrathin Al_2O_3 as buffer layers,” *J. Phys. D: Appl. Phys.*, vol. 47, p. 455304, 2014.

[112] V. Eyert, “The metal to insulator transitions of VO_2: A band theoretical approach,” *Annalen der Physik*, vol. 11, pp. 650–704, 2002.

[113] V. Eyert, “ VO_2: A Novel View from Band Theory,” *Phys. Rev. Lett.*, vol. 107, p. 016401, 2011.

[114] W. Fan, J. Cao, J. Seidel, Y. Gu, J. W. Yim, C. Barrett, K. M. Yu, J. Ji, R. Ramesh, L. Q. Chen, and J. Wu, “Large kinetic asymmetry in the metal-insulator transition nucleated at localized and extended defects,” *Phys. Rev. B*, vol. 83, p. 235102, 2011.

[115] W. Yi, K. K. Tsang, S. K. Lam, X. Bai, J. A. Crowell, and E. A. Flores, “Biological plausibility and stochasticity in scalable VO_2 active memristor neurons,” *Nature Communications*, vol. 9, p. 4661, 2018.

[116] M. D. Goldflam, T. Driscoll, B. Chapler, O. Khatib, N. Marie Jokerst, S. Palit, D. R. Smith, B.-J. Kim, G. Seo, H.-T. Kim, M. D. Ventra, and D. N. Basov, “Reconfigurable gradient index using VO_2 memory metamaterials,” *Applied Physics Letters*, vol. 99, p. 044103, 2011.

[117] I. Olivares, L. Sánchez, J. Parra, R. Larrea, A. Griol, M. Menghini, P. Homm, L.-W. Jang, B. van Bilzen, J. W. Seo, J.-P. Locquet, and P. Sanchis, “Optical switching in hybrid VO_2/Si waveguides thermally triggered by lateral microheaters,” *Opt. Express*, vol. 26, pp. 12387–12395, 2018.

[118] K. A. Richard F. Haglund, Sharon M. Weiss, “Photonic and plasmonic modulators based on optical switching in VO_2,” *Proc.SPIE*, vol. 9370, pp. 9370 – 9370, 2015.

[119] S. Kumar, J. P. Strachan, A. L. D. Kilcoyne, T. Tyliszczak, M. D. Pickett, C. Santori, G. Gibson, and R. S. Williams, “The phase transition in VO_2 probed using x-ray, visible and infrared radiations,” *Appl. Phys. Lett.*, vol. 108, p. 073102, 2016.

[120] M. M. Qazilbash, M. Brehm, B.-G. Chae, P.-C. Ho, G. O. Andreev, B.-J. Kim, S. J. Yun, A. V. Balatsky, M. B. Maple, F. Keilmann, H.-T. Kim, and D. N. Basov, “Mott transition in VO_2 revealed by infrared spectroscopy and nano-imaging,” *Science*, vol. 318, pp. 1750–1753, 2007.

[121] J. Feng, C. Yang, A. Zhang, Q. Li, Z. Fan, M. Qin, M. Zeng, X. Gao, Y. Lin, G. Zhou, X. Lu, and J.-M. Liu, “Direct evidence for the coexistence of nanoscale high-conduction and low-conduction phases in VO_2 films,” *Applied Physics Letters*, vol. 113, p. 173104, 2018.

[122] S. Kirkpatrick, “Percolation and conduction,” *Rev. Mod. Phys.*, vol. 45, pp. 574–588, 1973.

[123] J. Kim, C. Ko, A. Frenzel, S. Ramanathan, and J. E. Hoffman, “Nanoscale imaging and control of resistance switching in VO_2 at room temperature,” *Appl. Phys. Lett.*, vol. 96, p. 213106, 2010.

[124] C. Annasiwatta, J. Chen, J. M. Berg, A. Bernussi, Z. Fan, and B. Ren, “Multi-physics modeling of hysteresis in vanadium dioxide thin films,” in *2016 American Control Conference (ACC)*, pp. 6905–6910, 2016.

[125] M. M. Qazilbash, M. Brehm, G. O. Andreev, A. Frenzel, P. C. Ho, B. G. Chae, B. J. Kim, S. J. Yun, H. T. Kim, A. V. Balatsky, O. G. Shpyrko,

M. B. Maple, F. Keilmann, and D. N. Basov, “Infrared spectroscopy and nano-imaging of the insulator-to-metal transition in vanadium dioxide,” *Phys. Rev. B*, vol. 79, pp. 1–10, 2009.

[126] M. K. Dietrich, B. G. Kramm, M. Becker, B. K. Meyer, A. Polity, and P. J. Klar, “Influence of doping with alkaline earth metals on the optical properties of thermochromic VO_2,” *J. Appl. Phys.*, vol. 117, p. 185301, 2015.

[127] P. Petrik, L. Biro, M. Fried, T. Lohner, R. Berger, C. Schneider, J. Gyulai, and H. Ryssel, “Comparative study of surface roughness measured on polysilicon using spectroscopic ellipsometry and atomic force microscopy,” *Thin Solid Films*, vol. 315, pp. 186 – 191, 1998.

[128] H.-T. Zhang, L. Zhang, D. Mukherjee, Y.-X. Zheng, R. C. Haislmaier, N. Alem, and R. Engel-Herbert, “Wafer-scale growth of VO_2 thin films using a combinatorial approach,” *Nature Communications*, vol. 6, p. 8475, 2015.

[129] H. Kim, N. S. Bingham, N. A. Charipar, and A. Piqué, “Strain effect in epitaxial VO_2 thin films grown on sapphire substrates using SnO_2 buffer layers,” *AIP Advances*, vol. 7, p. 105116, 2017.

[130] J. Ma, G. Xu, L. Miao, M. Tazawa, and S. Tanemura, “Thickness-Dependent Structural and Optical Properties of VO_2 Thin Films,” *Japanese Journal of Applied Physics*, vol. 50, p. 020215, 2011.

[131] K. Hu, Y. Yang, B. Hong, J. Zhao, Z. Luo, X. Li, X. Zhang, Y. Gu, X. Gao, and C. Gao, “Thickness-dependent anisotropy of metal-insulator transition in (110)-VO_2/TiO_2 epitaxial thin films,” *Journal of Alloys and Compounds*, vol. 699, pp. 575 – 580, 2017.

[132] T. J. Huffman, P. Xu, M. M. Qazilbash, E. J. Walter, H. Krakauer, J. Wei, D. H. Cobden, H. A. Bechtel, M. C. Martin, G. L. Carr, and D. N. Basov, “Anisotropic infrared response of vanadium dioxide microcrystals,” *Phys. Rev. B*, vol. 87, pp. 1–7, 2013.

[133] H. W. Verleur, A. S. Barker, and C. N. Berglund, “Optical Properties of VO_2 between 0.25 and 5 eV,” *Rev. Mod. Phys.*, vol. 40, pp. 737–737, 1968.

[134] M. M. Qazilbash, K. S. Burch, D. Whisler, D. Shrekenhamer, B. G. Chae, H. T. Kim, and D. N. Basov, “Correlated metallic state of vanadium dioxide,” *Phys. Rev. B*, vol. 74, p. 205118, 2006.

[135] T. J. Huffman, C. Hendriks, E. J. Walter, J. Yoon, H. Ju, R. Smith, G. L. Carr, H. Krakauer, and M. M. Qazilbash, "Insulating phases of vanadium dioxide are Mott-Hubbard insulators," *Phys. Rev. B*, vol. 95, p. 075125, 2017.

[136] J. M. Tomczak and S. Biermann, "Materials design using correlated oxides: Optical properties of vanadium dioxide," *Europhys. Lett. (EPL)*, vol. 86, p. 37004, 2009.

[137] Z. Yang, C. Ko, V. Balakrishnan, G. Gopalakrishnan, and S. Ramanathan, "Dielectric and carrier transport properties of vanadium dioxide thin films across the phase transition utilizing gated capacitor devices," *Phys. Rev. B*, vol. 82, p. 205101, 2010.

[138] H. Zhou, M. F. Chisholm, T.-H. Yang, S. J. Pennycook, and J. Narayan, "Role of interfacial transition layers in VO_2/Al_2O_3 heterostructures," *Journal of Applied Physics*, vol. 110, p. 073515, 2011.

[139] V. Théry, A. Boulle, A. Crunteanu, and J. C. Orlianges, "Combined strain and composition-induced effects in the metal-insulator transition of epitaxial VO_2 films," *Applied Physics Letters*, vol. 111, p. 251902, 2017.

[140] D. Brassard, S. Fourmaux, M. Jean-Jacques, J. C. Kieffer, and M. A. El Khakani, "Grain size effect on the semiconductor-metal phase transition characteristics of magnetron-sputtered VO_2 thin films," *Applied Physics Letters*, vol. 87, p. 051910, 2005.

[141] J. Jian, A. Chen, W. Zhang, and H. Wang, "Sharp semiconductor-to-metal transition of VO_2 thin films on glass substrates," *Journal of Applied Physics*, vol. 114, p. 244301, 2013.

[142] J. Jian, W. Zhang, C. Jacob, A. Chen, H. Wang, J. Huang, and H. Wang, "Roles of grain boundaries on the semiconductor to metal phase transition of VO_2 thin films," *Applied Physics Letters*, vol. 107, p. 102105, 2015.

[143] B. Viswanath, Changhyun Ko, Z. Yang, and S. Ramanathan, "Geometric confinement effects on the metal-insulator transition temperature and stress relaxation in VO_2 thin films grown on silicon," *Journal of Applied Physics*, vol. 109, p. 063512, 2011.

[144] K. V. Krishna Rao, S. V. Nagender Naidu, and L. Iyengar, "Thermal Expansion of Tetragonal Phase of VO_2," *Journal of the Physical Society of Japan*, vol. 23, pp. 1380–1382, 1967.

[145] X. He, T. Xu, X. Xu, Y. Zeng, J. Xu, L. Sun, C. Wang, H. Xing, B. Wu, A. Lu, D. Liu, X. Chen, and J. Chu, “In Situ Atom Scale Visualization of Domain Wall Dynamics in VO_2 Insulator-Metal Phase Transition,” *Scientific Reports*, vol. 4, p. 6544, 2014.

[146] K. Nishikawa, Y. Kishida, K. Ito, S.-i. Tamura, and Y. Takeda, “Near-infrared localized surface plasmon resonance of self-growing W-doped VO_2 nanoparticles at room temperature,” *Applied Physics Letters*, vol. 111, p. 193102, 2017.

[147] K. Appavoo, D. Y. Lei, Y. Sonnefraud, B. Wang, S. T. Pantelides, S. A. Maier, and R. F. Haglund, “Role of Defects in the Phase Transition of VO_2 Nanoparticles Probed by Plasmon Resonance Spectroscopy,” *Nano Letters*, vol. 12, pp. 780–786, 2012.

Acknowledgements

First of all, I would like to thank Prof. Dr. Martin Dressel for giving me the opportunity to work on this interesting project at his institute and for his support and guidance during these years. I am especially thankful to Dr. Audrey Berrier, Dr. Bruno Gompf and Dr. Gabriel Schnoering for their patience and for all the help they gave me every day for the past years. I learned a lot from you and I would not have achieved this result without your contribution. I would also like to thank all the people involved in the sample production for my investigations. In particular, Dr. Florian Kuhl and Dr. Angelika Polity for providing high quality VO_2 thin films. Dr. Marcus Rommel, Ulrike Waizmann, Thomas Reindl and P.D. Dr. Jürgen Weis for fabricating state-of-the-art nanodisc samples. Many thanks to all the people of the 1. Physikalisches Institut, especially to Andrej Pustogow, Roland Rösselhuber, Weiwu Li, Olga Lukashova, Maximilian Gill who always could make my day. I enjoyed the time with you here in Stuttgart. Special thanks to Agnieszka Cienkowska-Schmidt who helped me a lot during my settlement and for the great help in many different occasions. I would also like to thank P.D. Dr. Jürgen Weis for kindly accepting to co-referee this thesis. Behind the scene, there were also a lot of people who supported me on good and bad days. I want to express my gratitude to my loving family, back in Kiev. Last but not the least, I want to thank my wife Karyna, for your everyday love and support. This work would be never be finished without you.

Appendix A

More information on the Mueller matrices of nanodisc samples

A.1 Linecut plots of the measured Mueller matrices on nanodisc samples

For the reader it might be easier to compare the measured Mueller matrices by looking on the linecut plots, at fixed azimuthal angles. The data for OD and RD samples, as well as the comparison of OD15 and HC190 samples is presented in Fig. A.1. Although for the OD05 sample the LSPR is strongly modified by the RWA, leading to the narrower spectral width and larger amplitude of the resonance, the elements of the OD10 sample Mueller matrix, display larger amplitude. As discussed in the main text, this is attributed to a larger asymmetry of the particles. One can also notice the difference in the depolarization amplitude between the samples, by looking at the M_{33}

and M_{44} elements. The random samples,as mentioned, display much smaller amplitudes, however the observed symmetry of the matrix as well as the features are the same. The amplitude of the elements in the HC190 sample is comparable to the amplitude of the OD15 sample, as demonstrated on panel (c).

In addition, one can be interested in pure depolarization index of the samples, as it is a common characteristic of the sample homogeneity. This information is presented in Fig. $A.2$. As discussed in the main text, the OD10 sample posses the strongest depolarization properties among the samples, concentrated around the LSPR, panel (a). In random samples the depolarization is small, however this can be a result of lower sensitivity, panel (b). It is interesting to note, that at oblique angles of incidence, in reflectivity configuration, the depolarization decreases, as demonstrated in panel (c), on the example of OD10 sample. In this case, the depolarization is caused by diffraction, which is apparent from an azimuthal dependence. This highlights the advantage of direct transmission measurements, where the homogeneity of the sample can be well resolved. Finally, panel (d) demonstrates that the honeycomb sample HC190 has almost no depolarization, in comparison with the OD15 sample, where the amplitude of the measured Mueller matrix elements is comparable.

A.2 Evaluation of the Mueller matrix from the dipole polarization

In both, Coupled Dipole Approximation and Discrete Dipole Approximation, the polarization vector P, containing the magnitude and the phase of the dipoles, is calculated. The information about the dipoles can be used to derive the Muller-Jones matrix. For this the dipole vector has to be evaluated for two orthogonal incident polarization states. To determine the Jones matrix elements, the dipoles are projected on the bases of the laboratory frame, defining the polarization bases, which is described as follows:

$$J_{ml}(\hat{n}_0,\hat{n}) = k^3 \sum_{j=1}^{N} \vec{p}_j^{\,l} \cdot \hat{e}_m^* exp(-ik\hat{n}\cdot\vec{r}_j), \tag{A.1}$$

where m, l=0 for p polarization and m, l=1 for s polarization. $\hat{n}_0$ defines the direction of propagation vector of incident light and $\hat{n}$ defines the direction of the propagation vector of scattered light. l stands for incident light polarization and e_m for polarization of scattered light. Once the Jones matrix is calculated it can be expanded to the form of Mueller-Jones matrix according to the equation 1.96, which is equivalent to:

$$\begin{aligned}
M_{11} &= (|J_1|^2+|J_2|^2+|J_3|^2+|J_4|^2)/2,\\
M_{12} &= (-|J_1|^2+|J_2|^2-|J_3|^2+|J_4|^2)/2,\\
M_{13} &= \Re(J_2J_3^*+J_1J_4^*),\\
M_{14} &= \Im(J_2J_3^*-J_1J_4^*),\\
M_{21} &= (-|J_1|^2+|J_2|^2+|J_3|^2-|J_4|^2)/2,\\
M_{22} &= (|J_1|^2+|J_2|^2-|J_3|^2-|J_4|^2)/2,\\
M_{23} &= \Re(J_2J_3^*-J_1J_4^*),\\
M_{24} &= \Im(J_2J_3^*+J_1J_4^*),\\
M_{31} &= \Re(J_2J_4^*+J_1J_3^*),\\
M_{32} &= \Im(J_2J_4^*-J_1J_3^*),\\
M_{33} &= \Re(J_1J_2^*+J_3J_4^*),\\
M_{34} &= \Im(J_2J_1^*+J_4J_3^*),\\
M_{41} &= \Im(J_4J_2^*+J_1J_3^*),\\
M_{42} &= \Im(J_4J_2^*-J_1J_3^*),\\
M_{43} &= \Im(J_1J_2^*-J_3J_4^*),\\
M_{44} &= \Re(J_1J_2^*-J_3J_4^*), \text{(A.2)}
\end{aligned}$$

where * denotes complex conjugate. The depolarizing Mueller matrix can be only obtained by averaging over several Mueller matrices, meaning that several Mueller-Jones matrices with different parameters, or simply with noise, has to be calculated.

At normal incidence, given that the symmetry of the system is known, calculations at only one azimuthal angle is required to recover the full azimuthal dependence. Other angles are recovered by applying rotation matrix R on the Mueller matrix:

$$M(\alpha) = R(-\alpha)MR(\alpha), \tag{A.3}$$

where R has the following form:

$$R = \begin{vmatrix} 1 & 0 & 0 & 0 \\ 0 & cos(2\alpha) & sin(2\alpha) & 0 \\ 0 & -sin(2\alpha) & cos(2\alpha) & 0 \\ 0 & 0 & 0 & 1 \end{vmatrix} \tag{A.4}$$

A.3 Validation of the regression analysis

To confirm validity of the regression algorithm, discussed in chapter 3 several test were conducted on the systems with known particle size distribution. As there is no possibility to produce samples with known distribution, synthetic distribution where pooled from combinations of simulated Muller-Jones matrices. The simplest case is with only one fixed size of the particles with r_{minor}= 94 nm and r_{major}= 104 nm. The resulting matrix is in fact a Mueller-Jones matrix, with no depolarization. The result of the fitting is presented in Fig. A.3. As expected all the weights, except one representing the known size get zero value, and the Muller-Jones matrix is successfully recovered. The same was tested on a distribution, consisting from two ellipticities, r_{minor}=92 nm, r_{major}= 103 nm and r_{minor}= 96 nm, r_{major}= 104 nm. Again, the ellipticities are successfully recovered, together with the Mueller matrix and its depolarization effects. The result of this fitting is shown in Fig. $A.4$.

Already from these two tests, it can be concluded that the algorithm correctly recovers the ellipticities from the given Mueller matrices, even despite the fact that the Mueller matrices in the population are non-trace orthonormal.

Fitting the measured Mueller matrix is however different from these tests. There are discrepancies between the simulations and the expected scattering cross section, governed by the simplifications done during the simulation. Nevertheless, there is a possibility to test if the algorithm finds an optimal solution, by adjusting the learning rate of the gradient descent.

It is observed that choosing a proper learning rate is very important to achieve convergence. For instance, the learning rate of ε=0.004, ten times larger than reported in the chapter 3, results in the MSE function as is demonstrated in Fig. $A.5$. The gradient descent first minimizes the MSE, however after reaching some minimal value the result becomes worse and an overfitting is observed. This is governed by the fact, that once the weight takes zero value, it remains 0 forever, since the gradient of zero is zero and the contribution of a specific ellipticity is lost. So it is necessary to update the weights with a proper step size, such that the weights can approach zero, but then recover its weight if necessary. Nevertheless, even with the higher learning rate, the optimal solution, with the lowest MSE, still provide a comparable result, to the one obtained in the chapter 3, as shown on the panel (d). While with lower learning rate a complete convergence of the algorithm is observed, it is possible to use higher learning rates to obtain some speed up, at the cost of accuracy.

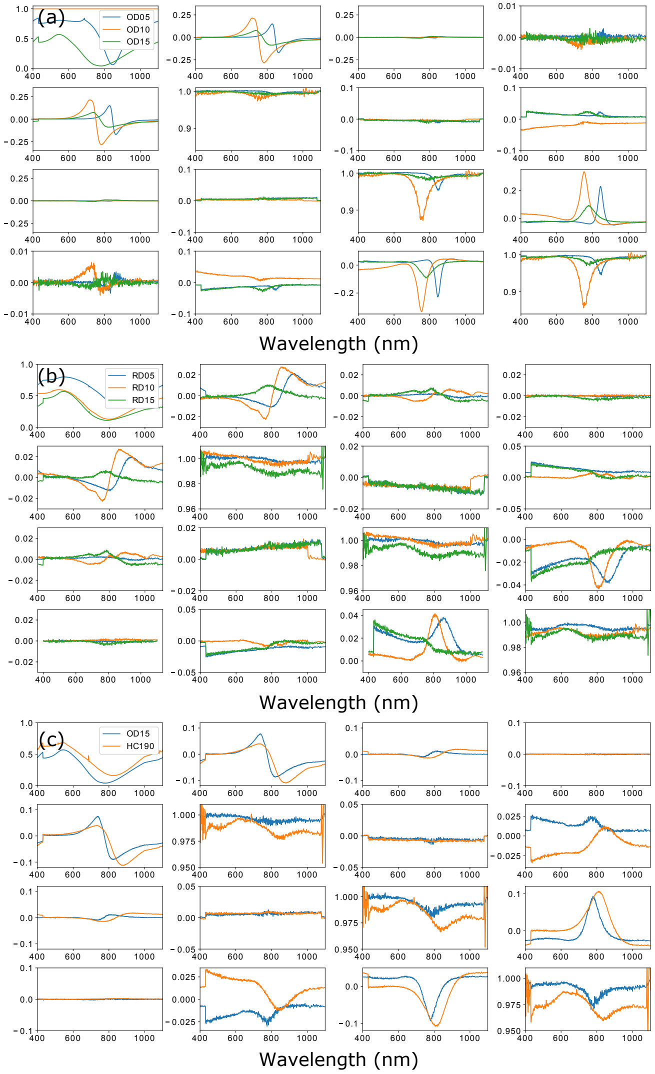

Figure A.1 (a) Comparison of the Mueller matrices of the OD samples. Intensity for the OD10 sample was not recorded (b) Comparison of the Mueller matrices of RD samples (c) Comparison of the Mueller matrix of OD15 and HC190 samples. The azimuthal angles for each sample are chosen such that the bases of the laboratory and sample frames coincide.

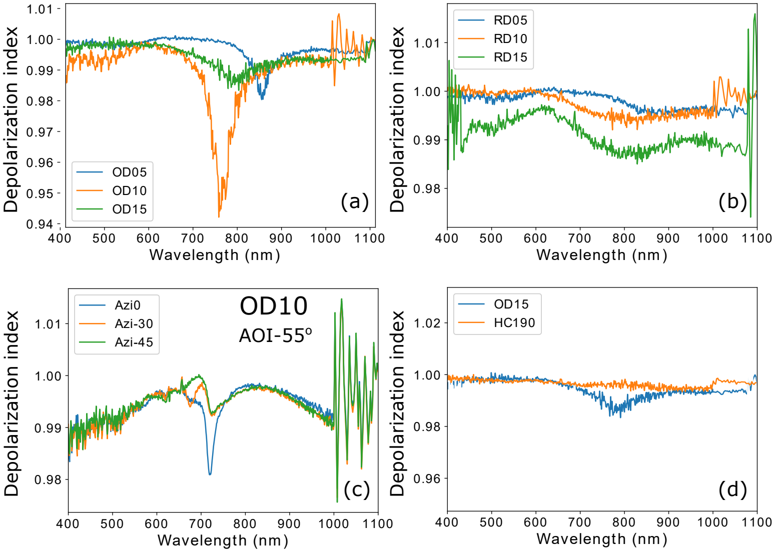

Figure A.2 (a) Depolarization index of the OD samples (b) Depolarization index of the RD samples. (c) Depolarization in the OD10 sample at different azimuthal angles measured at 55° AOI. (d) Depolarization index of the RD15 and HC190 sample.

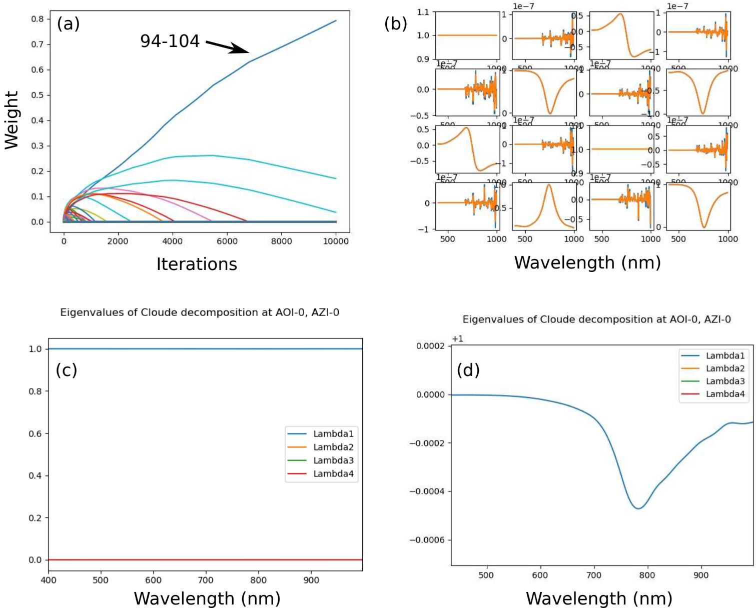

Figure A.3 Results of the fit of the known particle size distribution with r_{minor}= 94 nm and r_{major}= 104 nm. (a) The weights, representing different ellipticities of the nanoparticles versus the iterations. (b) Initial (orange) and regressed (blue) Mueller matrices. (c) The eigenvalues of the coherency matrices of the initial and the regression Mueller matrices. (d) The depolarization index of the regression Mueller matrix.

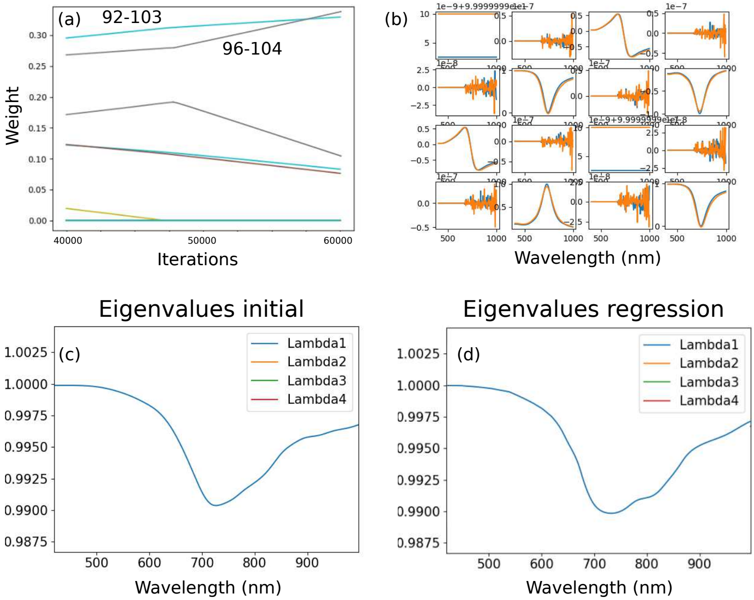

Figure A.4 Results of the fit of the known particle size distribution with r_{minor}= 92 nm, r_{major}= 103 nm and r_{minor}= 96 nm, r_{major}= 104 nm. (a) The weights, representing different ellipticities of the nanoparticles versus the iterations (after 40000 iteration). (b) Initial (orange) and regressed (blue) Mueller matrices. (c) The eigenvalues of the coherency matrices of the initial Mueller matrix. (d) The eigenvalues of the coherency matrices of the regression matrix.

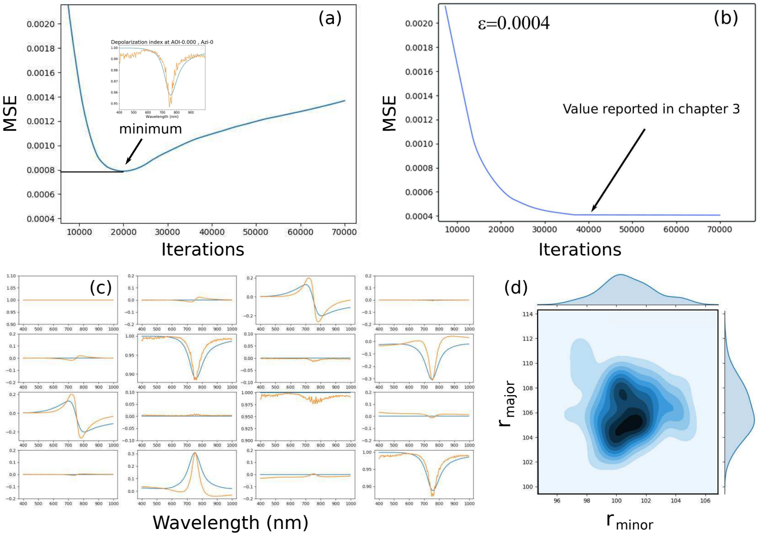

Figure A.5 (a) Mean square error of fitting with learning rate ε=0.004. The inset shows the depolarization index of the regression matrix, obtained at the minimum of the MSE, in comparison with the measured depolarization index (b) Mean square error of fitting with learning rate ε=0.0004, used for the final fitting. (c) Regression Mueller matrix obtained at the minimum of the MSE with the learning rate ε=0.004. (d) Bivariate size distribution obtained from fitting with learning rate ε=0.004, at the minimal value of MSE.

Appendix B

More information on VO_2 measurements

B.1 Depolarization in the samples

Measuring in reflectivity at oblique incidence, the superposition of reflected light from the film and the back side of the substrate occur. Since sapphire substrate is anisotropic and its thickness is well above the coherence length of the source, this superposition results in depolarization. It is crucial to get rid of the depolarization effect, as it leads to inaccurate extracted optical properties. Moreover, for temperature dependent measurements, it can lead to wrong conclusions about the statistics of the sample. As the sample becomes metallic, the reflections from the substrate are suppressed, since the light is absorbed, and depolarization index approaches 1. One might relate this effect with the percolation transition, as was done initially in this research, which is completely wrong.

Usually it is easy to get rid of this effect by roughening the back side of the substrate or merging it with the absorptive material. In case of this studies

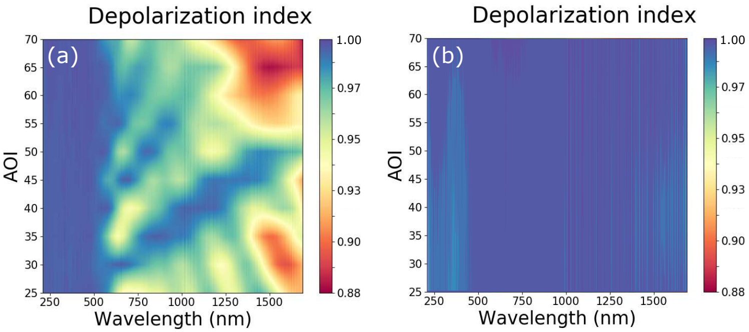

Figure B.1 Depolarization index as a function of wavelength and incident angle measured in 100 nm VO_2 film (a) without suppressing backside reflection, (b) with suppressing the backside reflection by placing the sample on a roughened copper plate.

it was impossible to apply the first option since the transmission measurement were also intended. Thus, the samples were attached to the rough copper plates. The Comparison of the measured depolarization before and after is presented in Fig. $B.1$.

B.2 Isotropic BEMA model

The isotropic BEMA model, with fixed grain shape fails to reproduce the measured optical properties of VO_2, especially with asymmetry of the transition. Even if the shape factor is adjusted to fit the heating part of the cycle, the cooling part can not be reproduced and *vice versa*. In addition, the temperature range where the discrepancy is observed strongly increases in the isotropic model. Some results of the fitting the ellipsometric parameter Ψ, with different fixed values of shape factor, are presented in Fig. $B.2$. The result signifies that the variable shape factor is crucial for describing the optical properties of the film above the plasma frequency over the complete cycle, as anisotropic transition, linked to the structural transformations influences the electronic properties by triggering changes in the shape of the clusters.

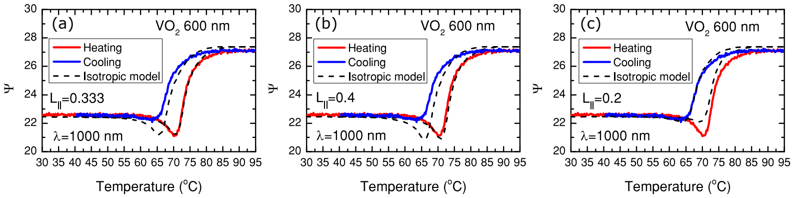

Figure B.2 BEMA fit of the ellipsometric parameter Ψ at λ=1000 nm of 600 nm thick VO_2 film during heating (red) and cooling (blue) cycles with different shape factor (a) $L_{||}$= 0.333, (b) $L_{||}$= 0.4 , (c) $L_{||}$= 0.2

B.3 FTIR measurements

In combination with ellipsometric measurements, FTIR measurements on VO_2 thin films have been performed. The data is obtained both in far-infrared (100-700 cm^{-1}) and mid-infrared (700-5000 cm^{-1}) ranges. The additional spectral range allows to determine the quality of the ellipsometric measurements and the optical models created for insulating and metallic phases. As is demonstrated in Fig. B.3(a), the measured reflectivity, obtained from FTIR measurements perfectly matches the ellipsometric data, simulated at normal incidence (AOI=0°) for insulating phase. The same is valid for the metallic phase (not shown). Thus, the optical models are justified.

The extracted conductivity for the insulating and the metallic phases is presented in panel (b). The obtained energy gap in the insulating phase of 0.62 eV as well as the dc-conductivity of $\approx$ 3000 $\Omega^{-1}cm^{-1}$ are in accord with previous studies. The overall change in conductivity demonstrates a high quality of the film. The interband transitions Δ and Ω, associated with transition from lower to upper Hubbard band and σ to π^* bands are also in perfect agreement with previous reports.

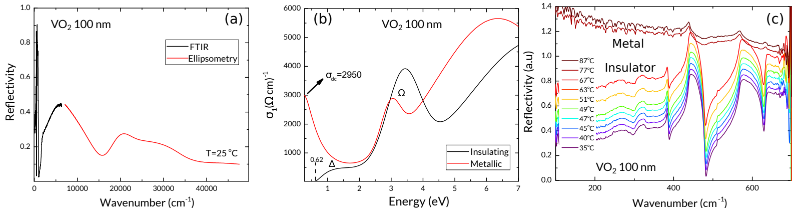

Figure B.3 (a) Measured FTIR (black) and simulated ellipsometric (red) reflectivity at normal incidence of the 100 nm VO_2 in the insulating phase. (b) Calculated spectral electrical conductivity of insulating (black) and metallic (red) phases. Δ and Ω indicate interband transitions associated with transition from lower to upper Hubbard band and σ to π^* bands respectively. (c) Measured temperature-dependent far-infrared spectra.

The far-infrared data provides information about molecular vibrations in VO_2, which are sensitive to structural changes and might serve as indication of structural transition. In particular, Raman spectroscopy allows to detect transformations associated with transition from insulating M_1 to insulating M_2 phase. Unfortunately, no indication of this transition is observed in the FTIR far-infrared spectra, shown in Fig. B.3(c), as the modes sensitive to structural changes are not IR active.

B.4 Films topography

The topography of the VO_2 films was investigated on three different scales, the macroscopic (much larger than the grain size), microscopic (comparable with the grain size) and the intermediate. While on the microscopic scale, no difference in topography is observed between the films, on the intermediate scale it is easy to evaluate both the differences in roughness and grain size, which are reported in chapter 4.

Figure B.4 presents the obtained 3D topography of the films in the insulating phase, as well as the masked 2D representation which was used

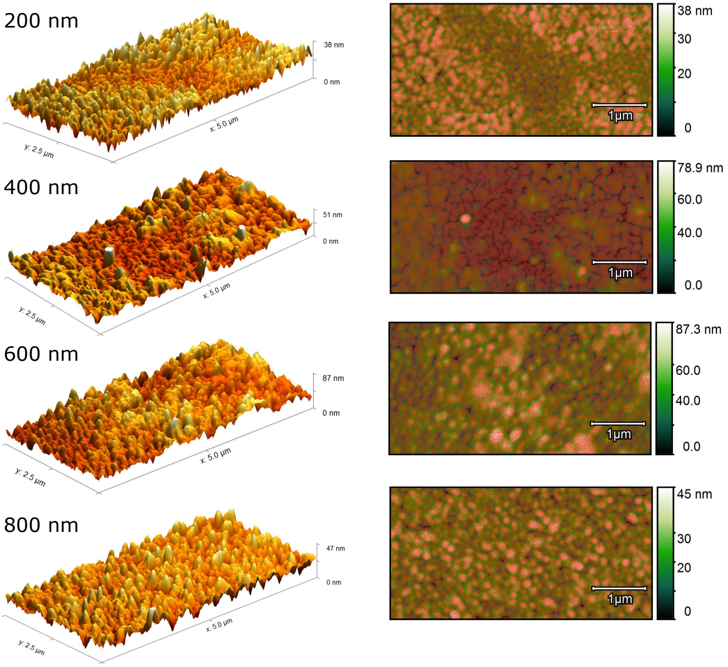
200 nm
38 nm
0 nm
y: 2.5 µm
x: 5.0 µm
400 nm
51 nm
0 nm
y: 2.5 µm
x: 5.0 µm
600 nm
87 nm
0 nm
y: 2.5 µm
x: 5.0 µm
800 nm
47 nm
0 nm
y: 2.5 µm
x: 5.0 µm
1µm
38 nm
30
20
0
1µm
78.9 nm
60.0
40.0
0.0
1µm
87.3 nm
60.0
40.0
0.0
1µm
45 nm
30
20
0

Figure B.4 3D topography of the films with 200-800 nm thick films (left column). 2D dimensional representation of the same data (right column) with the red segmentation mask used to extract the grain size properties.

to obtain an average grain size. It is clear even without the segmentation, that the grain size is the largest in the thickest films. It is also observed that there are macroscopic clusters of unconnected grains, meaning that the grain distribution is locally inhomogeneous. This means that to be able to compare the samples, when investigating the temperature dependence of the roughness, the macroscopic scale must be used.

On the macroscopic scale, two effects are observed. First, of course, is the change in roughness at higher temperatures. Second, is that the film drifts during heating. If one traces the residual particle the drift becomes clear, as

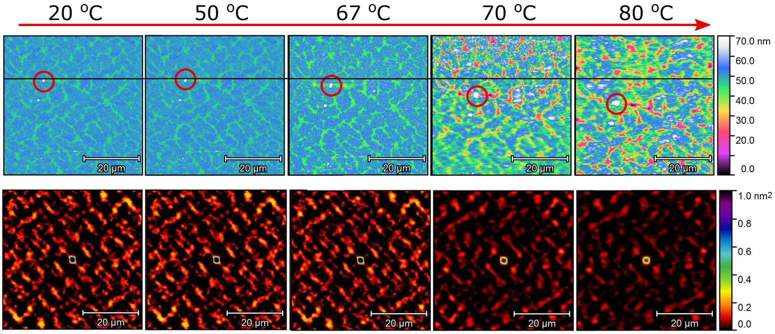
20 °C
50 °C
67 °C
70 °C
80 °C
20 µm
70.0 nm
60.0
50.0
40.0
30.0
20.0
0.0
1.0 nm2
0.8
0.6
0.4
0.2
0.0

Figure B.5 Temperature dependence of the 200 nm thick VO_2 films topography, measured during heating (upper row) and its corresponding autocorrelation function (bottom row).

shown in Fig B.5. This is the result of different thermal expansion coefficients between the copper heat-plate, the thermal grease and the substrate with the film. This is another important reason why the temperature dependent roughness measurements have been performed on the macroscopic scale, such that the drifts do not contribute much to the overall changes in roughness.